Quaternary Nanocrystal Solar Cells

Chris Cattley

Linacre College

A thesis submitted in fulfilment of the requirements for the degree of Doctor of Philosophy in Materials Science at the University of Oxford.

Dedicated to the loving memory of Edward and Edna Jennings.

Acknowledgements

I would like to thank the following, without whose help this thesis would not have been possible: Dr. Andrew Watt, for his outstanding supervision, Dr Hazel Assender for her wisdom and patience, Richard Turner, Gabriella Chapman and John Topping for their technical assistance, and everyone in the Solar Energy Materials Initiative group for their good humour and collaboration. I also wish to thank my family for their love and support, and finally Hannah for always being by my side.

Declaration

The work described in this thesis is entirely my own, except where I have either acknowledged help from a named person or given a reference to a published source.

Signed…… Date……..

Abstract

This thesis studies quaternary chalcogenide nanocrystals and their photovoltaic applications. A temperature-dependent phase change between two distinct crystallographic phases of stoichiometric Cu_2ZnSnS_4 is investigated through the development of a one pot synthesis method. Characterisation of the Cu_2ZnSnS_4 nanocrystals was performed using absorption spectroscopy, transmission electron microscopy (TEM) and powder X-ray diffraction (XRD). An investigation was conducted into the effects of using hexamethyldisilathiane (a volatile sulphur precursor) in the nucleation of small (<7nm), mono-dispersed and solution-stable quaternary Cu_2ZnSnS_4 nanocrystals.

A strategy to synthesize high quality thermodynamically stable kesterite Cu_2ZnSnS_4 nanocrystals is established, which subsequently enabled the systematic study of Cu_2ZnSnS_4 nanocrystal formation mechanisms, using optical characterization, XRD, TEM and Raman spectroscopy. Further studies employed scanning transmission electron microscopy (STEM) energy dispersive x-ray (EDX) mapping to examine the elemental spatial distributions of Cu_2ZnSnS_4 nanocrystals, in order to analyse their compositional uniformity. In addition, the stability of nanocrystals synthesised using alternative ligands is investigated using Fourier transform infrared spectroscopy, without solution based ligand substitution protocol is used to replace aliphatic reaction ligands with short, aromatic pyridine ligands in order to further improve Cu_2ZnSnS_4 colloid stability.

A layer-by-layer spin coating method is developed to fabricate a semiconductor heterojunction, using CdS as an n-type window, which is utilised to investigate the photovoltaic properties of Cu_2ZnSnS_4 nanocrystals. Finally, three novel passivation

techniques are investigated, in order to optimise the optoelectronic properties of the solar cells to the point where a power conversion efficiency (PCE) of 1.00±0.04% is achieved. Although seemingly modest when compared to the performance of leading devices (PCE>12%) this represents one of the highest obtained for a Cu_2ZnSnS_4 nanocrystal solar cell, fabricated completely under ambient conditions at low temperatures.

Statement of Originality

This thesis is an account of work carried out by the author in the Department of Materials, the University of Oxford under the supervision of Dr Andrew Watt and Dr Hazel Assender. Where the work of others has been drawn upon this is duly acknowledged in the text, and a list of references is presented at the end of each chapter. No part of this thesis has been submitted towards the completion of another degree at the University of Oxford or elsewhere. Parts of the thesis have been submitted to or published in the following scientific journals or conference presentations:

Journal Articles:

Low temperature phase selective synthesis of Cu_2ZnSnS_4 quantum dots. – Chem. Commun., 2013, 49, 3745-3747 - C.A. Cattley, C. Cheng, H.E. Assender and A. A. R. Watt.

Conference Proceedings:

Low Temperature Synthesis of $Cu_2Zn_{1-x}Sn_xS_4$ Quantum Dots for Earth Abundant Solar Cells - EU-PVSEC, Sep-2012 - Christopher A. Cattley, Cheng Cheng et al.

PbS and $Cu_2Zn_{1-x}Sn_xS_4$ Quantum Dots for Earth Abundant Solar Cells – 5th Annual IOPScience conference, -Jan 2011 - Christopher A. Cattley, Cheng Cheng et al.

Table of Contents

List of Abbreviations

$\alpha(\lambda)$	Absorption coefficient
Ag	Silver
Al	Aluminium
AM	Air Mass
Au	Gold
Btu	British Thermal Unit
c-Si	Crystalline silicon
CB	Conduction band
CdS	Cadmium Sulphide
CdTe	Cadmium Telluride
CIS	Copper Indium sulphide
CIGS/Se	Copper Indium Gallium sulphide/selenide
CTS	Copper Tin sulphide
CZTS/Se	Copper Zinc Tin sulphide/selenide
D	*Diffusion coefficient*
DOS	Density of states
DFT	Density functional theory
DSSC	Dye sensitized solar cells
EDS	Energy Dispersive X-Ray Spectrometry
E_g	Band gap
eV	Electron Volt
FF	Fill factor
FTO	Fluorine-doped tin oxide
$I_0(\lambda)$	Incident light intensity
$I(\lambda x)$	Monochromatic light intensity
J - V	Current density - voltage
J_{dark}	*Dark current density*
J_0	Reverse saturation current density
J_m	Current density that provides maximum power generation
J_{sc}	Short circuit current density
K	Kelvin
λ	*Wavelength*
l	*Charge carrier diffusion length*

μ	Charge carrier mobility
n^1, n^2	Ideality factors
NCs	Nanocrystals
NREL	National Renewable Energy Laboratory
OA	Oleic acid
ODE	1-Octadecene
OECD	Organisation for Economic Co-operation and Development
OPV	Organic photovoltaic cells
PCE	Power conversion efficiency
PL	Photoluminescence
QDSC	Quantum dot solar cells
P_{max}	Maximum power generated
p-n	positive-negative
PV	Photovoltaic
q	Charge
R_s	Series resistance
R_{sh}	Parallel resistance
SEM	Scanning electron microscope
τ	Charge carrier recombination lifetime
TCO	Transparent conductive oxide
TEM	Transmission electron microscope
TMSS	Hexamethyldisilathiane
TW	Terawatt
TWh	Terawatt hour
TWp	Terawatt-peak
US	The United States of America
UK	The United Kingdom of Great Britain and Northern Ireland
VB	Valence band
V_m	Voltage that provides maximum power generation
V_{oc}	Open circuit voltage
i-ZnO	Intrinsic Zinc oxide
n-ZnO	Negatively doped Zinc oxide
Wp	Watt-peak
XRD	X-ray diffraction
2D	Two dimensions

Chapter 1: Introduction

"The Stone Age came to an end, not because we ran out of stones, and the oil age will end, not because we've run out of oil" - Sheikh Ahmed-Zaki Yamani, Saudi Oil Minister

1.1 Solar Energy

1.1.1 Economic and Environmental Constraints

Following the fallout from the global recession of 2008, a number of key challenges have arisen which may pose a threat to the long term global economic recovery. In the short term concerns over the European debt crisis and the US housing market underline the financial imbalances that are present between indebted developed nations and developing nations such as China. However, it is the cost of energy that is predicted by many to be the biggest stumbling block on the road to a lasting recovery. The cost of energy to households and business in OECD countries has seen a dramatic rise over the last 10 years[1]. For the last three years, the price of a barrel of Brent crude oil (a representative indicator of the global oil price) has averaged more than $110, five times its price a decade ago[2]. The expectation is that the rising cost of energy may be subdued in the medium term as the impact of North American shale gas discoveries is factored into the global energy supply; however, we are unlikely to witness a return to the 1990s, when oil at $10 a barrel was one reason for strong global growth[2].

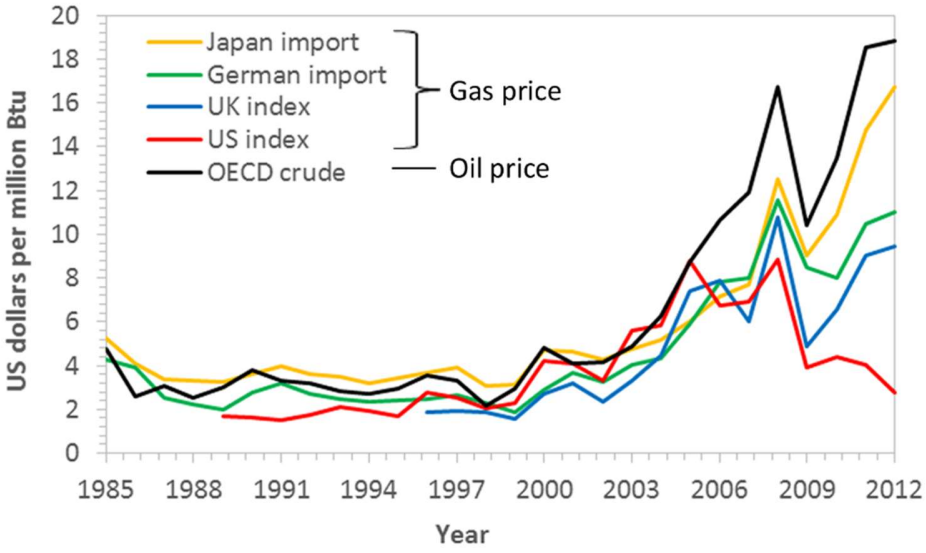

Figure 1.1-1 Graph illustrating the historic changes in gas and oil prices for selected OECD economies. Prices shown in US dollars per million British thermal units (btu)[2].

Renewables in Perspective

In the long term, global demand for electricity is set to double by 2030[3], [4] and the demand for heating and fuel is set to increase by 60% in the same period, but despite this, if renewable power generation is to realise its potential, it must first become competitive with conventional sources of power[4]. In conjunction with the projected energy deficit, there is also the issue of climate change. By one estimate the only hope of stabilizing CO_2 emissions by the middle of this century would be to generate at least 10-20 TW of our electricity supply by renewable means[5]. This equates to 50-100TWp (terawatt peak[a]) of installed PV capacity. To place this in perspective, 75TWp would require approximately 500,000 km^2 of 15% PV modules (or 0.8% of the earth's land

[a] Wp is the maximum power output of a 1m^2 panel under terrestrial insolation conditions (1.5AM) and at a temperature of 25°C. Wp and is used to compare the performance of solar panels that are made using different technologies.

surface)[6]. Given current production volumes, this would present an unassailable challenge, unless new technologies and market strategies can be developed[3].

No discussion of renewable energy would be complete without addressing the issue of government subsidies. The International Energy Agency, World Energy Outlook 2012 estimates that global subsidies to fossil fuels exceeded US$520 billion in 2011[3], compared to roughly US$90 billion in policy support for renewable energy. It is clear that renewables benefit from significantly more government support per unit of energy generated. Such a crude estimation, in no way representative of the many imbalances in the global energy market[7] however, it does help to illustrate the subsidy advantage enjoyed by renewable energy generation and it also helps to put the relative costs of implementing a renewable energy generation strategy into perspective.

The levelized cost of electricity (LCOE) generation for a given form of technology will vary wildly across the globe, due to the relative availabilities of fuel and/or the degree to which a particular generation technology is subsidised etc. For a large scale PV installation (>4kW generation capacity) the initial capital cost is typically £3000/kW[8]. The average number of sun hours for a summer day in the UK is between 4-5 hours, reducing to 1 hour in winter[3]. Averaged over a whole year, the total number of UK sun hours equals approximately 1100 hours. The warranty conditions for a commercially available PV panel typically guarantees that the panel can still produce at least 80% of its initial peak output after 20 years, representing an annual decrease in performance of approximately 1%[3]. Hence we can assume that the majority of PV panels will be replaced after 20 years of operation. The total number of hours of electricity generation for a given PV panel is approximately 22,000 hours and therefore, the capital cost per

unit energy of electricity generated is approximately £0.13/kWh[b]. This compares to £0.09/kWh[8] for a combined cycle gas turbine generator (CCGT), assuming it will generate for 24 hours a day for an equivalent lifespan of 20 years. However, the initial cost of installing the electricity generation capacity is only one side of the equation. The estimated costs of running a CCGT are significantly higher (£0.07/kWh) than those of a large scale PV facility (£0.02/kWh) due to the high price of the gas burnt to generate the electricity. When taking the operational costs into consideration the total cost of generating electricity using large scale PV becomes significantly more competitive. Despite this, fossil fuel related energy generation is still the most cost effective means of generating electricity in the UK, not least because the initial capital costs associated with renewable energy sources are so high[8].

It must not be forgotten that renewable energy is only part of the international effort to limit climate change. Other important measures to be considered include energy efficiency measures, nuclear energy, large hydro-electric generation and replacing coal-fired with gas-fired generation (particularly with the increasing accessibility of shale gas), plus carbon capture and storage, and reducing emissions from deforestation[5]. These social and political factors often combine to influence, both directly and indirectly, the strategies of both incumbent utilities as well as those businesses attempting to disrupt the market with renewable energy platforms[5]. Environmental factors also play a specific role in determining which type of renewable energy technology is most

[b] The kWh is a large unit of energy, used to measure how much energy is used on a national scale. 1 kWh is equal to 3,600,000 Joules

effective in a given region, which may explain the predominance of on and off shore wind in *blustery* northern Europe.

1.1.2 Solar Industry

Although the Sun supplies the Earth with enough energy in one hour to meet global electricity needs for one year[9], solar-generated electricity today supplies only around 0.5% of worldwide demand[6]. Efficient, robust solar cells can be produced on a truly industrial scale, illustrating that no fundamental obstacle exists to meeting an appreciable portion of our energy needs from solar-generated electricity. As a reflection of the growing strength of the industry, global investment in new solar generation jumped 52% to $147 billion in 2011[6]; almost double that of wind energy, which for so long has been the darling of the renewable energy world. The performance of solar owes much to booming rooftop PV installations in Germany, Italy and rest of Western Europe, as property owners moved to take advantage of falling panel prices[5].

Solar PV cell manufacturing capacity has grown rapidly in response to the booming global demand, initially in OECD countries, where demand first matured, and then in China, which expanded its manufacturing capacity to support growing exports. In recent years, manufacturing capacity has expanded much more quickly than the actual demand for PV panels[6]. By 2011, estimated solar cell production capacity was around 20 GW higher (two-thirds higher) than the new capacity installed worldwide that year[6]. Since 2008, there has also been a very sharp fall in the cost of purified silicon, a key

manufacturing input of so called first generation solar cells[c]. Along with cost reductions from technological learning, these two factors have driven down the cost of PV systems sharply.

Installers of solar PV systems and final electricity consumers have benefited greatly from falling solar PV prices, but solar PV manufacturers around the world, and particularly those in the United States and Europe, have suffered large financial losses[6]. A wave of consolidation has been triggered within the industry, with a view to reducing costs and boosting productivity. Several large companies have already gone bankrupt, even those manufacturers that don't rely on the silicon supply chain. Trade tensions have arisen between the United States, Europe and China, resulting in the imposition of import tariffs, on key manufacturing resources and equipment, by the United States in 2012, and Europe in 2013, on solar panels from China[10].

In spite of this short term industrial turmoil, the growing number of rooftop PV installations in Japan, US and Europe illustrate the potential demand for distributed power generation[6]. Coupled with the enthusiasm shown by individual property owners (early adopters) who have embraced the opportunity to invest, even in notoriously cloudy regions, suggests that a nascent market exists for such an application of this technology. Unlike wind or wave technology, where the efficacy of power generation increases with scale, solar PV generation is equally effective when operated

[c] Currently, 80%–90% of the PV market is based on crystalline silicon (c-Si) solar cells Although accurate data for the global consumer price of solar modules is difficult to ascertain, an estimate for the global price of c-Si PV modules in 2008 was US$ 4.05/Wp, which plummeted to just US$ 1.05/Wp by the middle of 2012[11].

in large arrays or when positioned on somebody's roof. In addition, zero moving parts and an effectively 2D construction means that Solar PV is more easily integrated in to overcrowded urban environments, where the majority of energy is consumed[1]. It is therefore uniquely capable of exploiting the inchoate demand for private, small scale power generation. As solar energy transitions from its 'alternative energy' status to a sustainably cost competitive source of energy demand can be expected to rise as both producers and consumers seek a viable hedge against the rising cost of electricity generation and fuel.

Towards this aim, semiconductor materials are being developed that can be applied, to flexible substrates, from the liquid phase (printing) or through vacuum deposition via continuous roll-to-roll processing techniques. Flexible, lightweight substrates offer the potential advantage of lowering the solar module weight, which reduce installation costs and paves the way for the wider integration of solar cells in our towns and cities, as a substitute for traditional construction materials.

1.2 References

[1] "Renewables Energy Outlook," *World Energy Outlook 2012*. pp. 210–242, 2012.

[2] T. D. Kelly and G. R. Matos, "Historical Statistics for Mineral and Material Commodities in the United States," Jan. 2014.

[3] B. a. Andersson, "Materials availability for large-scale thin-film photovoltaics," *Prog. Photovoltaics Res. Appl.*, vol. 8, no. 1, pp. 61–76, Feb. 2000.

[4] V. Sundström, "Solar energy conversion.," *Dalton Trans.*, vol. 1044, no. 45, p. 9951, 2009.

[5] "Does the world have enough materials for PV to help address climate change?," NREL, Washington D.C., Jun. 2005.

[6] "Solid State of the Market Q3 2008: The Rocky Road to $100 Billion, pp 90-95," Lux Research, Sep. 2008.

[7] C. Wadia, a. P. Alivisatos, and D. M. Kammen, “Materials availability expands the opportunity for large-scale photovoltaics deployment,” *Environ. Sci. Technol.*, vol. 43, no. 6, pp. 2072–2077, Mar. 2009.

[8] “UK Electricity Generation Costs,” London, 2013.

[9] N. S. Lewis, G. Crabtree, a J. Nozik, M. R. Wasielewski, P. Alivisatos, H. Kung, J. Tsao, E. Chandler, W. Walukiewicz, M. Spitler, R. Ellingson, R. Overend, J. Mazer, M. Gress, J. Horwitz, C. Ashton, B. Herndon, L. Shapard, and R. M. Nault, “Basic Research Needs for Solar Energy Utilization.,” in *Report of the Basic Energy Sciences Workshop on Solar Energy Utilization*, 2005, pp. 118–153.

[10] A. McCrone, V. Sonntag-O’Brien, J. G. Andreas, C. Gruening, N. Aspinall, D. Strahan, V. Gombar, V. Cuming, R. Boyle, K. Stopforth, and A. Bindingavale, “Global Trends in Renewable Energy Investments,” 2011.

[11] D. Mcginn, D. Green, R. Hinrichs-rahlwes, S. Sawyer, M. Sander, R. Taylor, I. Giner-reichl, S. Teske, H. Lehmann, and D. Hales, “Renewable Energy Policy Network for the 21st Century: Renewables Global Status Report 2013,” Milan, Italy, 2013.

Chapter 2: Literature Review

2.1 Solar Cells

2.1.1 Fundamental Physics of Solar Cells

The discovery of the photo-electrochemical effect is commonly ascribed to Becquerel who discovered a photocurrent when platinum electrodes, covered with silver bromide or chloride, were illuminated in aqueous solution[1]. Smith and Adams made the first reports on photoconductivity, in 1873 and 1876, respectively, whilst working on selenium[2], [3]. In principle, a material is said to be photovoltaic when an exposure to light of a wavelength that can be absorbed by the material is able to transform the energy of the absorbed photons into electrical energy in the form of a current and voltage. Many materials can perform this process but very few can perform it with sufficient efficiency and stability under practical operating conditions.

In reality, all solar cells are based on the absorption of radiation by a semiconductor which produces electron-hole-pairs that are segregated by a voltage[4]. These separated charge carriers perform work when the solar cell is connected to a load.

Absorption

The extra-terrestrial solar spectrum is analogous to the emission of a black body at 5760K[5]. The power density of the Sun's radiation at the edge of the earth's atmosphere is referred to as Air Mass (AM) 0[a] and is equal to 1353 W/m^2[5]. The radiation on earth's surface with perpendicular incidence of light is denoted by AM1

[a] Air Mass indicates how far the radiation has to travel through the atmosphere

and the standard spectrum used for the characterisation of solar cells is AM1.5, which equates to an effective angle of incidence of 48° and a power density of 1000 W/m^2[6]. Before reaching the earth's surface, the solar radiation is either absorbed or scattered by the atmosphere. This has the effect of moderating the intensity of radiation with different wavelengths by varying degrees as shown in Figure 2.1-1.

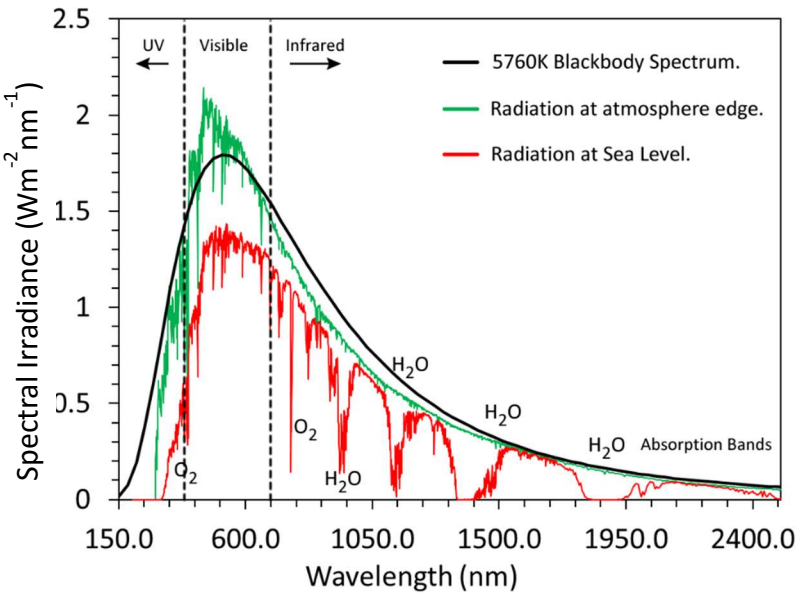

Figure 2.1-1 The spectrum of a 5760K black body, the solar spectrum at the edge of the earth's atmosphere and the spectrum at the sea level after attenuated by the earth atmosphere. (adapted from Bird et al.[5]*)*

For absorption to occur an incident photon of energy greater than the band-gap of a semiconductor material must excite a free electron from a low energy state (valence band) to a high energy state (conduction band), leaving behind a positively charged hole[b]. Due to the Columbic interaction between the oppositely charged carriers, the electron and hole pair can readily recombine. A junction is therefore necessary to extract the electrons to the external circuit before recombination can occur[4].

[b] The energy difference between the valence band (VB) and the conduction band (CB) determines the semiconductor's band gap[6].

This photon interaction with a solid material is described by the Beer-Lambert Law,

$$I(\lambda, x) = I_0(\lambda)e^{-\alpha(\lambda)x} \qquad 2.1\text{-}1$$

where $I(\lambda,x)$ is the intensity of monochromatic light, with wavelength λ, at a point x in an absorbing material, $I_0(\lambda)$ is the incident light intensity and $\alpha(\lambda)$ is absorption coefficient of the absorber material. In a conventional solar cell, the major contributory mechanism to $\alpha(\lambda)$ are band to band transitions; where photons with energy greater than the band gap (E_g) can excite an electron to a high energy state, creating a free electron-hole pair. From equation 2.1-1 we can see that if reflection and interference can be neglected, the optical penetration length of a material will be approximated to be $1/\alpha(\lambda)$. The absorption of incident photons can result in the occurrence of additional, optically stimulated transitions, within the absorber layer. These include intra-band, band to trapped-state, trapped-state to trapped-state transitions and phonon absorption[6].

PV Mechanism

Once the charge carriers are generated, some driving force must subsequently separate them. This is typically achieved by forming a junction between a positive and a negatively doped semiconductor (p-n junction). A built-in potential forms near the interface between the two oppositely doped semiconductors due to their asymmetrical electronic properties. Under equilibrium conditions a "space charge region" is formed at the junction, which is almost completely depleted of majority carriers. Consequently, the space charge region exhibits an average charge density that is equal to the net doping across the junction. The regions either side of the depletion region are commonly referred to as the neutral region[6].

There are two main routes for charge carrier separation: (i) diffusion to the junction based on carrier concentration profiles and (ii) drift, which is driven by a built-in electrostatic potential at the junction. After the charge carriers have been separated, they must be transported and extracted at the respective current collectors[4].

The flow of charge carriers constitutes a reverse current density J (Am^{-2}), known as the short circuit current density. The separation of charges sets up a forward potential difference between the two ends of the device which under open circuit conditions is known as the open circuit voltage (V_{oc}). The polarity of the open circuit voltage is such that it drives electrons in the opposite direction to that of the electron motion under short circuit current conditions. The polarity of the open circuit voltage is such that it drives holes in the opposite direction to that of the hole motion in the short circuit current configuration. This is the forward bias direction[7].

When a load is present in a circuit with an illuminated device, the overall current is decreased and a potential is developed between the terminals. The overall current can be regarded as the superposition of (i) the short circuit current, generated by photon absorption, and (ii) the reverse current, caused by the potential built-up under load. The reverse current is the current flowing through a cell in dark conditions under bias. According to the single-diode model, the dark current density is given by,

$$J_{dark}(V) = J_0(e^{\frac{qV}{nkT}} - 1) \qquad 2.1\text{-}2$$

where J_0 is the reverse saturation current density, which is a measure of recombination of a diode, V is the voltage between the cell terminals, n is the ideality

factor, k is the Boltzmann constant and T is temperature. The value of the ideality factor is dependent upon the recombination type: n=1 if recombination occurs in the neutral region and n=2 if it occurs in the depletion region[6].

The net current density of a solar cell under illumination is given by

$$J(V) = J_{sc} - J_{dark}(V) = J_{sc} - J_0(e^{\frac{qV}{nkT}} - 1) \quad \text{2.1-3}$$

Under open circuit conditions, the net current is zero, $J(V) = 0$. The open circuit voltage is given by the following equation:

$$V_{oc} = \frac{nkT}{q} ln(\frac{J_{sc}}{J_0} + 1) \quad \text{2.1-4}$$

Figure 2.1-2b shows the J – V characteristic curve of an illuminated solar cell.

90 The power density delivered by the solar cell is represented by:

$$P = JV \quad \text{2.1-5}$$

The maximum power point P_{max} is the operating point of a solar cell, corresponding to a voltage V_m and a current density J_m. The fill factor (FF) is used to describe the squareness of the J – V curve, and is given by the ratio,

$$FF = \frac{J_m V_m}{J_{sc} V_{oc}}. \quad \text{2.1-6}$$

The power conversion efficiency is the power density, at the operating point, as a fraction of the power density of the incident light, Ps,

$$\eta = \frac{J_m V_m}{P_s} = \frac{J_{sc} V_{oc} FF}{P_s}. \quad \text{2.1-7}$$

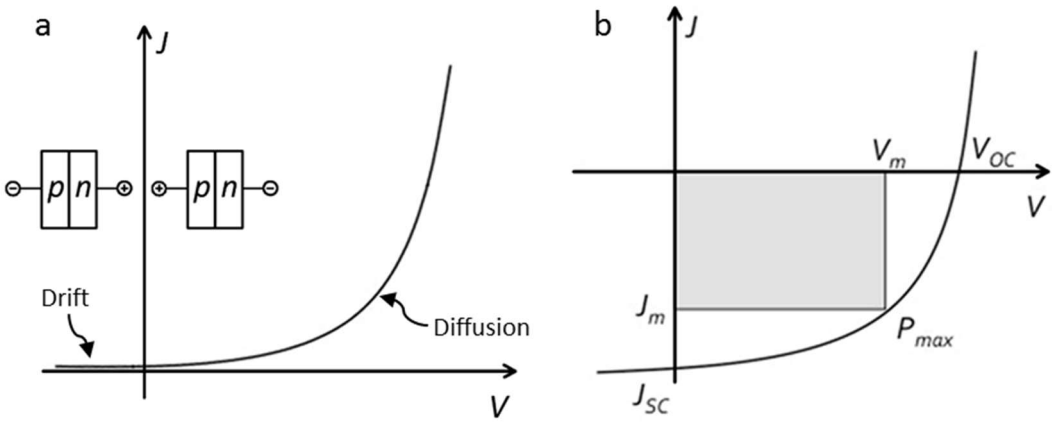

Figure 2.1-2 a) A schematic representation of an electrical circuit for a solar cell according to the 2-diode model. a) A graphical representation of the behaviour of a diode under external bias. A negative bias applied to the p-side (reverse bias) produces a small drift current whereas a positive bias to the p-side produces an exponential increase in the diffusion current (forward bias). b) Current density-voltage (J-V) characteristic curve of a solar cell. P_{max} is the operating point of the solar cell when the power density is maximum.

To maximise the short circuit current of a device it is favourable to use a material with a band-gap that is small enough to absorb photons over a wide energy range but large enough to establish a substantial potential barrier and subsequent photo-voltage[8], as well as exhibiting a high minority carrier lifetime and mobility[4]. The theoretical maximum J_{sc} can be calculated by assuming that all photons reaching the solar cell per second each create one electron-hole pair; this number multiplied by the elemental charge ($q= 1.6x10^{-19}$) represents the maximum short circuit current. The maximum value is highly dependent on the band gap, as all photons with energy less than the band gap of the absorber material will not produce any electron-hole-pairs[6].

For CZTS with a band gap of roughly 1.5 eV we can assume the maximum short circuit current to be approximately $24mAcm^{-2}$. To maximise the open circuit voltage it is important for the forward current to be as small as possible since this current will reduce the potential difference set up by the incident illumination[9].

2.1.2 Device Limitations

There are a number of loss mechanisms that determine the operational efficiency of thin film photovoltaic devices. Some of these processes can occur right at the photo excitation site before the electron and hole are sufficiently separated, while others can occur during charge transport through the film or at the interface of the film and at the metal/inorganic electrodes[10].

Optical Losses

Optical losses are associated with processes that prevent the absorption of photons in the photo-absorber, thereby inhibiting the formation of charge carriers, which may otherwise contribute to the J_{sc}[6]. A significant optical loss mechanism is reflection, whereby a proportion of the incident light, at the interface between the glass substrate and air is either reflected or scattered away from the photoactive area. Transmission is also a major optical loss mechanism, especially for long wavelength photons, which can be transmitted through the absorber[6]. In addition, light that in principle could generate charge carriers can be transmitted if the cell is too thin. The absorption coefficient is a factor that indicates how strong the absorption per unit depth of the material is, CZTS has an absorption coefficient of CZTS $104cm^{-1}$.

Recombination

Radiative recombination is an unavoidable process that results in spontaneous and stimulated optical emission[6]. The rate of radiative recombination is proportional to the product of the free carrier densities (i.e. the density of electrons multiplied by the density of holes). Auger recombination is also an unavoidable process that involves the interaction between an excited electron or hole with a second similar carrier[11]. This interaction causes a decay of one carrier across the

band gap and an increase in the kinetic energy of the other carrier by an amount equal to the band gap energy; which is ultimately lost as heat. Non-radiative recombination occurs in real devices due to the presence of trap states, typically located at surfaces or interfaces where the prevalence of defects is greatest. Traps are localized whereas the charge carriers are delocalized so the free carriers are effectively 'trapped' at these sites, which can result in non-radiative recombination. Deep traps are defined as states where, during a reasonable experimental time, charge carriers, once trapped, are not released. This not only reduces the number of extracted free charge carriers, but also results in the build-up of space charges, which can lead to the creation of an electric field that significantly inhibits the transport of other free charge carriers, and thus limits the performance of the device. Unlike radiative recombination, non-radiative recombination is an avoidable phenomenon and steps should be taken to minimize its effects.

Minimizing interfacial resistance and surface defects is key to reducing recombination, as well as optimizing carrier diffusion lengths, and ultimately maximizing device efficiency. The transport properties of NCs, which have abundant surface area, are limited by the defect states residing on the surface. These surface states, also known as mid-gap states, serve as recombination centres providing a pathway for non-radiative carrier recombination before the charges can be extracted[12], [13]. It is essential to passivate these defect states, as they lower the carrier mobility (μ) and recombination lifetime (τ), which determine the carrier diffusion length, l,

$$l = D\tau \qquad \text{2.1-8}$$

where D is the diffusion coefficient and $D = \frac{\mu kT}{q}$ according to the Einstein relation[11].

Thermalisation

Photons that exhibit energy higher than the band gap can only produce one electron-hole-pair[6]. The excess energy is lost by thermalisation, which means that the electrons that are excited to states above the conduction band emit phonons that only heat up the device. On the one hand, the band gap should be as high as possible, to reduce thermalisation[14]. On the other hand, a low band gap would be desirable to collect as many photons as possible without losing them by transmission. The optimum band gap is somewhere around 1.2-1.4 eV, which would allow a theoretical efficiency of around 30%[8]. The only possibility to avoid this problem is a multijunction cell (i.e. by having several cells with different band gaps stacked together to form a single device).

Electrical Losses

Series resistance R_s results from the internal resistance of the device material and shunt resistance R_{sh} results from short circuits forming across the p-n-junction[6]. Both R_s and R_{sh} represent a reduction in the overall device performance of a solar cell as outlined in Figure 2.1-3.

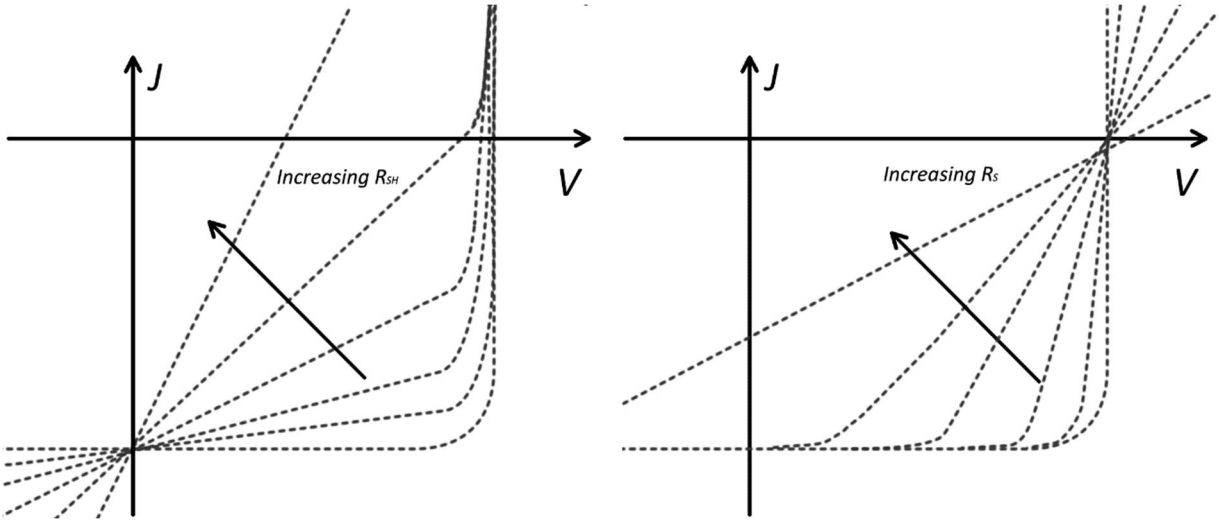

Figure 2.1-3 Representative diode curves highlighting the effects of R_{sh} and R_s. If the diode is shunted the current can partially flow back through the diode, consequently the parallel (shunt) resistance lowers the total current I: Delta J = V/R_{sh}. A completely shunted diode has an ohmic resistance, resulting in a drop in Voc. An increase in series resistance results in a larger change in voltage for a given current (Delta V = J.R_s). Very large R_s values result in a reduced J_{sc} value. In each case the loss of the rectangular shape of the diode curve results in a reduction in FF[6].

2.1.3 Characterisation

In order to identify and understand the loss mechanisms that are present in a given solar cell, a number of parameters can be extracted from the *J-V*-curve by comparing the experimental data with a suitable model.

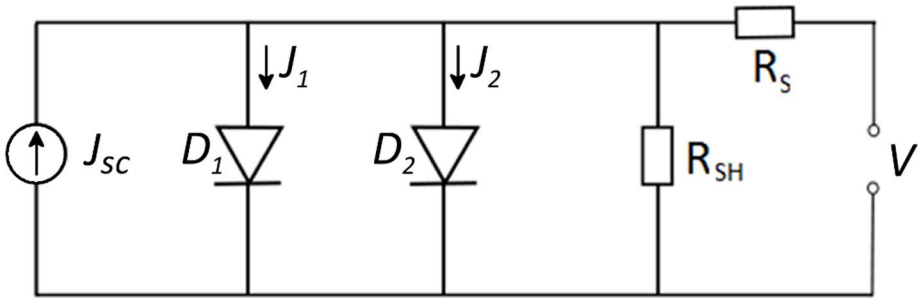

Figure 2.1-4 A schematic representation of an electrical circuit for a solar cell according to the 2-diode model.

The most commonly utilised model is the two diode model (illustrated in Figure 2.1-2 and), and is based on the assumption that the solar cell behaves like an ideal diode. The resulting diode equation for an illuminated solar cell can thus be written as:

$$J(V) = J_{sc} - J_1 - J_2 - \frac{V - JR_S}{R_{sh}}$$

2.1-9

$$= J_{sc} - J_{0^1}\left(e^{\frac{qV}{n1kT}} - 1\right) - J_{0^2}\left(e^{\frac{qV}{n2kT}} - 1\right) - \frac{V - JR_S}{R_{SH}}$$

The saturation current J_0^1 is proportional to the thermally induced charge carrier recombination/generation processes. J_0^1 increases exponentially with increasing temperature. However, in real devices the saturation current J_0 is found to be about three orders of magnitudes higher, which is due to non-irradiative charge carrier recombination/generation processes at trap states. That is why a second diode is introduced with a saturation current J_0^2. The ideality factor n^1 is normally set to be one and n^2 typically varies between one and two. The ideality factor n^2 is then used to predict the position of the trap states in the solar cell. In this simple model the photogenerated charge carriers are described by the short circuit current J_{sc}, which flows as an offset in the opposite direction. Finally, all series parallel resistances are summarized by R_s and R_{sh} respectively. That means the sum of all series resistances can be easily identified as the slope of the *J-V* curve at V_{oc} and the sum of all parallel resistance as the slope of the *J-V* curve at J_{sc}.

By measuring the dark curve of a solar cell, one can estimate the saturation current, which is mostly determined by the parallel resistance, then there is a branch where the device behaves like an ideal diode and once the internal electric field diminishes the current is determined by the total series resistance of the cell. Plotting the *J-V*-curve in a semi logarithmic scale (*ln J* vs. *V*), the exponential part becomes a straight line and extrapolating the line to the interception with the y-axis gives the saturation current J_0 (see Figure *2.1-5*a).

Recombination Limited Lifetime

Efficient device operation depends on the balance between light absorption and efficient carrier extraction[6]. A thick active layer may absorb more light and generate additional carriers but those generated near either contact may have transit times to the opposing contact that exceeds their respective lifetime. Analysis of the recombination limited lifetime of the carriers generated in a known thickness of materials sheds light on the prevalence of recombination sites within the active layer[4]. Comparing the carrier lifetime values within active layers of different thicknesses can identify the optimal thickness of a device[15]; i.e. the efficiency of thicker devices may be limited by the rate of carrier diffusion through the neutral region. This becomes significant when the device thickness is approximately equal to the sum of the minority carrier diffusion length and the depletion width. The recombination-limited lifetime is measured using the decay of the V_{oc} following illumination turn off. Figure *2.1-5*c shows a typical V_{oc} decay curve at 1000mWcm^{-2} illumination. The initial slope of the decay curve DV_{oc}/dt is related to the recombination limited lifetime (τ) by

$$\tau = -\frac{kT}{q}\frac{F_I}{\frac{dV_{oc}}{dt}} \qquad \text{2.1-10}$$

where k is the Boltzmann constant, T is the temperature, q is the elementary charge and F_I ranges between 1 at low injection and 2 at high injection rates.

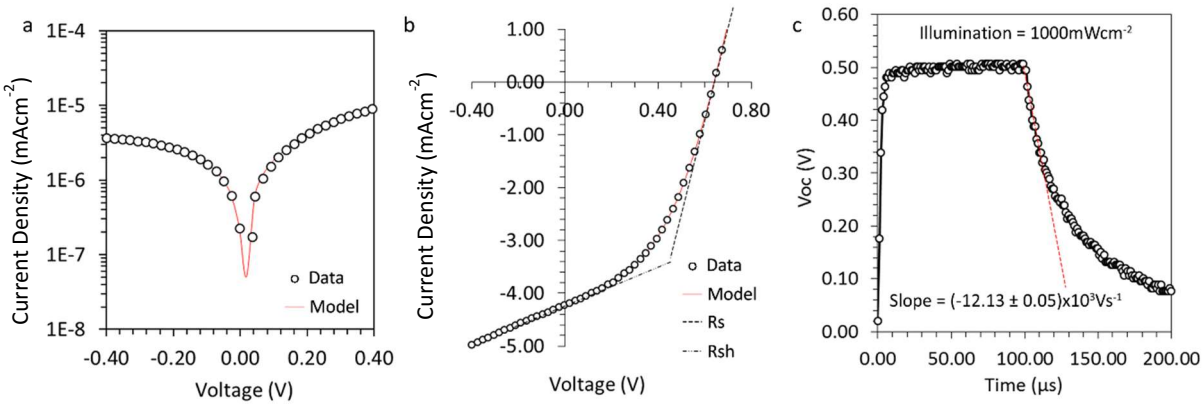

Figure 2.1-5. *a) Dark and b) light J-V characteristics of an experimental FTO/CdS/CZTS/Au solar cell. c) Representative V_{oc} decay signal (after 975 nm, 1000 mWcm^{-2} illumination turn off) and a linear best fit (dashed red line) used to determine the recombination-limited lifetime. The experimental data shown here has been analysed against a 2-diode model using a custom built Matlab™ program, based on the work of Stephen Suckow et al.*[16].

2.1.4 Solar Cell Technology

Silicon (Si) is the third most abundant element on Earth and has a near ideal band gap for maximizing the efficiency of a single junction solar cell. Silicon fabrication techniques developed by the microelectronics industry have played a critical role in the development of current Crystalline Silicon (c-Si) solar cell technology and while ground-breaking, this technology emerged with little concern for cost, capital efficiency and the product cost/performance ratio. Crystalline Silicon solar cells have now exceeded efficiency of 25% in the laboratory, and silicon modules have reached an efficiency of over 22%[8]. High purity Si used in the fabrication of conventional c-Si solar cells requires expensive and energy intensive refining of the Si feedstock. Material costs account for 40% of the total c-Si PV module[8]. Only 25% of the total costs are spent on actual cell fabrication. The rest is the module fabrication cost. Despite continued incremental improvements, crystalline silicon cells have a built-in disadvantage of fundamentally high wafer fabrication costs, caused by poor capital efficiencies and complex processing routes[8]. In addition, Si has a comparatively low absorption coefficient, which results in the transmission of useful light through thin absorber layers. It is also an indirect-

bandgap semiconductor, which means that photons with energy close to the band gap can only be absorbed in phonon-assisted processes[17]. The absorption of these photons is therefore weak, which places further restrictions on the minimum thickness for an optimal absorber layer[18]. As a result, Si based solar cells tend to be thick, inflexible and incompatible with continuous, roll-to-roll processing techniques.

So called second generation technologies use “thin film” techniques to lower materials usage, processing expenses and substrate costs. Solar cells based on chalcogenide films, such as Cadmium Telluride (CdTe) and $CuIn_{1-x}Gax(S_{1-y}Sey)_2$ (CIGS/Se), are at the forefront in thin film solar cell technology in terms of commercial production and with laboratory record efficiencies at 21% and 20.9% respectively[19]. Although commercial module efficiencies are still relatively low (10-12%) the reduction in cost per watt of power generated has moved towards 1$/W making it competitive with traditional generation methods and has resulted in a significant increase in market share[19]. In spite of this, the reliance on the heavy metal Cd and non-abundant elements Indium and Tellurium presents a barrier toward meeting the multi-terawatt target for photovoltaic power generation. Typically second generation semiconductor films are deposited using slow and expensive high-vacuum based processes[4].

2.1.5 Emerging Technology

So-called third generation technologies attempt to achieve a cost efficiency performance that is competitive with conventional electricity. Nanostructured architectures have facilitated the evolution of new strategies to design the next-generation of solar cells. Three major types of cells have dominated research in recent years: (i) dye-sensitized solar cells (DSSC), (ii) organic photovoltaic cells,

(OPV) and (iii) quantum dot solar cells (QDSC). The simplicity of the synthetic procedure, tunability of light absorption, sensitivity to diffused light, and ability to design flexible solar panels make nanostructured semiconductor materials important candidates for photovoltaic applications.

Unlike single-crystal semiconductor photovoltaics, the separation and transport of charge carriers in these cells is not exclusively driven by an electric field, the kinetics of the charge carriers also play a significant role. Typical diffusion lengths for the performance limiting photo-carriers are within the 5-500nm range in nanostructured semiconductors, but the absorber thickness required to achieve complete absorption of solar irradiation is often considerably greater. This results in a possible trade-off between electron/hole extraction and optical absorption if a planar absorber is used. To break this compromise, 3rd generation solar cells make use of their highly nanostructured interfaces. Nanostructured photovoltaic materials generally contain significant degrees of disorder, often because of the boundaries that define the randomly orientated crystalline domains in both organic and inorganic semiconductors. Transport within these domains, as well as at their boundaries (including transport-limiting mechanisms, such as charge carrier trapping), requires particular attention and optimization. It's not all bad news though; one unique example of a beneficial boundary effect is the quantum confinement of charge carriers to well-defined nanocrystalline domains, such as in semiconductor quantum dots[20]. This effect allows the tuning of energy levels in solar materials. Since relying on the band-gap of a single absorber limits the solar-cell power-conversion efficiency to 31%, determined by the Shockley-Quiesser limit, stacking cells with different band-gaps to create multi-junction configurations can increase the power-conversion efficiency to a theoretical limit of 68%[10]. Processing multiple semiconductor

materials within the same device structure is relatively simple when using NC synthesis techniques, making NC multi-junction solar cells an achievable goal for the future. In addition, the ability to effectively tune the band gap of a NC material allows for the selective transmittance or reflectance of light of different wavelengths. NC solar cells can therefore be designed to appear a variety of different colours, albeit at the cost of conversion efficiency.

Ultimately, by minimizing the recombination losses at the nanostructured interfaces, the charge carriers can be transported to the collecting electrodes and thus deliver good power conversion efficiency. Efficiencies in the range of 11.9% for both DSSC and OPV solar cells have already been achieved, while the PCE of QDSC devices has increased from 1 to 8.6% in last 5 of years. More recently, the reported efficiency of 17.9% for a solar cell, utilising a perovskite (CH3NH3)PbX3 (X = Cl, Br, I) photoactive layer, has been revealed as an additional contender to the now well-established DSSC and OPV solar cells[21]. Perovskite-based nanostructured solar cells commonly incorporate perovskite materials, such as $(CH_3NH_3)Pb(I_{1-x}Br_x)_3$ together with TiO_2 to form a p-n hetero-structure[22]. A number of studies have reported favourable charge transport properties for perovskite materials, which has led to high solar cell efficiencies. However, as with other 3rd generation technologies, the high temperatures required to produce the compact TiO_2 electron transport layer and the innately poor stability of lead based perovskites has, as of yet, limited the application of low cost processing techniques for the production of perovskite based solar cells[23].

2.2 Materials selection

The search for a suitable single band gap semiconductor material for terrestrial photovoltaic solar cell applications has been undertaken by numerous research bodies and commercial enterprises around the world[24].

2.2.1 Tertiary and Quaternary Chalcogenides

Chalcopyrite solar cells have progressed from first proof of concept on melt-grown crystals (Wagner et al. 1974) to high-efficiency thin-film laboratory devices[25]–[27]. The highest efficiency cells have been optimised to include a very thin yet highly graded (by composition) absorber layer. The composition gradient increases the conduction band energy and thus the driving force for minority charge carrier collection, whilst the minimal thickness reduces the risk of recombination during charge transport across the highly polycrystalline film structure[28]. To achieve this, careful control of the temperature and elemental composition is required during the deposition of the absorber layer and as such a three step co-evaporation technique is employed in the record CIGS/Se cell[27].

Würth Solar have pioneered the development of chalcopyrite PV modules however, as production volumes increase, concern has arisen as to whether limits in the world supply of In will restrict "low cost" production[29]. The current cost of In adds only 1 to 10 ¢/Watt to the price of a module since the current manufacturing rate is in the hundreds of MW/yr range. Manufacturing volumes are expected to push into the gigawatt/yr (GW/yr) range in coming years due to the combination of relatively high efficiency (compared to CdTe or α-Si) and potentially low processing costs (compared to single-crystal Si)[29]. A tenfold increase in the price of indium would be problematic for the necessary sub-$1/W manufacturing cost. Estimates of when In scarcity will become important to module prices range in CIGS/Se

manufacturing volumes from 4 GW/yr to over 100 GW/yr[30]. If estimates of 4 GW/yr are correct, indium scarcity could impact the industry within 10 years[31]. One estimate, based on the current demand for In from the flat panel display industry, predicts that the world supply of In could only support a CIGS/Se production capacity of ~70GW/yr, which is well below the desired TW power demand[32]. The emerging Kesterite $Cu_2Zn_{1-x}Sn_x(S_{1-y}Se_y)_4$ (CZTS/Se) material system provides a welcome diversification away from the non-abundant and toxic elements used in CdTe and CIGS/Se devices.

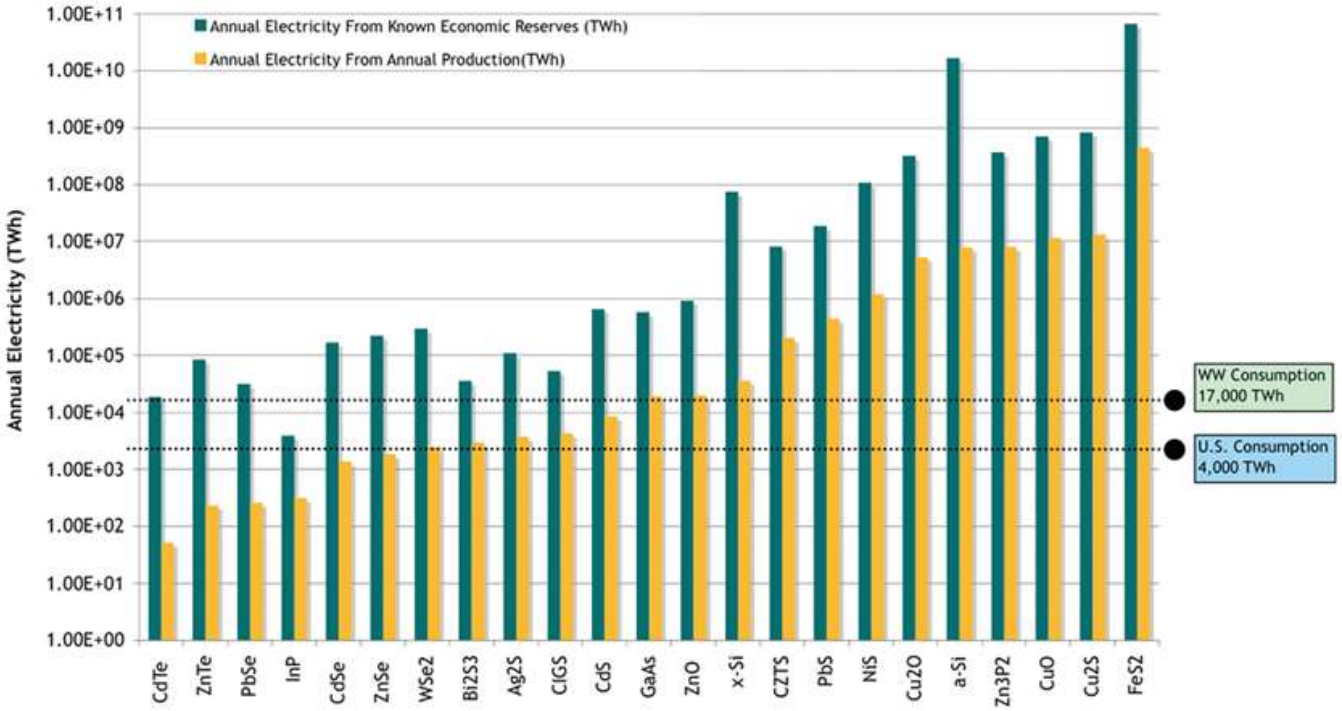

Figure 2.2-1 Annual electricity production potential for 23 inorganic photovoltaic materials together with the electricity consumption figures for comparison [taken with permission from[8]*].*

In a heavily cited review by Wadia et al.(Figure 2.2-1) based upon known economic reserves, it is suggested that CZTS/Se is one of a very small number of direct band gap semiconductor materials that could meet the current demand for power generation, whilst ensuring a significant cost advantage over conventional thin film PV technology[8], [32].

2.2.2 CZTS/Se Material System

Within the kesterite chalcogenide system there are a number of elemental variations that have garnered interest in the literature over the years[33]. Many of these different kesterite phases exhibit a direct band gap in the optimal range for photovoltaic energy conversion and all have been reported to exhibit p-type semiconductor characteristics[33]. Despite this, relatively few of these compounds have been employed for use in actual solar cells.

The Ternary Phase Diagram

A suitable phase diagram for CZTS would require the use of 3 dimensions, however if a fixed sulphur concentration is assumed then a ternary phase diagram can be used to visualise the formation of various binary and ternary phases. There are ten fields drawn in the phase diagram shown in Figure 2.2-2. Each field means the presence of CZTS plus the one or two secondary phases that are noted. The central region represents stoichiometric CZTS. All secondary phases contain sulphur and it is assumed that no metallic phases form as a sufficient sulphur concentration is used during the synthesis.

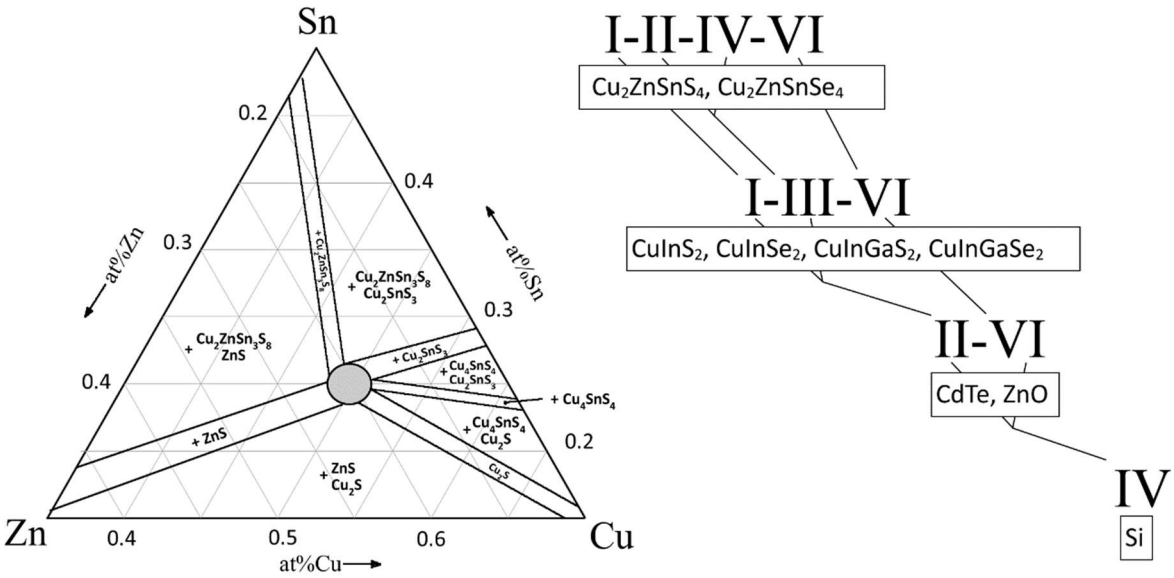

Figure 2.2-2 Equilibrium ternary phase diagram, valid at 400°C, labelled with the major secondary phases associated with the CZTS materials sytem (sulphur fraction =50%). The central shaded area represents pure CZTS. The diagram on the left illustrates how alternative compound semiconductors are obtained by substitution of elements from higher or lower periodic groups (adapted from study of phase instability by Scragg et al[34], [35]*) .*

Copper sulphide has been reported to form as many as thirteen different polymorphs, many of which have broad composition ranges. Of the major polymorphs, low chalcocite (monoclinic), high chalcocite (hexagonal) and djurleite contain hexagonal close packed lattices of sulphur atoms, while digenite (cubic) and tetragonal chalcocite form cubic close packed sublattices[36]. Monoclinic chalcocite is the only thermodynamically stable phase at room temperature. In bulk systems it transforms into hexagonal chalcocite at 103°C[37]. Above 435°C, hexagonal chalcocite converts to a cubic phase, which is equivalent to high digenite but shows a greater occupancy of the copper sites[38]. Monoclinic chalcocite possesses a distorted structure closely related to hexagonal chalcocite, and its stoichiometry can vary from $Cu_{1.98}S$ to Cu_2S[38]. Tetragonal chalcocite is a high pressure phase (>0.8kbar) but it can be quenched to ambient conditions. The monoclinic unit cell of djurleite consists of two types of hexagonal close packed sulphur atoms within each unit cell, where 20 and 32 copper atoms form triangular coordination units with sulphur atoms in and

between the layers of sulphur. Accompanying them are nine copper atoms in a distorted tetragonal coordination and one in linear coordination with the remaining sulphur atoms. Nanocrystals of chalcocite and the copper-deficient djurleite phase have been extensively studied in past years because of their photovoltaic and plasmonic properties using a number of synthetic techniques. The inherent phase-instability between low chalcocite and djurleite has inhibited the development of monoclinic-Cu_2S:CdS thin film cell photovoltaics[38]. Djurleite formation can reduce photovoltaic efficiency by up to 60% because of shifts in band gap and subsequent decreases in the minority carrier diffusion length[38]. The resultant partially filled bands give rise to plasmonic absorption in the near infrared[39]. The spontaneous transformation to djurleite is prevalent in many Cu_2S NC synthesises reported in the literature[39], [40], owing to the fact that it has a lower free energy than low chalcocite at room temperature because of its lower crystallographic symmetry[39]. In many cases this transformation makes it difficult to reliably obtain pure nanoscale monoclinic or hexagonal chalcocite using solution based NC synthesis techniques[39], [40].

The high concentration of intrinsic defects in Cu_2S means that any formation of this heavily doped phase within the CZTS cell will act as a metal[41]. Such conducting phases within a solar cell can significantly enhance recombination or even present shunt pathways through the absorber layer, thereby limiting the overall performance[6].

Tin sulphide (SnS_2) is an n-type semiconductor with a band gap of 2.2 eV[42]. This secondary phase could work as an insulator, but if existing in larger amounts it is also possible that it forms a second diode with opposite polarity to CZTS, which

would act as a barrier to carrier collection and reduce the fill factor. SnS is not noted in the ternary phase diagram but could be found in films with an excess of Sn.

Zinc sulphide can be found as a secondary phase in the Sn and Cu-poor region of the ternary phase diagram, as well as in the Zn-rich region. Due to its high band gap (3.54 eV), it is likely that any presence of ZnS would both reduce the active area (i.e. the area where electron-hole-pairs are produced) and inhibit the current conduction in the absorber later[43]. It crystallizes in the sphalerite and the wurtzite structure and forms a wide band gap semiconductor in either case[43]. Cu_2SnS_3 (CTS) is a secondary phase that is most likely to form in Zn-poor phases[44]. Similarly, to Cu_2S, it is highly doped and as such, tends to exhibit properties that make it a highly detrimental secondary phase. Due to its higher diffusion rate (compared to Zn and Sn, and particularly sulphur), Cu is likely to diffuse to the surface where it readily forms copper sulphides[44]. This phenomenon also means that copper sulphides are often found at the surface of CZTS phases.

2.2.3 CZTS Phase Stability

It has been well covered in the literature that other crystal structures with the same stoichiometry exist for I_2-II-IV-VI_4 compounds: kesterite, Stannite, or primitive mixed CuAu structures may form under different conditions[45]. Density functional theory (DFT) calculations predict that the kesterite structure is the lowest energy configuration for both the S and Se based system and thus is the most stable structure[46]. Part of the comprehensive theoretical study conducted by Walsh et al.[47] included an investigation of the stability of single-phase stoichiometric material which was calculated as a function of the chemical potential of constituent atoms for both kesterite systems[47]. Single phase kesterite CZTS only occurs within

a diminutive chemical potential space around: μCu = -0.20eV, μZn = -1.23eV and μSn = -0.50eV. By contrast the chemical potential range for single phase chalcopyrite $CuInSe_2$ is much greater: -0.4< μCu <0eV and -0.4eV< μIn <-1.8eV (as determined by Zhang et al.)[48]. Thus it is predicted by Walsh et al. that forming a single phase of kesterite material will be more difficult than forming a single phase of chalcopyrite[47], a view that is supported by other DFT studies[49]–[52]. The effect of alloying CZTS and CZTSe has also been investigated using DFT calculations. It was shown by Chen et al. that the enthalpy of formation for the CZT($S^{1-x}Se^x$) is very small, indicating that the mixed-anion alloys are highly miscible, and that the cations maintain the same ordering preferences as in pure kesterite[53].

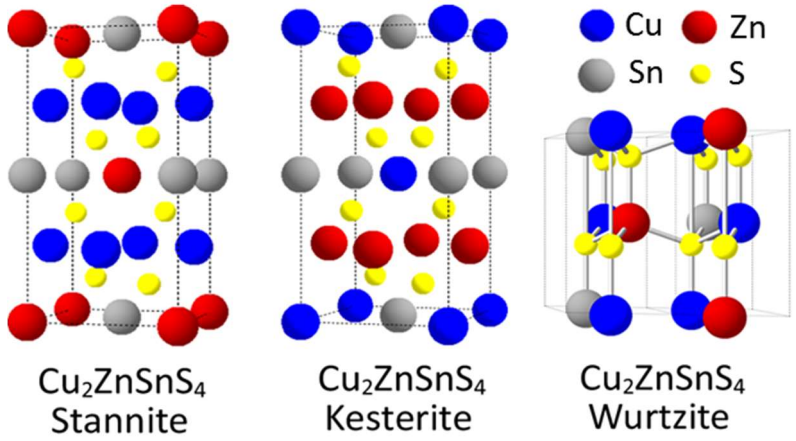

Figure 2.2-3 A schematic illustration of a unit cell of kesterite-tetragonal, stannite-tetragonal and wurtzite hexagonal(x2) Cu_2ZnSnS_4, illustrating the relative positions of the Cu, Zn, Sn and S atoms in each crystal structurs (image produced using CrystalMaker™ software).

Experimentally, bulk samples of CZTS and CZTSe are observed to crystallize in either kesterite[54] or stannite[55] structures (Figure 2.2-3). However, Schorr et al.[56], [57] have observed Cu and Zn partial disorder in Cu_2ZnSnS_4 samples using neutron scattering. Their measurements also showed that a partially disordered kesterite structure can exist, in which the atoms in the Cu+Zn (001) layer of the kesterite structure are disordered, while the atoms in the Cu+Sn layer reside in their original positions. The large chemical and size mismatch between Cu and Sn

compared to Cu and Zn, accounts for significantly different randomization energy values, as well as an order of magnitude difference in the relative volume expansion; brought about by the exchange of one atom for another in the crystal lattice. From the defect complex analysis discussed earlier it has been calculated that the anti-site pair [Cu^{-}_{Zn}+Zn^{+}_{Cu}] has a formation energy of 0.21 eV/pair, which is lower than all other defect complexes, thus indicating that a high population in Cu_2ZnSnS_4 is likely. This anti-site pair can also be taken as the occupational exchange between the Cu and Zn crystallographic sites, which helps to explain Cu and Zn partial disorder in Cu_2ZnSnS_4 samples. The crystallographic symmetry of partially disordered kesterite is equivalent to stannite, therefore it is argued that some of the experimental samples that have been identified as stannite may be the partially disordered kesterite instead[55], [58]. This may explain the discrepancies between theoretical and experimental values for opto-electronic properties of CZTS/Se kesterite and stannite structures that are present in the literature, which will now be discussed in more detail.

2.2.4 Optical Properties

The respective band-gap for selenide and sulphide kesterite crystals are reported to be very similar to their corresponding chalcopyrite equivalents[49]. Furthermore, each material is thought to maintain a good alignment with the CdS conduction band at -4.3 eV, which explains the success of the CdS (buffer) and i-ZnO/n-ZnO/Al (window) layers in finishing of Kesterite devices.

As part of the in-depth experimental and theoretical study into CZTS/Se, Walsh et al. have published the results from a series of density of states (DOS) studies for both kesterite and stannite structures These calculated band alignment results

provide basic physical parameters, which are important for the device simulation and optimization process. It was found that the band gap of stoichiometric kesterite CZTS is 1.50 eV, whereas the band gap of kesterite CZTSe is 0.96 eV. The upper valence band is mainly derived from the hybridization of anion-p and Cu-d states. This can be explained by the fact that Cu has a higher d-orbital energy than Zn and Sn, whilst the low conduction band is mainly formed by the hybridization of the anion-s,p and Sn-s orbitals, which can be explained by the s-orbital energy of Sn being much lower than the other cations. This observation however, does not agree with the interpretation of some of the experimental absorption data published by Wibowo[58], Matsushita[59] and Babu[55] et al. who interpret that the band gaps of both kesterite and stannite CZTSe are nearly the same as CZTS at approximately 1.5 eV. It is argued by Walsh et al. that the discrepancy between the predicted values and the experimental observations of Babu et al. could be attributed to either poor sample quality or incorrect linear interpolation in determining the band gap. Furthermore, Ahn et al.[60] have observed that there is an over reliance on XRD analysis for phase identification; despite there being substantial evidence for the coexistence of secondary phases (i.e. ZnS/Se and Cu_2SnS/Se_3) which cannot be distinguished from CZTS/Se by XRD analysis alone. In support of the theoretical results, a photoluminescence (PL) study conducted by Altosaar et al[61]. showed that the difference in PL peak energies between CZTS (1.3 eV) and CZTSe (0.8 eV) is approximately 0.5 eV, which is consistent with the values calculated by Walsh et al. as well as earlier transmission measurements published by Friedlmeier et al.[62] An alternative hypothesis proposed by Persson et al. is that the larger than expected experimental value for the CZTSe band gap can be accounted for by the presence of an absorption tail for photon energies 1.0-1.6eV[49]. The band gap of kesterite CZTS is

calculated to be 0.12 eV larger than that of stannite CZTS whilst the disorder associated with partially-kesterite CZTS is predicted to have a much smaller effect, resulting in a reduction in the band gap relative to pure kesterite of 0.04 eV. However, these values are yet to be confirmed, to this level of accuracy, by experimental measurement, indeed a number of researchers report that the crystal structure has a negligible effect on the band gap[45].

2.2.5 Defect Physics

Chemical defects impose limits on composition and synthesis routes that would traditionally yield high-efficiency solar cells[63]. One of the important factors that leads to high efficiency of the $CuIn_{1-x}Ga_xSe_2$ solar cells, despite having poor crystallinity, is that intrinsic defects in $CuInSe_2$ undergo self-passivation of the In_{Cu} deep donor level, by forming the $[2V^{-}_{Cu}+In^{2+}_{Cu}]$ complex[48], [64], which leads to the formation of charge separated α and β phases[48]. In addition, the region of $CuInSe_2$ at the interface with the CdS buffer layer can be type inverted to become n-type, which facilitates the separation of the electron-hole pairs. However, this electrically benign character disappears in the wider-gap $CuGaSe_2$ (1.68 eV), because of the deep Ga_{Cu} donor level forms an electron trap, which pins the Fermi level, thereby causing an n-type doping deficiency[49]. This restriction has limited the further improvement of the solar-cell efficiency through increasing the Ga:In ratio in order to increase the band gap and thus the open circuit voltage. The $CuIn^{1-x}Ga^xSe_2$ solar cell with the highest efficiency has an absorber band gap less than 1.2 eV[28] which is lower than the optimal band gap (1.4–1.5 eV) for a single-junction cell. CZTS has a band gap (1.5 eV) that is closer to the value of $CuGaSe_2$ (1.7 eV) and therefore it is important to know whether Cu_2ZnSnS_4 can be easily doped n-type and whether its defect properties give a similar electrically benign character as $CuInSe_2$. To address these

questions, a number of research groups have used DFT[65] to conduct theoretical studies into the structural, electronic, and defect properties of the Kesterite system. Many of these studies take the form of a comparison between Kesterite and its close cousin the Chalcopyrite system.

Due to the presence of the three cations (Cu^{2+}, Zn^{+} and Sn^{+}) there is the potential for a larger number of intrinsic defect states in kesterite (CZTS) than would be present in the ternary chalcopyrite (CIS) structure[63]. Unfortunately, the characterization of defect levels in CZTS/Se is so far very poor, partially because the synthesis of high-quality crystals with low-defect density has proven difficult and partially because the intense interest in this kesterite compound does not have a long history. However, formation energies and transition energy levels within the band gap have been calculated for the 13 dominant defects that do not involve the unlikely situation of a cation on an anion lattice site or vice versa[46]. Of these 13 defects, five have relatively low formation energy for Cu-poor kesterite. These five low-formation-energy defects are, in order of increasing formation energy: copper on zinc site (Cu_{Zn}), copper vacancy (V_{Cu}), zinc on tin site (Zn_{Sn}), zinc vacancy (V_{Zn}) and copper on tin site (Cu_{Sn}). The formation energy of Cu_{Zn} is significantly lower than that of V_{Cu} and Zn_{Sn}, predicting that Cu_{Zn} should be the dominant intrinsic defect for CZTS[47]. Cu has a valence of 1+ and Zn has a valence of 2+, which accounts for the predicted p-type behaviour, observed experimentally by Mitzi et al[66] (and others). A graphical representation of the calculated values published by Walsh et al. for the intrinsic defect ionization levels within the band gap of kesterite CZTS is shown in Figure 2.2-4 below. A study by Nagoya et al, performed at a similar level of theory, reports consistent ionization levels and thereby supports the conclusion of a small chemical potential range for stable kesterite CZTS[52]. The work of Biswas et al is more

focused on the higher energy (less abundant) defects involving Sn, and highlights the fact that the associated donor states are deep, arising from the accessibility of both Sn(II) and Sn(IV) oxidation states[63]. The existence of both oxidation states is well understood, and is associated with the fact that Sn has a low energy 5s and two higher energy 5p valence states[67].

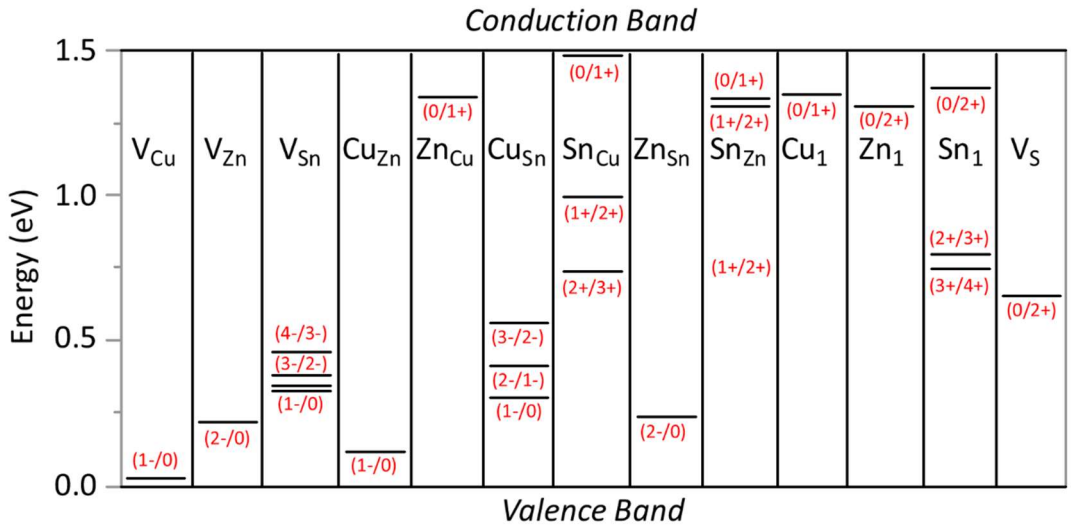

Figure 2.2-4: Calculated transition energy levels of intrinsic defects in the band gap of Cu_2ZnSnS_4 [adapted from[68]*].*

By also considering defect complexes under different structural configurations, Walsh et al.[53] have shed some light on the possible mechanisms behind the electro-optical properties of CZTS, whilst at the same time highlighting deficiencies in the conclusions posed by other studies. Due to charge compensation, or the charge transfer from donor to the acceptor, the defect states that form each complex are charged. The Coulomb interaction makes them attracted to each other and thus the most closely bound configuration exhibits the lowest formation energy[49]. By controlling the concentration of defects one can optimize the carrier concentration, and thus the electronic properties of the CZTS for solar cell applications. In practice, Cu-poor and Zn-rich conditions are predicted to optimize efficiency by encouraging the formation of a [V^{-}_{Cu}+Zn^{+}_{Cu}] pair[67], leading to the passivation of deep levels[51].

This effect is also predicted by Paier et al[51]. and has been observed experimentally by Tanaka et al[69] however, it is important to note that the precipitation of ZnS is to be avoided in order to optimise device efficiency. In comparison with CIGS/Se, the greater chemical freedom allowed by CZTS/Se increases the number of defect complexes meaning the passivation of deep traps is more probable[47]. This indicates that CZTS/Se thin film solar cells are predicted to possess a similarly benign electronic character. However, there is also the potential for a greater number of deep level traps and so despite the defect complex passivation effect, if a sample is very highly disordered, some deep traps may still exist, acting as free carrier traps or recombination centres.

N-type doping is unlikely (for both chalcopyrite and kesterite) due to the high formation energy of the donor defects and low formation energy of acceptor defects; although low formation energy defects with energy levels deep within the gap may still exist, they are predicted to be largely benign due to the formation of defect complexes[47].

The negative formation energy associated with the formation of the dominant defect (Cu_{zn}) accounts for the experimental observation that intrinsic CZTS samples are always p-type. As a consequence of the strong energetic preference for acceptor defects, any free electrons that may be used to n-type dope CZTS will be readily neutralized, thereby pinning the Fermi level away from the conduction band minimum. This theoretical observation suggests that severe difficulties may be encountered when doping CZTS n-type. Although yet to be experimentally verified, if accurate, this would mean that unlike with $CuInSe_2$, a doping type inversion cannot form at the interface between absorber and window layers to facilitate efficient electron hole separation[47], which in turn may limit the performance of CZTS solar

cells. The band gap of CZTSe is approximately 0.4 eV smaller than CZTS in the same crystal structure whereas the band gap of a mixed alloy of CZTS/CZTSe decreases with Se content almost linearly[47]. The conduction band down-shift contributes more to the gap decrease than to the upward shift of the valence band. This shift of the band edges makes the CZT($S^{1-x}Se^{x}$) alloys with high Se concentration easier to dope both n-type and p-type[47]. One important characteristic in the band alignment between CdS and CZTS is the type-II band offset, i.e. the conduction band minimum of the CdS window layer is lower and the valence band maximum of CZTS absorber layer is higher, which facilitates electron-hole separation. By contrast, the band offset between CdS and $CuInSe_2$ is type-I in nature[64]. However, it has been proposed that in CdS/$CuInSe_2$ solar cells, there is an ordered vacancy compound layer (such as $CuIn_3Se_5$) at the surface of the $CuInSe_2$ absorber layer, which exhibits a type-II band line-up with respect to $CuInSe_2$[47]. This band bending at the absorber layer benefits the electron-hole separation and is reported to be the major factor for $CuIn^{1-x}Ga^{x}Se_2$ cell performance, according to device simulation[70]–[72]. Although an ordered vacancy compound has not yet been observed for a Cu_2ZnSnS_4 structure, the type-II band line-up of CdS/Cu_2ZnSnS_4 can be a positive factor for achieving high conversion efficiencies in future CZTS solar-cell devices. The balance between the band gap size and the doping ability may be critically important in determining the optimal alloy composition to achieve high-efficiency CZT($S^{1-x}Se^{x}$) based solar cells and may in part explain the increased efficiencies observed with CZTSe solar cells.

2.2.6 Electronic Properties

A further theoretical analysis of the electronic properties of the CZTS/Se system has been carried out by Persson et al[49], [73]. In their research they have used multiple DFT techniques to obtain values for the dielectric function and electron-hole

masses (Table 2.2-1). The effective electron mass at the conduction band maximum is fairly isotropic, similar to what has been reported for CIGS and CIGSe[70], [71]. The Se-based compounds have smaller electron masses compared to the S-based compounds, which is strongly correlated with the reduced band gap. This is also similar to what is found in CIGS and CIGSe. Furthermore, the effective electron mass of CZTS and CZTSe is comparable to that of CIGS and CIGSe[70].

Table 2.2-1: Table of electronic property values for CZTS/Se kesterite structures[49], [73].

Characteristic	***CZTS***	***CZTSe***
Relative permittivity - ε_r (F/m)	6.8	8.6
Electron mobility - μ ($cm^2/V.s$)	9.54	4.31
Effective mass of an electron - m_e (kg)	$1.82e^{-31}$	$9.11e^{-32}$
Effective mass of a hole - m_h (kg)	$2.00e^{-31}$	$8.20e^{-32}$

This represents a distinct disadvantage of replacing CIGS/Se absorber layers with CZTS/Se due to the heavier mass of the minority carriers for the p-type semiconductor. The effective hole masses show strong anisotropy in all four materials. Overall, however, the two Se-based compounds have smaller hole masses compared to the corresponding S-based compounds. Hence, based on both the effective electron and hole mass tensors, one would expect that carriers in CZTSe to have better response to an applied electric field compared to CZTS, at least for moderate electric field.

Given the prevalence and importance of structural defects on the optoelectronic properties of CZTS, many have attempted to use high annealing temperatures and sulfurization/selenisation techniques to effectively control the stoichiometry and defect landscape; which require relatively high operating costs. There is of course,

more than one way to skin a cat and so a number of researchers have looked to other methods in the hope of optimising this material for photovoltaic applications.

2.3 Nanocrystal Synthesis

2.3.1 The Solvothermal Method

The research and development of inorganic nanocrystals (NCs) is increasingly focused towards utilising their unique photo-electric properties in the field of low cost photovoltaics[7]. In particular there has been a concerted drive to develop nanocrystalline semiconducting materials with an optimal bandgap of around 1.2-1.8eV using earth abundant elements, and environmentally benign composition methods[74]. NCs can be incorporated with each other or more conventional photovoltaic materials (e.g. polycrystalline silicon and photoactive polymers) in order to harness a greater proportion of the energy we receive from the sun[74].

Inorganic semiconductor NCs have been fabricated using a variety of techniques including metal-organic chemical vapour deposition, molecular beam epitaxy and colloidal synthesis. The latter is arguably the lowest cost and most versatile synthesis method and attracts considerable attention from the academic community[75]. The preparation of nanocrystals with uniform composition, size, shape, internal structure and surface chemistry is essential to the successful characterization and utilization of their properties[75]. Semiconductor NCs have been synthesised by a number of precursor routes. Most notably the organo-metallic precursor and hot coordinating solvent synthesis method has produced some of the highest synthetic yields of above 85%[75].

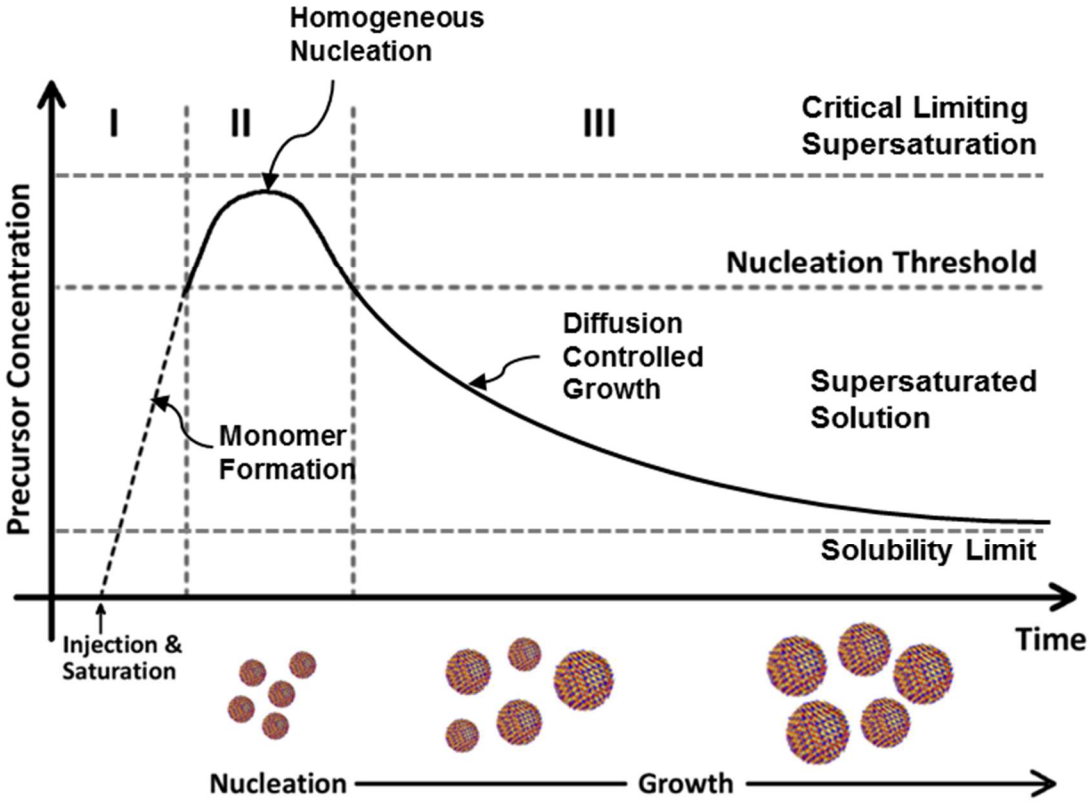

Figure 2.3-1 A plot of precursor concentration vs. time for a typical solvothermal NC reaction, showing the stages of nucleation and growth for the preparation of mono-disperse NCs in the framework of the La Mer model[76]*; wherein a rapid injection of precursors in region I leads to a sudden precursor supersaturation, rising above the nucleation threshold, resulting in a burst of spontaneous nanocrystal seed nucleation (region II). Provided no further reaction precursors are added, nucleation peaks below the critical limiting supersaturation point as precursor monomers are consumed due to the onset of seed growth. In region III, spontaneous nucleation ceases as the nanocrystals grow further (region III), depending on the reaction parameters.*

The traditional method for synthesising mono-dispersed NCs (i.e. particles with a standard deviation in diameter of <10%) requires a single, short, nucleation event followed by a longer, slow growth phase[75], [77], [78]. To achieve this, thermal decomposition and mixing of the reagents must be conducted at a temperature low enough to preclude any appreciable reaction. This is then followed by a controlled but rapid ramp of the solution temperature to accelerate the chemical reaction and produce the requisite super-saturation needed to form the driving force for nucleation to occur. A rapid burst of nucleation will relieve this driving force, consuming the reagents until the concentration falls below the super-saturation point. An alternative method (first described by La Mer et al.[76]), utilizes the rapid

addition of reagents into a well stirred reaction solution to raise the precursor concentration above the nucleation threshold (see Figure 2.3-1). As before, a short nucleation phase will partially relieve the super-saturation and no new nuclei will form so long as the consumption of reagents does not exceed the rate of precursor addition to the reaction solution[77]. The initial size distribution is largely determined by the initial nucleation stage, provided that the growth dynamics of each NC is equivalent [75].

A high supersaturation level is required to promote monomer formation and homogeneous NC nucleation. The nucleation and growth of particles rapidly lower the supersaturation level. Consequently, the nucleation process only lasts for a short time before being terminated by the sudden drop in supersaturation. In practice this "burst nucleation" does not guarantee monodispersity; a broad size distribution is inevitable because, during the "nucleation" period, nucleation and growth occur simultaneously. In other words, the high supersaturation level promotes both homogeneous nucleation and crystal growth[79]. The previously formed nuclei grow faster and become larger than those formed later, resulting in a broad size distribution, as shown in the nucleation phase of Figure 2.3-2.

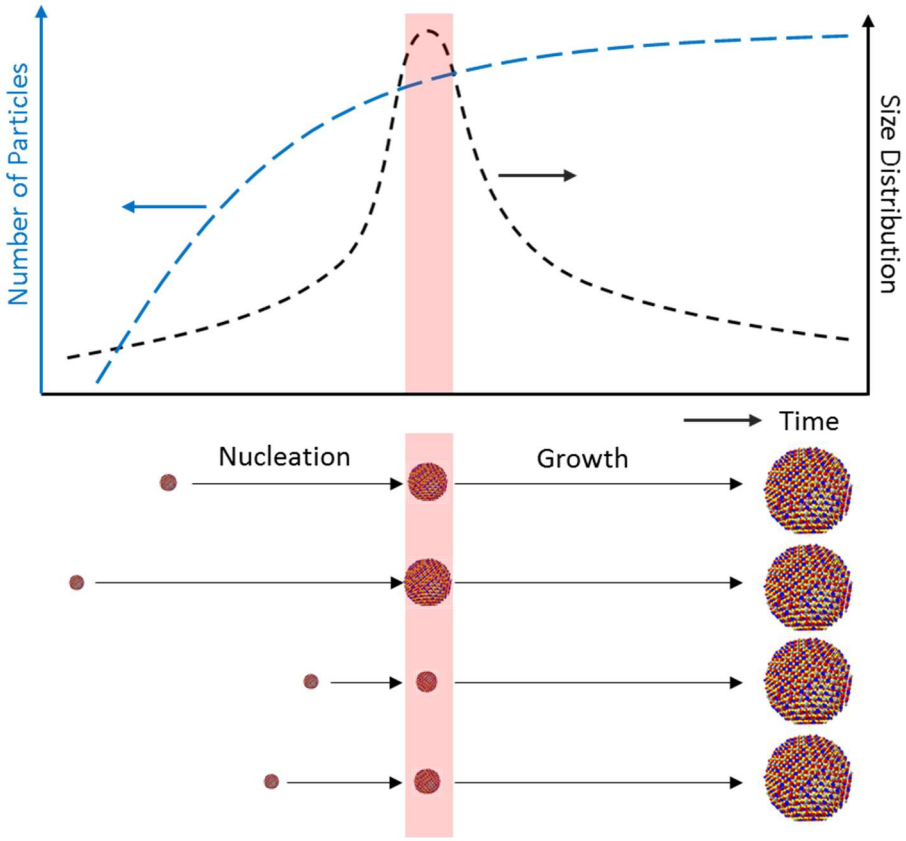

Figure 2.3-2 A plot of the number of NCs and NC size distribution vs. time for a typical solvothermal NC reaction, showing the stages of nucleation and growth according to the La Mer model[76]*, wherein NC nuclei form at different times during the nucleation phase causing a peak in the size distribution curve. Ostwald ripening then occurs causing the formation of a monodisperse array of NCs by the end of the growth phase [adapted from* [79]*].*

Following the nucleation phase, the newly formed NCs exhibit a large surface energy which provide sufficient energy for Ostwald ripening to occur. Consequently, the average particle size increases due to the mutual self-decomposition of smaller particles to feed the growth of larger particles with respectively smaller surface energies[77]. However, ripening NCs in this way does mean that final NCs, although monodisperse, do tend to be very large (>20nm)[77]. Both the nucleation and Ostwald ripening processes are highly dependent on temperature and reagent concentration, therefore any slight alteration to either of these parameters can lead to a significant change in the size and size distribution of the resulting NCs.

The three key parameters that can be manipulated to control nucleation and growth when using the hot injection method are the precursors, the ligands and the

reaction temperature[75], [80]. While each can be considered as an independent variable, they are greatly interrelated. Firstly, the rate of nucleation is directly proportional to the concentration of the monomer and the degree of supersaturation[81]. The precursor reactivity can determine the rate at which the precursors react or decompose to form the monomer species, which directly affects the monomer concentration.

A higher monomer concentration leads to fast nucleation and results in a large amount of smaller critical nuclei; a low monomer concentration slows the nucleation producing a smaller amount of larger critical nuclei. For this reason, the precursors need to rapidly decompose or react to yield a supersaturation of monomers immediately following injection[75]. Simple molecules that have leaving groups that readily detach are optimal choices for precursors. For example, Urban et al. have shown that a variation in the reactivity of different lead precursors can lead to different nanocrystal sizes[82]. The concentration of monomers also affects the growth kinetics as observed by Manna et al[83], [84]. The authors suggested that a high monomer concentration led to fast growth conditions producing either anisotropic shapes or monodisperse nanocrystals. With a low monomer concentration left after nucleation, a broad size distribution resulted, which they attributed to Ostwald ripening. Peng et al. demonstrated that the size of the nanocrystals could be focused and defocused by adjusting the concentration of monomers[84], [85]. They found that increasing the injection volume lead to an increase in the growth rate. Because higher energy facets grow faster, they were able to produce rods with very high aspect ratios.

All of the above examples are based on binary semiconducting materials with the elements being in their most common oxidation state. The precursor reactivity is

less influential on the composition as it is on the size and morphology. However, as the hot injection method is applied to other binary, ternary and quaternary materials, where the metals have multiple oxidation states, the precursor reactivity and relative concentration becomes even more important. Balancing the precursor reactivity is critical to obtain the desired composition and minimize the formation of impurities.

Ligands have a direct effect on the nucleation and growth kinetics of a reaction due to their interaction with precursors. More specifically, as the ligand concentration is increased, they coordinate with precursors forming more stable compounds and thereby reduce the overall monomer concentration. This decreases the concentration of nuclei, as a consequence of a lower nucleation rate, resulting in the formation of larger nuclei[80]. Ligands also play an active role in controlling the growth rate and morphology of the NCs by binding to specific crystallographic facets of the NCs and thereby determining their particular growth rate[75], [86].

Ligands can be broken into two groups: L-type and X-type[87]. L-type ligands such as phosphines, amines and thiols coordinate by donating their lone pair. These ligands are generally more labile and help passivate the nanocrystal surface. X-type ligands are the fatty acids, such as oleic acid, that can either bind through the OH group or by the lone pair on the double-bond oxygen, which makes them stronger binding ligands. It has been theoretically determined that primary amines can cover ~100% of the nanocrystal surface unlike other ligands such as trioctylphosphineoxide (TOPO) which can only cover 30%[88]. Amines bind to either cation or anion species, through the lone pair on the nitrogen, but amines favour interactions with the anions. It is often found in the literature that optimal nucleation and growth kinetics require the use of a mixed ligand system containing a pair of weakly and strongly binding ligands[89], [90]. Furthermore, ligands are crucial for

nanocrystals to be solution processed. The hydrophobic nature of the non-bonded ligand can be exploited to enable the extraction of the NCs from the colloidal system. This is achieved by introducing the NCs to a polar solvent that will flocculate the NCs out of the reaction solution, typically forming a nanocrystal aggregate. The supernatant can then be extracted and the NCs re-dispersed in a suitable non-polar solvent[75]. They also functionalise the NC surface and assist in substrate adhesion[88], [91]. Even though ligands have varying binding strengths, they are relatively labile in solution and can be exchanged post-synthesis at room temperature[89], [90].

The energy with which surfactants adhere to the nanocrystal surface should be such that they can exchange on and off, thereby enabling regions of the nanocrystal surface to be accessible for growth[75]. Ultimately, reaction temperature affects the binding strength of the ligand because at very high reaction temperatures, the ligand is not well-attached to the surface, which can lead to fast and uncontrolled growth. On the other hand, if the temperature is too low, then the ligands have a stronger attraction to the nanocrystal surface slowing growth, thereby exerting a direct influence on the nucleation and growth kinetics[76].

There are two temperatures used in the hot injection method, the nucleation temperature (injection) and the growth temperature; because the activation energy is higher for nucleation than for growth, the temperature can be optimized for each regime[81],[80]. The injection needs to take place at a temperature that is high enough for the precursors to have decomposed and form a supersaturation of monomers[92]. It must also be high enough to overcome the thermal barrier for the reaction to take place, and furthermore, to allow subsequent rearrangement of atoms to take place.

A higher temperature usually makes the precursors less stable, permitting the easy formation of supersaturated monomers[88], which results in a faster nucleation and a large concentration of small nuclei[80]. However, if the growth temperature is too high then uncontrolled growth can occur. For this reason, the growth temperature is typically lower than the nucleation temperature[75]. The growth temperature also affects the size distribution as well as the morphology[93]. Furthermore, the chain length of the surfactant used can also influence the growth temperature and resulting size dispersion. Murray et al. observed that the growth temperature required to synthesize monodisperse nanocrystals decreased with decreasing chain length[93].

Controlling the nucleation and growth kinetics in the hot injection method relies on both the absolute and relative concentration of the precursors and ligands, together with the injection and growth temperatures. The ultimate goal is to produce pure NCs with a small particle size, narrow size distribution and high solution stability[93].

2.3.2 Ligand Substitution

NC surfaces are covered by ligands which prevent the NCs from aggregating in solution[94], [95]. However, over time exposure to water together with the dynamic binding and unbinding between the inorganic NC surface and the stabilizing ligands can lead to aggregation of the particles[96]. In order to improve the NC stability, steric ligand molecules can be exchanged with new ligands, that can provide alternative properties or functionality to the particles[96]. The incoming ligand molecules tend to be chosen so that the ligands form a more secure bond to the inorganic NC surface[96], [97]. Ligand exchange reactions can proceed by simply mixing free ligands with NCs at room temperature (such as with the exchange of

oleylemaine with pyridine, illustrated in Figure 2.3-3). Other ligand exchange reactions require gentle heating or prolonged stirring of the nanocrystals in an excess of the substituting molecule, in order to effectively achieve an acceptable yield[98]. Such methodologies can also be used with the actual exchange often incorporated into a layer by layer thin are being Thus, ligand exchange is a simple and versatile approach to tune the ligand shell on solution synthesised NCs. Properties of the NCs, such as solubility as well as chemical and physical properties can be altered in this way[95], [97].

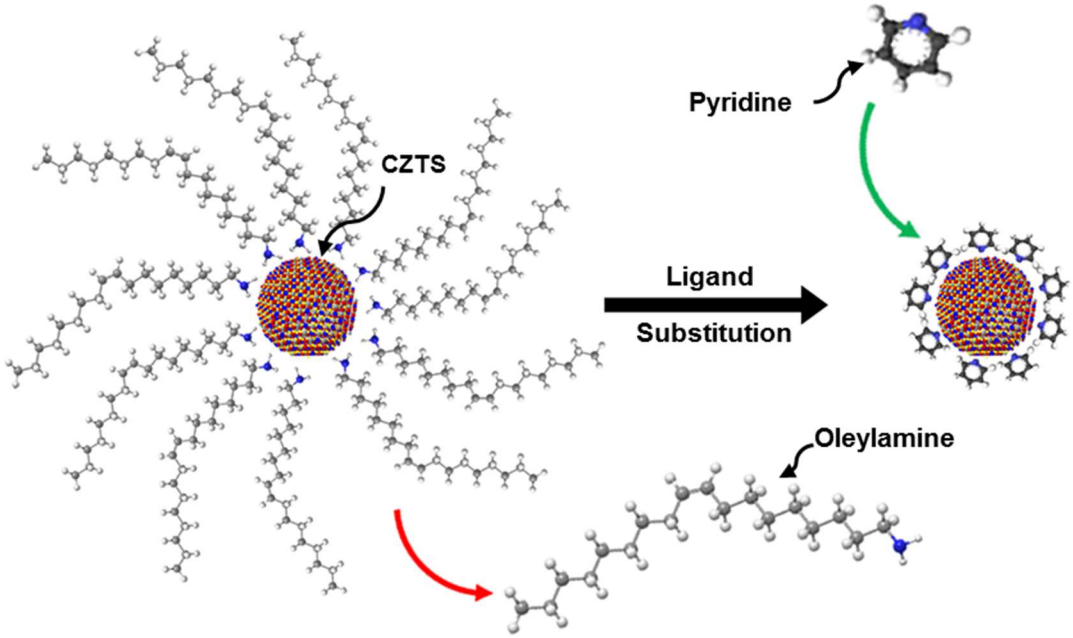

Figure 2.3-3 Schematic illustration of a ligand exchange reaction, replacing a shell of long chain oleylamine ligands from the surface of a CZTS NC core and substituting them with a shell of pyridine molecules.

The mechanism of ligand exchange was studied in detail by Murray et al.[93] and subsequently many other groups also investigated such processes. Thiols have been exchanged by other thiols[99]–[101], phosphines with thiols[102], [103], dimethylaminopyridine by thiols[104], amines by thiols[105], [106], amines with methyl iodine[107] and phosphines with pyridine[108]. One important aspect of ligand exchange is the morphology and size of the NCs. The NC surface can be

categorised into three different binding sites i.e. vertices (corner sites) and edges are defects sites whereas terrace (face sites) are known as non-defect sites[100], [101], [109]. These different surface sites have different electron densities and steric behaviour hence they will have different reactivity[100], [101], [109]. Fast ligand exchange occurs at edge and vertex sites, whereas the exchange process is much slower at near-edge and at terrace sites[100], [101], [109]. Furthermore, the reactivity of differently sized NCs may also differ due to the variation in surface curvature[110], [111]. For example, Kell et al.[111] observed an increase in reaction rate with decreasing particle size. It has also been shown that the rate of ligand exchange reaction decreases as the chain length and the steric bulk of the initial protecting ligand shell is increased[109].

2.3.3 CZTS Devices

To date there has been a limited representation of CZTS/Se NC solar cells in the literature. Despite this, a relatively narrow range of synthesis routes have been developed, with the ultimate aim of forming a slurry or paste from which a thin film can be formed[112]–[116]. Common among these techniques is the use of primary capping ligands, which are used to stabilize the relatively large NCs (10-20nm) in solution long enough to be either spin cast or doctor bladed into a thin film. In the majority of cases the thin films are then annealed at high temperature, in a sulphur or selenium rich environment, to facilitate grain growth and surface passivation.

In 1988, Ito et al. investigated the electrical and optical properties of CZTS and Cu_2CdSnS_4 (CCTS)[117] but it wasn't until 1996, when Katagiri et al. published a report on sequentially evaporated CTZS thin films within a glass/Mo/CZTS/CdS/i-ZnO/n-ZnO/Al device structure that complete devices were tested, with initial

efficiencies of 0.66%[118]. By 1997 the efficiency of devices such as these had reached 2.3%[33]. The record power conversion efficiency for vacuum-deposited kesterite thin film devices has improved to 3.2/6.8% for CZTS[119] and CZTSe[120] respectively. Although CZTS/Se kesterite films offer a significant potential for low-cost high-efficiency photovoltaic devices[33], the complicated multi-element nature of these materials generally leads to the requirement for more complex and costly deposition processes[24]. Owing to the growing reputation of CZTS/Se as a potentially ideal photovoltaic absorber material, there has been a wide range of deposition routes used for thin film fabrication with some promising results (summarized in Table 2.3-2).

Table 2.3-2: Summary of Cu_2ZnSnS/Se_4 kesterite photovoltaic device performance.

Group	***Material***	***Method***	***η (%)***	***FF (%)***	***Eg (eV)***	***Publication (Year)***
IBM[121]	CZTS/Se	Ink	12.6	70	1.13	2013
NNCT[122], [123]	CZTS	Sputtering	6.8	62	1.45	2008
IBM[120]	CZTS	Co-Evap	6.8	65	1.45	2011
Purdue[113]	CZTS/Se	Ink	7.2	53	1.05	2010
NNCT[124]	CZTS	Sol-gel	2.1	35	1.45	2010

Although some of these methods incorporate a solution processing step in their device fabrication, all require at least one high temperature annealing step in order to form the CZTS/Se photoactive semiconductor layer. In 2014, a report from researchers at IBM outlined a liquid-based process for the deposition of CZTS/Se absorber layers, which utilised a hybrid hydrazine-based slurry method[121]. The resulting devices exhibited device efficiencies of 12.6%, exceeding the previous kesterite performance record by ~15%.

CZTS nanocrystal based inks were first developed in 2009 with a number of published syntheses, which involved the nucleation and growth of NCs at elevated temperatures, utilising salts of Cu, Zn, and Sn (typically chlorides or acetylacetonates) complexed with oleylamine[112], [114], [116]. An oleylamine-sulphur complex was the predominant sulphur precursor used in these reactions. The synthesized NCs had diameters in the range 10-20 nm and a bandgap of ~1.5 eV[112], [114], [116]. Selenization of doctor bladed thin films from CZTS NCs dispersed in hexanethiol at 500°C for 20 min gave large grained CZTSSe films, with device efficiency of 7.2%[113]. Dai et al. developed a synthesis which allowed them to study the bandgap variation of ~3.5nm stoichiometrically different CZTS NCs, which were used as photo-absorbers in dye sensitized solar cells measured to be 0.03% efficient[85], [125]. CZTS nanorods of diameter ~ 200 nm were synthesized by Shi et al. using template directed synthesis with metal chlorides, ethylenediamine, and sulphur precursors. The nanowires could be easily extracted by dissolving the template using a NaOH solution[126]. By replacing oleylamine with dodecanethiol as the capping ligand, wurtzite phase CZTS nanoprisms and nanoplates with a typical bandgap of 1.4 eV have been synthesized by a number of groups[41], [127]–[129]. In particular, Singh et al. have synthesized wurtzite nanorods of diameter 11 nm and length 35 nm by using a mixture of dodecanethiol (1-DDT) and tert-dodecyl mercaptan (t-DDT) as capping ligands, which enable the nanorods to assemble into perpendicularly aligned arrays through controlled evaporation from solution[127]. However, neither of these promising developments have led to a successful application within solar cells. The most prominent account of a ligand substitution mechanism used for thin film deposition of CZTS/Se NCs is present in the supporting information of a paper by Riha et al. from which no device characteristics were reported[116]. In a subsequent

paper, published by the same research group, the efficiency of a NC thin film device prepared with no chemical or heat treatment achieved a PCE of 0.23%[112]. Although low by comparison with record efficiencies, these initial results represent the beginning of a distinct branch of research in to the development of CZTS/Se PV cells; one which combines low temperature, solution processing deposition techniques with this inherently low cost material system.

The best performing solution processed CZTS devices rely heavily on the application of metal hydrazine complexes[130] and high temperature sulphurization/selenization treatments to form crystalline CZTS[33], [131], which are inherently dangerous and increase the cost of fabrication

2.4 Conclusions

CZTS/Se based solar cells are inherently complex due to the quaternary absorber materials used to form the active layer. This review aims to address the most prominent issues that are present in the literature, focusing in particular on the problems that represent significant opportunities for the future development of the CZTS/Se PV system. As has been mentioned previously, the record CZTS/Se devices have been produced by Mitzi et al.[132] The dramatic increase in efficiency of the devices fabricated by this research team over recent years is attributed to the optimisation of the mechanisms used to encourage grain growth and passivation of the absorber surface, and is analogous to the development of CIGS/Se devices in the early part of the last decade. It is founded on comprehensive investigations into the optoelectronic properties of CZTS/Se, based on theoretical DFT analysis. However, there is still a noticeable lack of experimental verification for some of these assertions. The upward trajectory of these device efficiencies may signal great

promise for the material system. However, high temperature annealing steps and complex multi-stage processing routes are likely to undermine the likely cost savings associated with utilising earth abundant materials, when compared with conventional thin film solar cell technology.

It is important to note that to date the highest efficiency devices exhibit an initial solution processing step. The very high compositional control afforded by solution processing coupled with the elevated annealing process helps to optimise the optoelectronic properties for solar cell applications. There are few reports of low temperature, solution processed CZTS/Se devices and any attempts to produce such cells tend to produce remarkably poor efficiencies. This ominous revelation may represent an impasse between CZTS/Se (an earth abundant materials system) and low cost solution processing. However, there is very little evidence of colloidal NC solar cells that combine ligand substitution methods and CZTS/Se. Thus, it is in this area of research that opportunities for exploratory investigation still may hold the greatest reward.

2.5 References

[1] E. Becquerel, "Memoire sur les effets electriques produits sous l'influence des rayons solaires," *C. R. Acad. Sci.*, vol. 9, pp. 561–567, 1839.

[2] E. D. Adrian and R. Matthews, "The action of light on the eye," *J. Physiol.*, vol. 65, no. 3, pp. 273–298, 1928.

[3] W. Smith, "Effect of Light on Selenium During the Passage of An Electric Current," *Nature*, vol. 7, no. 173, pp. 303–303, 1873.

[4] K. W. Johnston, "Efficient Schottky quantum dot photovoltaics: The roles of depletion, drift, and diffusion," *Appl. Phys. Lett.*, vol. 92122111, no. 12, 2008.

[5] R. J. Matson, K. a. Emery, and R. E. Bird, "Terrestrial solar spectra, solar simulation and solar cell short-circuit current calibration: A review," *Sol. Cells*, vol. 11, no. 2, pp. 105–145, Mar. 1984.

[6] J. Nelson, *The Physics of Solar Cells*, vol. 53, no. 5. London: Imperial College Press, 2012.

[7] I. Gur, N. a Fromer, M. L. Geier, and a P. Alivisatos, “Air-stable all-inorganic nanocrystal solar cells processed from solution.,” *Science*, vol. 310, no. 5747, pp. 462–465, 2005.

[8] C. Wadia, a. P. Alivisatos, and D. M. Kammen, “Materials availability expands the opportunity for large-scale photovoltaics deployment,” *Environ. Sci. Technol.*, vol. 43, no. 6, pp. 2072–2077, Mar. 2009.

[9] A. K. Rath, M. Bernechea, L. Martinez, F. P. G. de Arquer, J. Osmond, and G. Konstantatos, “Solution-processed inorganic bulk nano-heterojunctions and their application to solar cells,” *Nat. Photonics*, vol. 6, no. 8, pp. 529–534, Jul. 2012.

[10] W. Shockley and H. J. Queisser, “Detailed Balance Limit of Efficiency of p-n Junction Solar Cells,” *J. App. Phys.*, vol. 32, no. 3, p. 510, 1961.

[11] P. Würfel, *Physics of Solar Cells: From Principles to New Concepts*. 2007.

[12] P. Nagpal and V. I. Klimov, “Role of mid-gap states in charge transport and photoconductivity in semiconductor nanocrystal films,” *Nat. Commun.*, vol. 2, p. 486, Sep. 2011.

[13] J. Gao and J. C. Johnson, “Charge trapping in bright and dark states of coupled PbS quantum dot films,” *ACS Nano*, vol. 6, no. 4, pp. 3292–3303, Apr. 2012.

[14] C. Persson, “Electronic and optical properties of Cu2ZnSnS4 and Cu2ZnSnSe4,” *J. Appl. Phys.*, vol. 107, no. 5, p. 053710, 2010.

[15] R. Debnath, M. T. Greiner, I. J. Kramer, A. Fischer, J. Tang, D. A. R. Barkhouse, X. Wang, L. Levina, Z. H. Lu, and E. H. Sargent, “Depleted-heterojunction colloidal quantum dot photovoltaics employing low-csost electrical contacts.pdf,” *Appl. Phys. Lett.*, vol. 97, p. 23109, 2010.

[16] S. Suckow, T. M. Pletzer, and H. Kurz, “Fast and reliable calculation of the two-diode model without simplifications,” *Prog. Photovoltaics Res. Appl.*, vol. 22, no. 4, pp. 494–501, Apr. 2014.

[17] M. Kirkengen, J. Bergli, and Y. M. Galperin, “Direct generation of charge carriers in c-Si solar cells due to embedded nanoparticles,” *J. Appl. Phys.*, vol. 102, no. 9, p. 093713, 2007.

[18] X. Deng and E. a. Schiff, “Amorphous Silicon-Based Solar Cells,” in *Handbook of Photovoltaic Science and Engineering*, 1st ed., A. Luque and S. Hegedus, Eds. John Wiley & Sons, Ltd, 2005, pp. 505–565.

[19] M. Gloeckler and J. R. Sites, “Efficiency limitations for wide-band-gap chalcopyrite solar cells,” *Thin Solid Films*, vol. 480–481, pp. 241–245, 2005.

[20] B. K. Hughes, J. M. Luther, and M. C. Beard, “The subtle chemistry of colloidal, quantum-confined semiconductor nanostructures,” *ACS Nano*, vol. 6, no. 6, pp. 4573–4579, 2012.

[21] B. E. Hardin, H. J. Snaith, and M. D. McGehee, “The renaissance of dye-sensitized solar cells,” *Nat. Photonics*, vol. 6, no. 3, pp. 162–169, Feb. 2012.

[22] M. Liu, M. B. Johnston, and H. J. Snaith, “Efficient planar heterojunction perovskite solar cells by vapour deposition.,” *Nature*, vol. 501, no. 7467, pp. 395–8, Sep. 2013.

[23] H. J. Snaith and L. Schmidt-Mende, “Advances in Liquid-Electrolyte and Solid-State Dye-Sensitized Solar Cells,” *Adv. Mater.*, vol. 19, no. 20, pp. 3187–3200, Sep. 2007.

[24] T. Todorov, O. Gunawan, S. J. Chey, T. G. De Monsabert, A. Prabhakar, and D. B. Mitzi, “Progress towards marketable earth-abundant chalcogenide solar cells,” *Thin Solid Films*, vol. 519, no. 21, pp. 7378–7381, Aug. 2011.

[25] S. Wagner, J. L. Shay, P. Migliorato, and H. M. Kasper, “CuInSe2/CdS heterojunction photovoltaic detectors,” *Appl. Phys. Lett.*, vol. 25, no. 8, pp. 434–435, 1974.

[26] D. A. R. Barkhouse, O. Gunawan, T. Gokmen, T. K. Todorov, and D. B. Mitzi, “Device characteristics of a 10.1% hydrazine-processed Cu2ZnSn(Se,S)4 solar cell,” *Prog. Photovoltaics Res. Appl.*, vol. 20, no. 1, pp. 6–11, 2012.

[27] D. A. R. Barkhouse, O. Gunawan, T. Gokmen, T. K. Todorov, and D. B. Mitzi, “Device characteristics of a 10.1% hydrazine-processed Cu2ZnSn(Se,S)4 solar cell,” *Prog. Photovoltaics Res. Appl.*, vol. 20, no. 1, pp. 6–11, Nov. 2012.

[28] S. Niki, M. Contreras, I. Repins, M. Powalla, K. Kushiya, S. Ishizuka, and K. Matsubara, “CIGS absorbers and processes,” *Prog. Photovoltaics Res. Appl.*, vol. 18, no. 6, pp. 453–466, Sep. 2010.

[29] A. N. Tiwari, D. Lincot, and M. Contreras, “Editorial: The time for CIGS,” *Prog. Photovoltaics Res. Appl.*, vol. 18, no. 6, p. 389, Sep. 2010.

[30] a. Feltrin and a. Freundlich, “Material challenges for terawatt level deployment of photovoltaics,” *Conf. Rec. 2006 IEEE 4th World Conf. Photovolt. Energy Conversion, WCPEC-4*, vol. 2, no. 2, pp. 2469–2472, 2007.

[31] N. G. D. Ã, “Present status and future prospects of CIGSS thin film solar cells,” *Sol. Energy Mater. Sol. Cells*, vol. 90, no. 15, pp. 2181–2190, 2006.

[32] B. a. Andersson, “Materials availability for large-scale thin-film photovoltaics,” *Prog. Photovoltaics Res. Appl.*, vol. 8, no. 1, pp. 61–76, Feb. 2000.

[33] D. B. Mitzi, O. Gunawan, T. K. Todorov, K. Wang, and S. Guha, “The path towards a high-performance solution-processed kesterite solar cell,” *Sol. Energy Mater. Sol. Cells*, vol. 95, no. 6, pp. 1421–1436, 2011.

[34] J. J. Scragg, T. Ericson, T. Kubart, M. Edoff, and C. Platzer-Björkman, “Chemical insights into the instability of Cu2ZnSnS4 films during annealing,” *Chem. Mater.*, vol. 23, no. 20, pp. 4625–4633, 2011.

[35] J. J. Scragg, P. J. Dale, L. M. Peter, G. Zoppi, and I. Forbes, “New routes to sustainable photovoltaics: Evaluation of Cu 2ZnSnS4 as an alternative absorber material,” *Phys. Status Solidi Basic Res.*, vol. 245, no. 9, pp. 1772–1778, Sep. 2008.

[36] I. Grozdanov and M. Najdoski, “Optical and Electrical Properties of Copper Sulfide Films of Variable Composition,” *J. Solid State Chem.*, vol. 114, no. 2, pp. 469–475, 1995.

[37] N. J. Freymeyer, P. D. Cunningham, E. C. Jones, B. J. Golden, A. M. Wiltrout, and K. E. Plass, "Influence of solvent reducing ability on copper sulfide crystal phase," *Cryst. Growth Des.*, vol. 13, no. 9, pp. 4059–4065, 2013.

[38] Q. Xu, B. Huang, Y. Zhao, Y. Yan, R. Noufi, and S.-H. Wei, "Crystal and electronic structures of CuxS solar cell absorbers," *Appl. Phys. Lett.*, vol. 100, no. 6, p. 061906, Feb. 2012.

[39] Y. Zhao, H. Pan, Y. Lou, X. Qiu, J. Zhu, and C. Burda, "Plasmonic Cu 2-xS nanocrystals: Optical and structural properties of copper-deficient copper(I) sulfides," *J. Am. Chem. Soc.*, vol. 131, no. 12, pp. 4253–4261, Apr. 2009.

[40] J. M. Luther, P. K. Jain, T. Ewers, and a P. Alivisatos, "Localized surface plasmon resonances arising from free carriers in doped quantum dots.," *Nat. Mater.*, vol. 10, no. 5, pp. 361–366, May 2011.

[41] H.-C. Liao, M.-H. Jao, J.-J. Shyue, Y.-F. Chen, and W.-F. Su, "Facile synthesis of wurtzite copper–zinc–tin sulfide nanocrystals from plasmonic djurleite nuclei," *J. Mater. Chem. A*, vol. 1, no. 2, p. 337, 2013.

[42] T. Shibata, Y. Muranushi, T. Miura, and T. Kishi, "Photoconductive properties of single-crystal 2H-SnS2," *J. Phys. Chem. Solids*, vol. 51, no. 11, pp. 1297–1300, 1990.

[43] M. V. Kovalenko, M. I. Bodnarchuk, J. Zaumseil, J. S. Lee, and D. V. Talapin, "Expanding the chemical versatility of colloidal nanocrystals capped with molecular metal chalcogenide ligands," *J. Am. Chem. Soc.*, vol. 132, no. 29, pp. 10085–10092, Jul. 2010.

[44] B. G. Mendis, M. C. J. Goodman, J. D. Major, A. a. Taylor, K. Durose, and D. P. Halliday, "The role of secondary phase precipitation on grain boundary electrical activity in Cu2ZnSnS4 (CZTS) photovoltaic absorber layer material," *J. Appl. Phys.*, vol. 112, no. 12, p. 124508, 2012.

[45] I. Repins, N. Vora, C. Beall, S.-H. Wei, Y. Yan, M. Romero, G. Teeter, H. Du, B. To, M. Young, and R. Noufi, "Kesterites and Chalcopyrites: A Comparison of Close Cousins," in *MRS Proceedings*, 2011, vol. 1324.

[46] S. Chen, J. H. Yang, X. G. Gong, A. Walsh, and S. H. Wei, "Intrinsic point defects and complexes in the quaternary kesterite semiconductor Cu2 ZnSnS4," *Phys. Rev. B - Condens. Matter Mater. Phys.*, vol. 81, no. 24, p. 245204, 2010.

[47] S. Chen, X. G. Gong, A. Walsh, and S.-H. Wei, "Defect physics of the kesterite thin-film solar cell absorber Cu[sub 2]ZnSnS[sub 4]," *Appl. Phys. Lett.*, vol. 96, no. 2, p. 021902, 2010.

[48] S. H. Wei and S. B. Zhang, "Defect properties of CuInSe2 and CuGaSe2," *J. Phys. Chem. Solids*, vol. 66, no. 11, pp. 1994–1999, Nov. 2005.

[49] C. Persson, "Electronic and optical properties of Cu2ZnSnS4 and Cu2ZnSnSe4," *J. Appl. Phys.*, vol. 107, no. 5, p. 053710, 2010.

[50] H. Zhao and C. Persson, "Optical properties of Cu(In,Ga)Se2 and Cu2ZnSn(S,Se)4," *Thin Solid Films*, vol. 519, no. 21, pp. 7508–7512, Jan. 2011.

[51] J. Paier, R. Asahi, A. Nagoya, and G. Kresse, "Cu2 ZnSnS4 as a potential photovoltaic material: A hybrid Hartree-Fock density functional theory study," *Phys. Rev. B - Condens. Matter Mater. Phys.*, vol. 79, no. 11, p. 115126, 2009.

[52] A. Nagoya, R. Asahi, R. Wahl, and G. Kresse, "Defect formation and phase stability of Cu2ZnSnS4 photovoltaic material," *Phys. Rev. B - Condens. Matter Mater. Phys.*, vol. 81, no. 11, p. 113202, 2010.

[53] S. Y. Chen, A. Walsh, J. H. Yang, X. G. Gong, L. Sun, P. X. Yang, J. H. Chu, and S. H. Wei, "Compositional dependence of structural and electronic properties of Cu(2)ZnSn(S,Se)(4) alloys for thin film solar cells," *Phys. Rev. B*, vol. 83, no. 12, pp. 1–5, Mar. 2011.

[54] K. Tanaka, M. Oonuki, N. Moritake, and H. Uchiki, "Cu2ZnSnS4Cu2ZnSnS4 thin film solar cells prepared by non-vacuum processing," *Sol. Energy Mater. Sol. Cells*, vol. 93, no. 5, pp. 583–587, May 2009.

[55] G. Suresh Babu, Y. B. Kishore Kumar, P. Uday Bhaskar, and V. Sundara Raja, "Thin Films for Photovoltaic Applications," *J. Phys. D. Appl. Phys.*, vol. 41, no. 20, p. 205305, Oct. 2008.

[56] S. Schorr, "Structural aspects of adamantine like multinary chalcogenides," *Thin Solid Films*, vol. 515, no. 15 SPEC. ISS., pp. 5985–5991, May 2007.

[57] S. Schorr, "The crystal structure of kesterite type compounds: A neutron and X-ray diffraction study," *Sol. Energy Mater. Sol. Cells*, vol. 95, no. 6, pp. 1482–1488, 2011.

[58] R. A. Wibowo, W. S. Kim, E. S. Lee, B. Munir, and K. H. Kim, "Single step preparation of quaternary Cu2 ZnSnSe4 thin films by RF magnetron sputtering from binary chalcogenide targets," *J. Phys. Chem. Solids*, vol. 68, no. 10, pp. 1908–1913, Oct. 2007.

[59] H. Matsushita, T. Maeda, A. Katsui, and T. Takizawa, "Thermal analysis and synthesis from the melts of Cu-based quaternary compounds Cu-III-IV-VI4 and Cu2-II-IV-VI4 (II = Zn, Cd; III = Ga, In; IV = Ge, Sn; VI = Se)," *J. Cryst. Growth*, vol. 208, no. 1, pp. 416–422, Jan. 2000.

[60] S. Ahn, S. Jung, J. Gwak, A. Cho, K. Shin, K. Yoon, D. Park, H. Cheong, and J. H. Yun, "Determination of band gap energy (Eg) of Cu2 ZnSnSe4 thin films: On the discrepancies of reported band gap values," *Appl. Phys. Lett.*, vol. 97, no. 2, p. 021905, 2010.

[61] M. Altosaar, J. Raudoja, K. Timmo, M. Danilson, M. Grossberg, J. Krustok, and E. Mellikov, "Cu 2Zn 1-xCd xSn(Se 1-yS y) 4 solid solutions as absorber materials for solar cells," *Phys. Status Solidi Appl. Mater. Sci.*, vol. 205, no. 1, pp. 167–170, Jan. 2008.

[62] M. Friedlmeier, N. Wiesser, T. Walter, H. Dittrich, and H.-W. Schock, "Growth and Characterization of Cu2SnZnS4 and Cu2SnZnSe4 Thin Films for Photovoltaic Applications," in *Proceedings of the 14th European Photovoltaic Specialists Conference*, 1997, p. 1242.

[63] K. Biswas, S. Lany, and A. Zunger, "The electronic consequences of multivalent elements in inorganic solar absorbers: Multivalency of Sn in Cu2 ZnSnS4," *Appl. Phys. Lett.*, vol. 96, no. 20, p. 201902, 2010.

[64] S. B. Zhang, S.-H. Wei, A. Zunger, and H. Katayama-Yoshida, “Defect physics of the CuInSe_{2} chalcopyrite semiconductor,” *Phys. Rev. B*, vol. 57, no. 16, pp. 9642–9656, 1998.

[65] G. Kresse, “Efficient iterative schemes for ab initio total-energy calculations using a plane-wave basis set,” *Phys. Rev. B*, vol. 54, no. 16, pp. 11169–11186, Oct. 1996.

[66] T. K. Todorov, K. B. Reuter, and D. B. Mitzi, “High-efficiency solar cell with earth-abundant liquid-processed absorber,” *Adv. Mater.*, vol. 22, no. 20, p. 156, May 2010.

[67] A. Walsh, S. Chen, X. G. Gong, and S. H. Wei, “Crystal structure and defect reactions in the kesterite solar cell absorber Cu2ZnSnS4 (CZTS): Theoretical insights,” *AIP Conf. Proc.*, vol. 1399, no. 2011, pp. 63–64, 2011.

[68] S. Chen, X. G. Gong, A. Walsh, and S. H. Wei, “Crystal and electronic band structure of Cu2 ZnSn X4 (X=S and Se) photovoltaic absorbers: First-principles insights,” *Appl. Phys. Lett.*, vol. 94, no. 4, p. 041903, 2009.

[69] K. Tanaka, Y. Fukui, N. Moritake, and H. Uchiki, “Chemical composition dependence of morphological and optical properties of Cu2ZnSnS4 thin films deposited by sol–gel sulfurization and Cu2ZnSnS4 thin film solar cell efficiency.,” *Sol. Energy Mater. Sol. Cells*, vol. 95, no. 3, pp. 838–842, 2011.

[70] L. Kronik, L. Burstein, M. Leibovitch, Y. Shapira, D. Gal, E. Moons, J. Beier, G. Hodes, D. Cahen, D. Hariskos, R. Klenk, and H. W. Schock, “Band diagram of the polycrystalline CdS/Cu(In,Ga)Se2 heterojunction,” *Appl. Phys. Lett.*, vol. 67, no. 10, pp. 1405–1407, 1995.

[71] D. Schmid, M. Ruckh, F. Grunwald, and H. W. Schock, “Chalcopyrite/defect chalcopyrite heterojunctions on the basis of CuInSe2,” *J. Appl. Phys.*, vol. 73, no. 6, pp. 2902–2909, 1993.

[72] H. Peng, C. Xie, D. T. Schoen, K. Mcllwrath, X. F. Zhang, and Y. Cui, “Ordered vacancy compounds and nanotube formation in CuInSe2-CdS core-shell nanowires,” *Nano Lett.*, vol. 7, no. 12, pp. 3734–3738, Dec. 2007.

[73] H. Zhao and C. Persson, “Optical properties of Cu (In, Ga) Se2 and Cu2ZnSn (S, Se) 4,” *Thin Solid Films*, vol. 519, no. 21, pp. 7508–7512, Jan. 2011.

[74] M. A. Green, “Third generation photovoltaics: comparative evaluation of advanced solar conversion options,” in *Conference Record of the Twenty-Ninth IEEE Photovoltaic Specialists Conference, 2002.*, pp. 1330–1334.

[75] Y. Yin and a P. Alivisatos, “Colloidal nanocrystal synthesis and the organic-inorganic interface.,” *Nature*, vol. 437, no. 7059, pp. 664–670, 2005.

[76] C. B. Murray, C. R. Kagan, and M. G. Bawendi, “Synthesis and charaterization of monodisperse nanocrystals and close-packes nanocrystal assemblies,” *Annu. Rev. Mater. Sci.*, vol. 30, no. 1, pp. 545–610, 2000.

[77] C. B. Murray, S. Sun, W. Gaschler, H. Doyle, T. a. Betley, and C. R. Kagan, “Colloidal synthesis of nanocrystals and nanocrystal superlattices,” *IBM J. Res. Dev.*, vol. 45, no. 1, pp. 47–56, 2001.

[78] J. Park, J. Joo, G. K. Soon, Y. Jang, and T. Hyeon, "Synthesis of monodisperse spherical nanocrystals," *Angew. Chemie - Int. Ed.*, vol. 46, no. 25, pp. 4630–4660, 2007.

[79] S. G. Kwon and T. Hyeon, "Formation mechanisms of uniform nanocrystals via hot-injection and heat-up methods," *Small*, vol. 7, no. 19, pp. 2685–2702, Aug. 2011.

[80] C. De Mello Donegá, P. Liljeroth, and D. Vanmaekelbergh, "Physicochemical evaluation of the hot-injection method, a synthesis route for monodisperse nanocrystals," *Small*, vol. 1, no. 12, pp. 1152–1162, Dec. 2005.

[81] D. V. Talapin, J. S. Lee, M. V. Kovalenko, and E. V. Shevchenko, "Prospects of colloidal nanocrystals for electronic and optoelectronic applications," *Chem. Rev.*, vol. 110, no. 1, pp. 389–458, Jan. 2010.

[82] J. J. Urban, D. V. Talapin, E. V. Shevchenko, and C. B. Murray, "Self-assembly of PbTe quantum dots into nanocrystal superlattices and glassy films," *J. Am. Chem. Soc.*, vol. 128, no. 10, pp. 3248–3255, Mar. 2006.

[83] L. Manna, E. C. Scher, and a. Paul Alivisatos, "Shape control of colloidal semiconductor nanocrystals," *J. Clust. Sci.*, vol. 13, no. 4, pp. 521–532, 2002.

[84] X. Peng, L. Manna, W. Yang, J. Wickham, E. Scher, a Kadavanich, and A. Alivisatos, "Shape control of CdSe nanocrystals," *Nature*, vol. 404, no. 6773, pp. 59–61, Mar. 2000.

[85] P. Dai, X. Shen, Z. Lin, Z. Feng, H. Xu, and J. Zhan, "Band-gap tunable (Cu2Sn)(x/3)Zn(1-x)S nanoparticles for solar cells.," *Chem. Commun. (Camb).*, vol. 46, no. 31, pp. 5749–5751, Aug. 2010.

[86] Y. Jun, J. Choi, and J. Cheon, "Shape control of semiconductor and metal oxide nanocrystals through nonhydrolytic colloidal routes.," *Angew. Chem. Int. Ed. Engl.*, vol. 45, no. 21, pp. 3414–3439, 2006.

[87] C. Surface, A. J. Morris-cohen, V. Vasilenko, V. a Amin, M. G. Reuter, and E. a Weiss, "Model for Adsorption of Ligands to Colloidal Quantum Dots with Structure," *ACS Nano*, vol. 6, no. 1, pp. 557–565, 2012.

[88] M. Green, "The nature of quantum dot capping ligands," *J. Mater. Chem.*, vol. 20, no. 28, p. 5797, 2010.

[89] J. M. Luther, M. Law, M. C. Beard, Q. Song, M. O. Reese, R. J. Ellingson, and A. J. Nozik, "Schottky solar cells based on colloidal nanocrystal films," *Nano Lett.*, vol. 8, no. 10, pp. 3488–3492, 2008.

[90] M. V Kovalenko, M. Scheele, and D. V Talapin, "Colloidal nanocrystals with molecular metal chalcogenide surface ligands.," *Science*, vol. 324, no. 5933, pp. 1417–1420, Jun. 2009.

[91] Q. Dai, Y. Zhang, Y. Wang, Y. Wang, B. Zou, W. W. Yu, and M. Z. Hu, "Ligand effects on synthesis and post-synthetic stability of PbSe nanocrystals," *J. Phys. Chem. C*, vol. 114, no. 39, pp. 16160–16167, Oct. 2010.

[92] C. Burda, X. Chen, R. Narayanan, and M. a. El-Sayed, *Chemistry and properties of nanocrystals of different shapes*, vol. 105, no. 4. 2005.

[93] R. Guo, Y. Song, G. Wang, and R. W. Murray, “Does core size matter in the kinetics of ligand exchanges of monolayer-protected Au clusters?,” *J. Am. Chem. Soc.*, vol. 127, no. 8, pp. 2752–2757, Mar. 2005.

[94] A. Haghofer, P. Sonström, D. Fenske, K. Föttinger, S. Schwarz, J. Bernardi, K. Al-Shamery, M. Bäumer, and G. Rupprechter, “Colloidally prepared Pt nanowires versus impregnated Pt nanoparticles: Comparison of adsorption and reaction properties,” *Langmuir*, vol. 26, no. 21, pp. 16330–16338, 2010.

[95] C. S. Weisbecker, M. V Merritt, and G. M. Whitesides, “Molecular Self-Assembly of Aliphatic Thiols on Gold Golloids,” *Langmuir*, vol. 12, no. 16, pp. 3763–3772, Jan. 1996.

[96] a Caragheorgheopol and V. Chechik, “Mechanistic aspects of ligand exchange in Au nanoparticles.,” *Phys. Chem. Chem. Phys.*, vol. 10, no. 33, pp. 5029–5041, 2008.

[97] C. N. Kostelansky, J. J. Pietron, M. S. Chen, W. J. Dressick, K. E. Swider-Lyons, D. E. Ramaker, R. M. Stroud, C. a. Klug, B. S. Zelakiewicz, and T. L. Schull, “Triarylphosphine-stabilized platinum nanoparticles in three-dimensional nanostructured films as active electrocatalysts,” *J. Phys. Chem. B*, vol. 110, no. 43, pp. 21487–21496, Nov. 2006.

[98] C. Stolle Jackson, M. G. Panthani, T. B. Harvey, V. a. Akhavan, and B. a. Korgel, “Comparison of the photovoltaic response of oleylamine and inorganic ligand-capped CuInSe 2 nanocrystals,” *ACS Appl. Mater. Interfaces*, vol. 4, no. 5, pp. 2757–2761, May 2012.

[99] A. Kassam, G. Bremner, B. Clark, G. Ulibarri, and R. B. Lennox, “Place exchange reactions of alkyl thiols on gold nanoparticles,” *J. Am. Chem. Soc.*, vol. 128, no. 11, pp. 3476–3477, Mar. 2006.

[100] R. L. Donkers, Y. Song, and R. W. Murray, “Substituent effects on the exchange dynamics of ligands on 1.6 nm diameter gold nanoparticles,” *Langmuir*, vol. 20, no. 11, pp. 4703–4707, May 2004.

[101] M. Montalti, L. Prodi, N. Zaccheroni, R. Baxter, G. Teobaldi, and F. Zerbetto, “Kinetics of place-exchange reactions of thiols on gold nanoparticles,” *Langmuir*, vol. 19, no. 12, pp. 5172–5174, Jun. 2003.

[102] G. H. Woehrle, M. G. Warner, and J. E. Hutchison, “Ligand exchange reactions yield subnanometer, thiol-stabilized gold particles with defined optical transitions,” *J. Phys. Chem. B*, vol. 106, no. 39, pp. 9979–9981, Oct. 2002.

[103] G. H. Woehrle and J. E. Hutchison, “Thiol-functionalized undecagold clusters by ligand exchange: Synthesis, mechanism, and properties,” *Inorg. Chem.*, vol. 44, no. 18, pp. 6149–6158, Sep. 2005.

[104] S. Rucareanu, V. J. Gandubert, and R. B. Lennox, “4-(N-dimethylamino)pyridine-protected au nanoparticles: Versatile precursors for water- and organic-soluble gold nanoparticles,” *Chem. Mater.*, vol. 18, no. 19, pp. 4674–4680, 2006.

[105] M. D. Regulacio, C. Ye, S. H. Lim, M. Bosman, L. Polavarapu, W. L. Koh, J. Zhang, Q.-H. Xu, and M.-Y. Han, “One-Pot Synthesis of Cu1. 94S− CdS and Cu1. 94S− Zn x Cd1− x S Nanodisk Heterostructures,” *J. Am. Chem. Soc.*, vol. 133, no. 77, pp. 2052–2055, 2011.

[106] L. Polavarapu and Q.-H. Xu, “A simple method for large scale synthesis of highly monodisperse gold nanoparticles at room temperature and their electron relaxation properties.,” *Nanotechnology*, vol. 20, no. 18, p. 185606, May 2009.

[107] S. Suehiro, K. Horita, K. Kumamoto, M. Yuasa, T. Tanaka, K. Fujita, K. Shimanoe, and T. Kida, “Solution-processed Cu2ZnSnS4 nanocrystal solar cells: Efficient stripping of surface insulating layers using alkylating agents,” *J. Phys. Chem. C*, vol. 118, no. 2, pp. 804–810, 2014.

[108] J. Jasieniak, B. I. MacDonald, S. E. Watkins, and P. Mulvaney, “Solution-processed sintered nanocrystal solar cells via layer-by-layer assembly,” *Nano Lett.*, vol. 11, no. 7, pp. 2856–2864, Jul. 2011.

[109] M. J. Hostetler, A. C. Templeton, and R. W. Murray, “Dynamics of place-exchange reactions on monolayer-protected gold cluster molecules,” *Langmuir*, vol. 15, no. 11, pp. 3782–3789, 1999.

[110] W. Wan and J. T. W. Yeow, “The effects of gold nanoparticles with different sizes on polymerase chain reaction efficiency.,” *Nanotechnology*, vol. 20, no. 32, p. 325702, Aug. 2009.

[111] A. J. Kell, R. L. Donkers, and M. S. Workentin, “Core size effects on the reactivity of organic substrates as monolayers on gold nanoparticles,” *Langmuir*, vol. 21, no. 2, pp. 735–742, Jan. 2005.

[112] C. Steinhagen, M. G. Panthani, V. Akhavan, B. Goodfellow, B. Koo, and B. a. Korgel, “Synthesis of Cu2ZnSnS4 nanocrystals for use in low-cost photovoltaics,” *J. Am. Chem. Soc.*, vol. 131, no. 35, pp. 12554–12555, Sep. 2009.

[113] Q. Guo, G. M. Ford, W. Yang, B. C. Walker, E. A. Stach, and H. W. Hillhouse, “Fabrication of 7.2% Efficient CZTSSe Solar Cells Using CZTS Nanocrystals.pdf,” *J. Am. Chem. Soc*, vol. 132, no. 49, pp. 17384–17386, 2010.

[114] Q. Guo, H. W. Hillhouse, and R. Agrawal, “Synthesis of Cu2ZnSnS4 nanocrystal ink and its use for solar cells,” *J. Am. Chem. Soc.*, vol. 131, no. 33, pp. 11672–11673, Aug. 2009.

[115] A. Shavel, J. Arbiol, and A. Cabot, “Synthesis of Quaternary Chalcogenide Nanocrystals: Stannite Cu2Zn x Sn y Se1+ x+ 2 y,” *J. Am. Chem. …*, vol. 132, no. Figure 2, pp. 4514–4515, 2010.

[116] S. C. Riha, B. a Parkinson, and A. L. Prieto, “Solution-based synthesis and characterization of Cu2ZnSnS4 nanocrystals.,” *J. Am. Chem. Soc.*, vol. 131, no. 34, pp. 12054–12055, Sep. 2009.

[117] T. Itoh and Y. Iwabuchi, “Quantum size effect on excitons in microcrystals of cuprous halides embedded in alkali halide matrices,” *J. Lumin.*, vol. 40–41, no. 2, pp. 737–738, 1988.

[118] H. Katagiri, N. Sasaguchi, S. Hando, S. Hoshino, J. Ohashi, and T. Yokota, “Preparation and evaluation of Cu2ZnSnS4 thin films by sulfurization of E□B evaporated precursors,” *Sol. Energy Mater. Sol. Cells*, vol. 49, no. 1–4, pp. 407–414, 1997.

[119] H. Katagiri, K. Jimbo, W. S. Maw, K. Oishi, M. Yamazaki, H. Araki, and A. Takeuchi, "Development of CZTS-based thin film solar cells," *Thin Solid Films*, vol. 517, no. 7, pp. 2455–2460, 2009.

[120] K. Wang, O. Gunawan, T. Todorov, B. Shin, S. J. Chey, N. A. Bojarczuk, D. Mitzi, and S. Guha, "Thermally evaporated Cu[sub 2]ZnSnS[sub 4] solar cells," *Appl. Phys. Lett.*, vol. 97, no. 14, p. 143508, 2010.

[121] W. Wang, M. T. Winkler, O. Gunawan, T. Gokmen, T. K. Todorov, Y. Zhu, and D. B. Mitzi, "Device characteristics of CZTSSe thin-film solar cells with 12.6% efficiency," *Adv. Energy Mater.*, vol. 4, no. 7, p. 1301465, May 2014.

[122] R. W. Martin, M. Moynihan, and I. Forbes, "Optical Properties of Thin Films of Cu2ZnSnSe4 Fabricated by Sequential Deposition and Selenisation," in *Proceedings of Photovoltaic Science (PVSAT)*, 2010, no. 3, pp. 29–32.

[123] H. Katagiri, K. Jimbo, S. Yamada, T. Kamimura, W. S. Maw, T. Fukano, T. Ito, and T. Motohiro, "Enhanced conversion efficiencies of Cu2ZnSnS4-based thin film solar cells by using preferential etching technique," *Appl. Phys. Express*, vol. 1, no. 4, pp. 0412011–0412012, Apr. 2008.

[124] K. Tanaka, Y. Fukui, N. Moritake, and H. Uchiki, "Chemical composition dependence of morphological and optical properties of Cu2ZnSnS4 thin films deposited by sol-gel sulfurization and Cu2ZnSnS4 thin film solar cell efficiency," *Sol. Energy Mater. Sol. Cells*, vol. 95, no. 3, pp. 838–842, Mar. 2011.

[125] H. Jiang, P. Dai, Z. Feng, W. Fan, and J. Zhan, "Phase selective synthesis of metastable orthorhombic Cu2ZnSnS4," *J. Mater. Chem.*, vol. 22, no. 15, p. 7502, 2012.

[126] L. Shi, C. Pei, Y. Xu, and Q. Li, "Template-directed synthesis of ordered single-crystalline nanowires arrays of Cu2ZnSnS4 and Cu2ZnSnSe4," *J. Am. Chem. Soc.*, vol. 133, no. 27, pp. 10328–10331, Jul. 2011.

[127] A. Singh, H. Geaney, F. Laffir, and K. M. Ryan, "Colloidal synthesis of wurtzite Cu 2ZnSnS 4 nanorods and their perpendicular assembly," *J. Am. Chem. Soc.*, vol. 134, no. 6, pp. 2910–2913, 2012.

[128] F. J. Fan, L. Wu, M. Gong, G. Liu, Y. X. Wang, S. H. Yu, S. Chen, L. W. Wang, and X. G. Gong, "Composition-and band-gap-tunable synthesis of wurtzite-derived Cu 2ZnSn(S1-xSex)4 nanocrystals: Theoretical and experimental insights," *ACS Nano*, vol. 7, no. 2, pp. 1454–1463, Jan. 2013.

[129] K. Ramasamy, X. Zhang, R. D. Bennett, and A. Gupta, "Synthesis, photoconductivity and self-assembly of wurtzite phase Cu2CdxZn1−xSnS4 nanorods," *RSC Adv.*, vol. 3, no. 4, p. 1186, 2013.

[130] O. Gunawan, T. K. Todorov, and D. B. Mitzi, "Loss mechanisms in hydrazine-processed Cu2ZnSn(Se,S)4 solar cells," *Appl. Phys. Lett.*, vol. 97, no. 23, p. 233506, 2010.

[131] D. B. Mitzi, M. Yuan, W. Liu, A. J. Kellock, S. J. Chey, L. Gignac, and A. G. Schrott, "Hydrazine-based deposition route for device-quality CIGS films," *Thin Solid Films*, vol. 517, no. 7, pp. 2158–2162, 2009.

[132] T. K. Todorov, J. Tang, S. Bag, O. Gunawan, T. Gokmen, Y. Zhu, and D. B. Mitzi, “Beyond 11% Efficiency: Characteristics of State-of-the-Art Cu2ZnSn(S,Se) 4 Solar Cells,” *Adv. Energy Mater.*, vol. 3, no. 1, pp. 34–38, Jan. 2013.

Chapter 3: Experimental Methods

3.1 Introduction

This chapter contains a discussion of the experimental methods of fabrication and characterisation used during the course of this research. Specific details of particular experimental procedures are outlined in each of the relevant results chapters.

3.2 Fabrication Techniques

As part of this work, a number of different fabrication techniques were used to a) synthesise quaternary nanocrystals, b) process the nanocrystals to form stable colloidal solutions and c) to deposit the nanocrystals from solution, thereby forming nanocrystalline thin films for use in photovoltaic devices.

3.2.1 Synthesis Techniques

CZTS nanocrystals were synthesised using a novel injection technique adapted from a method developed by Hines and Scholes[1] which has extensively been used to synthesise other chalcogenide nanocrystals (e.g. PbS, CdS etc.)[1]. All syntheses were performed in an argon purged atmosphere, in glassware vessels attached to a Schlenk line. A diagram of the reaction set-up is shown in Figure 3.2-1

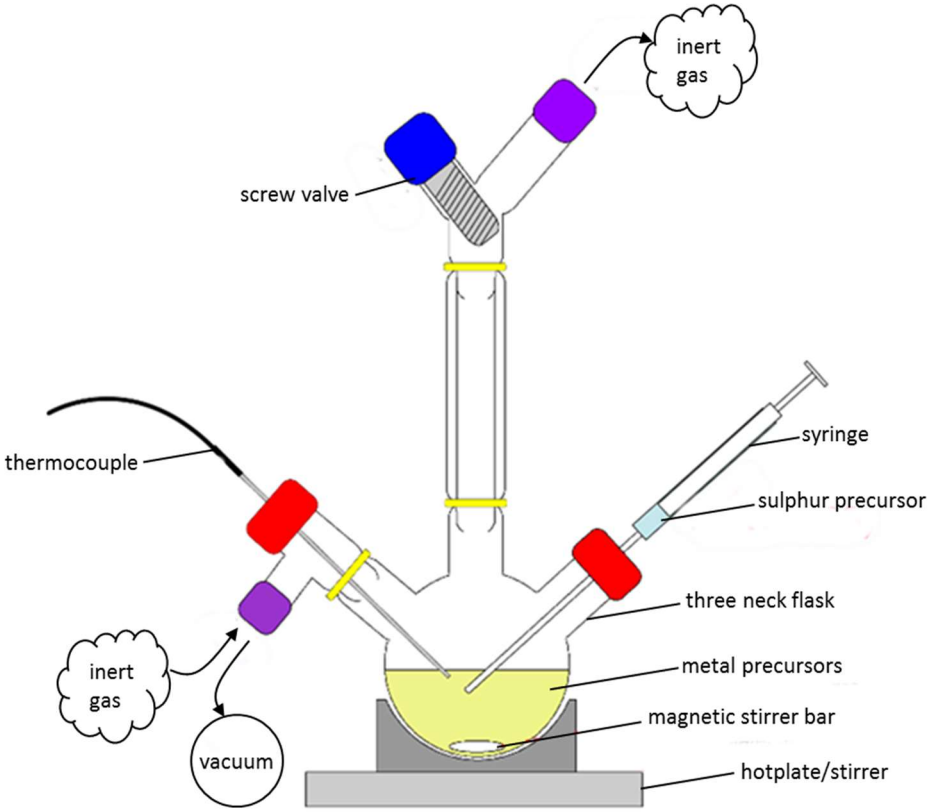

Figure 3.2-1 A schematic illustration showing the experimental set-up for synthesising CZTS nanocrystals, the set-up comprising a three neck flask (containing metal precursors being stirred by a magnetic stirrer bar under the influence of a stirrer/hotplate). One of the flask-necks is directly sealed with a rubber bung (shown in red), through which a needle may be inserted, thereby allowing for a sulphur precursor solution to be injected into the reaction solution, via a syringe. A glassware T-junction is secured in the second flask-neck; a second rubber bung is used to seal an open end of the T-junction, through which a thermocouple is inserted and placed in contact with the reaction solution, thereby enabling the measurement of the reaction temperature; the second opening of the T-junction is coupled to a schlenk line system providing either a vacuum source (rotary pump) or inert gas supply (e.g. N_2 or Ar). The third flask-neck acts as an exhaust for the reaction vessel and is connected to an oil bubbler (not shown), via a condensation tube and a screw valve. The screw valve is engaged when the reaction vessel is exposed to the vacuum so as to prevent any oil or gas in the exhaust line from being drawn into the reaction vessel.

Hot Injection

All chemicals were used without purification. Bis(trimethylsilyl) sulphide [TMSS] (Aldrich) and 1-octadecene [ODE] (Aldrich 99.5%) and oleylamine [OLA] (Aldrich 70%) were stored in a nitrogen filled glovebox maintained at >10ppm O_2 and 0.1ppm H_2O atmospheric conditions. $Cu(C_5H_7O_2)_2$ (Aldrich 99.99%), $Zn(O_2CCH_3)_2$ (Aldrich 99.99%) and $SnCl_4{\cdot}(H_2O)_5$ (Aldrich 98%) were stored outside of a glovebox. Due to the extremely volatile nature of TMSS an appropriate quantity (0.475ml,

4mmol) for each reaction was diluted in 10ml of ODE and placed in sealed glass vials, inside the glovebox. The TMSS solution was then transferred to the reaction fume-hood in an air tight (and solvent resistant) container immediately before it was injected into the reaction vessel, in order to limit oxidation of the reaction precursors and to reduce the risk of exposing laboratory workers to toxic reagents.

In a typical preparation $Cu(C_5H_7O_2)_2$ (0.52mg, 2mmol), $Zn(O_2CCH_3)_2$ (29mg, 1mmol), $SnCl4•(H_2O)_5$ (35mg, 1mmol) and OLA (20ml) are placed in a three-neck flask and heated under vacuum and constant stirring to 75°C. The flask is then purged with argon as the temperature is increased to 130°C until a yellowish transparent solution is formed, at which point these conditions are maintained for 1hr. After the reaction solution has reached the appropriate reaction temperature (e.g. 140°C) the TMSS-ODE solution is injected into the three neck flask. Immediately prior to injection, the glass syringe is purged with argon 10 times to reduce the likelihood of oxygen/moisture entering the reaction vessel. Upon injection of the TMSS, the reaction mixture changes from a clear yellow liquid to a viscous brown colloid and the reaction solution temperature dropped 5-10°C. After 2 minutes of constant heat and continuous stirring, the reaction vessel was removed from the heat and placed in an ice bath where it was allowed to cool below 60°C.

Initially copper acetylacetonate, zinc acetate and tin chloride were employed as the metal cation precursors. Each experiment was later repeated using alternative copper and zinc nitrate precursors, achieving the same result. Following the preliminary investigations using copper acetylacetonates and zinc acetate, all subsequent syntheses used nitrate precursors in order to aid cleaning of the nanocrystals. Acetylonates in particular are known to stick to the glass vials used in processing of colloidal NCs and as such require more rigorous cleaning procedures to

prevent contamination of characterisation samples. Achieving the same result with multiple copper and zinc cation precursors helps to demonstrate the robustness of this synthesis method.

Developing a robust and repeatable synthesis methodology is key to accurately investigating the properties of solution synthesised nanocrystals. In order to achieve consistent synthesis, each experiment was carried out under standard conditions using personalised laboratory equipment, so as to prevent contamination with the experiments of other lab users. To prevent the accumulation of experimental errors all reaction precursors were measured to within a high degree of accuracy (i.e. solid precursors were measured to within ±0.01g, and solution precursors to within ±1µl), using regularly calibrated measuring equipment. Gas purity and flow rates were also monitored and calibrated before each experiment. Finally, the temperature of each reaction was monitored to within 0.5°C.

Nanocrystal Cleaning

A purged 10ml syringe was used to transfer the nanoparticle colloid to a 50ml vial containing a 50/50 mix of a non-polar/ polar solvent. Examples of non-polar solvents used include hexane, chloroform, toluene and chloro-benzene, whereas acetone, ethanol, isopropanol and methanol are examples of polar solvents. The mixture was then agitated in an ultrasonic bath for 5mins and then centrifuged at 4000-6000rpm for 10mins. This process precipitated the nanocrystals out of solution, forming a solid pellet at the bottom of the vial. Any unreacted reagents and poorly dissolved by-products suspended in the supernatant solution could then be poured away. 5ml of toluene was then added to the vial which was then vigorously shaken until the nanocrystals had visibly redispersed. The precipitation-centrifugation-

dispersion process was performed twice more. Typically, a milder polar solvent was used to precipitate the nanocrystals at this stage. Repeated use of highly polar solvents such as acetone, can result in the removal of ligands and subsequent agglomeration of the nanocrystals. After cleaning, CZTS nanocrystal solids were dried under argon and the dry weight of the CZTS nanocrystal solid was measured and then re-dispersed in 5ml to form a viscous (~30mg/ml) stock solution suitable for thin film coating. The solution concentration was measured by incrementally dropping 0.25ml of nanocrystal-toluene solution on to a microscope slide (using a 1000µl Eppendorf™ pipette), allowing 5 minutes for the toluene to evaporate and measuring the subsequent change in mass. The accuracy of this result was periodically calibrated by TGA/DTA gravimetric analysis. Finally, the CZTS nanocrystal solutions were stored in a N_2-filled glovebox for further use. Aliquots of stock nanocrystal solutions were dispersed in anhydrous polar solvents in order to form weak solutions (<1mg/ml) prior to characterization.

Solution Ligand Exchange

Before depositing CZTS nanocrystals onto a substrate, a ligand exchange was performed to replace the oleylamine and/oleic acid ligands with much shorter and more volatile pyridine ligands. The stock solution of CZTS nanocrystals was precipitated with ethanol, dried under a flow of nitrogen and then dispersed in an excess (50ml) of pyridine. This solution was transferred to a two neck flask, which was suspended in a beaker of silicone oil and connected to a Schlenk line. Under constant stirring, the pyridine-nanocrystal mixture was evacuated using a rotary pump for 1 hour at room temperature. It was then heated to 130°C for ~24 hours under a gentle flow of argon. After heating, the solution was transferred to a nitrogen filled glovebox whereupon the nanocrystals were precipitated with anhydrous

hexane, centrifuged at 4000rpm for 5 minutes and redispersed in pyridine. The now pyridine-capped CZTS nanoparticles were precipitated and redispersed a further two times in order to remove the dissociated oleylamine/oleic acid molecules, together with any poorly capped nanocrystals.

3.2.2 Device Fabrication

Following the synthesis of the CZTS NCs, further experiments required the fabrication of thin film photovoltaic devices, in order to investigate the opto-electronic properties of CZTS. Direct film formation from solution precursors is highly attractive for commercial production of CZTS thin films due to its compatibility with high throughput roll-to-roll processing techniques[2]. On a smaller scale, spin coating, dip coating, drop casting, and doctor blading are typically used for laboratory-scale solar cell research. Dip coating, although highly successful for fabricating quantum dot solar cells, is only suitable for depositing several hundred nanometre thick films[3]. Each dipping cycle deposits only a few monolayers of NCs. Consequently, it may take hundreds of dipping cycles to deposit 1-2μm thick films (typical thickness of a CZTS absorber layer) from 5 nm diameter NCs[3]. As a result, layer-by-layer dip coating is unsuitable for industrial fabrication as well as being tediously slow for laboratory research. Drop casting from NC dispersions was extensively used in the early days of nanocrystal thin film deposition[4]. Although very simple to perform, drop casting from NC dispersions is also difficult to scale up for industrial production, and offers particularly poor control of nanocrystal film thickness and uniformity[4]. Doctor blading is frequently used for commercial thin film production however, it is difficult to consistently deposit films thinner than ~1μm using this technique. Spin coating wastes up to 90% of the initial solution during deposition and is difficult to scale up for large scale industrial applications[4] however, it does offer excellent

control over thin film thickness, uniformity and provides a model system to experiment and analyse multiple fabrication parameters[4]. For this reason, spin coating was used as to primary means of fabricating the thin film solar cells used in this work.

A number of distinct fabrication steps were required to produce working photovoltaic devices, including: a substrate etching and cleaning step, an n-type window layer (CdS thin film) deposition step, a p-type absorber layer (CZTS NCs thin film) deposition step and a metal electrode (Au) thermal evaporation step (as shown in Figure 3.2-2).

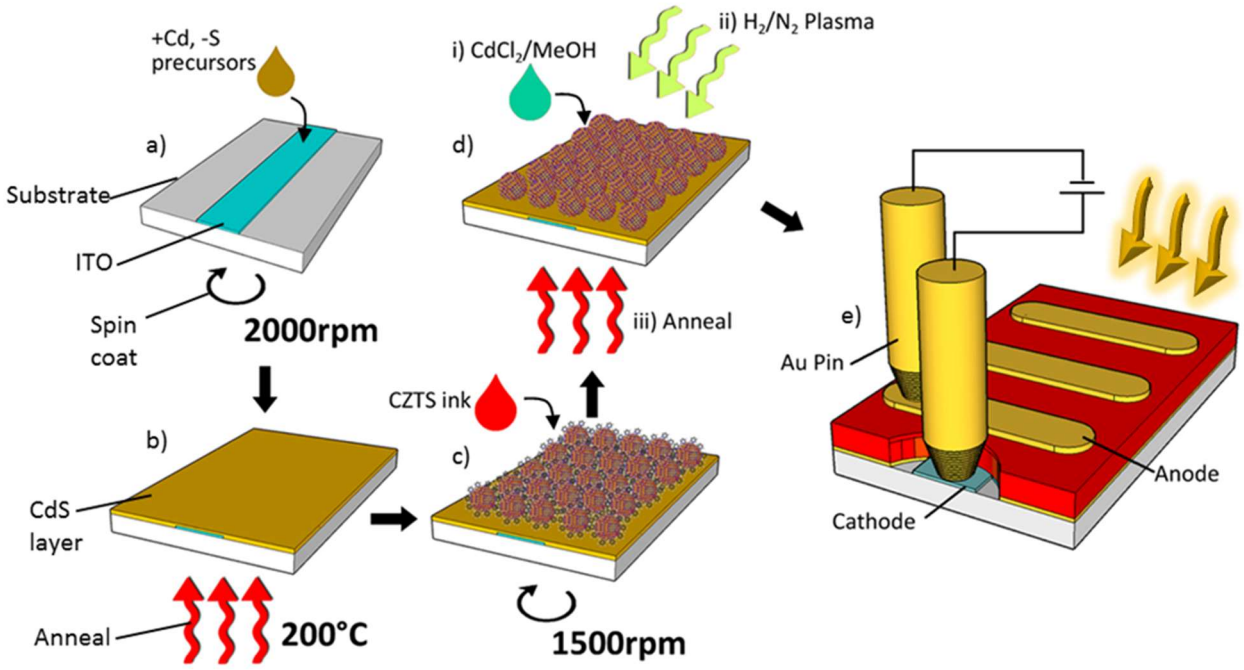

Figure 3.2-2 A schematic illustration of the step-by-step process of fabricating a FTO-CdS-CZTS-Au device, the process including a) spin coating a CdS precursor solution onto a rectangular glass substrate, adorned with a pre-etched FTO strip, at 2000rpm for 60s b) annealing the CdS spin coated n-type window layer at 200°C for 60 mins, c) spin coating a CZTS NC solution onto the underlying CdS thin film at 1500rpm for 30s, d) applying (i) a $CdCl_2$ solution treatment, (ii) an H_2/N_2 plasma treatment or (iii) an ambient annealing treatment to the deposited CZTS NC thin film and d) depositing Au top electrodes to form a complete circuit for testing.

Glass Substrate Etching and Cleaning- [Figure 3.2-2a]

In order form the transparent bottom electrode of the experimental device, fluorine doped tin oxide (FTO) coated glass substrates, measuring 10 x 12 x 1.1mm, were masked with a polyimide tape to protect the underlying FTO. The unmasked area was then covered with a thin layer of zinc-powder. By adding 2-3 drops of 2M hydrochloric acid (HCl)-solution, the FTO-layer was reduced by the evolving hydrogen and could therefore be removed. The resultant FTO strip (120nm thick and 2.5mm wide) running the length of the device formed the bottom electrode (cathode) of the device with a sheet resistance of $\sim 5.4\times10^{-4}$ Ωcm.

To clean the surface of the newly etched bottom electrode, multiple substrates were suspended on metal supports in a beaker of detergent solution (4ml DECON90 soap + 800ml de-ionised water), heated to 60°C, and then sonicated for 5 minutes. The substrates were sonicated for a further 5 minutes at the same temperature in a beaker of de-ionised water to remove any soap solution before placing the substrates in acetone ($OC(CH_3)_2$) and then isopropanol (C_3H_7OH) at 50° for a further 3 minutes each. The acetone is used to remove any organic matter while the isopropanol is used to dissolve any water and acetone left over from the previous cleaning steps.

Finally, the substrates were oxygen plasma treated for 10 seconds, using a Nanotech PLASMOD plasma chamber, to remove any remaining organic material that had bonded to the substrate surface. The O_2 plasma passivation also reduces the contact angle formed between the glass/FTO surface and the droplet of nanocrystal solution, thus helping to wet the glass/FTO substrate before spin coating. This in turn helps to improve the uniformity of the resultant thin film and reduces solution wastage.

CdS Thin Film Deposition [Figure 3.2-2a-b]

A simple additive process, adapted from a method developed by J.C. Ramos et al.[5], was used to grow n-type CdS thin films. A precursor solution comprising cadmium acetate dihydrate ($Cd(CH_3COO)_2 \cdot 2H_2O$) [0.1 M] and thiourea ($CH_4N_2S$) [0.2 M] mixed in methanol/ethylene glycol (ratio 95:05) was first prepared in a fume hood. 100µl was then spin coated at 2000rpm for 60s on to O_2 plasma treated substrates. This was then immediately placed onto a hot plate at 200°C for 60 min to allow the growth of the CdS thin film and for the removal of unwanted organic by-products. The thickness of CdS films were measured (using a DEKTAK surface profiler) to be ~60-70nm (±6nm).

CZTS NC Thin Film Deposition- [Figure 3.2-2c]

A typical spin deposition cycle starts with the cleaning and functionalization of the substrate (as described above). The solution to be spin coted is typically passed through a filter to prevent any coagulated particles from disrupting the spin-off of the solvent during the deposition. Spin coating is typically carried out in a layer-by layer process and for each spin cycle, the substrate is continuously spun until an equilibrium film thickness has been reached. This is quickly followed by an annealing step which helps to alleviate any radial orientation of the spun solution and additionally eliminates any remaining solvent.

Several variables can control the thickness of the final film, including solvent polarity, viscosity and solubility. Typically, film thickness increases as spin speed decreases. Providing that sufficient solution is applied to the substrate surface, the amount of solution used per spin cycle does not affect the resulting film thickness; as any excess solution is ejected from the surface, due to the resulting centripetal forces.

To form a CZTS nanocrystal thin film, 2ml of pyridine-NCs solution was transferred to a 5ml plastic syringe in a nitrogen filled glovebox. Two drops (approximately 20µl) were passed through a 4µm PVDF filter and spin coated on to CdS coated substrate, spinning at 1500rpm, for 30 seconds. The substrate was then transferred to a hotplate set to 150°C for 10 minutes, to allow for the pyridine to evaporate (illustrated by the red arrows in Figure 3.2 2d(iii)). The substrate was removed from the hotplate for 5 minutes to allow it to cool down before returning it to the spin coater for the deposition of another layer.

$CdCl_2$ Solution Treatment- [Figure 3.2-2d(i)]

As the part of the investigations reported in Chapter 6 of this work, some of the fabricated devices underwent an additional chemical processing step. In such cases, a solution of $CdCl_2$ powder dissolved in methanol was dropped onto the device surface, following the annealing and cooling of each CZTS NCs thin film.

Plasma Treatments- [Figure 3.2-2d(ii)]

A Nanotech PLASMOD plasma chamber purged with H_2/N_2 gas was used to treat the thin film top surface with a highly charged H_2 plasma. The chamber was initially evacuated to below 30mTorr using a rotary pump. The chamber was subsequently purged three times with H_2/N_2 gas at a pressure of 20Torr for 10 seconds. A plasma would then be formed in the chamber under constant H_2/N_2 gas flow of 100mTorr.

Top Electrode Deposition- [Figure 3.2-2e]

To complete each device three metal electrodes, each 110nm thick and 1.1mm wide, were thermally evaporated under vacuum ($1x10^{-6}$Torr) on to the exposed thin film surface, perpendicular to the underlying FTO strip. These parallel metal contacts form the anode of the photovoltaic device, thus forming an active cell area of $2.2mm^2$.

In order to connect each electrode up to an external circuit, a small square section of the nanocrystal thin film at each end of the device was removed using a sharpened, wooden cotton-bud stick to reveal the FTO cathode beneath.

3.3 Characterisation Techniques

Characterisation forms a central role in much of the analysis featured in each of the experimental chapters of this work. A number of characterisation techniques were used to investigate the properties of CZTS NCs when stabilised in solution and also when deposited in semiconductor thin films.

3.3.1 Structural and Elemental Characterisation of Nanocrystals

The structural characterisation of solution synthesised NCs was carried out using a number of techniques including transmission electron microscopy (TEM), scanning transmission electron microscopy (STEM), high angle annular dark field microscopy (HAADF) and X-ray diffraction (XRD) spectroscopy. Elemental characterisation was further carried out using energy dispersive X-ray spectroscopy (EDS/EDX), thermo-gravimetric calorimetry and Raman spectroscopy.

X-Ray Diffraction (XRD) Spectral Characterisation

XRD was used in this study to identify alternative CZTS crystal structures along with secondary phases formed during the nanocrystal synthesis. XRD analysis was performed using a Philips Theta-2-Theta X-ray diffractometer. The instrumental broadening line width was determined by a Si-reference standard (NIST 640c) and subtracted from the spectra prior to the peak analysis using PANalytical - HighScore™ software. Samples were prepared by drop casting thick (>100mg/ml) NC dispersions onto 25x25mm silicon wafers. For analysis of the thin films, the volume of material

that contributes to the signal is typically very small. Spectra acquisition requires very long integration times leading to a large background signal.

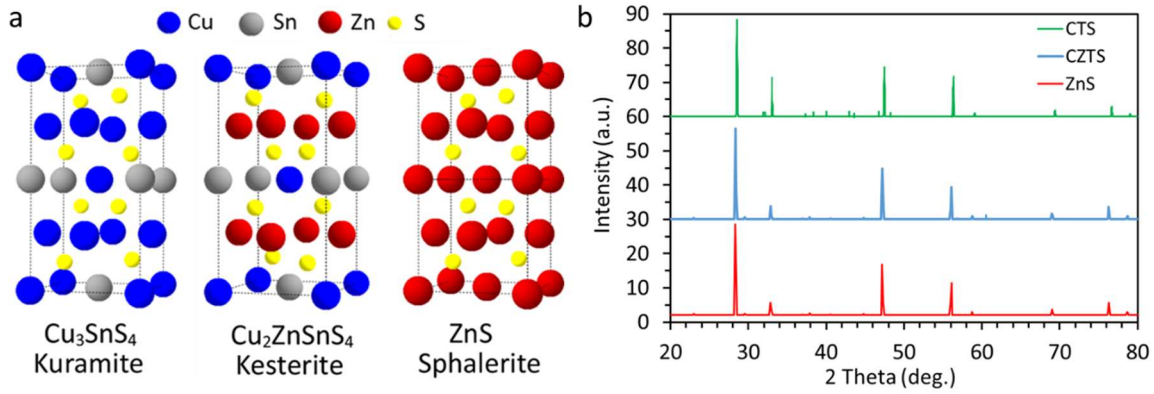

Figure 3.3-1 a) Model crystal structures of the tetragonal forms of Cu_2SnS_3 (CTS), Cu_2ZnSnS_4 (CZTS) and ZnS generated using CrystalMaker™. b) Model X-Ray diffraction traces of CTS, CZTS and ZnS crystal structures generated using Crystal Diffract™.

The XRD peaks of different crystallographic phases often overlap: For example, Cu_2ZnSnS_4 (CZTS), Cu_2SnS_3 (CTS) and ZnS can all exhibit tetragonal (sphalerite) structures (see Figure 3.3-1a), which results in an overlap of the dominant experimental peaks of their respective XRD spectra as shown in Figure 3.3-1b. It is therefore difficult to identify CZTS clearly despite the presence of some small extra peaks which ZnS does not show. As ZnS has no unique peak its presence can never be proven or excluded using this technique alone, as long as there is crystalline CZTS and CTS present in the sample. Furthermore, the absence of an XRD signal does not necessarily mean that the secondary phase is also absent from the specimen, since it could still be present in an amorphous form. Experimentally acquired XRD peaks can also appear at different intensities compared to database values. Typically reference spectra are derived from powder diffraction samples which exhibit no preferred crystal orientation. By contrast, for the case of directionally grown nanocrystals, some peaks may not be present.

Transmission Electron Microscopy (TEM) Characterisation

Transmission electron microscope samples were prepared by dipping an ultra-thin carbon coated gold grid into a very dilute solution of cleaned NCs dispersed in toluene/hexane. Each grid was air plasma treated for 5 seconds using a Nanotech PLASMOD plasma chamber, to remove any remaining organic material. Acquisition of low and high resolution images and selected area diffraction patterns was carried out using a JEOL-JEM 2010 LaB6 microscope, at an accelerating voltage of 200 kV. Imaging of individual lattice planes and corresponding twinning analysis of CZTS nanoparticles was carried out using an Oxford-JEOL 2200MCO aberration corrected microscope.

Scanning Transmission Electron Microscopy (STEM), High Angle Annular Dark Field Imaging (HAADF) Characterisation

Scanning transmission electron microscopy elemental mapping and high angle annular dark field imaging was carried out using a JEOL 3000F field emission gun microscope at an accelerating voltage of 300kV (equipped with an Oxford Instruments LZ5 windowless energy dispersive X-ray spectrometer).

Energy Dispersive X-Ray Spectrometry (EDS/EDX)

Energy dispersive X-Ray spectrometry is typically used to analyse the elemental composition of a sample. The technique relies on a phenomenon wherein a high energy electron (from a collimated electron beam) may excite an electron that is bound within the atomic structure of a sample atom. The excited electron may be ejected from the electron shell, resulting in the formation of a vacancy. The vacancy is then filled by an electron from a higher shell, within the atomic structure, resulting in the release of an X-ray photon, with a characteristic energy that is specific to the sample atom[6]. The X-ray photons that emanate from the sample are detected and

their energies are analysed in order to determine the elemental makeup of the sample. Each photon that arrives at the detector may be absorbed by a lithium doped silicon detector, producing an electron-hole-pair. The number of electron-hole pairs is linear to the energy of the X-ray photon[6].

To a first approximation X-ray absorption and secondary X-ray fluorescence within thin samples, such as those used in TEM-EDS spectrometry, can be ignored[7]. The absolute X-ray intensity therefore a function of specimen thickness, as well as composition. However, under these 'thin film criterion' conditions, the ratio of two observed X-ray intensities $\frac{I_A}{I_B}$, is independent of thickness. Hence, this ratio can be related directly to the corresponding weight-fraction ratio, $\frac{C_A}{C_B}$ by equation 3.3-1:

$$\frac{C_A}{C_B} = k_{AB} \frac{I_A}{I_B} \qquad 3.3\text{-}1$$

where k_{AB} is a factor which accounts for the relative efficiency of X-ray production and detection. At a given accelerating voltage (>100kV), k_{AB} is effectively independent of specimen thickness and composition[7].

In this work, individual elements or their associated peaks, are identified automatically and the atomic mass percentage is immediately computed using INCA Energy Software (Oxford Instruments), which calculates the ratios of elemental peak intensities and employs the relevant k_{AB} value (the k-factor) in order to relate the intensity ratio to the elemental concentration ratio (using an equivalent relationship as that shown in equation 3.3-1). Elements that are known not to be present in the sample or that are irrelevant for the considerations were removed manually, and the composition was calculated for the remaining elements. The characteristic peaks are

labelled according to the corresponding shell from which the electrons were ejected (i.e. K-, L-, M-shell etc.), and the shell from which it has been substituted (i.e. α for the next higher shell, β for the next but one shell etc.).

The typical EDS spectrum is predominantly dependent on the intensity of the incoming electron beam, the atomic concentration in the sample, the ionization cross section, the X-ray absorption coefficient in the material and the detector efficiency[7]. A considerable barrier to performing an accurate EDS analysis is the overlapping of spectra peaks associated with different elements. Not all the characteristic X-ray photons reach the detector leading to a reduced peak height and a subsequent reduction in the energy resolution of the spectra. Counting for a longer time period increases the total count, which helps reduce the statistical scatter of the background radiation. Increasing the probe current or analysing a thicker area of the specimen also improves the total count, although this does significantly reduce the maximum achievable spatial resolution, since overlapping NCs can mask the presence of distinct NC species[6].

The INCA Energy software suppresses the background, using a filtering method which avoids any specific shape calculation. It then performs a deconvolution of any overlapping energy peaks and then extracts the intensity of each peak using a filtered least squares method.

Thermo-Gravimetric Characterisation

DTA/TGA analysis was carried out using a Perkin Elmer Pyris TGA. Samples were prepared by pipetting 30mg/ml of CZTS nanocrystals-toluene solutions, in to a 50µl ceramic crucible and heated under a N_2 flow up to 850°C at a rate of 1°C/5 seconds.

Raman Infrared Spectroscopy

Raman spectroscopy analysis was carried out using a JY Horiba LabRAM ARAMIS imaging confocal Raman microscope. Samples were prepared by drop casting 30mg/ml solutions of CZTS nanocrystals in hexane/toluene on to silicon wafer substrates and allowing for the hexane/toluene to evaporate, thus forming a thin CZTS nanocrystal film.

Nanocrystal Size Analysis

During the course of this work, both XRD and Raman spectral characterisation is used to investigate the crystallite size of nanocrystals in solution or of crystalline thin films. In each case the observed spectrum is analysed to approximate the average diameter (D) of crystalline materials within a given sample using the Debye-Sherrer formula, (shown in equation 3.3-2):

$$\mathrm{D} = \frac{0.9\lambda}{\beta cos\theta} \qquad 3.3\text{-}2$$

where λ is the wavelength of radiation used (CuKα 0.15418 nm) and β is the corrected (Gaussian) full width at half maximum in radian 2θ at angle 2θ. The full width at half maximum (FWHM) measurement identifies the width of the diffraction peak, in radians, at a height that is half-way between background signal and the peak maximum.

For any given sample, there are a number of factors that may contribute to the observed peak profile including; sample crystallite size, structural microstrain, non-uniform lattice distortions, dislocations, antiphase domain boundaries as well as numerous instrumental factors such as, for example, temperature dependent peak broadening[8]. Due to the small size of the nanocrystals, each technique produces only very weak signals. Therefore, the overall contribution of the signal noise is

significantly more important than the contribution of any instrumental factors (instrumental broadening). The broadening, caused by the very small crystallite size (specimen broadening), will also be significantly larger than the instrumental broadening[8]. In order to limit the influence of instrumental factors on the nanocrystal size analysis, each characterisation experiment was undertaken using the same apparatus, operated under equivalent experimental conditions (e.g. scan speed, sample volume/thickness etc.). Each sample was characterised at least three times from which an average FWHM value was then determined. When analysing XRD spectra peaks, FWHM and peak position values were determined using Highscore Plus™ software, whereas Origin Pro™ was used to analyse the spectra resulting from Raman spectroscopy measurements. The Origin Pro™ software in particular, was used to fit hybrid Gaussian-Lorentzian curves from which an accurate FWHM value could be extracted.

3.3.2 Optical Characterisation

Ultraviolet–Visible-Near-Infrared (UVVIS-NIR) Photo-Absorption

Samples were prepared by dissolving CZTS nanoparticles in hexane/toluene to form weak solutions (10mg/ml), which were then spin-cast onto quartz slides which were then air plasma treated for 30s before spectral analysis.

3.3.3 Surface Characterisation

Dektak Stylus Profilometry

Thickness and roughness measurements of nanocrystal thin film devices were characterised using a Surface Veeco DekTak 6M stylus profiler. A clean scalpel blade was used to partially scrape away the thin films so as to achieve a suitable step profile from which to measure the thickness,

Scanning Electron Microscopy (SEM)

SEM analysis was carried out using a JEOL-JEM 840F microscope to determine the topographical morphology of the surface and cross section of each device. Samples were mounted on to 5x25Θmm aluminium stubs using silver conductive paint and coated with a 3nm layer of platinum using a Cressington 208HR sputter coater.

3.3.4 Chemical Characterisation of Ligand Substitution

Fourier Transfer Infrared (FTIR) Spectroscopy

Fourier Transform Infra-Red (FTIR) spectral analysis was carried out using a Varian Excalibur Series FSE 3500 spectrometer. Solution samples were analysed by drop casting 20µl on to the diamond window of the Attenuated Total Reflectance (ATR) attachment. Peak deconvolution and identification was undertaken using Origin Pro™ software. In order to reduce the cumulative experimental errors, each solution had a concentration of 15mg/ml. The diamond window was cleaned and recalibrated between measurements so as not to influence any subsequent reading.

Thin film samples, prepared on borosilicate glass, were characterised in transmission mode using a purpose built sample support. The relative peak intensities of each measurement were normalised according to the average thin film thickness, which was determined using DEKTAK stylus profilometry.

3.3.5 Opto-Electronic Device Characterisation

Current-Voltage (I-V) Characterisation

All devices were loaded into an airtight chamber for characterisation in inert atmosphere flushed with N_2 constantly. Current-voltage (*I-V*) measurement was performed on a Keithley 2400 Source meter. The voltage was swept from -0.5 to 1.0V

at a step size of 0.025 V. An AM1.5 solar spectrum was produced by a Newport 96000 150W solar simulator fitted with an AM1.5 filter. The power density of the light source was calibrated with an Abet Technologies 15151 Low Cost Reference Cell to 100mWcm^{-1}.

Transient Photovoltage Measurements

The voltage of the illuminated solar cell as a function of time was recorded with a Teledyne Lecroy Wavejet 354A USB storage oscilloscope. The scope is equipped with two channels with a maximum resolution of 16 bits for an input voltage between ± 100 mV and ± 10 V, measured with a 1M Ohm coupling and a maximum time resolution was 1 μs. The light source was supplied by a Thorlabs, MCWHL5 Cold White Mounted High-Power LED with a High-Power, 1-Channel LED Driver with Pulse Modulation, DC2100. The applied pulse length ranged from 50ns - 5s, the pulse amplitude between 0.1V and 10V and the repetition rate between 0.1Hz and 10MHz.

3.4 References

[1] M. Hines and G. Scholes, "Colloidal PbS nanocrystals with size tunable near infrared emission: observation of post synthesis self narrowing of the particle size distribution," *Adv. Mater.*, vol. 15, no. 21, pp. 1844–1849, 2003.

[2] T. K. Todorov, J. Tang, S. Bag, O. Gunawan, T. Gokmen, Y. Zhu, and D. B. Mitzi, "Beyond 11% Efficiency: Characteristics of State-of-the-Art Cu2ZnSn(S,Se) 4 Solar Cells," *Adv. Energy Mater.*, vol. 3, no. 1, pp. 34–38, Jan. 2013.

[3] E. H. Sargent, "Solar cells, photodetectors, and optical sources from infrared colloidal quantum dots," *Adv. Mater.*, vol. 20, no. 20, pp. 3958–3964, Oct. 2008.

[4] S. E. Habas, H. a S. Platt, M. F. a M. Van Hest, and D. S. Ginley, "Low-cost inorganic solar cells: From ink to printed device," *Chem. Rev.*, vol. 110, no. 11, pp. 6571–6594, 2010.

[5] J. C. Ramos, D. L. Kabir, I. Mejia, M. Mireles, C. a. Martinez, and M. a. Quevedo-Lopez, "Inkjet Printed Thin Film Transistors Using Cadmium Sulfide as Active Layer Prepared by In-Situ Micro-Reaction," *ECS Solid State Lett.*, vol. 2, no. 9, pp. P67–P69, 2013.

[6] M. Watanabe and D. B. Williams, "The quantitative analysis of thin specimens: A review of progress from the Cliff-Lorimer to the new ζ-factor methods," *J. Microsc.*, vol. 221, no. 2, pp. 89–109, 2006.

[7] G. Lorimer, "Quantitative X-ray microanalysis of thin specimens in the transmission electron microscope; a review," *Mineral. Mag.*, vol. 51, no. 359, pp. 49–60, 1987.

[8] J. I. Langford and A. J. C. Wilson, “Scherrer after sixty years: A survey and some new results in the determination of crystallite size,” *J. Appl. Crystallogr.*, vol. 11, no. 2, pp. 102–113, Apr. 1978.

Chapter 4 - Temperature Dependent Phase Change

"Physics is like sex: sure, it may give some practical results, but that's not why we do it" - Richard P. Feynman

Part of this thesis chapter was published in Chem. Commun., 2013,49, 3745-3747 and presents the first investigation of the temperature dependent phase change in Cu_2ZnSnS_4 nanocrystals. The synthetic method was developed by Chris Cattley, who also prepared the manuscript with the help of Dr Cheng Cheng, Prof. Hazel E. Assender and Prof. Andrew A. R. Watt.

4.1 Introduction

The application of indium-free quaternary chalcogenides, such as Cu_2ZnSnS_4 (CZTS), in photovoltaics has created tremendous interest in recent years[1]. Theoretical studies have predicted the degree to which the optoelectronic properties of CZTS can be tuned by altering the elemental and morphological composition[2].

Meanwhile significant improvements in shape control and mono-dispersity, a necessary requirement for effective application of QDs in electronic devices[3], have been achieved using highly reactive sulphur precursors[4], [5]. Previous studies have reported relatively low temperature (<200°C) synthesis of wurtzite phase CZTS nanocrystals (NCs)[4] and rods[5] and there is much speculation as to the influence of 1-dodecanethiol in preferentially selecting hexagonal phase CZTS[4], [5]. Until now low temperature synthesis has been limited to the formation of hexagonal phase CZTS nanocrystals.

This chapter reports the temperature-dependent phase change between two distinct crystallographic phases of stoichiometric CZTS using a one pot synthesis method to produce homogeneous NC colloids.

4.2 Nanocrystal Synthesis

Synthesising a complicated multi-component quaternary nanocrystal presents many challenges[6]–[8] especially if a one-pot synthesis is desired[2], [9], [10]. In principle, CZTS NCs can be obtained when a stoichiometric mixture of the three metal precursors is heated together with sulphur in a high temperature reaction solvent (e.g. octadecene). However, since the decomposition temperatures of copper, zinc and tin metal-salts vary, owing to their different electronegativities, decomposition of each metal precursor at different temperatures can result in the formation of unwanted phases such as ZnS, SnS, and CuS[6], [11]. To help mitigate this, oleylamine is utilized to reduce the metal salt precursors and form metal-organic complexes which can react together over a similar temperature range[11], [12].

Oleylamine is commonly used as a primary ligand in nanocrystal synthesis. Its low melting point means it is liquid at room temperature[13], which simplifies the cleaning procedure, while a high boiling point enables the use of high temperature heating conditions[13]. In addition, its relatively high molecular weight and reactive amine group enable it to coordinate solvothermal reactions[13]. Not only can oleylamine be used as a solvent and surfactant for many organic and inorganic compounds, it can also be used as an electron donor at elevated temperatures, thus making it a mild reducing agent of the precursors[13]. Such properties are strongly correlated to the specific nature of the target NC and reaction conditions.

Riha et al. demonstrated the effectiveness of oleylamine for preparing high quality CZTS nanocrystals from a mix of metal cations using a hot injection synthesis[2], [6]. However, in order to decompose the sulphur precursor, so as to promote reaction and nucleation of the nanocrystals, a high reaction temperature is required[6]. High reaction temperatures typically limit the control of the nucleation and growth of nanocrystals, which therefore inhibits the formation of small, yet highly monodisperse nanocrystals[14].

The use of hexamethyldisilathiane (TMSS) has been widely reported in the literature as a means of synthesising binary chalcogenide nanocrystals (e.g. CdS[15] and PbS[16], [17]) at very low temperatures, offering great control of the nanocrystal nucleation and growth characteristics[14], [18]. The method reported here combines elements of the hot injection CZTS nanocrystal synthesis reported by Riha et al.[6] with the low temperature control of nanocrystal nucleation and growth afforded by using TMSS as the sulphur precursor. The method used here and described in chapter 3 is general and may be expanded to other non-quaternary chalcogenides NCs associated with CZTS.

4.2.1 Binary Metal Sulphide Nanocrystal Formation.

Preliminary experiments were performed to investigate the temperatures and conditions in which Cu, Zn, and Sn precursors decompose into complexed metal ions in a standardised reaction environment. It was important to understand the reaction kinetics between TMSS with the reduced metal complexes and its role in nucleating Cu, Zn, and Sn sulphide nanocrystals using a low temperature synthesis regime. Precursor ratios for each reaction are set out in Table 4.2-1. The precursor ratios are representative of the equivalent molar ratios that would be present in the combined

quaternary reaction I envisaged at the time of injecting the TMSS. After degassing at room temperature under alternating argon and vacuum atmospheres, the solution temperature of each precursor solution was slowly increased to determine at what temperature the metal cation was decomposed by oleylamine. A DTA-TGA analysis was carried out to help determine at what temperature each of the metal precursors would decompose. Due to high average thermal decomposition temperature of $Cu(NO_3)_2{\cdot}3H_2O$ ~250°C, $Zn(NO_3)_2{\cdot}6H_2O$ ~300°C and $SnCl_4{\cdot}5H_2O$ ~310°C (as identified by the sharp reduction in mass for each metal precursor as shown in Figure 4.2-2a), it was clear that a strong reducing environment would be needed to break down each of the metal precursors, in order to form a supersaturated solution of monomer species, from which to produce either binary and quaternary NCs.

Table 4.2-1: Summary of CZTS nanocrystal synthesis reaction precursors and the relative thermal decomposition temperatures of the Cu, Sn and Zn metal cation precursors in excess oleylamine.

Stage	***Reagents***	***Moles (mmol)***			***Decomposition Temp. in OLA***
Precursor	$Cu(NO_3)_2 \cdot 3H_2O$	`1.00	-	-	>115°C
	$Zn(NO_3)_2 \cdot 6H_2O$	-	0.67	-	>30°C
	SnCl4 · 5H2O	-	-	0.56	>120°C
	$CH_3(CH_2)_7CH{=}CH(CH_2)_7CH_2NH_2$	30.00	15.00	15.00	-
Injection	$CH_3(CH_2)_{15}CH{=}CH_2$	7.5	3.25	3.25	-
	$(CH_3)_3SiSSi(CH_3)_3$	1.10	0.55	0.55	-

It is reported in the literature that $Cu(NO)_3$ and $Zn(NO)_3$ react with an excess of OLA to form $Cu(NH_2R)_n$ and $Zn(NH_2R)_n$ complexes, which appear transparent blue and faint yellow when dissolved in toluene respectively[13], [19]. By contrast, oleylamine firstly chelates with $SnCl_2$ to form a $SnCl_x(OLA)_{2-x}$ complex, which remains

stable in solution until a further reaction with sulphur ions expel the chloride ions and thus form SnS NCs[20].

Oleylamine serves as a weak ligand for copper and sulphur ions and so needs to be present in high concentrations to effectively break down the copper precursor[6], [13]. Initial observations indicated that $Cu(NO)_3$ and $Zn(NO)_3$ dissolved readily in oleylamine at room temperature while $SnCl_2$ remained cloudy until the temperature was raised above 120°C. Notably, the colour of the $Cu(NH_2R)_n$ solution changed dramatically as the temperature was raised above 115°C. This can be attributed to the reduction of the copper precursor from dark blue (Cu^{2+} complexed to excess of NH2 ions) to green (Cu^{2+} ions) to yellow and finally to a pale orange/red (Cu^{+} ions) by oleylamine. Above 130°C all three precursor solutions appeared clear and even increasing the temperature above 200°C caused no further colour change (see Figure 4.2-3a). In each case a solution of TMSS in ODE was injected in to the reaction vessel at 140°C in order to stimulate nanocrystal nucleation. The reaction proceeded at this temperature for five minutes before being quenched in an ice bath. Precipitation and cleaning of the nanocrystals, as outlined in chapter 3, then took place before each sample was redispersed in either toluene or hexane ready to be analysed.

The TEM micrographs in Figure 4.2-1 indicate that each NC sample is well separated and dispersed, suggesting that they are well stabilised by oleylamine. High-resolution TEM (HRTEM) analysis of the copper, zinc and tin sulphide NCs identified all three samples to be composed of single-domain nanocrystals (see Figure 4.2-1a, c+e).

Tin Sulphide

Previous studies have reported the co-existence of orthorhombic and zinc-blende SnS in NCs when using oleylamine as the primary ligand in syntheses with a reaction temperature below 200°C[17]. However, the NCs produced during this investigation nucleated from a reaction between $SnCl_x(OLA)_{2-x}$ and TMSS at a 140°C to form purely orthorhombic SnS (JCPDS 39-0354) (shown in Figure 4.2-1e). This was confirmed upon indexing of the XRD trace in Figure 4.2-2c. The UVVIS-NIR absorption spectra for SnS (Figure 4.2-2b) shows an onset of absorption of ~845nm (1.45eV).

120 This is consistent with a similar reported SnS NC syntheses[17], [21] and is consistent with published direct band gap values for bulk SnS (1.43eV)[17].

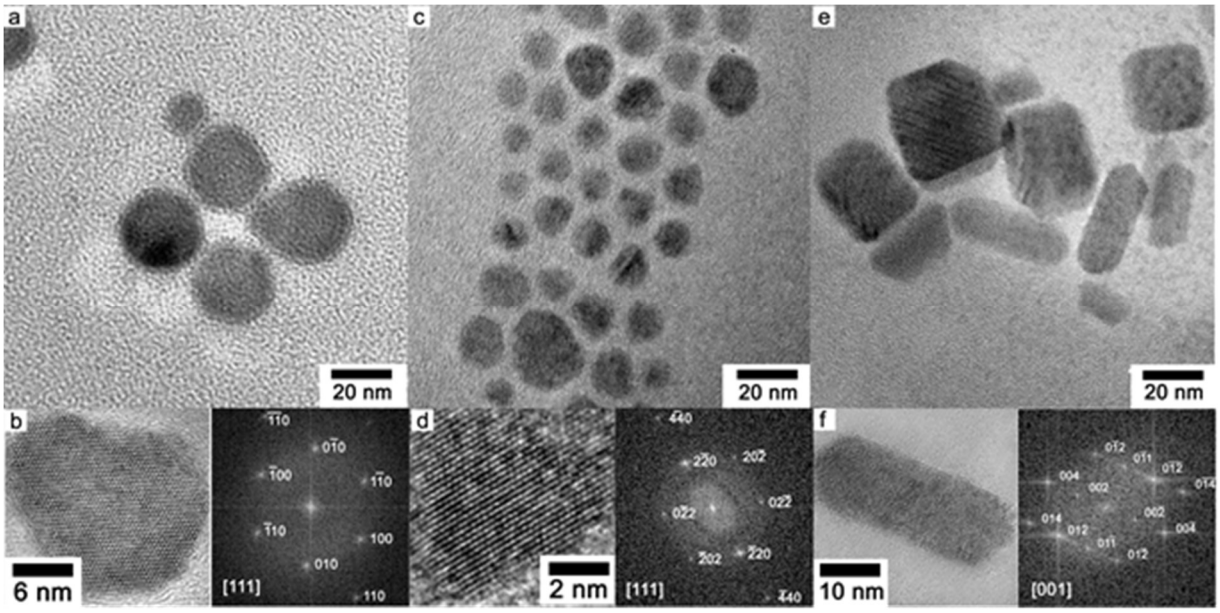

Figure 4.2-1 TEM micrographs inset with HREM micrographs and corresponding FFT images of a-b) Cu_2S, c-d) ZnS and e-f) SnS NCs.

Copper Sulphide

Copper sulphide exists in a variety of crystallographic phases, based on a hexagonal close packing of the sulphur atoms. The stable phase above 104°C is high chalcocite (Cu_2S), a structure in which copper atoms act almost as a fluid, resulting in a hexagonal crystallography defined by the sulphur framework. Below 104°C, the

copper atoms pack in a complex interstitial manner, giving rise to a lower symmetry monoclinic phase, which has a near-stoichiometric composition[22], [23].

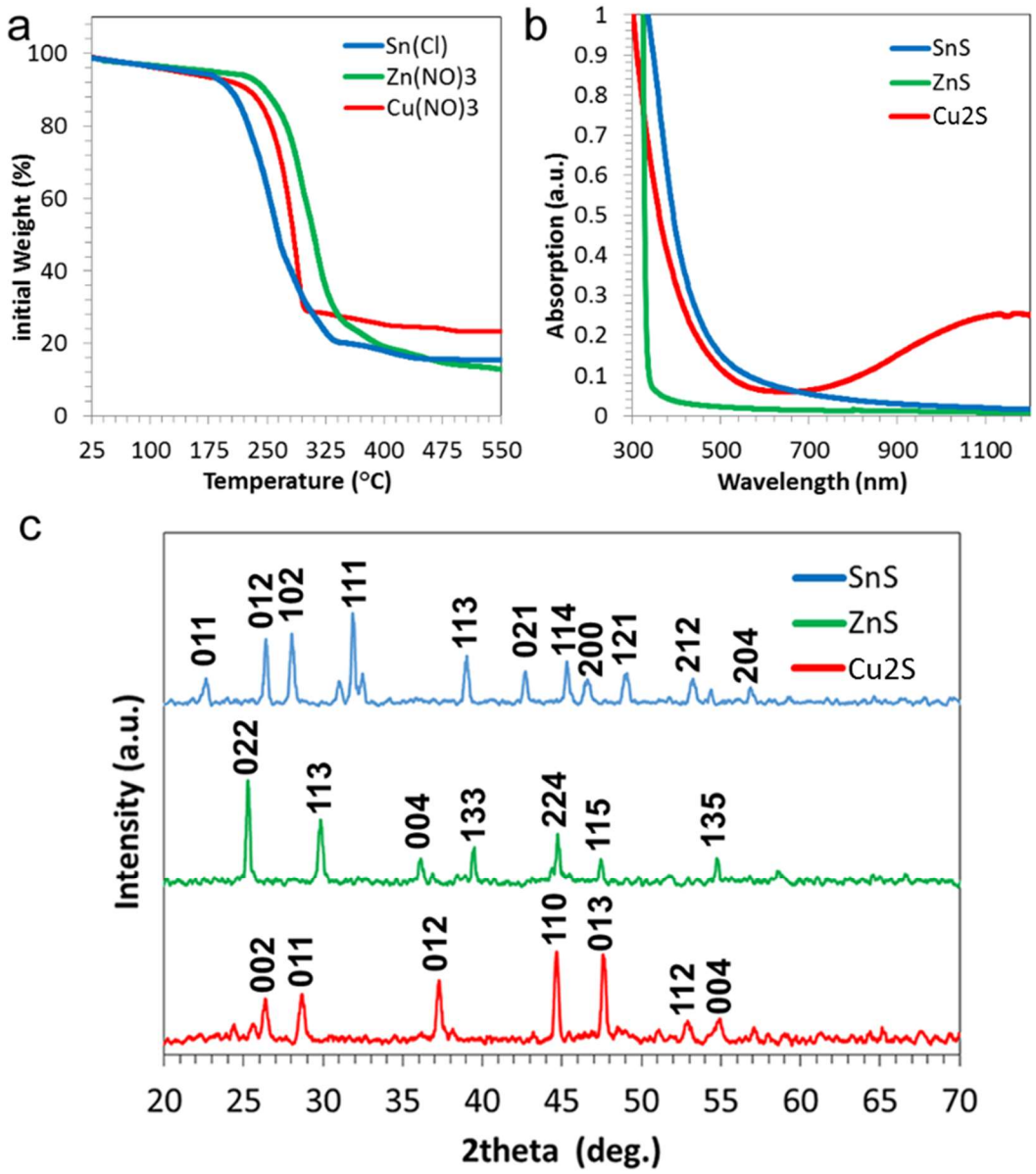

Figure 4.2-2 a) A DTA/TGA analysis of the change in mass with increasing temperature of Cu, Zn and Sn metal precursors, identifying the relative temperature at which each metal precursor breaks down under a continuous flow of nitrogen, b) UVVIS absorption spectra and c) X-Ray diffraction traces of Cu_2S, ZnS and SnS nanocrystals.

Upon indexing the lattice fringes of the NC, presented in Figure 4.2-1b, it was determined that the crystallographic structure of the NCs nucleated in the reaction between $Cu(NH_2R)_n$ and TMSS matched the hexagonal (high chalcocite) Cu_2S (JCPDS 46-1195) structure. This was confirmed upon indexing of the XRD trace in Figure

4.2-2c. The Cu_2S NC absorption spectra (Figure 4.2-2b) shows a strong absorption in the NIR region which is typical of Cu_2S nanostructures and its derivatives[23]–[25].

Zinc Sulphide

The NCs nucleated from the reaction between $Zn(NH_2R)_n$ and TMSS appear to match the zinc blende ZnS structure (JCPDS: 77-2100). This was confirmed upon indexing of the XRD trace Figure 4.2-2c. The UVVIS-NIR absorption spectra for ZnS (Figure 4.2-2b) shows an absorption onset of ~365nm (3.39eV). This is consistent with a similar reported ZnS NC[26] syntheses and close to the known direct band gap values for bulk ZnS (3.54eV)[27].

This series of experiments yielded useful information about the precursor formation of each metal cation and their relative reactivities with oleylamine. By observing the reaction dynamics of TMSS with each of the metal cation complexes in isolation, it also helps to indicate which would be the most likely stable binary compound in a quaternary one pot synthesis. This information is now used in the rest of the chapter to inform the synthesis of quaternary nanocrystals and to develop strategies to establish control over which CZTS crystal phase is formed.

4.2.2 CZTS Nanocrystal Synthesis

The next step on the journey toward making good CZTS semiconductor films is to control the crystallographic phases of stoichiometric CZTS nanocrystals. A number of experimental studies have shown this to be possible through direct solution phase synthesis of CZTS NCs. Initially, changes to the stoichiometry were used to alter the band gap (E_g)[2], [28], [29] and more recent studies have shown that E_g is dependent on crystal structure, namely tetragonal[6], [30] and hexagonal[5] kesterite CZTS (the two major structural phases). Among the numerous CZTS NC syntheses described in the literature, the majority report the fabrication of kesterite CZTS NCs consisting of the tetragonal (I42m) phase (JCPDS 26-0575)[31], [32]. More recently, the use of hot injection synthesis methods has been reported to preferentially form hexagonal (wurtzite) phase CZTS nanocrystals[4], [5], [33]. These investigations indicate that the formation of a particular crystal phase is closely related to the reaction conditions.

Table 4.2-2: Summary of CZTS nanocrystal synthesis reaction precursors.

Stage	***Reagents***	***Moles (mmol)***	***Mass (g)***	***Vol. (ml)***
Precursor	Cu(NO3)2 · 3H2O	1.00	0.24	-
	Zn(NO3)2 · 6H2O	0.67	0.20	-
	SnCl4 · 5H2O	0.56	0.19	-
	CH3(CH2)7CH=CH(CH2)7CH2NH2	60.00	16.05	19.74
Injection	CH3(CH2)15CH=CH2	15.00	3.79	4.80
	(CH3)3SiSSi(CH3)3	2.20	0.40	0.47

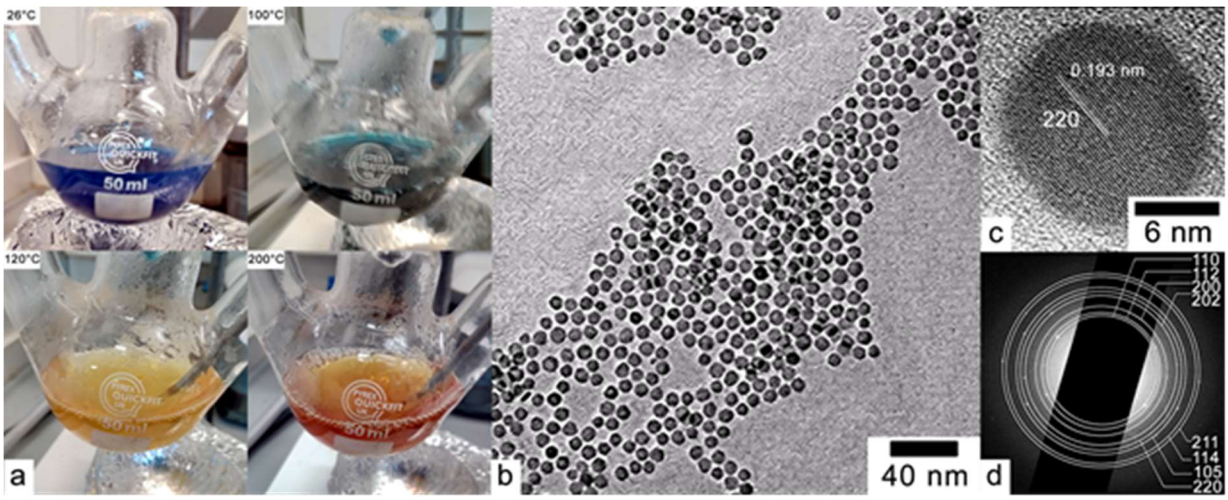

Figure 4.2-3 a) Photographs taken of precursor solution heated under argon atmosphere prior to TMSS injection representing the reduction of the constituent copper, zinc and tin precursors. b) TEM images of CZTS QDs synthesized at 140°C, with an average size of 9.4 ± 0.6nm c) HRTEM image shows inter-planar distance of 0.193nm, which corresponds to the tetragonal (220) plane. D) SAED pattern indexed to kesterite-tetragonal phase CZTS.

180 To investigate this, CZTS NCs were prepared by reacting all three amine-salt complexes with TMSS at different temperatures using the parameters set out in Table 4.2-2. In each case a solution of TMSS in ODE was injected in to the reaction vessel to stimulate nanocrystal nucleation followed by 30 seconds of ageing and then quenching of the nanocrystal solution in an ice bath. Precipitation and cleaning of the nanocrystals then took place before each sample was redispersed in either toluene or hexane ready to be analysed.

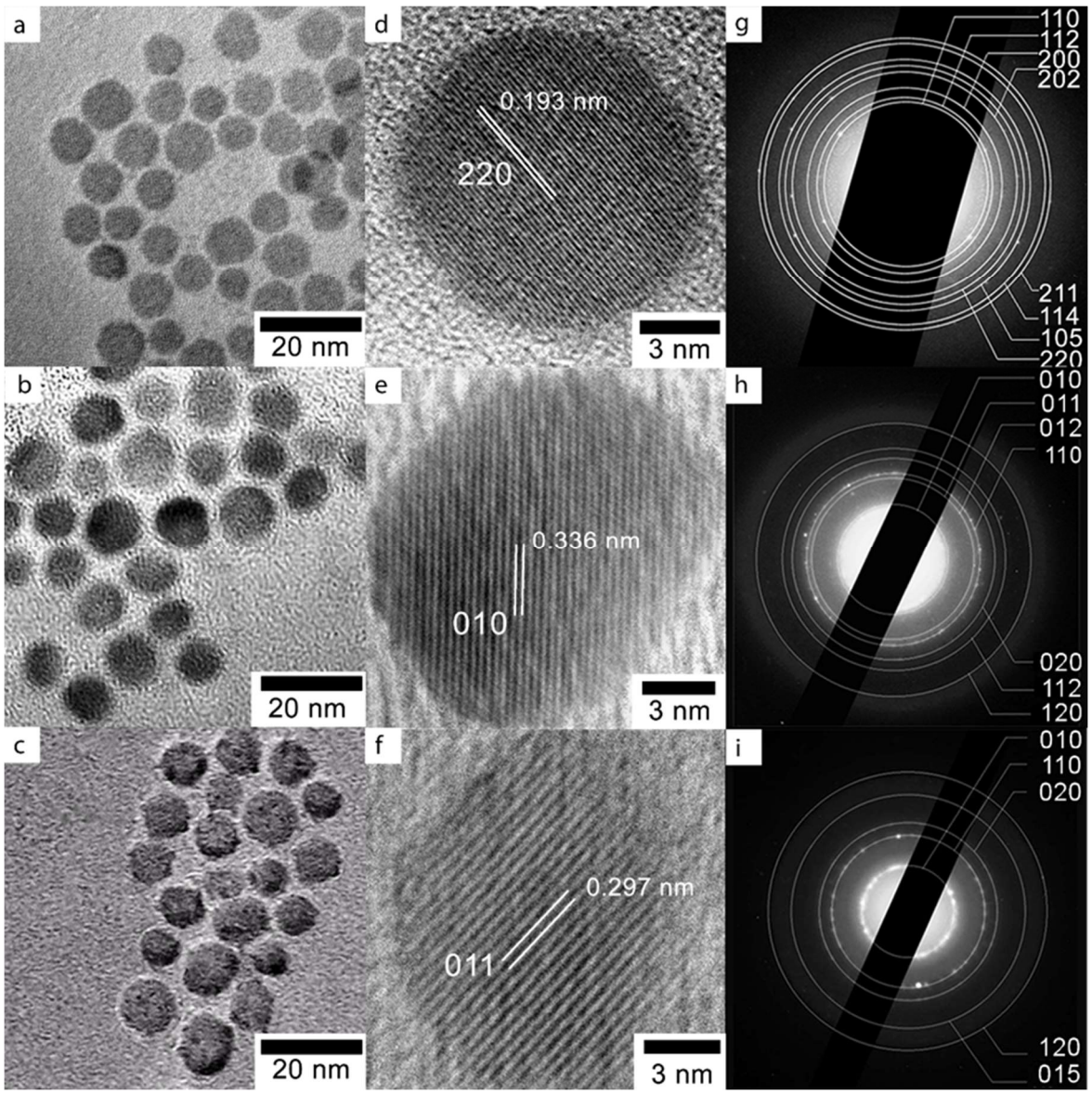

Figure 4.2-4: TEM images of CZTS NCs synthesized at 140°C (a, d, g), 170°C (b, e, h) and 190°C (c, f, i) respectively. The CZTS NCs in (a, b, c) have an average size of 9.4 ± 0.6nm, 9.5 ± 1.6nm and 9.6 ± 1.8nm respectively. The HRTEM images in e, f and g show interplanar spacings of 0.193nm, 0.336nm and 0.297nm, which correspond to the tetragonal (220) and hexagonal (100), (110) planes respectively. The SAED patterns in g and h + i were indexed to tetragonal and hexagonal phase CZTS, respectively.

Figure 4.2-4 shows a transmission electron micrograph (TEM) of CZTS NCs obtained 30 seconds after nucleation at 140°C, 170°C and 190°C. In each case the as-prepared NCs exhibit variably faceted polyhedral geometries.

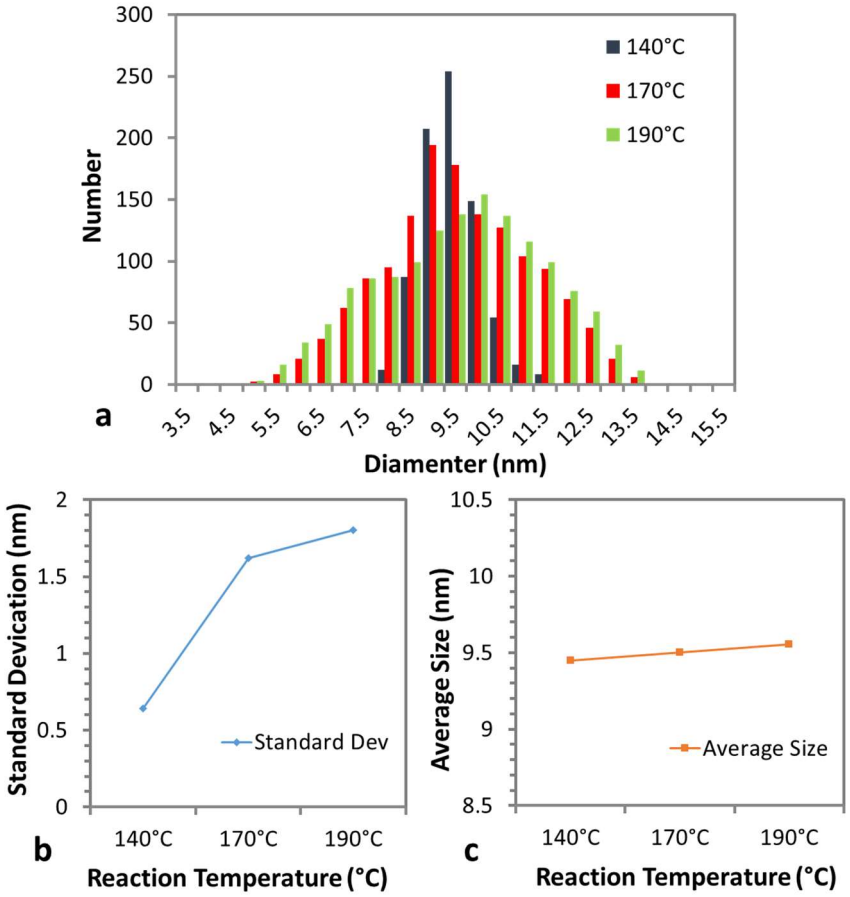

Figure 4.2-5: a) Size distribution analysis of low resolution TEM micrographs of CZTS samples nucleated at 140°C, 170°C and 190°C. b) Graphs of standard deviation and c) average (mean) NC diameter with increasing nucleation temperature.

A numerical analysis of the change in NC diameter with reaction temperature is shown in Figure 4.2-5. The standard deviation (σ) of the NC diameters indicates the spread of the NC diameter values about the mean value (μ). When determining the average NC size, each measured value has been categorised into groups with a 0.5nm range. Owing to the generally small size of the NCs (<50nm) and the relatively large grouping size, this value has been represented here as a significant experimental error that is to be considered when analysing the average NC size of each sample. The relative standard deviation (or coefficient of variation) equals the standard deviation divided by the mean, and represents a commonly used approximation of the relative NC size distribution for a given sample. The standard deviation values for each NC sample is shown in Figure 4.2-5c. NCs synthesised at 140°C (Figure 4.2-4a) exhibit a

monodisperse relative size distribution (6.4%) with an average NC diameter of 9.4 ± 0.5nm while the NCs nucleated at 170°C and 190°C exhibit much broader relative size distributions (16.8% and 18.8%) with an average NC diameter 9.5 ± 0.5nm and 9.6 ± 0.5nm respectively (as shown in Figure 4.2-4c). The apparent increase in NC size distribution with reaction temperature is most likely due to an increase in the nucleation and growth rate of NCs at higher temperatures, leading to poorly controlled growth[34]. Inherently, smaller NCs will exhibit a larger relative size distribution compared with larger NCs, therefore this metric is perhaps not the best means of comparing size distribution between NCs with orders of magnitude differences in size.

High-resolution TEM (HRTEM) analysis of the NCs (Figure 4.2-4) identified all three samples to be single-crystal. Upon indexing of the lattice fringes it was determined that the crystallographic structure of the NCs nucleated at 140°C matched the CZTS tetragonal (I42m) phase (JCPDS 20-0575). By contrast, those NCs nucleated at 170°C and 190°C exhibited wurtzite structural characteristics. Confirmation of this finding was achieved using selected area diffraction (SAED) analysis; meanwhile an X-ray diffraction (XRD) study of the NCs' crystallographic structure indicated a change in phase with a reduction in nucleation temperature, as displayed in Figure 4.2-6. Nanocrystal samples produced upon injecting at 140°C were found to exhibit the major 112, 220 and 312 peaks of the tetragonal phase; whereas those samples synthesised at 170°C and 190°C exhibited peaks, indexed to the 100, 101, 110, 103 and 112 planes of the hexagonal CZTS phase. Unfortunately, XRD analysis did not allow for a clear distinction to be made between CZTS and other possible chalcogenides, such as Cu_2SnS_4 (cubic F43m) or ZnS (cubic F43m), which have similar X-ray diffraction traces to ensure the presence of Cu, Zn and S STEM-XRD was used.

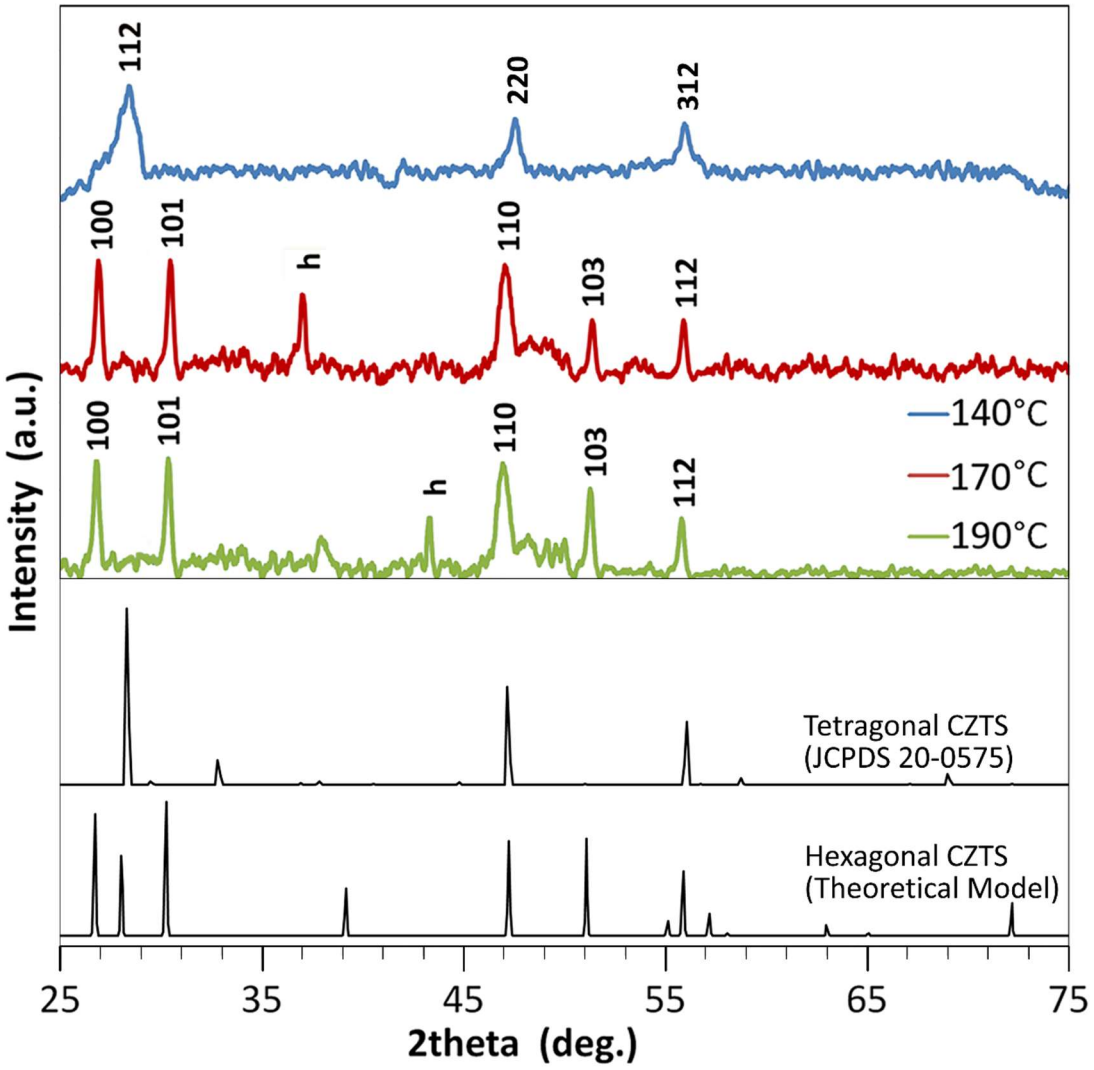

Figure 4.2-6: X-Ray diffraction traces of CZTS QDs synthesized at 140°C, 170°C and 190°C. The h labelled peaks are only present in high signal to noise ratio measurements and are associated with the sample holder.

240

The crystallographic parameters of the model used to analyse the Hexagonal CZTS structure, calculated, using Crystalmaker Software, from the lattice parameters published by Lu et al[4], are shown in Table 4.2-3.

Table 4.2-3: Calculated crystallographic parameters for the Hexagonal CZTS structure.

Wurtzite			***d [A]***	***2 θ***	***Intensity***
0	1	0	3.32441	26.7938	77.61
0	0	2	3.1694	28.1305	51.03
0	1	1	2.94409	30.3331	85.64
0	1	2	2.29395	39.2393	30.46
1	1	0	1.91935	47.3199	60.49
0	1	3	1.78323	51.1815	62.23
0	2	0	1.66221	55.2122	9.29
1	1	2	1.64177	55.9594	41.01
0	2	1	1.60784	57.2477	13.82
0	0	4	1.5847	58.1631	1.61
0	2	2	1.47204	63.1013	6.96
0	1	4	1.43049	65.1567	1.65
0	2	3	1.30641	72.2563	20.84
1	2	0	1.25651	75.6146	6.94
1	2	1	1.23253	77.3549	10.46
1	1	4	1.22201	78.1467	3.57
0	1	5	1.18455	81.1205	14.97

4.3 Stoichiometric Properties

4.3.1 Identifying Nanocrystal Chemistry

In order to verify that all four constituent elements were present in each individual NC, chemical analysis with nanoscale spatial resolution was performed[a].

[a] EDX elemental mapping was carried out using a 1nm probe diameter, while the NCs under examination tended to exhibit an average diameter of 5-10nm. Thus, the resulting resolution of the STEM-EDX elemental micrographs allowed for a qualitative analysis of elemental makeup of individual CZTS NCs.

Figure 4.3-1, Figure 4.3-2 and Figure 4.3-3 display electron energy dispersive X-ray (EDX) image maps showing the elemental composition of individual NCs from each synthesis.

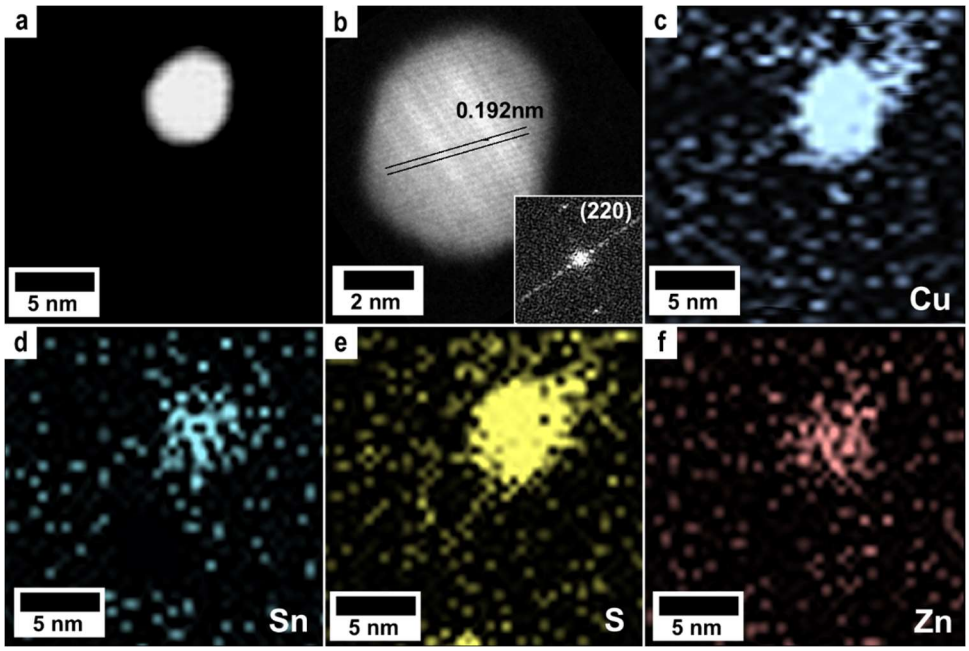

Figure 4.3-1 Low a) and high b) resolution scanning transmission electron micrographs of tetragonal kesterite CZTS QD show an inter-planar spacing of 0.192nm which corresponds to the (220) planes, indexed in the Fourier transform inset. c-f) STEM-EDX micrographs measuring the presence of Cu, Sn, S and Zn.

This analysis shows a homogeneous distribution of the four elements Cu, Sn, Zn, and S on the 2D-projected chemical maps of the NCs. Through extensive STEM-EDX imaging, the homogeneous composition each sample was confirmed; no binary or ternary particles, with different compositions, were found in the samples examined. Further analysis of the STEM-EDX data revealed that the stoichiometric ratio of Cu:Zn:Sn:S elements in each sample to be close to 2:1:1:4, which corresponds well with the elemental ratio of CZTS.

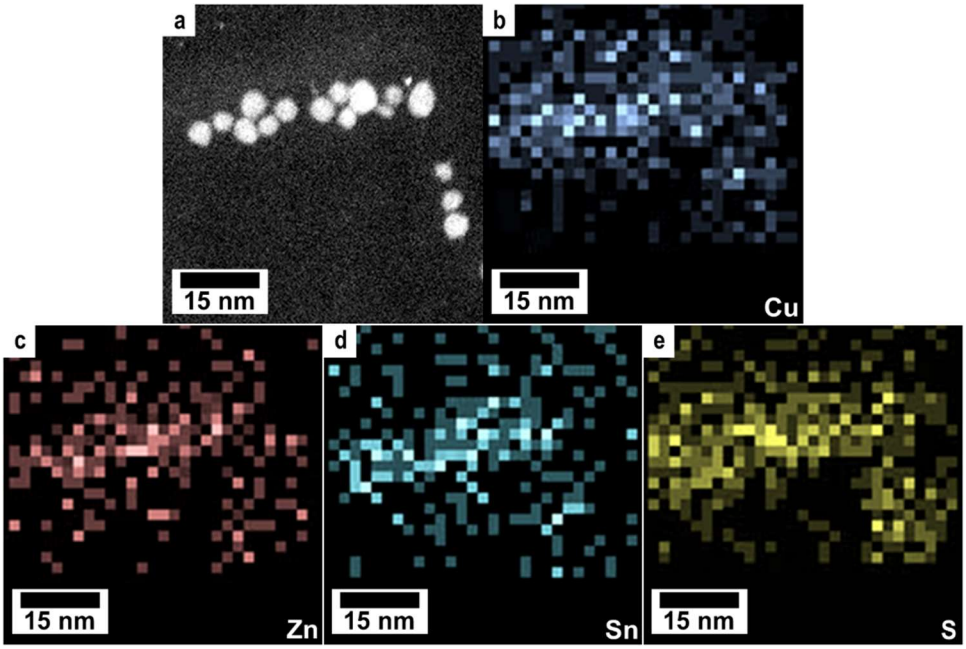

Figure 4.3-2 a) High angle annular dark field (HAADF) STEM image of CZTS NCs nucleated at 170°C b-e) STEM-EDX elemental mapping micrographs identifying Sn, Cu, Zn and S present in each region.

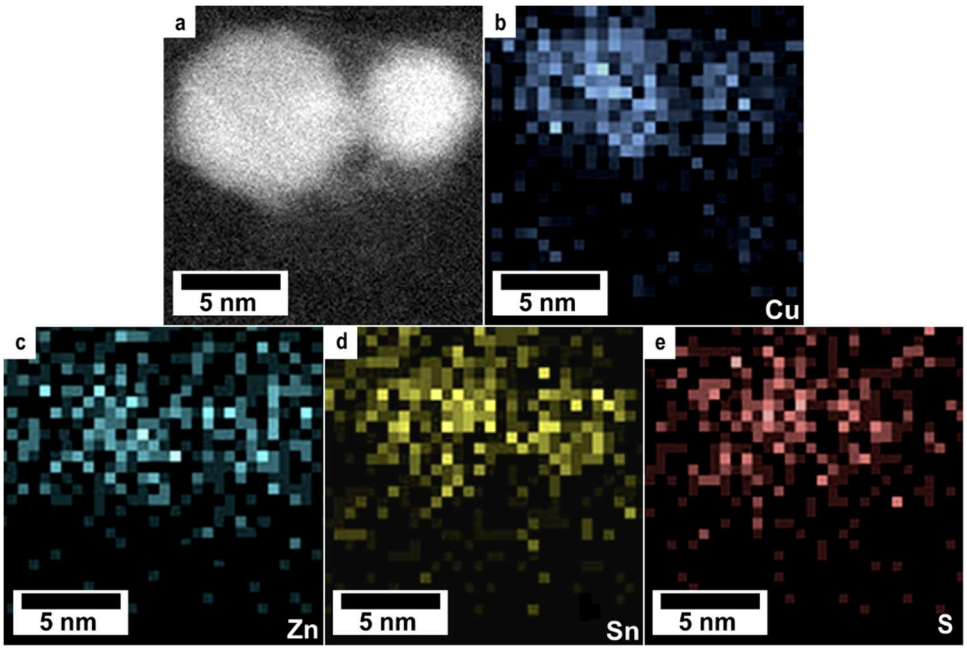

Figure 4.3-3 a) High angle annular dark field (HAADF) STEM image of CZTS NCs nucleated at 190°C b-e) STEM-EDX elemental mapping micrographs identifying Sn, Cu, Zn and S present in each region.

In order to estimate the relative elemental composition of each NC sample, EDX spectra from each of corresponding STEM-EDX maps shown in Figure 4.3-1,2 and 3 were further analysed using the Cliff-Lorimer approximation [35]. Each of the spectra shown in Figure 4.3-4a-c, corresponding to CZTS NCs nucleated at a) 140°C, b) 170°C

and c) 190°C respectively, show a number of strong X-ray emission peaks, corresponding to Cu-Kα (8.04keV), Cu-Lα (0.93keV), Zn-Lα (1.012), Sn-Lα (3.44keV) and S-Kα (2.31keV).

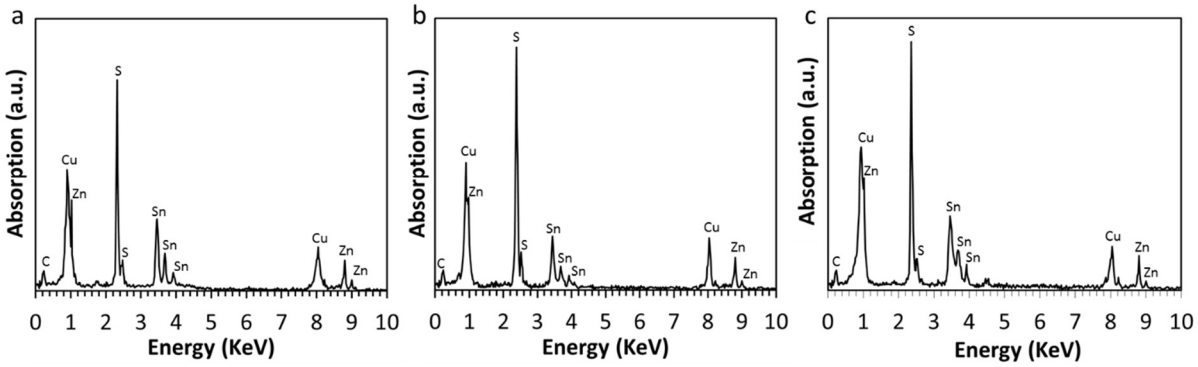

Figure 4.3-4 Energy dispersive X-ray spectra for nanocrystals nucleated at a) 140°C, b) 170°C and c) 190°C (corresponding to the STEM-EDX micrographs shown in Figure 4.3-1, 2 and 3 respectively).

The area under the peaks corresponding to Cu-L, Zn-L, Sn-L and S-K were each analysed according to the standard-less Cliff-Lorimer method, of which the results are shown in Table 4.3-1. The atomic ratios laid out in Table 4.3-1 suggest that the composition of each NC sample is approximately stoichiometric Cu_2ZnSnS_4. The NCs nucleated at 140°C is appreciably deficient in sulphur, zinc and tin in comparison to the NCs nucleated at 170°C and 190°C, although in each case the NCs appear copper rich compared with purely stoichiometric Cu_2ZnSnS_4. The observed sulphur deficiency may be due to the oxidation and depletion of sulphur atoms from the surface of the NCs over time, which can be attributed to the poor adsorption properties of the oleylamine ligand[13].

Table 4.3-1: Cliff-Lorimer analysis of the relative elemental composition of the CZTS NCs nucleated at 140°C, 170°C and 190°C, identifying the weight% and atomic% of the constituent elements (Cu, Zn, Sn and S) for each sample, calculated from the respective EDX spectra shown in Figure 4.3-4.

Sample	Element	Weight%	σ - Weight%	Atomic%	Ratio
140°C	Cu	32.36	0.31	27.56	2.00
	Sn	24.62	0.52	11.22	0.81
	Zn	13.34	0.46	11.03	0.80
	S	29.68	0.30	50.18	3.64
170°C	Cu	30.80	0.47	26.08	2.00
	Sn	24.26	0.52	10.99	0.84
	Zn	14.66	0.62	12.06	0.92
	S	30.27	0.41	50.87	3.90
190°C	Cu	30.36	0.50	25.86	2.00
	Sn	25.32	0.62	11.54	0.89
	Zn	14.28	0.71	11.82	0.91
	S	30.04	0.44	50.79	3.93

A significant factor in the accuracy of the weight fraction ratio obtained using the Cliff-Lorimer analysis arises from the X-ray counting statistics, which exhibit Gaussian behaviour. For a Gaussian distribution the probability that the true value of N (the number of X-ray counts) will lie within 2σ of the mean is approximately 95%. Hence the standard deviation of the weight% for each element is shown in Table 4.3-1, thereby emphasising the significant deviation in the compositional values for each NC sample [36]. Despite this inherent uncertainty, it would appear that the respective ratio of Cu:Zn:Sn:S observed in each NC sample is consistent with the characteristic ratios of kesterite and wurtzite CZTS NC formations that have been reported by others in the literature[37], [38].

DTA-TGA analysis was carried out to help determine whether the synthesised nanocrystals were pure CZTS or a combination of CTS and ZnS nanocrystals. The data presented in Figure 4.3-5(a) suggests there is a single transition for each sample at approximately ~ 830°C. For each sample, the presence of additional transitions at lower temperatures (<500°C) may suggest the presence of unreacted precursors, left over from each synthesis, which undergo oxidation at these temperatures.

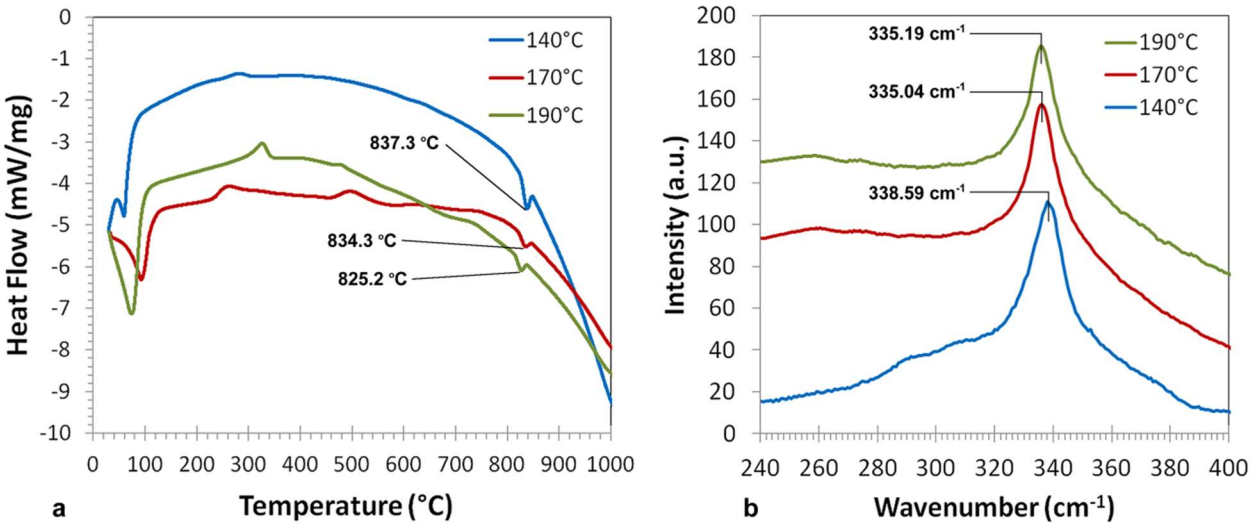

Figure 4.3-5 a) DTA/TGA analysis and b) Raman spectra of CZTS nanocrystals nucleated at 140°C, 170°C and 190°C.

320 The results of Raman spectroscopy analysis shown in Figure 4.3-5b suggest that a single crystalline species of CZTS is present in each sample. All three spectra display an intense peak in the 331-338cm^{-1} region associated with bulk CZTS. The intense peak observed for the sample nucleated at 140°C (tetragonal CZTS) had a fractionally higher peak position compared to those samples nucleated at 170°C and 190°C (hexagonal CZTS). The different Raman shift values for tetragonal and hexagonal CZTS would suggest that the characteristic peak for hexagonal CZTS may differ from that of tetragonal[39]. This phenomenon may be caused by the different arrangements of atoms in each respective crystal structure. Apart from the above mentioned Raman peaks, no other characteristic peaks of impurities such as $Cu_{1.97}S$

330 (475 cm^{-1}) ZnS (351 and 274cm^{-1}) Cu_3SnS_4 (318, 348 and 295cm^{-1}), SnS_2 (315 cm^{-1})[40]–[43] were observed.

4.4 Optoelectronic Properties

The band gap of the hexagonal (wurtzite) structure is predicted to be larger than that of the tetragonal structure[44] and it has been shown that compositional changes in CZTS particles can have profound effects on the optical band gap of the material[2]. To date, there has been little evidence in the literature of quantum confinement in CZTS nanocrystals. The Bohr radius of CZTS is estimated to be 2.7-3.3nm[11] and so in order for Quantum effects to be observed, a nanocrystal diameter of <2nm must be achieved. In which case, the resolution of the experimental
340 techniques used to distinguish between compositional and quantum confinement effects have a significant impact on the ability to distinguish between them. Khare et al. observed a shift in the band gap of 1.5eV to 1.8eV for CZTS NCs. This result is consistent with quantum confinement theory, namely that optical transitions of bulk semiconductors should shift to a higher energy if the optically excited electron hole pair is confined within a nanocrystal boundary that is smaller than the associated Bohr radius. However, this result is yet to be confirmed elsewhere in the literature[11]. As such, it is likely that the size of the nanocrystals synthesised in this study are generally too large to be influenced by this phenomenon. Optical characterization of NCs prepared using our synthesis route provides evidence to
350 suggest that the phase of the CZTS NCs does affect the band gap of the material, as theoretically predicted[44]. Room temperature UV-VIS-NIR absorption spectroscopy was used to analyse the optical properties of the as-synthesized CZTS crystals. The band gap (E_g) can be estimated by plotting $(\alpha h\nu)^2$ vs. $h\nu$, where α is the absorption

coefficient and *hν* represents the photon energy. The value of E_g is estimated by extrapolating the linear portion to the x axis (*hν*).

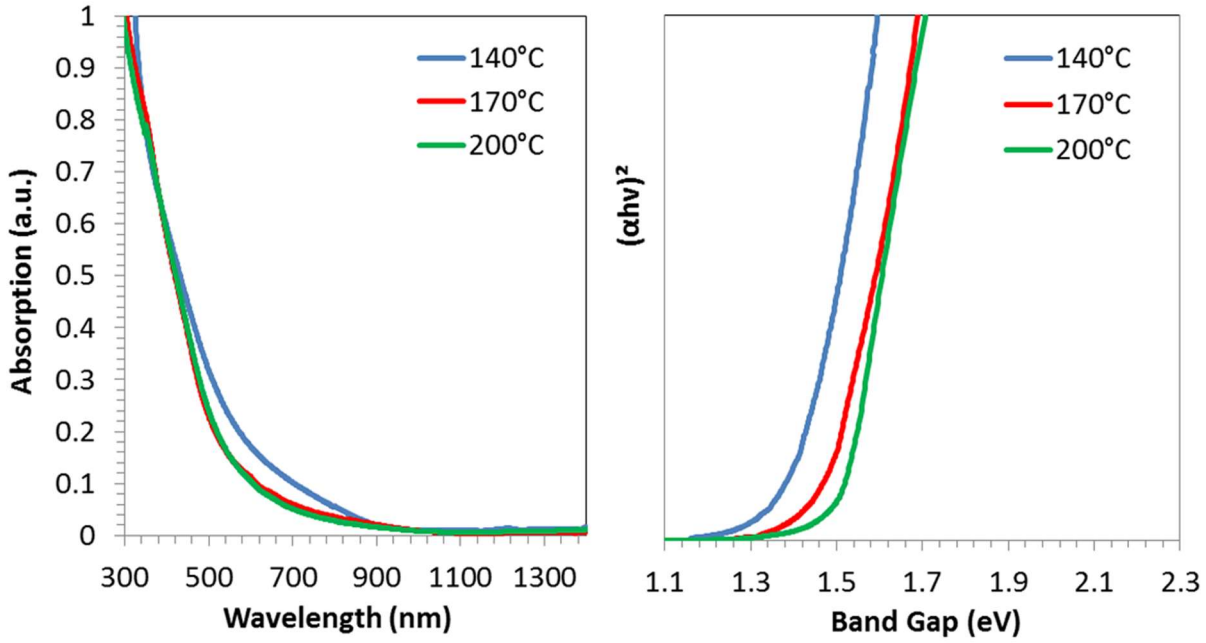

Figure 4.4-1 Plot of $(\alpha h\nu)^2$ as a function of hν (photon energy, in eV) for the measured UV-VIS absorption plot of CZTS QDs synthesized at 140°C, 170°C and 190°C. In each case the extrapolated linear fit estimates the band gap of the QD at the crossing point of the x-axis.

Existing experimental data devoted to the characterisation of the optical properties of CZTS provide inconsistent values for the band gap of this material system. The majority of the experimentally determined values are between 1.4 and 1.5 eV. An extended discussion on the band gap values of CZTSe and CZTS is reported elsewhere[45]. Previous studies have used DFT calculations to theoretically predict the band gaps of CZTS and CZTSe, and concluded that the band gap of CZTS should be around 1.5 eV[46] (see Chapter 2 for more details of this result), which is consistent with the experimental value for CZTS NCs prepared using this method (Figure 4.4-1). Further investigation of how the composition affects the band gap of these CZTS NCs is needed. The band gap of kesterite is calculated to be larger than that of stannite CZTS whereas the hexagonal (wurtzite) derived kesterite structure is predicted to be larger than the tetragonal structure[44]. However, these values have yet to be

confirmed by experimental measurement to a high degree of accuracy, indeed a number of researchers report that the crystal structure has a negligible effect on the band gap[47]. However, the results of this study provide evidence to suggest that the phase of the CZTS NCs does affect the band gap of the material.

Figure 4.4-1 presents the estimated values for the band gap of the three NC samples. The tetragonal structure exhibits a band gap of around 1.4eV (±0.04) which compares favourably with previously reported values for kesterite CZTS (1.4–1.6 eV)[6], [48] whereas for the hexagonal phase CZTS the value is closer to 1.5eV (±0.07). This increase in the band gap, relative to the tetragonal phase, is not consistent with experimental values presented in the literature[4], [5] however, it does fall in line with theoretical predictions[44], [49]. For each CZTS NC nucleation temperature, the aforementioned synthesis was carried out on three separate occasions. From each synthesis, two aliquots were extracted and analysed in the UV-VIS/NIR spectrometer. An estimated band gap value was extracted from each spectra and an average value calculated for CZTS NC samples nucleated at 140°C, 170°C and 190°C. Due to the relatively small data set, associated with this experiment, the error values are representative of the range (i.e. the maximum value minus the minimum value) of each experimental data set.

4.4.1 Twinning and Structural Defects

The presence of a twin formation in the tetragonal structure of a CZTS nanocrystal, aged at 140°C for 4hrs, was identified using HRTEM (Figure 4.4-2a-e). Twinning, together with other forms of Polytypism, has been observed in a number of tetrahedrally coordinated semiconductor nanocrystals [50]. Twinning, in particular, has also been observed to be a defective growth mechanism in ternary and

quaternary copper-based chalcogenides[51]. In such materials, the (111) atomic planes of the zinc-blende structure are equivalent to the (0001) atomic planes of the hexagonal wurtzite structure, wherein the only difference being apparent in the different stacking of the atoms along, being abcabc and abab for zinc-blende and wurtzite, respectively[51]. For example, Rupich et al. have previously demonstrated how twinning energy is strongly size-dependent during the formation of face cantered cubic PbS NCs. The twinning growth mechanism caused the resulting PbS NCs to exhibit crystallographically forbidden five-fold symmetry elements[52]. However, to date there is no evidence of this phenomena having been observed in ternary or quaternary systems.

As shown in Figure 4.2-1, the intersecting planes of the untwinned region have been indexed to be (211) and (200) respectively. By comparing the Fourier transforms of both the twinned and untwinned regions of the crystal, the twin transformation about the 102 zone axis has been indexed. The is no evidence of the wurtzite structure being present in the NC shown in Figure 4.2-1 and hence the twinning has most likely originated as result of the defective growth of the NCs. It is noted that the CZTS NC shown in Figure 4.4-2 was prepared especially for this experiment and thus underwent a prolonged period of ageing at an elevated temperature (140°C), hence none of these nanocrystals were included in the nanocrystal size distribution analysis described in Figure 4.2-5.

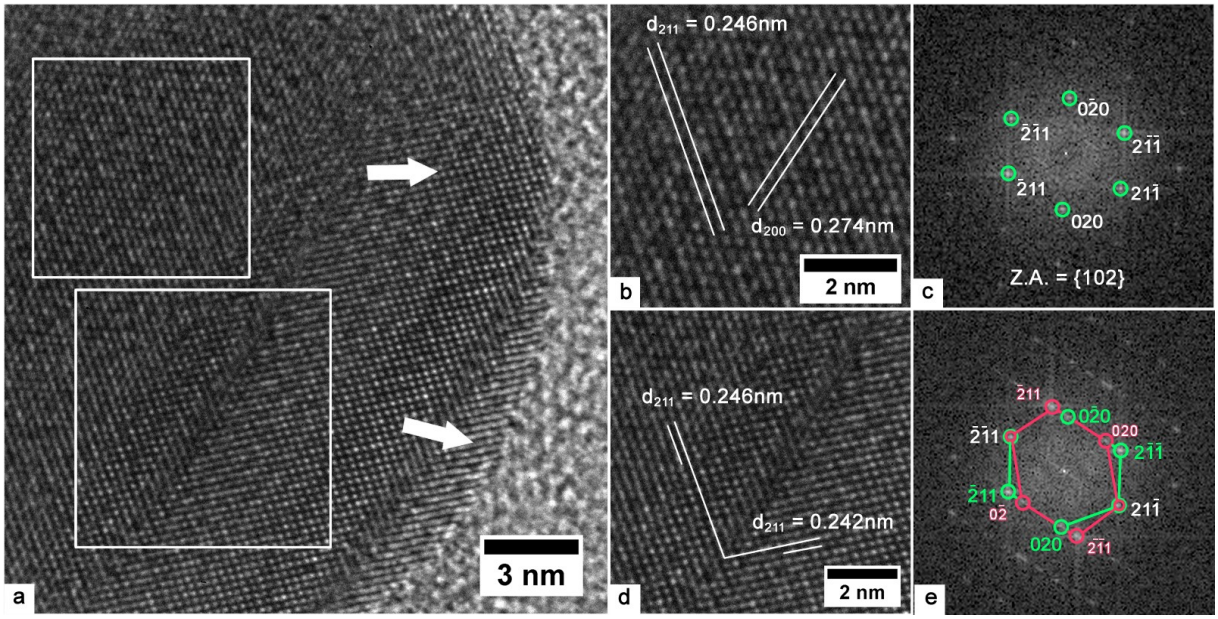

Figure 4.4-2 a) HRTEM images of CZTS nanocrystals nucleated at 140°C, b) enlarged micrograph and c) corresponding Fourier transform of an un-twinned region with indexed interplanar spacings of 0.24nm and 0.27nm, which correspond to the (211) and (200) planes respectively, d) enlarged micrograph of a twinned region and e) corresponding Fourier transform with indexed interplanar spacing of 0.24nm and 0.25nm which correspond to the twinned (211) planes of the tetragonal CZTS structure. Due to the prolonged ageing of CZTS NCs synthesised as part of this twinning analysis, measurements of their relative diameters were not included in the size distribution analysis shown in Figure 4.2-5.

4.4.2 CZTS Nanocrystal Solar Cells

At the outset it appeared that a stable colloid could be achieved in ambient conditions. However, when used in thin film photovoltaic devices with the geometry used later in Figure 6.2 1c it was found that all devices short circuited and showed no photovoltaic response. Some evidence of non-linear *J-V* characteristics for thicker films was measured but characteristics were dominated by parasitic resistance. This was due to poor film morphology as shown in Figure 4.4-3. The most likely cause for the poor coating conformity is the formation of nanocrystal aggregates, which the SEM and TEM in Figure 4.4-3 demonstrate.

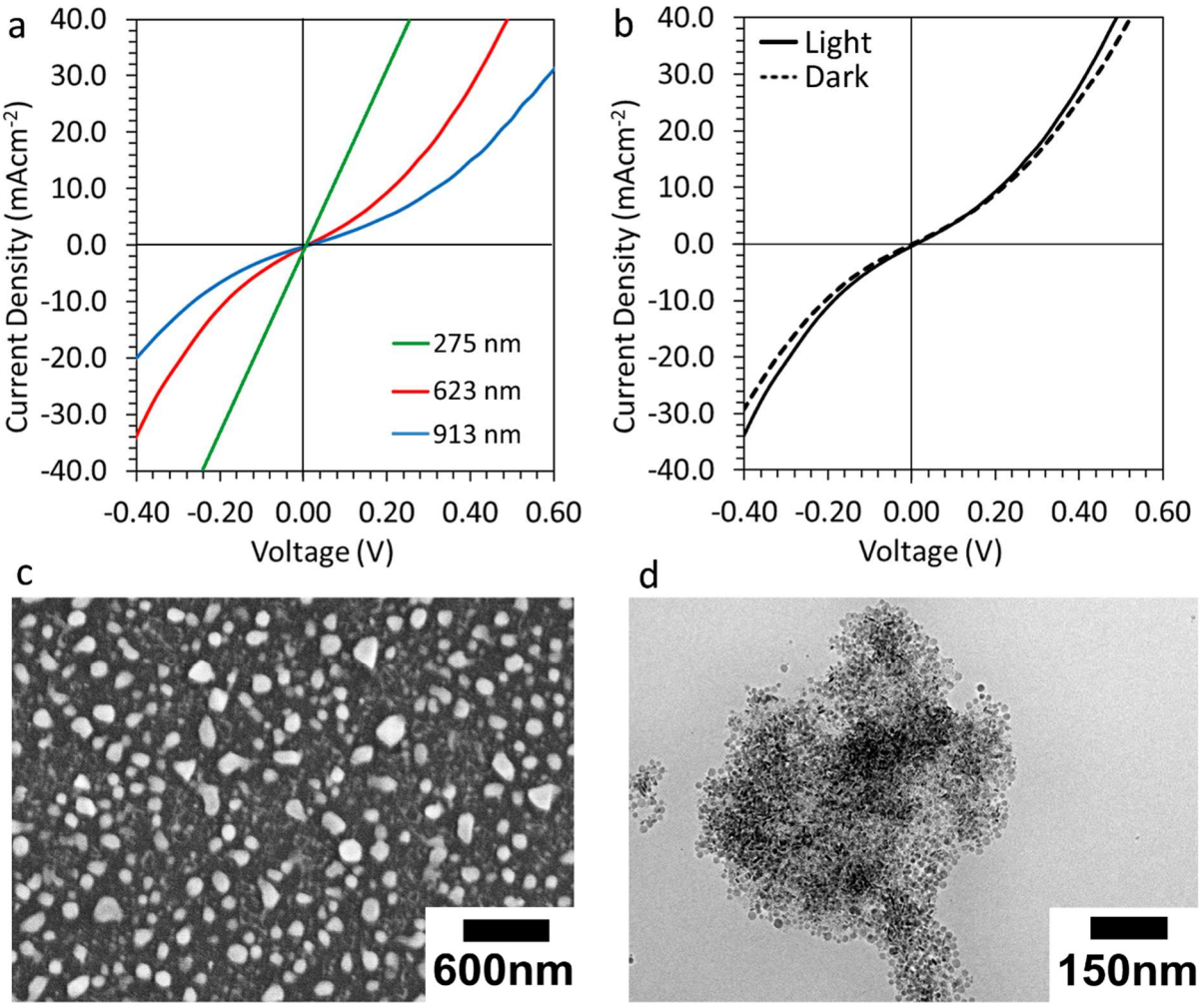

Figure 4.4-3 a) Light J-V curves for FTO/CdS/CZTS/Au devices with increasing thickness b) Light and dark J-V curve of 623nm thick CZTS absorber layer device. c) SEM image of agglomerated CZTS clusters formed after spin coating poorly dispersed CZTS NC solution. d) TEM of agglomerated CZTS NCs.

4.5 Conclusion

Nearly mono-disperse CZTS nanocrystals were synthesised from the reaction of metal amine complexes with an excess of TMSS over a range of temperatures to produce two distinct CZTS phases. The NCs prepared at 140°C have the tetragonal CZTS crystallographic structure, as shown by HRTEM, SAED and XRD analyses. Nanoscale-resolved STEM-EDX mapping identified the presence of the four elements in each individual nanocrystal. TEM and HAADF STEM analyses indicated a homogeneous composition in each individual nanocrystal. Various combinations of non-polar/polar solvent cleaning strategies were employed in an attempt to process

the Kesterite-CZTS NC solution, ready for the application within solar cell devices. However, outside the controlled (moisture free) glovebox environment, excessive agglomeration of the CZTS NCs lead to heavily aggregated semiconductor thin films with poor optoelectronic properties. To combat this a strategy was devised to improve the NC surface passivation using a co-ligand synthesis method, the results of which are discussed in Chapter 5.

4.6 References

[1] T. Todorov, O. Gunawan, S. J. Chey, T. G. De Monsabert, A. Prabhakar, and D. B. Mitzi, "Progress towards marketable earth-abundant chalcogenide solar cells," *Thin Solid Films*, vol. 519, no. 21, pp. 7378–7381, Aug. 2011.

[2] S. C. Riha, B. a Parkinson, and A. L. Prieto, "Compositionally Tunable Cu 2 ZnSn (S 1-x Se <sub> x < / sub >) 4 Nanocrystals : Probing the Effect of Se-Inclusion in Mixed Chalcogenide Thin Films," *Communication*, vol. 133, no. 39, pp. 1–6, 2011.

[3] D. Zhitomirsky, I. J. Kramer, A. J. Labelle, A. Fischer, R. Debnath, J. Pan, O. M. Bakr, and E. H. Sargent, "Colloidal quantum dot photovoltaics: The effect of polydispersity," *Nano Lett.*, vol. 12, no. 2, pp. 1007–1012, Feb. 2012.

[4] X. Lu, Z. Zhuang, Q. Peng, and Y. Li, "Wurtzite Cu2ZnSnS4 nanocrystals: a novel quaternary semiconductor.," *Chem. Commun. (Camb).*, vol. 47, no. 11, pp. 3141–3143, Mar. 2011.

[5] A. Singh, H. Geaney, F. Laffir, and K. M. Ryan, "Colloidal synthesis of Wurtzite Cu2ZnSnS4 nanorods and their perpendicular assembly," *J. Am. Chem. Soc.*, vol. 134, no. 6, pp. 2910–2913, Jan. 2012.

[6] S. C. Riha, B. a Parkinson, and A. L. Prieto, "Solution-based synthesis and characterization of Cu2ZnSnS4 nanocrystals.," *J. Am. Chem. Soc.*, vol. 131, no. 34, pp. 12054–12055, Sep. 2009.

[7] A. Singh, H. Geaney, F. Laffir, and K. M. Ryan, "Colloidal synthesis of wurtzite Cu 2ZnSnS 4 nanorods and their perpendicular assembly," *J. Am. Chem. Soc.*, vol. 134, no. 6, pp. 2910–2913, 2012.

[8] F. J. Fan, L. Wu, M. Gong, G. Liu, Y. X. Wang, S. H. Yu, S. Chen, L. W. Wang, and X. G. Gong, "Composition-and band-gap-tunable synthesis of wurtzite-derived Cu 2ZnSn(S1-xSex)4 nanocrystals: Theoretical and experimental insights," *ACS Nano*, vol. 7, no. 2, pp. 1454–1463, Jan. 2013.

[9] K. Ramasamy, M. a. Malik, and P. O'Brien, "Routes to copper zinc tin sulfide Cu2ZnSnS4 a potential material for solar cells," *Chem. Commun.*, vol. 48, no. 46, p. 5703, Jun. 2012.

[10] K. Ramasamy, X. Zhang, R. D. Bennett, and A. Gupta, “Synthesis, photoconductivity and self-assembly of wurtzite phase Cu2CdxZn1−xSnS4 nanorods,” *RSC Adv.*, vol. 3, no. 4, p. 1186, 2013.

[11] A. Khare, A. W. Wills, L. M. Ammerman, D. J. Norris, and E. S. Aydil, “Size control and quantum confinement in Cu2ZnSnS4 nanocrystals,” *Chem. Commun.*, vol. 47, no. 42, p. 11721, 2011.

[12] Y. Zhou, W. Zhou, and M. Li, “Hierarchical Cu2ZnSnS4 Particles for a Low-Cost Solar Cell: Morphology Control and Growth Mechanism,” *J. Phys. Chem. C*, vol. 115, no. 40, pp. 19632–19639, 2011.

[13] S. Mourdikoudis and L. M. Liz-Marzán, “Oleylamine in nanoparticle synthesis,” *Chem. Mater.*, vol. 25, no. 9, pp. 1465–1476, 2013.

[14] J. Y. Rempel, M. G. Bawendi, and K. F. Jensen, “Insights into the kinetics of semiconductor nanocrystal nucleation and growth,” *J. Am. Chem. Soc.*, vol. 131, no. 12, pp. 4479–4489, Apr. 2009.

[15] M. Protière and P. Reiss, “Facile synthesis of monodisperse ZnS capped CdS nanocrystals exhibiting efficient blue emission,” *Nanoscale Res. Lett.*, vol. 1, no. 1, pp. 62–67, Jul. 2006.

[16] J. M. Luther, M. Law, M. C. Beard, Q. Song, M. O. Reese, R. J. Ellingson, and A. J. Nozik, “Schottky solar cells based on colloidal nanocrystal films,” *Nano Lett.*, vol. 8, no. 10, pp. 3488–3492, 2008.

[17] A. Stavrinadis, J. M. Smith, C. a Cattley, A. G. Cook, P. S. Grant, and A. a R. Watt, “SnS/PbS nanocrystal heterojunction photovoltaics.,” *Nanotechnology*, vol. 21, no. 18, p. 185202, May 2010.

[18] C. B. Murray, C. R. Kagan, and M. G. Bawendi, “Synthesis and charaterization of monodisperse nanocrystals and close-packes nanocrystal assemblies,” *Annu. Rev. Mater. Sci.*, vol. 30, no. 1, pp. 545–610, 2000.

[19] J. W. Thomson, K. Nagashima, P. M. MacDonald, and G. a. Ozin, “From sulfur-amine solutions to metal sulfide nanocrystals: Peering into the oleylamine-sulfur black box,” *J. Am. Chem. Soc.*, vol. 133, no. 13, pp. 5036–5041, Apr. 2011.

[20] H. Liu, Y. Liu, Z. Wang, and P. He, “Facile synthesis of monodisperse, size-tunable SnS nanoparticles potentially for solar cell energy conversion.,” *Nanotechnology*, vol. 21, no. 10, p. 105707, Mar. 2010.

[21] S. Hori, T. Suzuki, T. Suzuki, T. Suzuki, and S. Nonomura, “Synthesis and characterization of tin monosulfide nanosheets,” *Jpn. J. Appl. Phys.*, vol. 53, no. 2 (PART 1), p. 021801, Feb. 2014.

[22] A. Tang, S. Qu, K. Li, Y. Hou, F. Teng, J. Cao, Y. Wang, and Z. Wang, “One-pot synthesis and self-assembly of colloidal copper(I) sulfide nanocrystals.,” *Nanotechnology*, vol. 21, no. 28, p. 285602, Jul. 2010.

[23] S.-W. Hsu, K. On, and A. R. Tao, "Localized surface plasmon resonances of anisotropic semiconductor nanocrystals.," *J. Am. Chem. Soc.*, vol. 133, no. 47, pp. 19072–5, Nov. 2011.

[24] Y. Xie, L. Carbone, C. Nobile, V. Grillo, S. D'Agostino, F. Della Sala, C. Giannini, D. Altamura, C. Oelsner, C. Kryschi, and P. D. Cozzoli, "Metallic-like stoichiometric copper sulfide nanocrystals: Phase- and shape-selective synthesis, near-infrared surface plasmon resonance properties, and their modeling," *ACS Nano*, vol. 7, no. 8, pp. 7352–7369, 2013.

[25] Y. Zhao, H. Pan, Y. Lou, X. Qiu, J. Zhu, and C. Burda, "Plasmonic Cu 2-xS nanocrystals: Optical and structural properties of copper-deficient copper(I) sulfides," *J. Am. Chem. Soc.*, vol. 131, no. 12, pp. 4253–4261, Apr. 2009.

[26] J. Joo, H. Bin Na, T. Yu, J. H. Yu, Y. W. Kim, F. Wu, J. Z. Zhang, and T. Hyeon, "Generalized and facile synthesis of semiconducting metal sulfide nanocrystals," *J. Am. Chem. Soc.*, vol. 125, no. 36, pp. 11100–5, 2003.

[27] C. Yeh, Z. W. Lu, S. Froyen, and A. Zunger, "Zinc-blende-Wurzite polytypism in semiconductors," *Phys. Rev. B*, vol. 46, no. 16, p. 10086, 1992.

[28] Q. Guo, G. M. Ford, W. Yang, B. C. Walker, E. A. Stach, and H. W. Hillhouse, "Fabrication of 7.2% Efficient CZTSSe Solar Cells Using CZTS Nanocrystals.pdf," *J. Am. Chem. Soc*, vol. 132, no. 49, pp. 17384–17386, 2010.

[29] G. M. Ford, Q. Guo, R. Agrawal, and H. W. Hillhouse, "Earth abundant element Cu2Zn(Sn1-xGex)S4 nanocrystals for tunable band gap solar cells: 6.8% Efficient device fabrication," *Chem. Mater.*, vol. 23, no. 10, pp. 2626–2629, 2011.

[30] C. Steinhagen, M. G. Panthani, V. Akhavan, B. Goodfellow, B. Koo, and B. a Korgel, "Synthesis of Cu(2)ZnSnS(4) nanocrystals for use in low-cost photovoltaics.," *J. Am. Chem. Soc.*, vol. 131, no. 35, pp. 12554–5, Sep. 2009.

[31] Q. Guo, H. W. Hillhouse, and R. Agrawal, "Synthesis of Cu2ZnSnS4 nanocrystal ink and its use for solar cells," *J. Am. Chem. Soc.*, vol. 131, no. 33, pp. 11672–11673, Aug. 2009.

[32] T. K. Todorov, K. B. Reuter, and D. B. Mitzi, "High-efficiency solar cell with earth-abundant liquid-processed absorber," *Adv. Mater.*, vol. 22, no. 20, p. 156, May 2010.

[33] J.-J. Wang, J.-S. Hu, Y.-G. Guo, and L.-J. Wan, "Wurtzite Cu2ZnSnSe4 nanocrystals for high-performance organic–inorganic hybrid photodetectors," *NPG Asia Mater.*, vol. 4, no. 1, p. 12, Jan. 2012.

[34] Y. Yin and a P. Alivisatos, "Colloidal nanocrystal synthesis and the organic-inorganic interface.," *Nature*, vol. 437, no. 7059, pp. 664–670, 2005.

[35] G. Lorimer, "Quantitative X-ray microanalysis of thin specimens in the transmission electron microscope; a review," *Mineral. Mag.*, vol. 51, no. 359, pp. 49–60, 1987.

[36] M. Watanabe and D. B. Williams, "The quantitative analysis of thin specimens: A review of progress from the Cliff-Lorimer to the new ζ-factor methods," *J. Microsc.*, vol. 221, no. 2, pp. 89–109, 2006.

[37] M. Edler, T. Rath, A. Schenk, A. Fischereder, W. Haas, M. Edler, B. Chernev, B. Kunert, F. Hofer, R. Resel, and G. Trimmel, "Copper zinc tin sulfide layers prepared from solution processable metal dithiocarbamate precursors," *Mater. Chem. Phys.*, vol. 136, no. 2–3, pp. 582–588, Oct. 2012.

[38] T. Rath, W. Haas, A. Pein, R. Saf, E. Maier, B. Kunert, F. Hofer, R. Resel, and G. Trimmel, "Synthesis and characterization of copper zinc tin chalcogenide nanoparticles: Influence of reactants on the chemical composition," *Sol. Energy Mater. Sol. Cells*, vol. 101, pp. 87–94, 2012.

[39] M. Li, W. H. Zhou, J. Guo, Y. L. Zhou, Z. L. Hou, J. Jiao, Z. J. Zhou, Z. L. Du, and S. X. Wu, "Synthesis of pure metastable wurtzite CZTS nanocrystals by facile one-pot method," *J. Phys. Chem. C*, vol. 116, no. 50, pp. 26507–26516, Dec. 2012.

[40] H. Katagiri, K. Jimbo, W. S. Maw, K. Oishi, M. Yamazaki, H. Araki, and A. Takeuchi, "Development of CZTS-based thin film solar cells," *Thin Solid Films*, vol. 517, no. 7, pp. 2455–2460, 2009.

[41] M. D. Regulacio, C. Ye, S. H. Lim, M. Bosman, E. Ye, S. Chen, Q. H. Xu, and M. Y. Han, "Colloidal nanocrystals of wurtzite-type Cu2ZnSnS4: Facile noninjection synthesis and formation mechanism," *Chem. - A Eur. J.*, vol. 18, no. 11, pp. 3127–3131, Mar. 2012.

[42] H. Jiang, P. Dai, Z. Feng, W. Fan, and J. Zhan, "Phase selective synthesis of metastable orthorhombic Cu2ZnSnS4," *J. Mater. Chem.*, vol. 22, no. 15, p. 7502, 2012.

[43] M. Grossberg, J. Krustok, J. Raudoja, K. Timmo, M. Altosaar, and T. Raadik, "Photoluminescence and Raman study of Cu2ZnSn(SexS1−x)4 monograins for photovoltaic applications," *Thin Solid Films*, vol. 519, no. 21, pp. 7403–7406, Aug. 2011.

[44] S. Chen, A. Walsh, Y. Luo, J. H. Yang, X. G. Gong, and S. H. Wei, "Wurtzite-derived polytypes of kesterite and stannite quaternary chalcogenide semiconductors," *Phys. Rev. B - Condens. Matter Mater. Phys.*, vol. 82, no. 19, pp. 1–8, Nov. 2010.

[45] A. Walsh, S. Chen, X. G. Gong, and S. H. Wei, "Crystal structure and defect reactions in the kesterite solar cell absorber Cu2ZnSnS4 (CZTS): Theoretical insights," *AIP Conf. Proc.*, vol. 1399, no. 2011, pp. 63–64, 2011.

[46] S. Y. Chen, A. Walsh, J. H. Yang, X. G. Gong, L. Sun, P. X. Yang, J. H. Chu, and S. H. Wei, "Compositional dependence of structural and electronic properties of Cu(2)ZnSn(S,Se)(4) alloys for thin film solar cells," *Phys. Rev. B*, vol. 83, no. 12, pp. 1–5, Mar. 2011.

[47] I. Repins, N. Vora, C. Beall, S.-H. Wei, Y. Yan, M. Romero, G. Teeter, H. Du, B. To, M. Young, and R. Noufi, "Kesterites and Chalcopyrites: A Comparison of Close Cousins," in *MRS Proceedings*, 2011, vol. 1324.

[48] X. Wang, Z. Sun, C. Shao, D. M. Boye, and J. Zhao, "A facile and general approach to polynary semiconductor nanocrystals via a modified two-phase method.," *Nanotechnology*, vol. 22, no. 24, p. 245605, Jun. 2011.

[49] S. Chen, X. G. Gong, A. Walsh, and S.-H. Wei, "Crystal and electronic band structure of Cu[sub 2]ZnSnX[sub 4] (X=S and Se) photovoltaic absorbers: First-principles insights," *Appl. Phys. Lett.*, vol. 94, no. 4, p. 041903, 2009.

[50] R. R. Zamani, M. Ibáñez, M. Luysberg, N. García-Castelló, L. Houben, J. D. Prades, V. Grillo, R. E. Dunin-Borkowski, J. R. Morante, A. Cabot, and J. Arbiol, "Polarity-driven polytypic branching in cu-based quaternary chalcogenide nanostructures.," *ACS Nano*, vol. 8, no. 3, pp. 2290–301, Mar. 2014.

[51] S. Singh and K. M. Ryan, "Occurrence of Polytypism in Compound Colloidal Metal Chalcogenide Nanocrystals, Opportunities, and Challenges," *J. Phys. Chem. Lett.*, pp. 3141–3148, Jul. 2015.

[52] S. M. Rupich, E. V Shevchenko, M. I. Bodnarchuk, B. Lee, and D. V Talapin, "Size-dependent multiple twinning in nanocrystal superlattices.," *J. Am. Chem. Soc.*, vol. 132, no. 1, pp. 289–96, Jan. 2010.

Chapter 5 – Designing a CZTS Nanocrystal Synthesis for Colloidal Nanocrystal Photovoltaics

"There is a single light of science, and to brighten it anywhere is to brighten it everywhere." Isaac Asimov

5.1 Introduction

In the previous chapter a synthesis was developed that facilitated an investigation into the change in CZTS phase with reaction temperature. The stability of the NCs was such that thin film devices, with good optoelectronic properties, could not be fabricated due to a lack of colloidal stability. This was attributed to poor NC surface passivation, exhibited by oleylamine when used as the only reaction ligand in the NC synthesis. In order to design a NC system suitable for making PV devices the following parameters must be understood and controlled:

1. Stoichiometry, phase, size and shape.
2. Colloidal stability in ambient conditions.
3. Ligand exchange protocols to form conformal, dense, semiconducting thin films.

In this chapter a strategy to synthesize high quality thermodynamically stable kesterite CZTS NCs is described.

5.2 Co-operative Ligand Synthesis

Oleic acid has been successfully used in the synthesis of many chalcogenide NCs[1]–[5] and its ligand exchange dynamics are well defined[3], [4], [6]. In this chapter we investigate the minimum amount of oleic acid needed to work cooperatively with oleylamine[1], [7] in order to affect the surface chemistry in such a way as to enhance CZTS NCs stability; with the ultimate goal of fabricating solar cell devices in ambient conditions. The effects of introducing this secondary ligand on the nucleation and growth of the NCs are investigated using the parameters outlined in Table 5.2-1. Of the five molar ratios here, the minimum ratio of OLA/OA required to sufficiently enhance the stability of the synthesised NCs, was determined to be 5:1. This was experimentally determined by washing each sample sufficiently enough to effectively clean away unreacted reaction precursors.

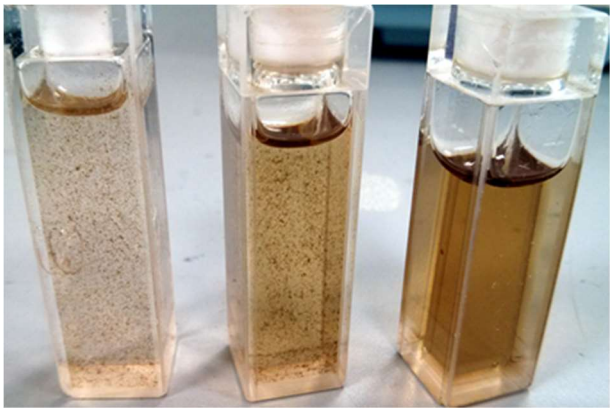

Figure 5.2-1 Photograph of 0.5mg/ml CZTS-toluene NC solutions, displayed left to right, synthesised with OLA/OA ligand ratios of 1:0, 11:1 and 5:1 respectively. Increasing the concentration of OA, relative to the OLA, had the effect of stabilising CZTS NCs in toluene, as is demonstrated by a reduction in the formation of solid aggregates and the deepening colour of the CZTS-toluene solution (from left to right).

The method, adapted from a procedure commonly reported in the literature[1], [8]–[12], consisted of cleaning the NCs once with acetone:toluene and then three times with ethanol:toluene and once with methanol:hexane (1:1 mixtures) before

dispersing each sample in 20ml of hexane to be stored in ambient conditions. The NC sample that was synthesised using 100% OLA, fell out of solution after the second cleaning step (as shown in Figure 5.2-1) and could not be redispersed, whereas each of the OA syntheses survived the entire cleaning procedure and remained in solution several days hence.

Table 5.2-1: Summary of CZTS NC synthesis reaction precursors.

Reaction	***Oleylamine***	***Oleic Acid***	***Ratio***
1	60.00	0.00	1:0
2	55.00	5.00	11:1
3	50.00	10.00	5:1
4	40.00	20.00	2:1
5	20.00	40.00	1:2

Having established that the co-operative ligand strategy had been successful in enhancing the colloidal stability of CZTS NCs produced using this method, it is important to determine how the introduction of OA had affected the NC growth. Figure 5.2-4 shows the XRD traces of the NC samples synthesised, at a reaction temperature of 140°C, with the different ligand molar ratios outlined in Table 5.2-1. The predominant diffraction peaks of each sample can be indexed to the kesterite CZTS crystal structure, which has a tetragonal arrangement of sulphur anions with corresponding cations at the interstices. The corresponding planes are indexed according to the CZTS Kesterite structure (JCPDS 01-075-4122). For the NCs that were quenched after 20s at 140°C, additional diffraction peaks appear in the XRD trace, which can be indexed to the high chalcocite Cu_2S (JCPDS 00-046-1195)

structure. The characteristic 011, 012 and 110 peaks of the XRD reference pattern for Cu_2S, reported in Figure 4.2.2, match with the additional peaks present in the diffraction traces for CZTS nanocrystals formed using a high molar ratio of oleic acid (see Figure 5.2-4).

The presence of characteristic Cu_2S peaks in the XRD spectra for the NC sample quenched after 20s could be due to the presence of the Cu_2S NCs in the reaction solution. Alternatively, the characteristic peaks could be representative of a mixture of Cu_2S and other chalcogenide species with similar, tetragonal, crystal structures to
70 that of kesterite CZTS. Two potential candidates include ZnS and Cu_2SnS_3 (CTS) both of which have been shown to form during the synthesis of CZTS NCs[13]. To make matters worse, the XRD peaks of different crystallographic phases often overlap: For example, CZTS, CTS and ZnS can all exhibit tetragonal (sphalerite) structures (see Figure 5.2-2a), which results in an overlap of the dominant experimental peaks of their respective XRD spectra as shown in Figure 5.2-2b. This is also case with the commonly observed hexagonal forms of ZnS, SnS and CZTS (wurtzite) species. It is therefore difficult to identify CZTS clearly. There is always the potential to form a number of unwanted bi-products for a given synthesis method, including unreacted precursors or uncapped and poorly stabilised NCs[14].

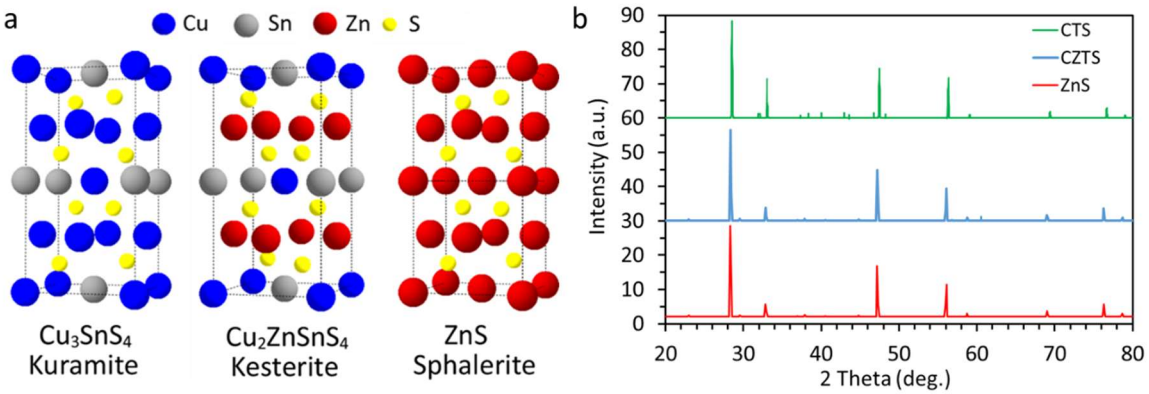

Figure 5.2-2 a) Model crystal structures of the tetragonal forms of Cu_2SnS_3 (CTS), Cu_2ZnSnS_4 (CZTS) and ZnS generated using CrystalMaker™. b) Model X-Ray diffraction traces of CTS, CZTS and ZnS crystal structures generated using Crystal Diffract™.

The composition and crystallographic phase of the CZTS NCs formed during the synthesis is heavily influenced by the precursors and surfactants that are used[14]. In particular, the precursor reactivity can determine the rate at which the precursors react or decompose in order to form the pre-requisite monomer species[14]. This then directly affects the monomer concentration[14]. Previous studies have described the important role that the reaction rate, between the Cu, Zn, Sn and S precursors, plays in determining the formation of CZTS nanocrystals with different crystallographic phases. Cu+, Zn2+, and Sn4+ are soft, intermediate, and hard Lewis acids, respectively and so their reactivity towards the S precursor (itself a soft Lewis base) increases from Sn^{4+} to Zn^{2+} and finally to Cu^{+}[15]. Hence, the Cu precursor is the most likely of the three metal cation precursors to nucleate, forming hexagonal Cu_xS nuclei, which is known to be the most stable binary copper chalcogenide have the greatest chance of initially forming. The formation of hexagonal CZTS nanocrystals is often attributed to the induced growth from preferentially formed Cu_2S NCs due to the high reactivity of the Cu precursor toward the sulphur precursor[15]. This is consistent with the previously described synthesis, in chapter 4, wherein $Cu(C_5H_7O_2)_2$

was reacted with TMSS, resulting in the nucleation of stable Cu_2S NCs. Shavel et al. found that the kinetics of the reaction between each cation with sulphur is fastest for Cu and slowest for Zn in forming kesterite CZTS NCs when reacting metal salts with elemental sulphur in OLA[16]. Furthermore, the exchange of Cu^+ and Zn^{2+} ions in the crystal lattice is energetically inexpensive, owing to their similar physical properties[15].

To determine whether multiple NC species are formed using this adapted synthesis, the crystallographic structure of individual NCs are investigated using TEM, as shown in Figure 5.3-1. If different NC species were present, having been simultaneously nucleated during the synthesis, we may expect to observe individual NCs with substantially different crystallographic structures. Each of the NCs, formed from the synthesis with a ligand molar ratio of 5:1 (OLA/OA), were found to exhibit only one NC structure, that of hexagonal Cu_2S (an example of which is shown in Figure 5.3-1a, and no NCs were found to exhibit a clearly tetragonal CZTS structure, which would suggest that NCs formed during the initial stages of the reaction have a predominantly Cu_2S crystal structure. We may also expect to observe individual NCs with substantially different elemental compositions, when examining each sample with STEM-EDX. As shown in Figure 5.3-5, each of the NCs examined under STEM-EDX appear to comprise Cu, Zn, Sn and S constituent elements. Thus, it is hereby proposed that a Cu_2S-CZTS hetero-structure is likely to be the origin of the additional peaks shown in the XRD spectra of the 20s sample shown in Figure 5.2-4.

An equivalent hetero-structure composed of copper sulphide and other metal sulphides has also been observed in other materials, caused by the preferential

reaction between Cu+ and S_2^-, making copper sulphide a general nucleating phase (Figure 5.2-3b)[10], [17], [18]. Following the nucleation of copper sulphide, the arrangement of the S_2- anions serving as the backbone enables the subsequent incorporation and growth of other metal sulphides based on the same anion arrangement structure (Figure 5.2-3c).

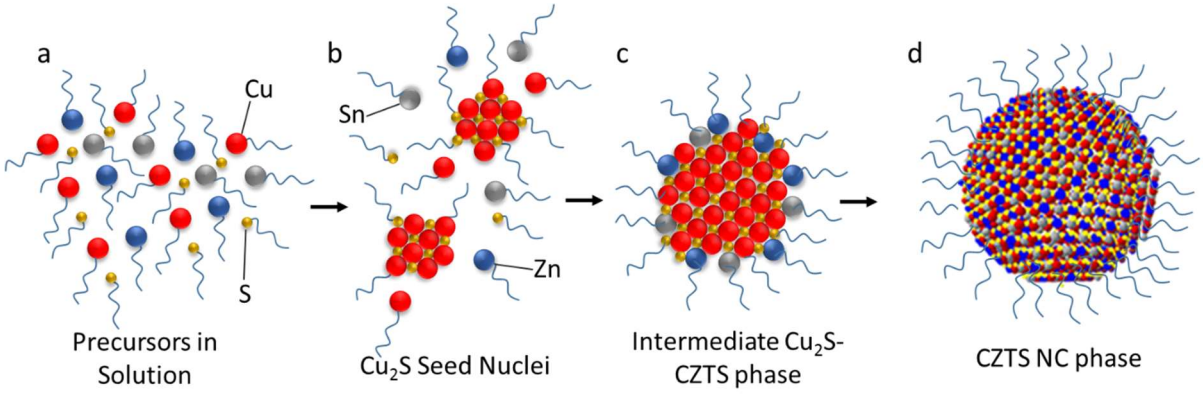

Figure 5.2-3 An illustrative diagram of the a proposed CZTS NC nucleation mechanism over time, the mechanism comprising a) Cu, Zn, Sn and S precursors in solution, b) intermediate phase Cu_2S NC seeds, c) larger Cu_2S nuclei with interpenetrating Zn and Sn cations at the surface and d) a CZTS NC.

The Cu_2S phase has a hexagonally packed backbone of S_2-, which forms preferentially during heating of the reaction. A phase change then occurs to transform this hexagonally packed structure to the tetragonal CZTS following the inter-diffusion of the Zn and Sn cation species (Figure 5.2-3d). Therefore, it is envisaged that the so called Cu_2S-CZTS acts as an intermediate stage between the initial nucleated Cu_2S seeds and the final CZTS NCs. Due to high reactivity of the S precursor it is conceivable that the reaction dynamics inhibit the characterisation of the Cu_2S seeds using conventional TEM techniques. However, any further investigation of this initial nucleation phase would prove invaluable to the greater understanding of the formation of CZTS NCs. It is noteworthy that the final products reported in similar NC formation processes are typically copper sulphide–metal sulphide hetero-structures,

which consist of both a starting phase (copper sulphide) and a multi-component phase (metal sulphide)[17], [18].

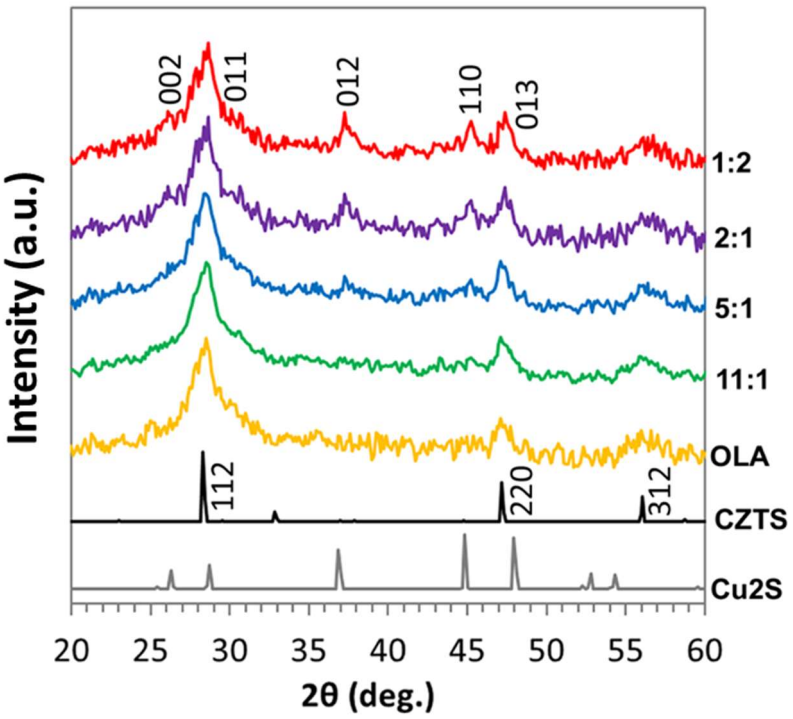

Figure 5.2-4 XRD traces of CZTS NCs synthesised with an OLA:OA molar ratio of 1:0, 11:1, 5:1, 2:1 and 1:2. Also shown in black and grey are the model spectra of CZTS (kesterite) and Cu_2S (hexagonal) underneath, calculated using Crystal Diffract™ crystallographic software. The spectra from with CZTS NCs nucleated from syntheses with higher molar concentrations of OA, exhibit additional peaks that are indexed to the (112) and (110) planes of the Cu_2S crystal structure.

The coordination of the capping ligands in the reaction system can also alter the reactivity of the metal precursors. OLA is a relatively good reducing agent but is generally considered to be poor in comparison with the other aliphatic ligands used in NC synthesise that have been reported in the literature[19] By contrast, the carboxylic group of the OA is a much stronger coordinating ligand[4], [20]. In terms of the Lewis acid-base model set out by G.N. Lewis[21], oleic acid acts as a much stronger Lewis base, reacting preferentially with the Cu^+ ions. Therefore, using OA in combination with OLA is likely to reduce the Cu+ monomer concentration by forming

more stable oleate precursors, i.e. a greater concentration of the reaction monomers are stabilised using OA than when OLA is used exclusively as both ligand and reducing agent.

A lower monomer concentration leads to low supersaturation which suppresses the nucleation of CZTS[20], [22]. In this environment there is a preference for forming Cu_2S seed structures, into which Zn and Sn cations inter-diffuse over time. Therefore, the resulting reaction, with higher concentrations of OA, proceeds more slowly and gives rise to Cu_2S-type CZTS NCs. The interaction between OLA and TMSS may also play an influential role in the preferential nucleation of Cu_2S. OLA is thought to react with TMSS to form a TMSS-alkylamine association and so by decreasing the relative concentration of oleylamine in the reaction, the sulfurization speed is inhibited, thus slowing down the speed of the reaction and further promoting the formation of a Cu_2S-CZTS hetero-structured NCs.

Localised Surface Plasmonic Response

A surface plasmon arises from coherent electron oscillations at a material interface and can be analysed to understand the surface chemistry of copper based NCs[23]–[26]. LSPR is observed when the NC size is smaller than the excitation wavelength resulting in the confinement of the surface plasmon[25]. A LSPR results in a short range electric field enhancement at the particle's surface, which leads to an optical extinction at a particular characteristic resonant frequency that can be measured using UV-Vis-NIR absorption spectroscopy[23]. This effect was initially observed in noble metal NCs where LSPR occurs at visible wavelengths and is strongly dependent on NC size and shape[23], [24]. This has led to the application of

Ag and Au anisotropic NCs within photovoltaics[27] and surface enhanced Raman spectroscopy[28]. LSPR has more recently been reported for non-metallic NCs composed of doped semiconductor materials, including intrinsically doped Cu_2S[23]–[26]. It has been shown that by chemically or electrochemically doping these materials, changes in the free carrier density leads to a variation in LSPR wavelength[25].

Bulk $Cu_{2-x}S$ exhibits a free-carrier absorption in the NIR region caused by an excess of holes in the valence band due to copper deficiencies [29]. All copper sulphide polymorphs have a thermodynamic propensity towards copper deficiency owing to the low chemical potential of Cu, so much so that vacancies can be easily formed by the loss of copper to carbon dioxide or oxygen at a free surface. Hole densities of $10^{21}cm^{-3}$ are typically found in copper chalcogenide films[29]. In bulk material, the free carrier absorption intensity increases with the decreasing atomic% of S and therefore, no absorption is seen for perfectly stoichiometric Cu_2S[29]. Solution synthesised $Cu_{2-x}S$ NCs also exhibit a similar trend in their NIR absorption as a function of stoichiometry[25].

Plasmonic optical absorption can be used to characterize the composition of the copper sulphide. The five NC samples synthesized with different molar ratios of OLA and OA exhibit optical absorbance in the visible light region (Figure 5.2-5), which corresponds to the band gap transition of the CZTS (E_g ~1.5eV). The suspected plasmonic absorption peak interferes with extraction of a band gap from the absorption spectra of NCs synthesised with ligand ratios less than 11:1. This is

because the rising edge of the absorption spectrum is covered by the plasmonic absorption peak (as shown in Figure 5.2-5).

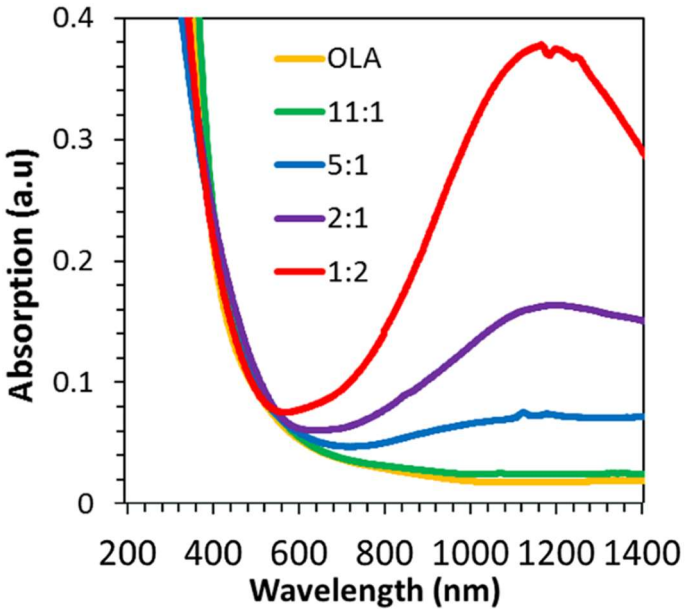

Figure 5.2-5 UVVIS-NIR absorption spectra of CZTS NCs synthesised with an OLA:OA molar ratio of 1:0, 11:1, 5:1, 2:1 and 1:2, showing a strong absorption peak corresponding with the CZTS band gap transition (E_g ~1.5eV). Also showing an increasingly prominent second absorption peak in the infrared region, with increasing molar concentration of OA, owing to the LSPR response of the respective NCs in solution.

However, the NCs synthesized with molar ratios below 11:1 (OLA: OA) all show a broad absorption peak in the near-infrared region. According to the dipole surface plasmon, the LSPR frequency (ω_{sp}) can be expressed as:

$$\omega_{sp} = \frac{E_{sp}}{\hbar} = \sqrt{\frac{\omega_p^2}{1 + 2\varepsilon_m} - \gamma^2} \qquad 5.2\text{-}1$$

where ε_m is the dielectric constant of the solvent, $\omega_p$is the plasmon frequency of the free electron gas and γ represents the linewidth of the plasmon resonance band (also referred to as the collision frequency). The LSPR frequency and line-width were determined by fitting the NIR absorption band to a Gaussian function using Origin Pro™. For each NC sample we assume that the dielectric function of CZTS in the NIR

region is dominated by free carriers, because the bandgap contribution can be neglected[25]. The absorption spectra of the NCs in Figure 5.2-5 exhibit a clear LSPR in the near infrared region centred at ~1245 nm, indicating an LSPR resonance energy (E_{sp}) of 0.99eV. The linewidth (γ) of the absorbance peak was measured to be ~285nm, and the dielectric constant of toluene is ε_m = 2.28. Hence, from equation 5.2-1 the bulk plasmon resonance energy (E_p) is estimated to be 2.07eV, which then can be used to calculate the free carrier density of the material, using equation 5.2-2 below.

$$\omega_p = \frac{E_{sp}}{\hbar} = \sqrt{\frac{N_h e^2}{\varepsilon_0 m_h}} \qquad 5.2\text{-}2$$

where N_h is the free carrier density and m_h is the effective hole mass, which is approximately 0.8 times the mass of an electron. The LSPR serves to profile the stoichiometric state of the NC lattice. Assuming each excess hole originates from one copper vacancy, copper deficiency can be determined to be 6.8%, therefore the composition can be estimated to be $Cu_{1.93}S$, which is within the range of chalcocite and its copper deficient derivative Djurleite – $Cu_{1.93\text{-}97}S$. It is important to note that with this calculation, N_h is overestimated, because the experimental LSPR linewidth includes inhomogeneous broadening due to the dispersion in NC size and vacancy density, in addition to the intrinsic broadening γ. A degree of imprecision is also present in the LSPR estimate because of the uncertainty of m_h and the assumption that all copper vacancies are ionized. Despite these shortcomings, this result suggests the presence of a Cu_2S nanostructure within the CZTS NC sample.

The experiments that now follow focus on the sample with a 5:1 OLA: OA surfactant ratio, which provides adequate colloidal stability whilst minimally altering the original synthesis.

5.2.1 Effect of Environment on LSPR

The previous set of experiments were conducted in close to dry-conditions. If an absorption sample is left out in ambient light and atmosphere, the LSPR peak increases in magnitude and blue-shifts over time as shown in Figure 5.2-6. When left in air, $Cu_{2-x}S$ species are known to oxidize or lose copper via diffusion[25]. Recent reports have shown that the plasmon frequency shifts to lower wavelengths with a corresponding decrease in the Cu:S ratio: as the number of vacancies increases, injecting more charge carriers into the valence band, the free carrier density increases. As Luther et al. discuss in their highly cited paper, copper chalcogenide NCs can undergo changes in composition and vacancy density over time caused by oxidation or field-assisted copper migration, thus modifying the critical optoelectronic properties[25], [30], [31]. This has a dramatic consequence for the use of these NCs when utilised in photovoltaic devices. Clearly any device fabrication undertaken in ambient conditions will most likely result in the significant oxidation of the Cu_2S nanostructure, which will have a profound effect on device performance. Cu_2S and some of its derived copper deficient structures have an indirect bandgap, which prevents full exploitation of its low optical band-gap (~1.2 eV) in applications demanding good light harvesting properties in the visible part of the spectrum (i.e. where the solar spectrum has the maximum photon fluence).

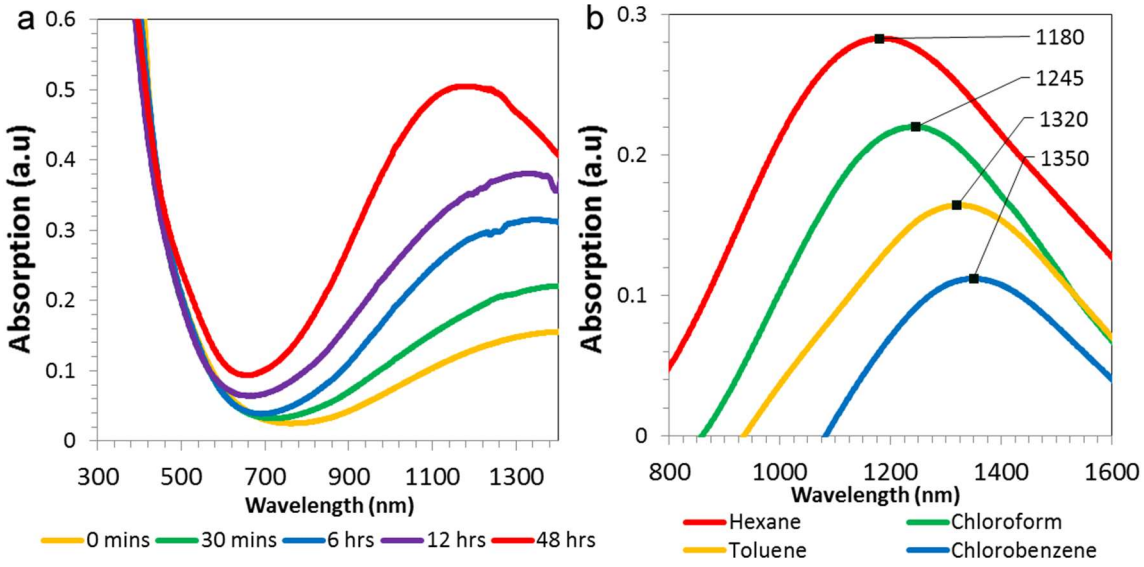

Figure 5.2-6 a) UVVIS-NIR absorption spectra from NCs synthesised with an OLA:OA molar ratio of 1:0, 11:1, 5:1, 2:1 and 1:2, showing the effects that a) exposure to air and b) NC solvent has on the LSPR-absorption of Cu_2S-CZTS NCs.

Sub-bandgap absorption can arise from phenomena other than LSPR, such as scattering or from interactions with sample impurities, but we can assign the NIR absorption bands to LSPR by analysing the effect of the solvent medium on the absorption band position. As shown in Figure 5.2-6b the NIR absorption band is successively red shifted as hexane is replaced with chloroform, toluene and chlorobenzene, which each exhibit increasing refractive indices of 1.446, 1.496 and1.524 respectively. This characteristic red shift of the LSPR peak is to be expected and has been demonstrated for previously for other Cu based chalcogenide NCs that exhibit an LSPR response [25]. The magnitude of spectral shift is complicated by the contribution of the ligand shell to the effective local medium index, however the observation of a clear red shift in the NIR absorption peak indicates the prevalence of an LSPR.

5.2.2 Cooperative Ligand

Understanding how OA and OLA interact with the NC surface was achieved using FTIR to investigate the Cu_2S-CZTS NC synthesis incorporating a 5:1 (OLA: OA) ligand ratio, as shown in Figure 5.2-7. The prevalence of the major bonding groups associated with OA, OLA and TMSS are outlined in Table 5.2-2 for each stage of the reaction. Evidence of OA and OLA is present in the metal cation precursor solution prior to TMSS injection.

Table 5.2-2: Indexed FTIR peaks visible in Figure 5.2-7.

Band (cm^{-1})	***Group***	***Pre-***	***Post-***	***Cleaned***
1500-1430	CH2 scissors	Present	Present	Faint
1460-1390	CH3 antisym.	Present	Present	Faint
1400-1320	CH3 sym.	Present	Present	Faint
1050-860	C=CH2	Present	Present	-
810-725	N-H wag	Present	-	-
1300-1200	Si-CH3	-	Present	-
1150-1000	Si-O-Si	-	Present	-
910-800	Si-C	-	Present	-
1610-1550	COO- antisym. stretch	-	Faint	Faint
1400-1320	COO- sym. stretch	-	Faint	Faint

Following the injection of TMSS a prominent Si-O-Si bond can be identified in the FTIR spectra indicating that Si is no longer bound to sulphur, which is likely to have complexed with the oleylamine ligands and precipitated the formation of CZTS NCs. At this stage excess oleic acid is still present in the solution as indicated by the presence of –OH and –C=O peaks.

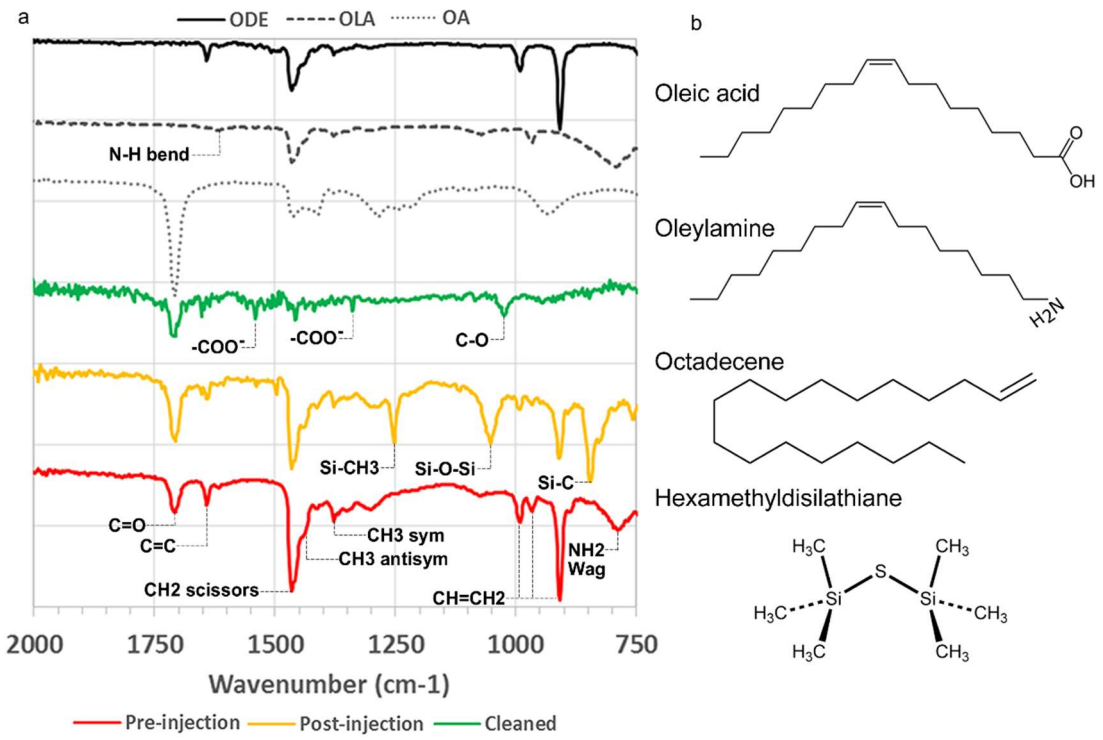

Figure 5.2-7 a) FTIR spectra of CZTS NC synthesis, and cleaning. Individual FTIR spectra have been offset for clarity. NC b) Schematic representations of oleic acid, oleylamine, octadecene and hexamethyldisilathiane.

Precipitation and cleaning the NCs results in the peaks related to the aliphatic chains of the ligands and co-solvent being removed, leaving behind faint traces of the
300 N-H bend associated with oleylamine. Further evidence of the oleylamine capping on the NCs is given by the similarity in the C–H bending modes (~1450cm^{-1}) observed in both NCs and oleylamine spectra. A broad feature at~1500–1580cm^{-1} appears in the NC spectrum, with a peak at 1538 cm^{-1}.[4] These features cannot be related to pure OLA or OA however, the 1538cm^{-1} is located in the region where the (COO)– asymmetric mode appears when carboxylates are attached to metal atoms[32], [33]. If in addition, the weaker feature at 1508cm^{-1} is attributed to the (COO)–symmetric mode, a model can be suggested: that the oleic acid is chelated to the metal atoms in a bidentate fashion. This model has been previously described in the literature[32],

[33] for similar chalcogenide systems and this suggests that both OA and OLA ligands play a role in the formation and stabilisation of NCs.

At this point I have identified the parameters needed to form a stable Cu_2S-CZTS NC colloid, the next step is to further understand the role OA plays in the growth and stabilisation of these NCs. Steps must also be taken to investigate the reaction conditions required to promote the growth of pure CZTS NCs, and eradicate Cu_2S from the NC hetero-structure. This would reduce the impact of the optoelectronic defects associated with Cu_2S, which would otherwise compromise the photovoltaic performance of CZTS NCs employed in thin film solar cells.

5.3 Influence of nanocrystal growth time

The three key reaction parameters that can be manipulated to control nucleation and growth when using the hot injection method are; the precursors, the ligands and the reaction temperature[20], [34]. While each can be considered as an independent variable, they are greatly interrelated. In particular, the rate of nucleation is directly proportional to the concentration of the monomer and therefore the degree of supersaturation[35]. The precursor reactivity can determine the rate at which the precursors react or decompose to form the monomer species, which directly affects the monomer concentration.

A higher monomer concentration leads to fast nucleation and results in a large number of smaller critical nuclei; a low monomer concentration slows the nucleation producing a smaller number of larger critical nuclei. For this reason, the precursors need to rapidly decompose or react to yield a supersaturation of monomers immediately following the TMSS injection[20]. Simple molecules that have leaving

groups that readily detach are therefore ideal candidates for NC reaction precursors, as they are more easily decomposed thereby facilitating the growth of NCs more effectively.

The work of Liao et al. investigated the dynamics of growth-time using dodecanethiol as the sulphur precursor. They found that djurleite ($Cu_{1.94}S$-CZTS) NC seeds nucleate and then grow as the reaction proceeds to form pure hexagonal CZTS[36]. Similarly, here we investigate the evolution of the Cu_2S-CZTS NC over time using TMSS as the sulphur precursor. It has been reported in the literature that equivalent Cu_2S–CZTS hetero-structures exhibit high mobility cations and a high concentration of vacancies suggested by the presence of the plasmonic features. Both characteristics facilitate the inter-diffusion of free cations, analogous to a fluid that flows around the sulphur anions. Therefore, the longer reaction time, allows for more inter-diffusion of Zn and Sn metal cations, which results in the growth of the NCs and consequent expulsion of the Cu_2S starting phase.

Figure 5.3-1 shows the corresponding TEM images of NCs synthesized for different reaction times. A qualitative analysis of the NCs shown in Figure 5.3-1a, d + g reveals that the NCs that have been aged for 20s appear to form small pseudo-spheroidal NCs, whereas the NCs aged for 1hr appear much larger. In each case the NCs are well dispersed suggesting that the surface ligands are providing sufficient steric repulsion to keep the NCs apart.

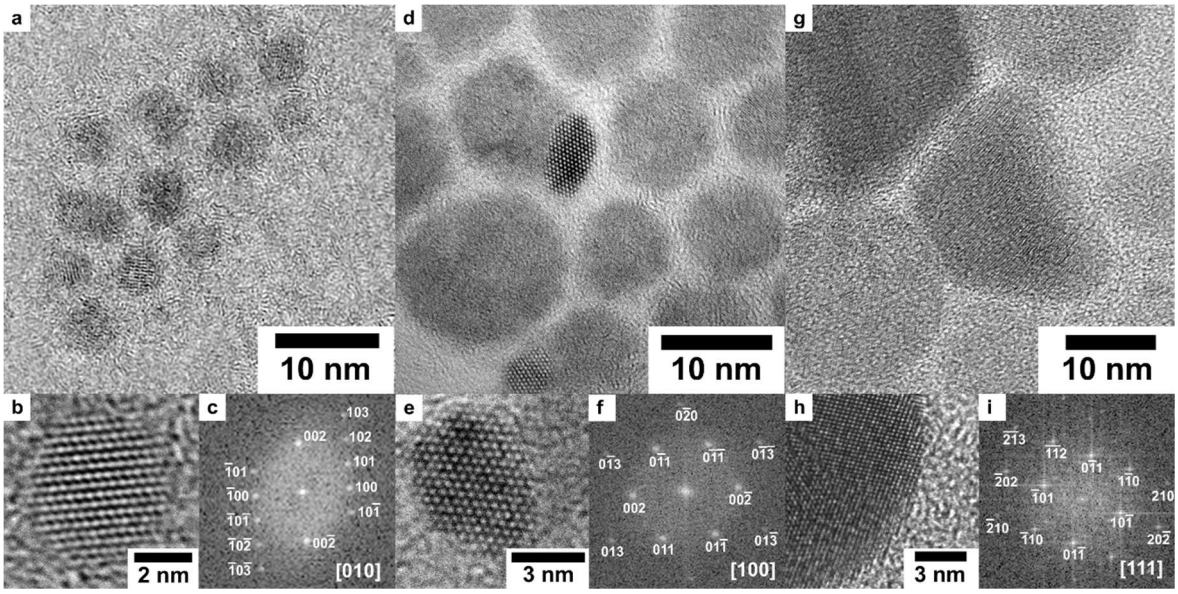

Figure 5.3-1 (a, d+g) TEM micrographs, inset with (b, e+h) HTEM micrographs and (c, f+i) FFT of CZTS NCs nucleated at 140°C and aged at 140°C for a-c)20 seconds, d-f)1 hour and g-i)4 hours.

Consequently, the NCs aged for 4hrs (Figure 5.3-1g) appear to form a range of 4-5 sided 2D plates. Figure 5.3-1h shows a high resolution TEM (HRTEM) image of a sample NC with a single highly crystalline structure; the lattice fringes of which have been indexed in Figure 5.3-1h to the corresponding (012) and (011) planes of the CZTS structure. By contrast, Figure 5.3-1b+e appear to show single crystalline NCs where the predominant crystal structure is analogous to that of Cu_2S; the lattice fringes of which are indexed along the [010] and [100] lattice direction respectively.

A numerical analysis of the change in NC diameter with reaction temperature is shown in Figure 5.3-2. As with the NC size distribution analysis carried out in Chapter 4 (see Figure 4.2-5), each measured NC diameter value has been categorised into groups with a 0.5nm range. As with the analysis featured in the previous chapter, the experimental error that this represents has once again been included here, so as to highlight the limitations of the size distribution analysis in determining the average NC diameter of each sample. The relative standard deviation is also used as an

approximation of the relative NC size distribution for each sample. The standard deviation values for the NCs samples nucleated at 140°C, and aged for 20s, 1hr and 4hrs are shown in Figure 5.3-2b. The NCs aged for 20s exhibit an average NC diameter of 4.9 ±0.5nm with a relative size distribution of 13%. The NCs aged for 1hr exhibit an average NC diameter of 11.5 ±0.5nm, with a corresponding relative size distribution of 15%, while the NCs aged for 4hrs exhibit an average NC diameter of 28.9 ±0.5nm and a corresponding relative size distribution of 14% (as shown in Figure 5.3-2c).

The high reactivity of the Cu^{+} cation, which induces the formation and growth of stable Cu_2S nuclei, immediately following the injection of the S precursor, is likely to be significant in the formation of Cu_2S-CZTS NCs with a relatively narrow size distribution (< 10%), as observed in Figure 5.3-1a[37]. As the reaction proceeds for more than one hour the further nucleation and growth of the NCs occurs resulting in more irregularly shaped NCs as seen in Figure 5.3-1g. The injection needs to take place at a temperature that is high enough for the precursors to have decomposed and form a supersaturation of monomers[38]. It must also be high enough to overcome the thermal barrier for the reaction, and furthermore to allow for the subsequent rearrangement of atoms, to take place.

A higher nucleation temperature usually makes the precursors less stable, permitting the easy formation of supersaturated monomers[33], which results in a faster nucleation and a large concentration of small nuclei[34]. However, if the growth temperature is too high then uncontrolled growth can occur. For this reason, the growth temperature is typically lower than the nucleation temperature[20].

For this synthesis condition, both the temperature of nucleation (at injection) and the subsequent growth temperature (immediately post injection) are the same. In real conditions, not all the nucleation events occurs simultaneously hence, at any given moment following the initial injection, there are a range of NC nuclei at different stages of their growth phase[35],[34]. Traditionally, the NCs would be quenched to inhibit further nucleation and growth of the NCs however, in this experiment the NCs have been allowed to continue to grow at an elevated temperature leading to the increasing NC diameter and size distribution, as identified in Figure 5.3-2. In such a prolonged and uncontrolled growth regime, the OA and OLA reaction ligands are unable to regulate the growth of individual NC facets[35],[34], leading to anisotropic growth with increasing ageing time that can be seen in Figure 5.2-1a, d and g.

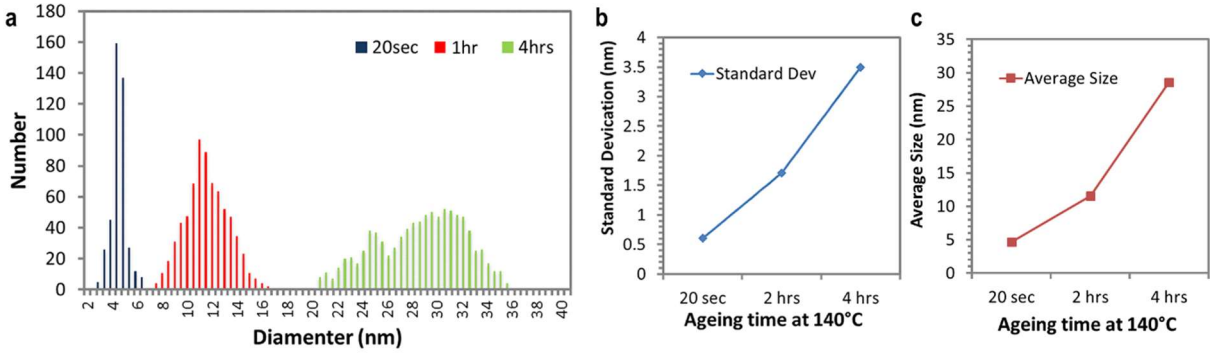

Figure 5.3-2 a) Size distribution, b) standard deviation and c) average (mean) particle size analysis of CZTS NCs nucleated at 140°C and aged for 20s, 1hr and 4hrs taken from low resolution TEM micrographs.

In order to help distinguish CZTS phases from Cu_2S and any other potential metal sulphides that may be present in the reaction solution, Raman scattering was used to analyse each NC sample. Figure 5.3-3b shows Raman scattering data from NC films cast onto silicon substrates from colloidal dispersions. Raman scattering data for five different NC sizes are shown. In each case, a Raman peak at 339cm^{-1} is

detected. The location of this peak matches that expected from bulk CZTS (338cm^{-1}). For shorter reaction times, Raman peaks at 472cm^{-1} and 315cm^{-1} are observed, which match the position of peaks you would expect for bulk Cu_2S (473cm^{-1}) and SnS_2 (310cm^{-1}) respectively. The observed peak widths are larger than those typically observed in bulk CZTS however, broadening of Raman peaks is widely reported in the literature for NCs and is primarily attributed to phonon confinement within the NCs volume. The apparent narrowing of the predominant CZTS peak with increasing reaction time is also concurrent with the increase in the NC size. In principle, this phenomenon could mask the presence of ZnS and SnS_2 Raman peaks. However, annealed films of these NCs produced a single sharp peak at 339 cm^{-1} with no detectable Raman scattering at the frequencies expected for ZnS or SnS_2 (see Chapter 6). Figure 5.3-3 plots the absorption spectra of the NCs nucleated at 140°C for 20 seconds, 30 minutes, 1 hour, 2 hours and 4 hours, which further shows a diminishing of the plasmonic absorbance as the Cu_2S starting phase is expelled, leading to a typical absorbance spectrum for a tetragonal CZTS semiconductor. The band gap of the pure CZTS is measured to be 1.52eV which is close to the value for tetragonal CZTS NCs reported in Chapter 4 previously.

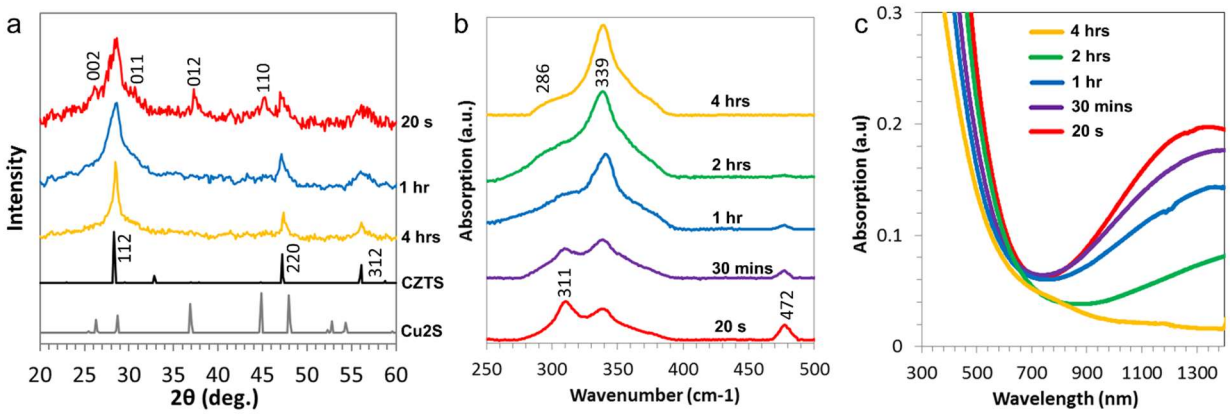

Figure 5.3-3 a) XRD traces of NCs aged for 20s, 1hr and 4hrs. The reference powder XRD patterns are that of the CZTS Kesterite structure (JCPDS 01-075-4122) and high chalcocite Cu_2S (JCPDS 00-046-1195). b) Raman spectra and c) UV-VIS absorption spectra of NC samples aged for 20s, 30mins, 1hr, 2hrs and 4hrs.

Discernible X-ray diffraction peaks resulting from Cu_2S are observed in Figure 5.3-3a from the NC sample taken at the beginning of the reaction (20 seconds), which confirms that Cu_2S is present in the starting phase. After a prolonged period of ageing, the Cu_2S-CZTS starting phase tends to diminish as indicated by the decreased diffraction intensity of Cu_2S peaks in the XRD pattern shown in Figure 5.3-3a. Specifically, increasing the reaction time beyond 1 hour reduces the intensity of the (002), (012) and (110) so that it can no longer be seen in the XRD trace. In addition, the NC sizes extracted from the width of the (112) diffraction peak at 28.5° using the Debye-Scherrer equation range from 6 (±1.3)nm to 24(±0.9)nm, with increased reaction time, which is in agreement with the TEM size distribution analysis.

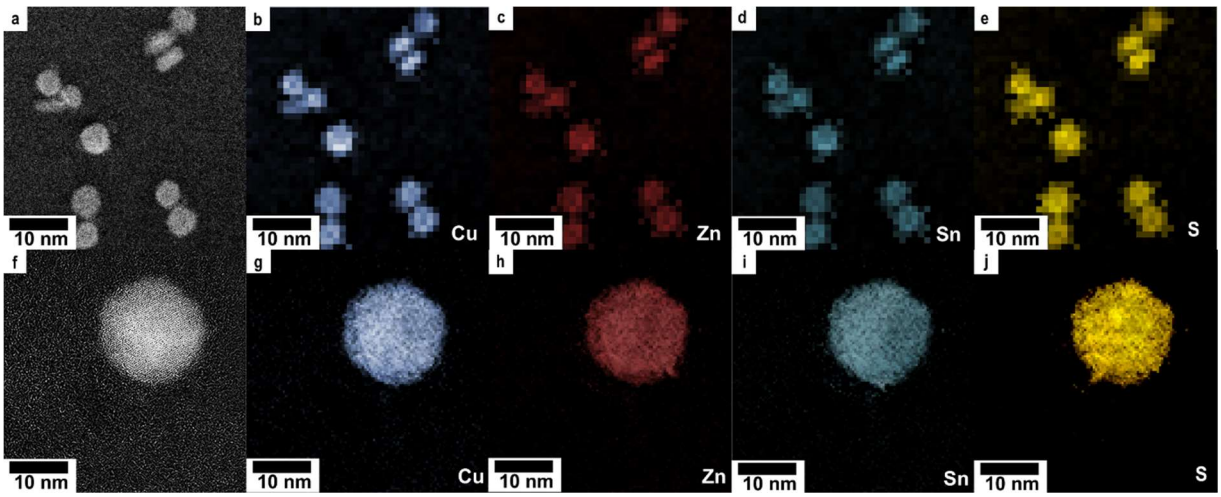

Figure 5.3-4 High angle annular dark field (HAADF) STEM image and STEM-EDX elemental mapping micrographs identifying the presence of Sn, Cu, Zn and S in CZTS NCs, nucleated at 140°C and aged at that temperature for a-e)20s and f-j) 4hrs.

To confirm whether all four constituent elements are uniformly present in both the Cu_2S-CZTS NCs and the CZTS NCs, STEM EDX mapping, with nanoscale resolution, was performed on NC samples taken after 20s (a-e) and 4hrs (f-j). Each of the set of images shown in Figure 5.3-4 show an HAADF-STEM image (a/f) and a corresponding set of STEM EDX elemental mappings of Cu, Zn, Sn and S respectively (g-i/b-e). Each of the constituent elements appear to be homogeneously distributed across the NCs of both samples. This suggests that the NCs have a uniform composition. All four constituent elements are also present in each of the NCs shown, suggesting that, at least in the area of the TEM grid under investigation.

In order to estimate the relative elemental composition of each NC sample, EDX spectra from each of corresponding STEM-EDX maps shown in Figure 5.3-4 were further analysed using the standard-less Cliff-Lorimer approximation [35]. Each of the spectra shown in Figure 5.3-5, corresponding to CZTS NCs nucleated at 140°C and aged at that temperature for 20s and 4hrs, show a number of strong X-ray emission peaks, corresponding to Cu-Kα (0.93keV), Zn-Lα (1.012), Sn-Lα (3.44keV)

and S-Kα (2.31keV). The area under the experimental peaks were analysed according to the Cliff-Lorimer method, the results of which are shown in Table 5.3-1.

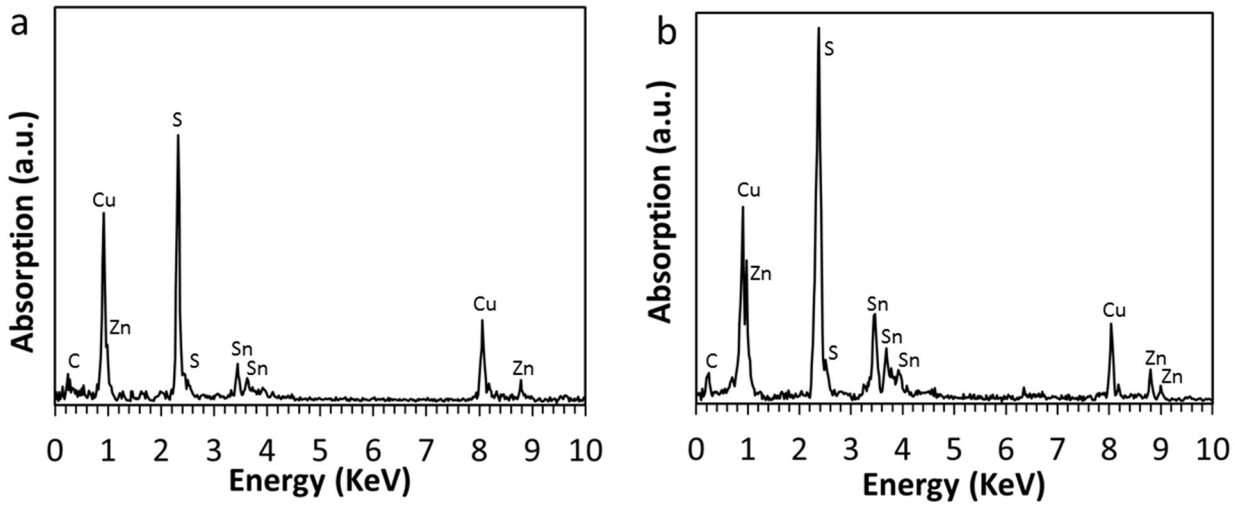

Figure 5.3-5 Energy dispersive X-ray spectra for nanocrystals nucleated at 140°C and aged at that temperature for a)20s and b) 4hrs (corresponding to the STEM-EDX micrographs shown in Figure 5.3-4(a-e) and (f-j) respectively).

The atomic ratios shown in Table 5.3-1 suggests that neither composition of the NC samples is stoichiometric Cu_2ZnSnS_4. However, the NCs aged for 20s show a significant deficiency of Zn, Sn and S. The lower sulphur concentration could be representative of the dominant Cu_2S structure within the Cu_2S-CZTS NCs, while the lower Sn and Zn concentration is likely to represent the incomplete inter-diffusion of Sn and Zn into the NC structure. The pure CZTS NCs appear to be close to 2:1:1:4 which corresponds well with the elemental ratio of CZTS. As with the NCs synthesised in Chapter 4, the σ- weight% for each of the respective elements of each NC sample, indicate a significant deviation within the statistical data [40]. However, it would appear that the respective ratio of Cu:Zn:Sn:S for the NC sample aged for 4hrs is consistent with the characteristic ratios of kesterite and wurtzite CZTS NC formations that have been reported in the literature[41], [42].

Notably the sulphur deficiency highlighted in the OLA single ligand synthesis (Chapter 4) is also present here, which suggests that OA plays no more of a beneficial role in stabilising the sulphur atoms on the surface of the CZTS NCs than when using OLA on its own.

Table 5.3-1 Cliff-Lorimer analysis of the relative elemental composition of the CZTS NCs nucleated at 140°C and aged at that temperature for 0s and 4hrs, identifying the weight% and atomic% of the constituent elements (Cu, Zn, Sn and S) for each sample, calculated from the respective EDX spectra shown in Figure 5.3-5.

Ageing Time	Element	Weight%	σ - Weight%	Atomic%	Ratio
20s	Cu	39.76	0.71	34.60	2.00
	Sn	22.55	0.72	10.50	0.61
	Zn	11.55	0.96	9.76	0.56
	S	26.14	0.83	45.14	2.61
4hrs	Cu	32.72	0.46	27.60	2.00
	Sn	24.36	0.0	10.99	0.80
	Zn	12.20	0.91	9.99	0.72
	S	30.72	0.65	51.41	3.73

Thus we conclude that through the extended growth of Cu_2S seeds, NCs of highly crystalline and pure kesterite-CZTS are produced without the presence of other sulphide phases. Oleic acid has been successfully incorporated in to the synthesis to allow simple solution cleaning of the NCs with polar solvents without a detrimental drop in yield. However, the reaction time required to perform this transformation results in excessive Ostwald ripening leading to a broad size distribution upon transformation in to pure CZTS. Size inhomogeneity is not conducive to semiconductor thin film formation, and the size distribution shown here is too large

to sustain a stable colloid for processing layer by layer NC devices. The next step is to investigate using a lower nucleation temperature to encourage supersaturation to create a higher concentration of nuclei and a more homogeneous NC colloid.

5.3.1 Low Temperature Injection and Growth

The strategy we now adopt is to use a lower reaction temperature to stimulate more seed nuclei followed by a steady ramping of the reaction temperature to the point at which there is transformation from Cu_2S-CZTS to kesterite CZTS. In doing so it is hypothesised that pure CZTS NCs with a smaller size distribution, more suited to NC solar cell solution fabrication can be achieved. To validate this strategy, the reaction parameters and preparation outlined in the previous experiment were maintained, including the decomposition of reaction precursors in a reaction solution made up of a ratio of 5:1 ligand ratio of OLA: OA. However, in this instance, after decomposition of the metal precursors at 140°C, the temperature of the reaction vessel was rapidly reduced to 35°C using an ice bath at which point the TMSS precursor solution was quickly injected. The now nucleated NC solution was quickly returned to the heating mantle and the temperature gently ramped up to 135°C at a rate of ~2°C/min. Aliquots were taken at 45°C, 65°C, 90°C, 115°C and 135°C (corresponding to approximately 5mins, 15mins, 30mins, 40mins and 1hr of reaction time), and once cleaned each sample was again characterised using TEM, HRTEM, XRD, UVVIS and STEM-EDX in order to analyse whether such a strategy was capable of producing pure CZTS NCs with a more favourable size distribution.

Figure 5.3-6 shows a plot of the absorption spectra taken from a sample of NCs nucleated at 35°C and quenched at 45°C, 65°C, 90°C, 115°C and 135°C. As with the

previous experiment, the LSPR peak is shown to diminish as the reaction proceeds with increasing temperature, as the Cu_2S starting phase is expelled from the NC, leading to a typical absorbance spectrum for a tetragonal CZTS semiconductor. The band gap of the pure CZTS is measured to be 1.53eV which is consistent with the values previously obtained for tetragonal CZTS NCs in this study.

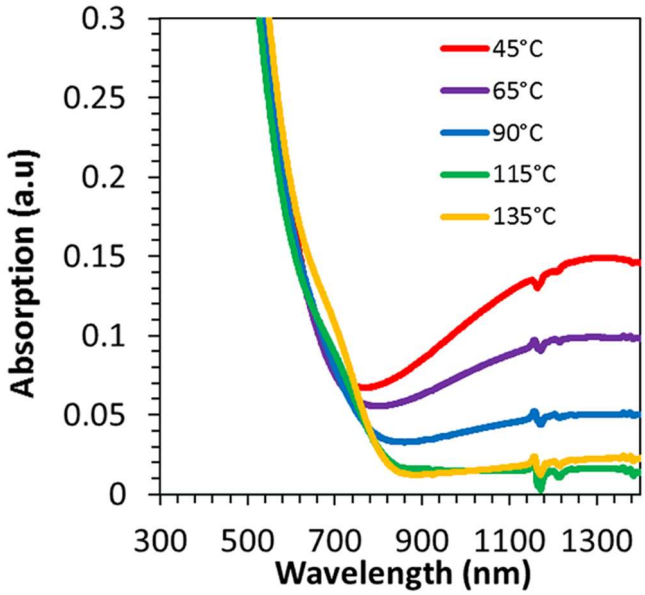

Figure 5.3-6 UV-VIS absorption spectra of NC samples quenched at 45°C, 65°C, 90°C, 115°C and 135°C.

Figure 5.3-7 shows the corresponding TEM images of the NCs nucleated at 35°C and quenched at 45°C, 90°C and 135°C. A numerical analysis of the change in NC diameter with reaction temperature is shown in Figure 5.3-8. The NCs quenched at 35°C appear pseudo-spheroidal, with an average diameter of ~4.5 ±0.5nm with a moderate size distribution (8.6%). As the reaction proceeds and the temperature is increased, the NCs appear to grow modestly (to ~6 ±0.5nm) and develop a distinctly faceted morphology. Unlike with the higher temperature reaction, both the average size and the relative size distribution remains relatively small with increasing temperature, rising only to ~11%. Which may account for the increased solution

stability exhibited by the NCs synthesised by this method. It should also prove beneficial for NC solution processing and thin film device fabrication.

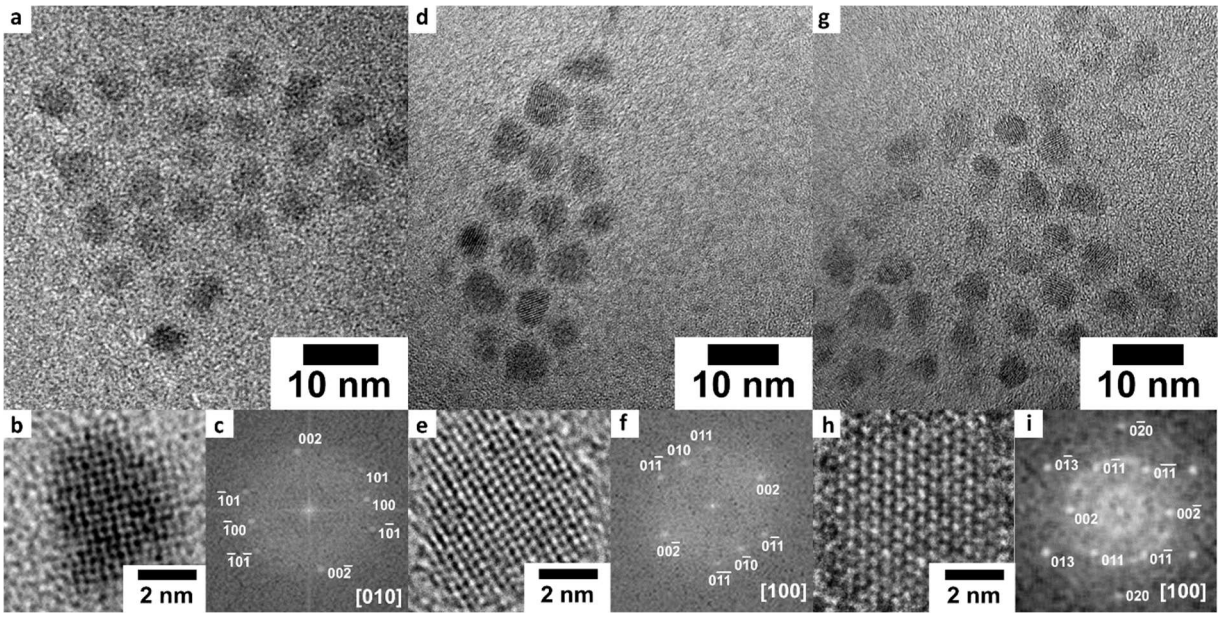

Figure 5.3-7 (a, d+g) TEM micrographs, inset with (b, e+h) HTEM micrographs and (c, f+i) FFTs of CZTS NCs nucleated at 35°C and quenched at a-c) 45°C, d-f) 90°C and g-i) 135°C.

The inset in Figure 5.3-7h shows the high resolution TEM (HRTEM) image of CZTS with the lattice fringe of the (002) and (011) planes, which suggests the presence of a single crystalline structure and high crystallinity of the CZTS NCs. The single crystals shown in Figure 5.3-7b+e HRTEM micrographs also appear to be single crystalline NCs however, the predominant crystal structure is analogous to that of Cu_2S, and can be indexed along the [010] and [100] lattice directions respectively. Notably the transformation of the NCs from Cu_2S-CZTS to pure CZTS is complete after a 1hr despite a lower average reaction temperature, compared with NCs nucleated at 140°C. This may be facilitated by the smaller average NC size, which may promote the inter-diffusion and re-ordering of the metal cation species.

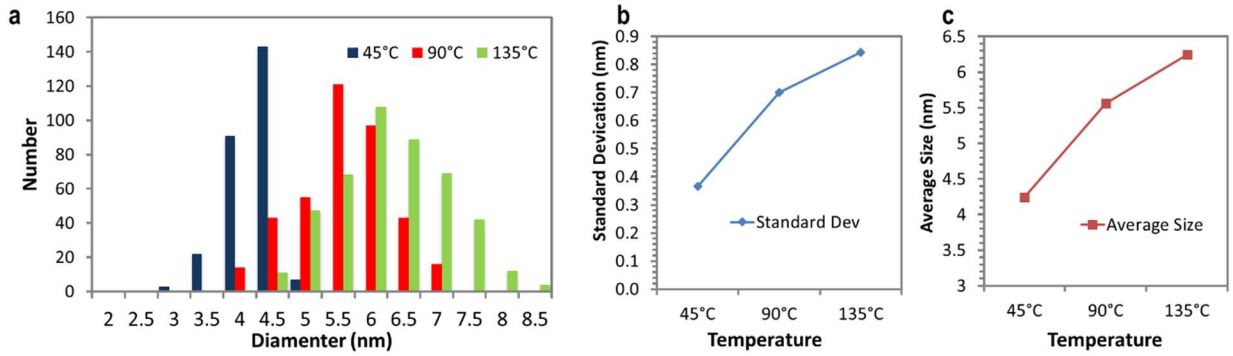

Figure 5.3-8 a) Size distribution, b) standard deviation and c) average (mean) particle size analysis of CZTS NCs nucleated at 35°C and quenched at 45°C, 90°C and 135°C, taken from low resolution TEM micrographs.

To confirm whether all four elements are uniformly present within both the Cu_2S-CZTS NCs and the CZTS NCs, STEM EDX mapping was performed on NC samples nucleated at 35°C and quenched at 45°C (a-e) and 135°C (f-j). Each set of images, shown in Figure 5.3-9, shows an HAADF-STEM image with a corresponding set of STEM EDX elemental mappings for Cu, Zn, Sn and S respectively.

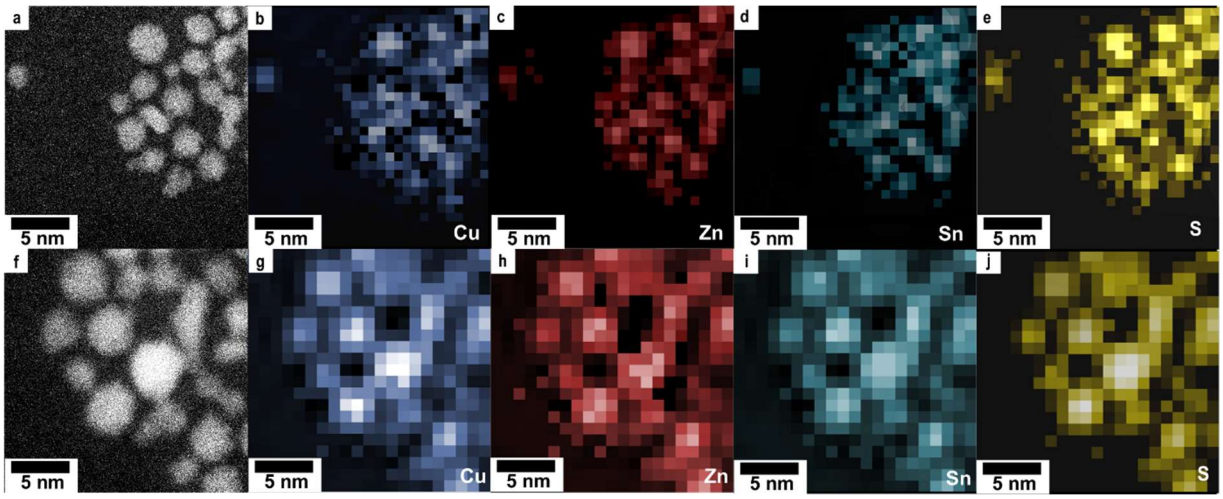

Figure 5.3-9 High angle annular dark field (HAADF) STEM image and STEM-EDX elemental mapping micrographs identifying the presence of Sn, Cu, Zn and S in CZTS NCs, nucleated at 35°C and quenched at a-e)45°C and f-j) 135°C.

All four constituent elements are seen to be present in each of the NCs shown, suggesting that, at least in the area of the TEM grid under investigation. Each of the

570 constituent elements also appear to be homogeneously distributed across the NCs of both samples. Thus implying that the NCs have a uniform composition.

In order to estimate the relative elemental composition of each NC sample, EDX spectra from each of corresponding STEM-EDX maps shown in Figure 5.3-9 were further analysed using the Cliff-Lorimer approximation [43]. Each of the spectra shown in Figure 5.3-10, corresponding to CZTS NCs nucleated at 35°C and quenched at a)45°C and b) 135°C, show a number of strong X-ray emission peaks, corresponding to Cu-K (8.04keV), Cu-L (0.93keV), Zn-L (1.012), Sn-L (3.44keV) and S-K (2.31keV).

The area under the peaks corresponding to Cu-L, Zn-L, Sn-L and S-K were each
580 analysed according to the standard-less Cliff-Lorimer method, of which the results are shown in Table 5.3-2. The NCs quenched at 45°C show a small yet significant deficiency of Zn, Sn and S while the “pure CZTS NCs” (shown in Figure 5.3-9(g-j)) appear to exhibit an atomic ratio that is closer to 2:1:1:4, which corresponds to the prescribed elemental ratio of CZTS.

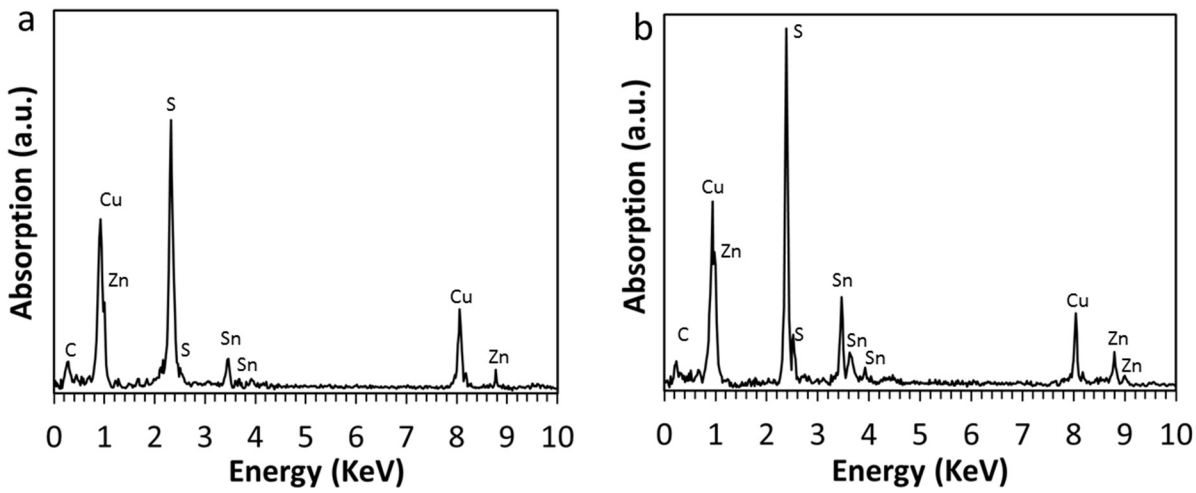

Figure 5.3-10 Energy dispersive X-ray spectra for nanocrystals nucleated at nucleated at nucleated at 35°C and quenched at a)45°C and b) 135°C (corresponding to the STEM-EDX micrographs shown in Figure 5.3-9(a-e) and (f-j) respectively).

This is consistent with the STEM-EDX analysis of the CZTS NCs aged at 140°C and indicates that the growth and development of each set of NCs proceeds in a similar fashion.

Table 5.3-2 Cliff-Lorimer analysis of the relative elemental composition of the CZTS NCs nucleated 35°C and quenched at 45°C and 135°, identifying the weight% and atomic% of the constituent elements (Cu, Zn, Sn and S) for each sample- calculated from the respective EDX spectra (shown in Figure 5.3-10).

Quench Temp.	Element	Weight%	σ - Weight%	Atomic%	Ratio
35°C	Cu	40.23	0.98	35.11	2.00
	Sn	22.16	2.34	10.35	0.59
	Zn	11.98	1.58	10.15	0.58
	S	25.64	0.83	44.40	2.53
135°C	Cu	29.60	0.80	25.57	2.00
	Sn	27.95	1.09	12.92	1.01
	Zn	12.89	0.77	10.81	0.85
	S	29.56	0.91	50.69	3.96

The challenge of balancing the reactivity among all of the cation precursors in order to avoid a second phase or composition non-uniformity can be overcome when preparing multi-component NCs through the formation of homogeneous nuclei by a single cation. In this study, the nucleation is well controlled by the preferentially formed Cu_2S NCs with near mono-dispersity. This starting phase is completely expelled and transformed to pure CZTS due to the extremely high mobility of the cations thereby enabling highly effective cation inter-diffusion. By conducting the injection at very low temperatures and controlling the inter-diffusion by slowly increasing the reaction temperature, the same pure CZTS NCs with good size uniformity can be achieved while using a two ligand protocol that enables post reaction cleaning to take place in ambient environment. The next step on the path

towards semiconducting thin films is exchanging ligands to shorter ones which allow electronic coupling.

5.4 Ligand substitution

Electrical transport in closely assembled NC solids is highly dependent on NC surface functionalization[44]–[47]. Long-chained organic capping agents like OLA suppress effective inter-particle coupling and lead to high tunnelling barriers for electrons and thus insulating behaviour of the materials. Reduced inter-particle distance improves particle coupling and hence charge transport in NC assemblies. This has been shown by Stolle et al. who compare the performance of Au/CIS/ZnO/ITO devices with and without the presence of oleylamine[48]. The method of exchanging long chained capping ligands with pyridine by extended reflux reaction was first reported by Alivisatos et al. The more weakly adherent but more abundant pyridine molecules displace the capping ligands by mass action[49] (illustrated in Figure 5.4-1). Owing to its inherently weaker energy of adhesion with the NC surface, pyridine has been shown to dynamically solvate chalcogenide NCs at room temperature.

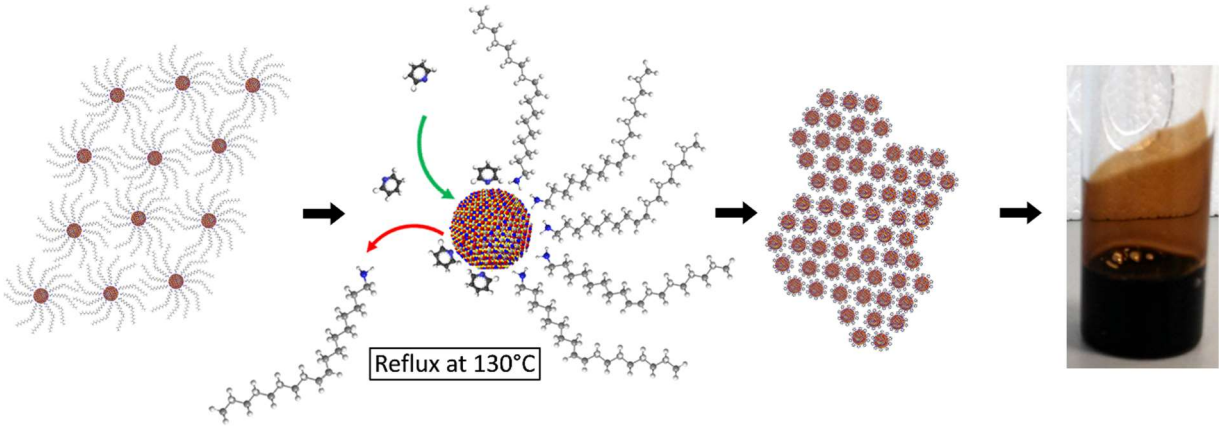

Figure 5.4-1 Illustration of a CZTS NC ligand exchange reaction at 130°C. Removal of long chain oleylamine ligands are replaced with much smaller heterocyclic pyridine molecules, resulting in

a significant reduction in the inter-particle distance. The NC ink following ligand substitution appeared stable and could readily coat the inside of a glass vial when agitated.

As-synthesized NCs are capped with oleylamine and oleic acid ligands as evidenced from FTIR data presented in Figure 5.4-2. The presence of long alkyl-chain ligands on the NC surface prevents the close packing of the NCs and increases the film's porosity. In addition, annealing NC films containing long chain carbon ligands may lead to residual carbon in the annealed film, thereby affecting the device performance.

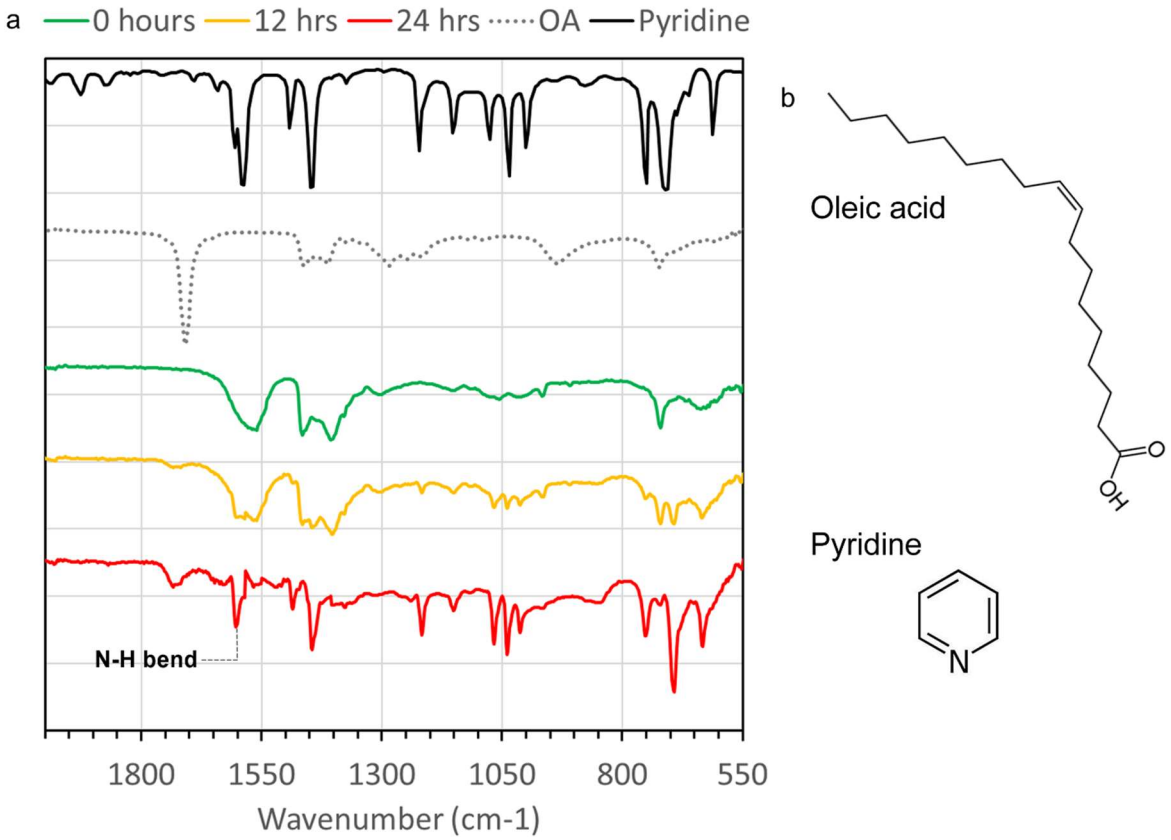

Figure 5.4-2 FTIR spectra of refluxed CZTS NCs in pyridine following 0, 12 and 24hrs. Individual FTIR spectra have been offset for clarity. b) Schematic representations of oleic acid and pyridine.

To remove the oleylamine and oleic acid ligands from the NC surface, we explored the possibility of exchanging them with pyridine using a technique first established by Alivisatos et. al[49] for CdSe NCs. CZTS-hexane solutions were

precipitated with ethanol, gently dried with a flow of argon gas and then redispersed in excess anhydrous pyridine. This solution was then refluxed in an argon atmosphere for many hours at 120°C. Aliquots were taken at regular intervals, precipitated with hexane and redispersed in pyridine to be stored. Each sample was left under ambient conditions and periodically monitored to determine how well the CZTS NCs were solvated. NCs that had been refluxed for <1hr would crash out of solution after only a few minutes while those that had been refluxed for 12hrs would crash out after several hours. Those NCs that were refluxed for >24hrs formed a stable solution for several days in ambient conditions and could be safely stored in a nitrogen glovebox for several months. Due to the volatile nature of pyridine, FTIR samples were prepared by drop casting aliquots of the refluxed solution onto silicon wafers. Each sample was left in ambient conditions inside a fume hood to allow the excess pyridine to evaporate before being transferred to the spectrometer. The prevalence of the major bonding groups associated with OA, OLA and pyridine, before and after 24hr of pyridine reflux, are outlined in Table 5.4-1. Evidence of OA and OLA after 12hrs of reflux is still present in the FTIR spectra however, the characteristic C=O, C-O and O-H vibrations of OA are significantly reduced after 24hrs. Conversely there is little evidence for the presence of pyridine early on in the exchange reaction but after 24hrs it appears to be particularly prominent in the drop cast NC films.

Table 5.4-1 Indexed FTIR peaks visible in Figure 5.4-2.

Band (cm^{-1})	***Group***	***After Reflux***
1650-1580	N-H bend	Present
1550-1350	Aromatic C=C bend	Present
1335-1250	C-N stretch	Present
1150-900	In plane C-H bend	Present
810-725	N-H wag	Present
750-650	Out of plane C-H bend	Present
1750-1735	C=O stretch	Reduced
1440-1395	C-H scissor	Reduced
1350-1050	C-O stretch	Reduced
950-910	O-H bend	Reduced
800-740	C-H rock	Reduced

This would suggest that the carboxylic acid bonded OA ligands are successfully substituted with aromatic-amine bonded pyridine ligands after 24hrs of gentle reflux,

5.5 Conclusions

In summary, a simple one-pot heating synthesis strategy for preparing CZTS NCs is demonstrated herein. High quality CZTS NCs with high crystallinity, single phase, uniform spatial composition and uniform size distribution are obtained. The NC formation mechanism for the nucleation, growth and cation inter-diffusion is explored. This distinctive mechanism enables non-discriminative selection of zinc and tin precursors without the complicated control of cation reactivity. In doing so, the present work extends the current knowledge of multi-component NC chemical synthesis, which can be now be scaled up for practical applications.

5.6 References

[1] A. Stavrinadis, J. M. Smith, C. a Cattley, A. G. Cook, P. S. Grant, and A. a R. Watt, "SnS/PbS nanocrystal heterojunction photovoltaics.," *Nanotechnology*, vol. 21, no. 18, p. 185202, May 2010.

[2] S. a McDonald, G. Konstantatos, S. Zhang, P. W. Cyr, E. J. D. Klem, L. Levina, and E. H. Sargent, "Solution-processed PbS quantum dot infrared photodetectors and photovoltaics.," *Nat. Mater.*, vol. 4, no. 2, pp. 138–142, 2005.

[3] C. R. Bealing, W. J. Baumgardner, J. J. Choi, T. Hanrath, and R. G. Hennig, "Predicting nanocrystal shape through consideration of surface-ligand interactions," *ACS Nano*, vol. 6, no. 3, pp. 2118–2127, Mar. 2012.

[4] N. Wu, L. Fu, M. Su, M. Aslam, K. C. Wong, and V. P. Dravid, "Interaction of Fatty Acid Monolayers with Cobalt Nanoparticles," *Nano Lett.*, vol. 4, no. 2, pp. 383–386, 2004.

[5] S. Chen and W. Liu, "Oleic acid capped PbS nanoparticles: Synthesis, characterization and tribological properties," *Mater. Chem. Phys.*, vol. 98, no. 1, pp. 183–189, 2006.

[6] J. Y. Rempel, M. G. Bawendi, and K. F. Jensen, "Insights into the kinetics of semiconductor nanocrystal nucleation and growth," *J. Am. Chem. Soc.*, vol. 131, no. 12, pp. 4479–4489, Apr. 2009.

[7] A. Khare, A. W. Wills, L. M. Ammerman, D. J. Norris, and E. S. Aydil, "Size control and quantum confinement in Cu2ZnSnS4 nanocrystals," *Chem. Commun.*, vol. 47, no. 42, p. 11721-11723, 2011.

[8] J. M. Luther, M. Law, M. C. Beard, Q. Song, M. O. Reese, R. J. Ellingson, and A. J. Nozik, "Schottky solar cells based on colloidal nanocrystal films," *Nano Lett.*, vol. 8, no. 10, pp. 3488–3492, 2008.

[9] E. H. Sargent, "Infrared photovoltaics made by solution processing," *Nat. Photonics*, vol. 3, no. 6, pp. 325–331, 2009.

[10] J.-Y. Chang and C.-Y. Cheng, "Facile one-pot synthesis of copper sulfide-metal chalcogenide anisotropic heteronanostructures in a noncoordinating solvent.," *Chem. Commun. (Camb).*, vol. 47, no. 32, pp. 9089–9091, Aug. 2011.

[11] W. U. Huynh, J. J. Dittmer, and A. P. Alivisatos, "Hybrid Nanorod-Polymer Solar Cells," *Science (80-.).*, vol. 295, no. 5564, pp. 2425–2427, 2002.

[12] C. a Cattley, A. Stavrinadis, R. Beal, J. Moghal, A. G. Cook, P. S. Grant, J. M. Smith, H. Assender, and A. a R. Watt, "Colloidal synthesis of lead oxide nanocrystals for photovoltaics.," *Chem. Commun. (Camb).*, vol. 46, no. 16, pp. 2802–2804, Apr. 2010.

[13] B. Zhou, D. Xia, and Y. Wang, "Phase-selective synthesis and formation mechanism of CZTS nanocrystals," *RSC Adv.*, vol. 5, no. 86, pp. 70117–70126, Aug. 2015.

[14] C. B. Murray, C. R. Kagan, and M. G. Bawendi, "Synthesis and charaterization of monodisperse nanocrystals and close-packes nanocrystal assemblies," *Annu. Rev. Mater. Sci.*, vol. 30, no. 1, pp. 545–610, 2000.

[15] Y. Zou, X. Su, and J. Jiang, "Phase-controlled synthesis of Cu2ZnSnS4 nanocrystals: the role of reactivity between Zn and S.," *J. Am. Chem. Soc.*, vol. 135, no. 49, pp. 18377–84, Dec. 2013.

[16] A. Shavel, J. Arbiol, and A. Cabot, "Synthesis of Quaternary Chalcogenide Nanocrystals: Stannite Cu2Zn x Sn y Se1+ x+ 2 y," *J. Am. Chem.*, vol. 132, no. Figure 2, pp. 4514–4515, 2010.

[17] Y. Zhao, H. Pan, Y. Lou, X. Qiu, J. Zhu, and C. Burda, "Plasmonic Cu 2-xS nanocrystals: Optical and structural properties of copper-deficient copper(I) sulfides," *J. Am. Chem. Soc.*, vol. 131, no. 12, pp. 4253–4261, Apr. 2009.

[18] S.-H. H. Wei, Q. Xu, B. Huang, Y. Zhao, Y. Yan, and R. Noufi, "Stability and electronic structures of CuxS solar cell absorbers," in *Conference Record of the IEEE Photovoltaic Specialists Conference*, 2012, pp. 118–120.

[19] S. Mourdikoudis and L. M. Liz-Marzán, "Oleylamine in nanoparticle synthesis," *Chem. Mater.*, vol. 25, no. 9, pp. 1465–1476, 2013.

[20] Y. Yin and a P. Alivisatos, "Colloidal nanocrystal synthesis and the organic-inorganic interface.," *Nature*, vol. 437, no. 7059, pp. 664–670, 2005.

[21] J. S. Owen, J. Park, P. Trudeau, and a P. Alivisatos, "Reaction Chemistry and Ligand Exchange at Cadmium - Selenide Nanocrystal Surfaces," *J. Am. Chem. Soc.*, vol. 130, no. 37, pp. 12279–12281, 2008.

[22] S. G. Kwon and T. Hyeon, "Formation mechanisms of uniform nanocrystals via hot-injection and heat-up methods," *Small*, vol. 7, no. 19, pp. 2685–2702, Aug. 2011.

[23] K. Manthiram and a. P. Alivisatos, "Tunable localized surface plasmon resonances in tungsten oxide nanocrystals," *J. Am. Chem. Soc.*, vol. 134, no. 9, pp. 3995–3998, Mar. 2012.

[24] S.-W. Hsu, K. On, and A. R. Tao, "Localized surface plasmon resonances of anisotropic semiconductor nanocrystals.," *J. Am. Chem. Soc.*, vol. 133, no. 47, pp. 19072–5, Nov. 2011.

[25] J. M. Luther, P. K. Jain, T. Ewers, and a P. Alivisatos, "Localized surface plasmon resonances arising from free carriers in doped quantum dots.," *Nat. Mater.*, vol. 10, no. 5, pp. 361–366, May 2011.

[26] Y. Xie, L. Carbone, C. Nobile, V. Grillo, S. D'Agostino, F. Della Sala, C. Giannini, D. Altamura, C. Oelsner, C. Kryschi, and P. D. Cozzoli, "Metallic-like stoichiometric copper sulfide nanocrystals: Phase- and shape-selective synthesis, near-infrared surface plasmon resonance properties, and their modeling," *ACS Nano*, vol. 7, no. 8, pp. 7352–7369, 2013.

[27] J. a. Scholl, A. L. Koh, and J. a. Dionne, "Quantum plasmon resonances of individual metallic nanoparticles," *Nature*, vol. 483, no. 7390, pp. 421–427, Mar. 2012.

[28] V. Dzhagan, I. Lokteva, C. Himcinschi, X. Jin, J. Kolny-Olesiak, and D. R. Zahn, "Phonon Raman spectra of colloidal CdTe nanocrystals: effect of size, non-stoichiometry and ligand exchange.," *Nanoscale Res. Lett.*, vol. 6, no. 1, p. 79, Jan. 2011.

[29] I. Grozdanov and M. Najdoski, "Optical and Electrical Properties of Copper Sulfide Films of Variable Composition," *J. Solid State Chem.*, vol. 114, no. 2, pp. 469–475, 1995.

[30] a. Putnis, “The transformation behaviour of cuprous sulphides and its application to the efficiency of Cu x S–CdS solar cells,” *Philos. Mag.*, vol. 34, no. 6, pp. 1083–1086, Dec. 1976.

[31] S. Gupta, Y. Batra, B. R. Mehta, and V. R. Satsangi, “Study of charge separation and interface formation in a single nanorod CdS-Cu(x)S heterojunction solar cell using Kelvin probe force microscopy.,” *Nanotechnology*, vol. 24, no. 25, p. 255703, 2013.

[32] C. Surface, A. J. Morris-cohen, V. Vasilenko, V. a Amin, M. G. Reuter, and E. a Weiss, “Model for Adsorption of Ligands to Colloidal Quantum Dots with Structure,” *ACS Nano*, vol. 6, no. 1, pp. 557–565, 2012.

[33] M. Green, “The nature of quantum dot capping ligands,” *J. Mater. Chem.*, vol. 20, no. 28, p. 5797, 2010.

[34] C. De Mello Donegá, P. Liljeroth, and D. Vanmaekelbergh, “Physicochemical evaluation of the hot-injection method, a synthesis route for monodisperse nanocrystals,” *Small*, vol. 1, no. 12, pp. 1152–1162, Dec. 2005.

[35] D. V. Talapin, J. S. Lee, M. V. Kovalenko, and E. V. Shevchenko, “Prospects of colloidal nanocrystals for electronic and optoelectronic applications,” *Chem. Rev.*, vol. 110, no. 1, pp. 389–458, Jan. 2010.

[36] H.-C. Liao, M.-H. Jao, J. J. Shyue, Y.-F. Chen, and W.-F. Su, “Facile synthesis of wurtzite copper–zinc–tin sulfide nanocrystals from plasmonic djurleite nuclei,” *J. Mater. Chem. A*, vol. 1, no. 2, p. 337, 2013.

[37] S. Chen, A. Walsh, Y. Luo, J. H. Yang, X. G. Gong, and S. H. Wei, “Wurtzite-derived polytypes of kesterite and stannite quaternary chalcogenide semiconductors,” *Phys. Rev. B - Condens. Matter Mater. Phys.*, vol. 82, no. 19, pp. 1–8, Nov. 2010.

[38] C. Burda, X. Chen, R. Narayanan, and M. a. El-Sayed, *Chemistry and properties of nanocrystals of different shapes*, vol. 105, no. 4. pp. 7-12 2005.

[39] R. Guo, Y. Song, G. Wang, and R. W. Murray, “Does core size matter in the kinetics of ligand exchanges of monolayer-protected Au clusters?,” *J. Am. Chem. Soc.*, vol. 127, no. 8, pp. 2752–2757, Mar. 2005.

[40] M. Watanabe and D. B. Williams, “The quantitative analysis of thin specimens: A review of progress from the Cliff-Lorimer to the new ζ-factor methods,” *J. Microsc.*, vol. 221, no. 2, pp. 89–109, 2006.

[41] M. Edler, T. Rath, A. Schenk, A. Fischereder, W. Haas, M. Edler, B. Chernev, B. Kunert, F. Hofer, R. Resel, and G. Trimmel, “Copper zinc tin sulfide layers prepared from solution processable metal dithiocarbamate precursors,” *Mater. Chem. Phys.*, vol. 136, no. 2–3, pp. 582–588, Oct. 2012.

[42] T. Rath, W. Haas, A. Pein, R. Saf, E. Maier, B. Kunert, F. Hofer, R. Resel, and G. Trimmel, “Synthesis and characterization of copper zinc tin chalcogenide nanoparticles: Influence of reactants on the chemical composition,” *Sol. Energy Mater. Sol. Cells*, vol. 101, pp. 87–94, 2012.

[43] G. Lorimer, “Quantitative X-ray microanalysis of thin specimens in the transmission electron microscope; a review,” *Mineral. Mag.*, vol. 51, no. 359, pp. 49–60, 1987.

[44] M. Law, J. M. Luther, Q. Song, B. K. Hughes, C. L. Perkins, and A. J. Nozik, "Structural, optical, and electrical properties of PbSe nanocrystal solids treated thermally or with simple amines," *J. Am. Chem. Soc.*, vol. 130, no. 18, pp. 5974–5985, 2008.

[45] A. Nag, M. V. Kovalenko, J. S. Lee, W. Liu, B. Spokoyny, and D. V. Talapin, "Metal-free inorganic ligands for colloidal nanocrystals: S2-, HS-, Se2-, HSe-, Te2-, HTe -, TeS3 2-, OH-, and NH 2 - as surface ligands," *J. Am. Chem. Soc.*, vol. 133, no. 27, pp. 10612–10620, Jul. 2011.

[46] P. Nagpal and V. I. Klimov, "Role of mid-gap states in charge transport and photoconductivity in semiconductor nanocrystal films," *Nat. Commun.*, vol. 2, p. 486-493, Sep. 2011.

[47] A. Zabet-Khosousi and A. A. Dhirani, "Charge transport in nanoparticle assemblies.," *Chem. Rev.*, vol. 108, no. 10, pp. 4072–4124, Oct. 2008.

[48] C. Stolle Jackson, M. G. Panthani, T. B. Harvey, V. a. Akhavan, and B. A. Korgel, "Comparison of the photovoltaic response of oleylamine and inorganic ligand-capped CuInSe 2 nanocrystals," *ACS Appl. Mater. Interfaces*, vol. 4, no. 5, pp. 2757–2761, May 2012.

[49] X. Peng, M. C. Schlamp, A. V Kadavanich, and a P. Alivisatos, "Epitaxial Growth of Highly Luminescent CdSe / CdS Core / Shell Nanocrystals with Photostability and Electronic Accessibility," *J. Am. Chem. Soc.*, vol. 7863, no. 25, pp. 7019–7029, 1997.

Chapter 6- Low Temperature Processed CZTS Photovoltaics

"An expert is a person who has made all the mistakes that can be made in a very narrow field" – Niels Bohr

6.1 Solution Processed CZTS Devices

In 2014, a report from researchers at IBM outlined a liquid-based process for the deposition of CZTS/Se absorber layers, which utilised a hybrid hydrazine-based slurry method[1]. The resulting devices exhibited device efficiencies of 12.6%, exceeding the previous kesterite performance record by ~15%. This method to make quaternary chalcogenide solar cells requires a high temperature anneal (>500°C) in a sulphur or selenium environment [2], [3]. This chapter seeks to find a low temperature processing route to CZTS.

The purpose of the anneal is to prevent the loss of sulphur and tin, promote grain growth and passivates dangling bonds at grain boundaries[2]–[6]. However, high temperature sulphurization/selenization is cumbersome and potentially dangerous, especially when using H_2S or H_2Se gas as the sulphur source[7]–[10].

Low temperature copper chalcogenide based NC solar cell fabrication has not been extensively studied in the literature due to its inherent instability; particularly with regard to observed oxidation of the NC surface and the stripping of reaction ligands during solution processing under ambient conditions[11]. Despite this, the field of low temperature CZTS thin film fabrication has had something of a resurgence through a better understanding of copper's complex chemistries[12]–[16].

Table 6.1-1 outlines some of the key technical characteristics of a number of CZTS based devices that have been produced using a variety of different fabrication techniques and materials. Although some of these methods incorporate a solution processing step in their device fabrication, all require at least one high temperature (>500 °C) annealing step in order to form the CZTS/Se photoactive semiconductor layer. Furthermore, each of the fabrication methods requires at least one of the processing steps to take place in a dry box environment, thereby mitigating the adverse effects of oxygen and/or moisture on the resulting NC devices.

Table 6.1-1: Summary of reported CZTS NC solar cells utilising novel device architectures and/or hybrid passivation techniques.

Author	***J_{sc} (mAcm^{-2})***	***V_{oc} (V)***	***FF (%)***	***η (%)***	***Comments***
Steinhagen et al.[17]	1.95	0.32	37	0.23	Au/CZTS/CdS/ZnO/ITO device dry box fabrication with no NC processing.
Dasgupta et al.[18]	5.87	0.46	42	1.13	Fully depleted ITO/CZTS/$AgInS_2$, dry box fabrication utilising pyridine exchange
Suehiro et al.[19]	0.40	0.40	32	0.05	Au/CZTS/CdS/ZnO/ITO, dry box fabrication with solution passivation
Lee et al.[20]	4.10	0.68	44	1.2	Au/CZTS/CdS/ZnO/ITO, precursor solution anneal with highly doped ZnO n-type layer

The starting point for this work is a paper by Wu et al. in which they demonstrate a simple method for making Cu_2S-CdS heterojunction NC solar cells on flexible substrates[12] requiring dry-box processing to prevent oxidation of the NC surfaces. This work seeks to use novel thin film processing routes and passivation to make CZTS-CdS heterojunction devices under ambient conditions.

6.2 Novel Thin Film Processing Methodology

In this chapter I will discuss the process of depositing CZTS thin films from a stable NCs colloidal solution and establish an effective methodology for the fabrication of working CZTS based photovoltaic devices. Starting with the materials developed in chapters 3 and 4, the fabricated photovoltaic devices will be used as a platform from which to test a number of low temperature, ambient processing methods in order to investigate the passivation of CZTS grain boundaries and/or grain growth of CZTS NC thin films, with a view to optimising the photovoltaic properties of in-air fabricated CZTS solar cells.

6.2.1 Device Limitation

There are a number of loss mechanisms that directly determine the operational efficiency of thin film photovoltaic devices[21]. Some of these processes can occur right at the photo excitation site before the electron and hole are sufficiently separated, while others can occur during charge transport through the semiconductor layers or at the interfaces between the semiconductor layers and the metal/inorganic electrodes[21]. Minimizing interfacial resistance and surface defects is key to reducing recombination, as well as optimizing carrier diffusion lengths, and ultimately maximizing device efficiency[22]. The transport properties of NCs, which have abundant surface area, are limited by the defect states residing on the surface. These surface states, also known as mid-gap states, serve as recombination centres providing a pathway for non-radiative carrier recombination before the charges can be extracted[23], [24]. It is essential to passivate these defect states, as they lower the carrier mobility (μ) and recombination lifetime (τ), which determine the carrier diffusion length, (l).

As part of this work, the following processing methods are investigated in order to form a greater understanding of the interfacial chemistry of the NC thin films, which remains a significant limiting factor in the device performance of CZTS devices fabricated using low temperature fabrication methods[25]:

$CdCl_2$ Solution Treatments

Cadmium chloride chemical treatments have been used in combination with a low temperature thermal annealing[26], [27] to promote grain growth in CdTe and CIGS materials systems. This principle will be applied to our system to form a methodology for passivation of the CZTS NC surface.

H_2/N_2 Plasma Treatments

H_2/N_2 plasma treatments have been shown to produce highly reactive environments that can modify the surface chemistries of a variety of semiconductor thin films[28]. The associated ion bombardment of semiconductor thin films has also been shown to achieve enhanced passivation of recombination centres[29].

Thin Film Annealing Treatments

Of the three proposed surface treatments, annealing is the most established means of promoting grain growth in crystalline semiconductors[2], [5]. As mentioned previously, the use of high temperature annealing, in conjunction with sulphurisation or selenisation treatments for the fabrication of CZTS thin films is well documented in the literature[2], [5].. Since the purpose of this study is to work in a lower temperature regime and with non-corrosive atmospheres, a temperature range of 50-300°C has been chosen with which to investigate the effects of the low temperature annealing on the CZTS NC thin films. Previous studies have shown that annealing above 350°C in air leads to the breakdown of the CZTS and to the subsequent

formation of binary oxides and sulphides, such as Cu_2S and SnO_2[6]. By limiting the annealing temperature to below 400°C it will also help to mitigate the potential for thermal inter-diffusion of CdS into the CZTS layer, which is a widely documented degradation mechanism observed in CdS-CZTS devices[19], [20].

6.2.2 Layer-By-Layer Nanocrystal Coating

Surface cracks, and other in-homogeneities, are known to cause multiple pathways to form in semiconductor thin films through which charge carriers are able to travel[26]. These charge carriers are thereby prevented from playing a role in the PV diode, which ultimately lowers the efficiency of the device[30], [31]. Low temperature annealing treatments can lead to crack formation and propagation within semiconductor thin films[2], [32]. Previous studies have reported the formation of large cracks spanning the entire thickness of NC films sintered at temperatures as low as 100°C[33]. It is therefore crucial to fabricate characteristically conformal thin films over the active area of any photovoltaic device in order to minimise associated loss mechanisms.

A layer by layer approach helps to overcome this in two ways. Firstly by applying relatively thin layers, the stress built up in each layer is reduced[26], [34], [35]. Secondly any defects that form during the annealing process can be filled in by the deposition of subsequent layers[26], [34]. Layer by layer processing involves the deposition of nanoparticles with long chain surfactants which are subsequently exchanged with shorter ligands thereby creating electronically active films. The precise method of fabrication used here is outlined in chapter 3 of this thesis.

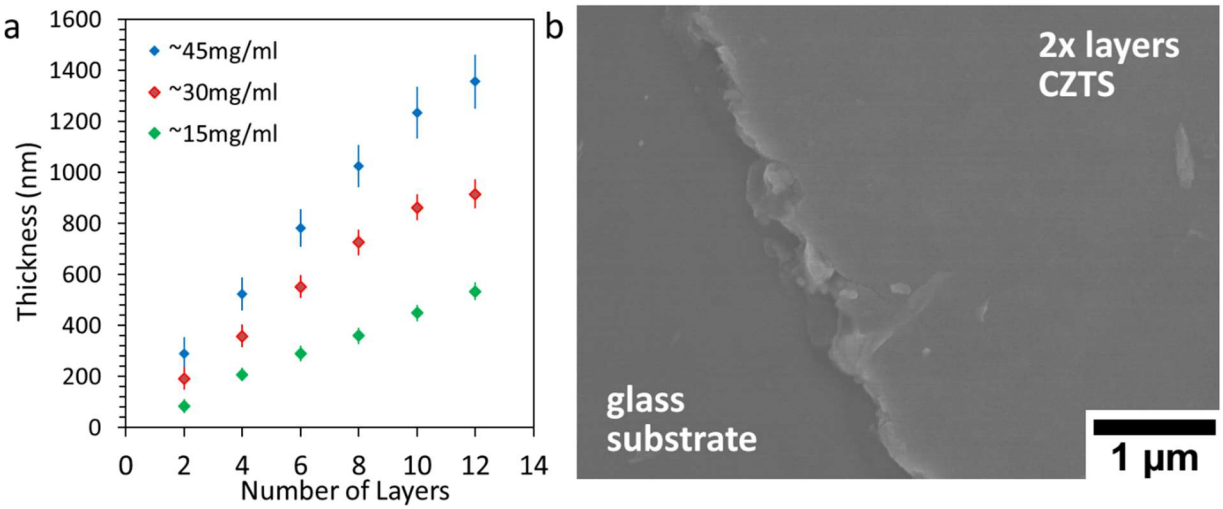

Figure 6.2-1 a) Film thickness vs number of layers, spin coated from a 15-45mg/ml colloidal solutions of pyridine capped CZTS NCs, measured using DEKTAK profilometry. Error bars represent surface roughness (Ra). B) SEM image of 4 layers of two layered CZTS NC thin film on glass (spun from 30mg/ml solution).

Here an in-solution exchange of the long chain OA and OLA ligands by pyridine is used. Due to the volatile nature of pyridine, upon spin coating it quickly evaporates leaving a conformal thin film as shown in Figure 6.2-1b. Due to the spontaneous removal of the pyridine, multiple layers can be built up. Three different NC concentrations were trialled, as shown in Figure 6.2-1a, and it was found that higher NC concentrations lead to rougher films. A concentration of 30 mg/ml CZTS was chosen as a trade-off between processing time and surface roughness, as is evident in the DEKTAK profilometry data shown in Figure 6.2-1a; wherein the surface roughness (identified by the y-axis error bars) is shown to increase with increasing NC solution concentration.

6.2.3 CdS Window Layer

Key to making a functional solar cell is the formation of a junction. Traditionally, a Schottky barrier junction would represent the first experimental device structure utilised to test a new solar cell material[31] (owing to the inherent simplicity of the Schottky junction formed between the photoactive semiconductor and the metal/inorganic electrode). However, all attempts to form a working Schottky barrier

PV cell were unsuccessful as the resulting device properties were dominated by short circuit pathways. This would suggest that the CZTS layer by layer deposition method was unable to form a homogeneous semiconductor layer directly on to the transparent conductive oxide layer. It was therefore important to find a suitable intermediate layer which could operate as a smoothing layer, thereby inhibiting the formation of shorting pathways through the device. There are a number of n-type materials, including ZnO[20], CdS[36] and TiO_2[37], that have been reported in the literature to form type-II p-n heterojunctions with CZTS. For this study, a CdS-CZTS
140 heterojunction, outlined in Figure 6.3-1a, was found to form a working solar cell, which could form the foundation for further investigations into the optimisation of the nanocrystalline CZTS absorber layer.

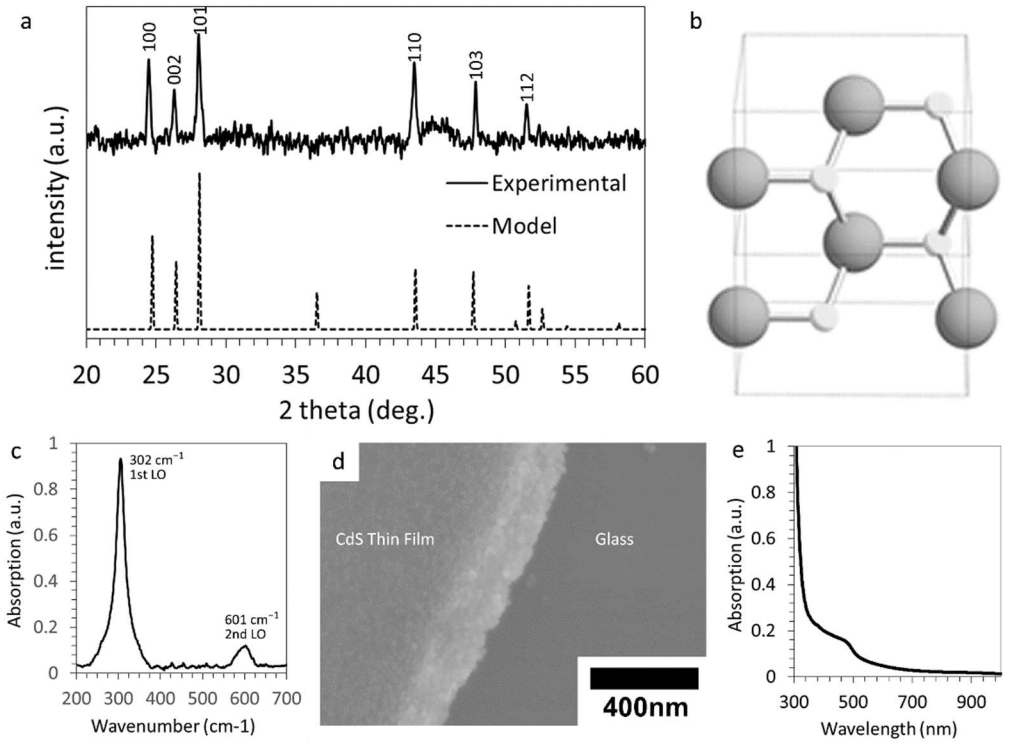

Figure 6.2-2 (a) XRD trace, (b) unit cell (x2) of Wurtzite CdS crystal structure, (c) Raman spectra showing the longitudinal optical (LO) phonon peaks of CdS at 302 and 601 cm^{-1}, (d) SEM micrograph and (e) UV–visible spectrum of CdS thin film.

In this study CdS is used to a) form a smoothing layer on which to deposit the CZTS thin film and b) as an n-type semiconductor material, with which to form a p-n

junction with the CZTS. CdS is more commonly used in CIGS photovoltaics as a type-I buffer layer, where rather than forming a junction it acts as a hole blocking layer which limits photo-generated carrier recombination and hence increasing minority carrier lifetime[22], [38], [39]. This results in higher efficiency devices[22], [38]–[40]. In this project we use CdS as an n-type semiconductor to form a junction with the inherently p-type CZTS absorber layer. Huang et al. show that the CZTS conduction band is 0.28 eV higher than that of CdS creating a type II junction[36], [41] which is also supported by the calculations of Bao et al.[42] From established theory and literature this conduction band offset would create a very low V_{oc}. However as will be shown later this is not the case (as is evident in Figure 6.3-2).

The method described in Chapter 3 produces good quality CdS films of around 60nm as confirmed by the XRD and Raman shown in Figure 6.2-2a. The XRD diffraction peaks can be indexed to the Wurtzite structure CdS with cell constants a = 4.136, c = 6.713 Å which correlates well with the JCPDS card No. 41-1049 values[43]. Evaluation of the average crystallite size using the Scherrer equation estimates them to be ~400 nm. Raman shows characteristic longitudinal optical phonon responses at 302 and 601 cm^{-1}[44]. The spectra in Figure 6.2-2e shows the onset of absorption close to the 515nm (~2.40eV), consistent with other reported values from the literature[43]–[45], this is sufficiently blue shifted from the CZTS band edge as to act as a window layer (i.e. a semiconducting transparent transport layer).

6.3 Device Fabrication

The device geometry, shown in Figure 6.3-1a, was built using the methods described in Chapter 3. Unlike the device architecture outlined in the Alivisatos paper[12] (ITO/Cu_2S/CdS/Al) the devices presented here have been inverted,

depositing the CdS layers first and the CZTS layer second. This allows for the investigation of each processing treatment, independent of the 200°C 1hr anneal, required for the CdS film fabrication. Additionally, the surface roughness of the CdS thin film is significantly smoother than the underlying FTO and so is able to act as a smoothing layer, which may help to prevent shunt pathways forming within the devices. As can be seen in Figure 6.3-1b, the cross section SEM of a typical 12-layer device indicates that the coating of CZTS on top of the CdS layer is broadly conformal.

180 Au was chosen, over the more traditional Mo, as the metal top electrode for collecting photogenerated charge carriers due to lack of access to a suitable deposition system. Not only does Au have a higher work function[46] thereby forming a better ohmic contact with the p-type CZTS, but it is also compatible with thermal evaporation techniques, which make it far easier to deposit. FTO was chosen over ITO due to the deterioration of the conductivity properties of ITO at temperatures above 200°C[47]–[49].

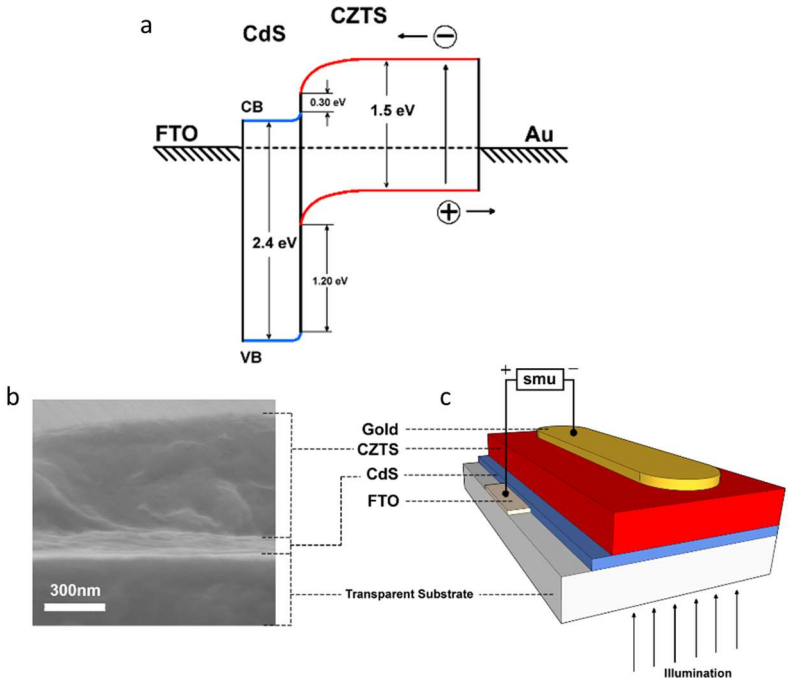

Figure 6.3-1(a) Schematic diagram of theoretical band allignment, (b) cross-section SEM image and (c) schematic model of FTO/CdS/CZTS/Au device structure.

It is postulated that an ohmic junction formed between Au and CZTS [46] while the CdS forms a type-II heterojunction [36], [41]. A typical light and dark *J-V* response is shown in Figure 6.3-2.

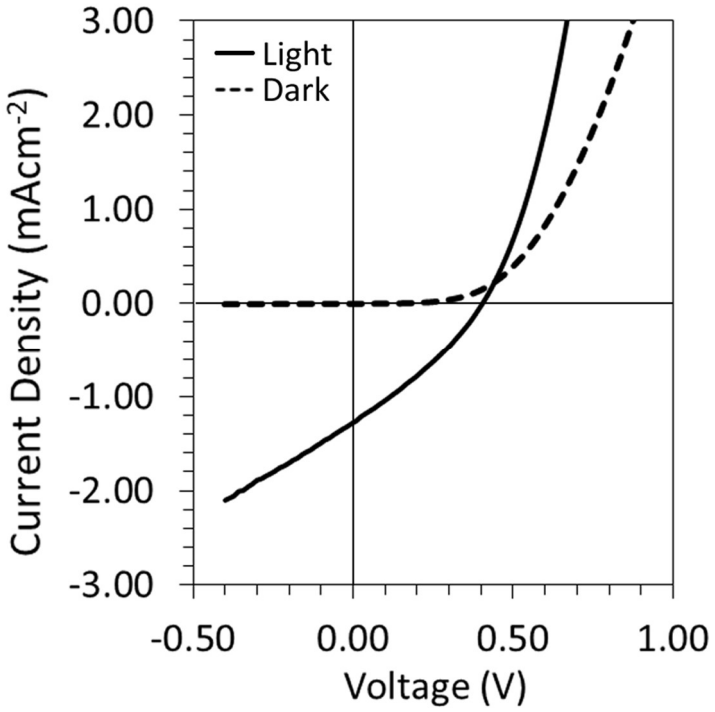

Figure 6.3-2 J-V device characteristics of an FTO/CdS/CZTS/Au device, with a 1130nm CZTS photoactive layer, having been annealed at: 200°C for 10 mins.

The performance of a PV device can be characterised by examining the four most common metrics of photovoltaic analysis, namely the power conversion efficiency (PCE), the fill-factor (FF), the short circuit current (J_{sc}) and the open circuit voltage (V_{oc}). Each of these parameters and how they are obtained are defined in chapter 2 of this thesis. Functional photovoltaic devices with power conversion efficiencies of around 0.22% were achieved. The PCE was limited by all of the major device metrics, J_{sc} = 1.47±0.14 mAcm^{-2}, V_{oc} = 0.42±0.2V, *FF* = 32±0.6%, and PCE = 0.22 ± 0.29%, which appear poor by the standards of similar devices reported in the literature (and outlined in Table 6.1-1). However, the performance of these initial devices were taken as a starting point for the optimisation of future devices.

With reference to the band diagram of the CZTS-CdS heterojunction, as shown in Figure 6.3-1a, the predicted V_{oc} for an ideal device comprising such a junction would be ~0.30V. The significantly larger experimental value that was achieved in each of the initial devices could be ascribed to the formation of interface states, forming a quasi-semiconductor-insulator-metal junction at the CdS-FTO interface(as depicted in Figure 6.3-3)[50], [51].

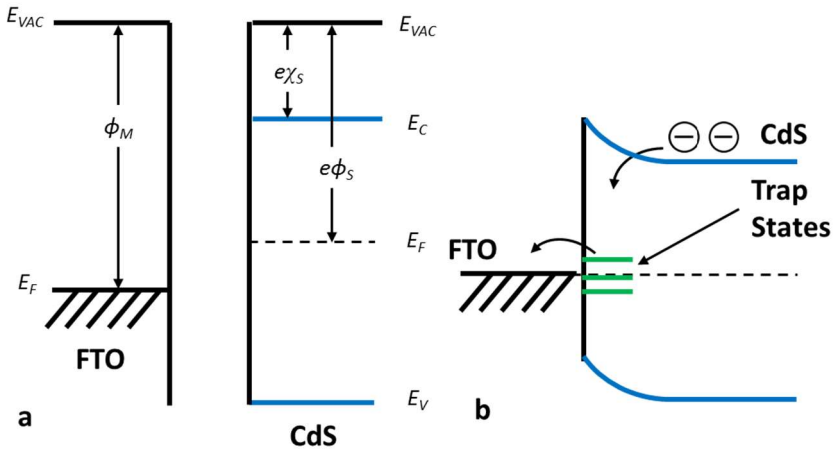

Figure 6.3-3 A schematic illustration of a band diagram for a FTO-CdS junction under (a) flat band conditions and (b) with Fermi energies lined up identifying the where trap states are formed.

The insulator barrier formed between CdS-FTO interface causes the build-up of space charge due to a potential barrier forming at the insulator barrier[50], [51], thereby contributing to the enhance V_{oc} of the CZTS-CdS junction of the experimental devices. The comprehensive analysis of this phenomena is outside the scope of this thesis however, it does represent a significant result due to its remarkable beneficial impact on overall device efficiency.

The intersection of the light and dark *J-V* curves is known as the cross over effect[52], [53] as seen in Figure 6.3-2. This phenomenon is characteristic of an energetic barrier for electrons being formed at the interface between the CZTS and CdS layers, due to the diffusion of Cu^+ ions into the CdS layer[52], [53].

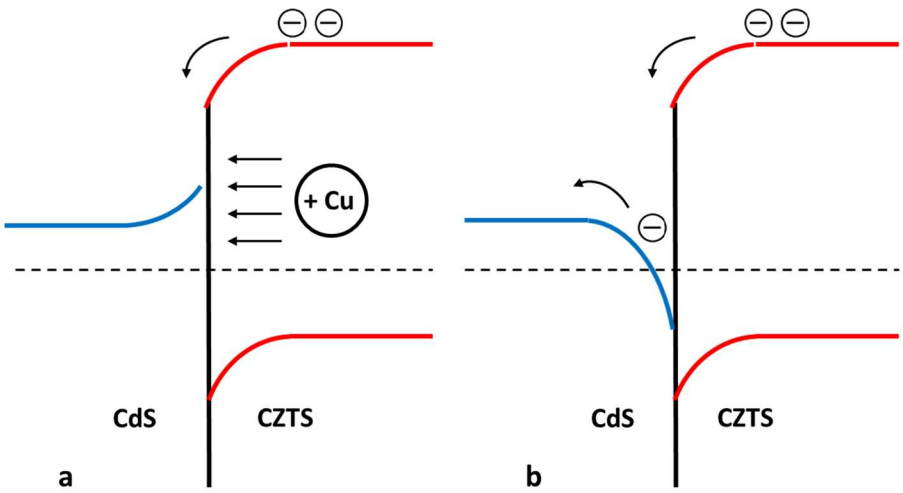

Figure 6.3-4 A schematic illustration of the effect of Cu^{2+} migration on the band structure at the CdS:CZTS interface with Fermi energies aligned, showing the CdS-CZTS band structure a) before and b) after to the diffusion of Cu^{+} ions into the CdS layer.

The difference between the dark and light *J-V* curves therefore arises because the photo excited electrons possess sufficient energy to overcome this increase in electron potential whereas those in the dark do not[54], [55].

In order to further understand the origin of the device performance, both the light and dark J-V curves were analysed further as a function of film thickness.

6.3.1 Optimisation of the Photoactive Layer Thickness

The next step was to study the effect of the CZTS layer thickness on overall device performance, in order to ascertain whether it is the respective semiconducting or light absorbing properties, which had limited overall device performance [16], [18], [56]. There is a trade off in PV devices between film thickness and efficiency arising from the conversion of absorbed light to charge and the depletion width of the heterojunction, typically the absorber is only marginally thicker than the depletion width. Figure 6.3-5a shows the effect of changing CZTS absorber thickness on the light J-V curve. It is clear that a thickness of 240nm operates with an optimum efficiency of 0.22% and as the thickness increases, the efficiency steadily decreases to a minimal value of 0.05%. This is most likely due to the fact that the extraction of

charge carriers becomes more difficult, with thicker films due most likely to radiative and non-radiative recombination pathways (in other words, the overall path length of photo-excited charge is small, relative to the device thickness). It is noted that films less than 240nm did not operate as solar cells because short circuits between anode and cathode formed preventing photovoltaic operation.

Considering Figure 6.3-5b in more detail, it is clear that the J_{sc} decreases with thickness which is consistent with the absorber film being thicker than the depletion width[16], [18], [56]. *The* V_{oc} also decreases as device thickness increases from around 0.42V to 0.34V. This is unlikely to be caused by a decrease in R_{sh}. Figure 6.3-7 shows R_{sh} to increase with device thickness as expected because fewer shorting pathways are formed within thicker films[31], [46]. However, the increase in J_0 observed would suggest increased recombination and a lower V_{oc}, as described by the Shockley equation. J_0 gives an indication of the degree of recombination occurring within the device. Typically for a good solar device, J_0 should be in the order of 10^{-17},[31] here they are 10^{-10} indicating that recombination is high. This is mostly likely a result of defects forming within the CZTS absorber layer. The fact that the NCs are two orders of magnitude smaller than the film means that a large number of grain boundaries have to be crossed in order to be collected by the device electrodes. The FF (as shown in Figure 6.3-5b) is poor in general but relatively invariant with thickness. A good device would exhibit a large fill factor as it is directly correlated to the balance charge transport within the device. This would indicate that the carrier properties of the films are poor, which in turn affects the depletion width, which is ultimately dependent on carrier concentration[31], [46].

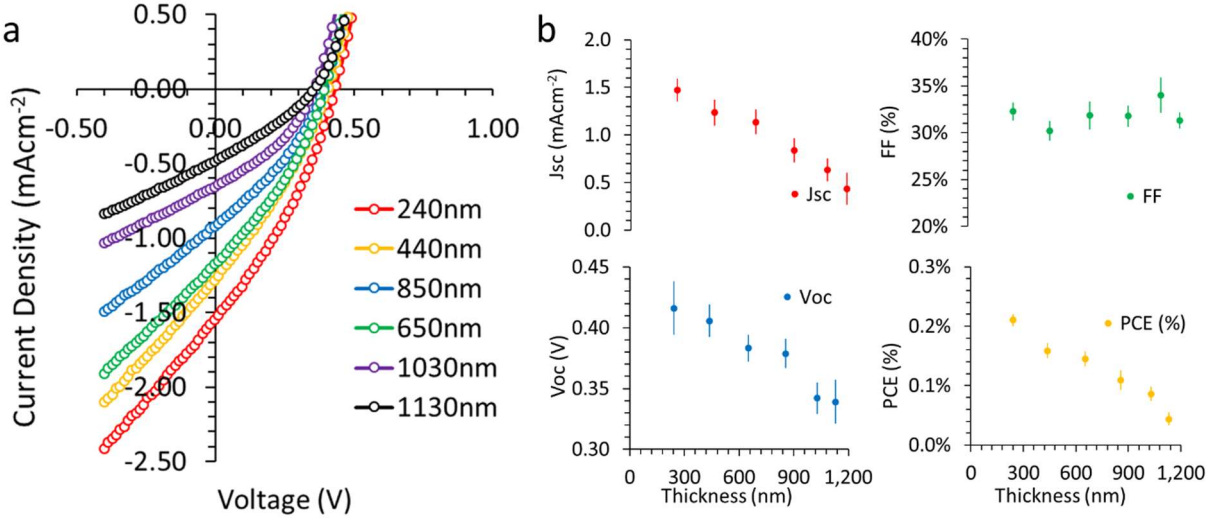

Figure 6.3-5 a) J_{sc}, V_{oc}, FF and PCE characteristics of FTO/CdS/CZTS/Au devices with increasing CZTS absorber layer thickness (between 240nm and 1130nm). b) Device performance characteristics; filled circles and error bars correspond to the average and standard deviation across seven to nine devices across three substrates.

As can be seen in Figure 6.3-6b, the absorption increases with film thickness. This would normally lead to high J_{sc} however, as is shown in Figure 6.3-5b, the J_{sc} decreases with increasing thickness for these devices. This would suggest that while a greater number of photons are absorbed by thicker CZTS layers, fewer photo-excited charge carriers are extracted from the solar cell.

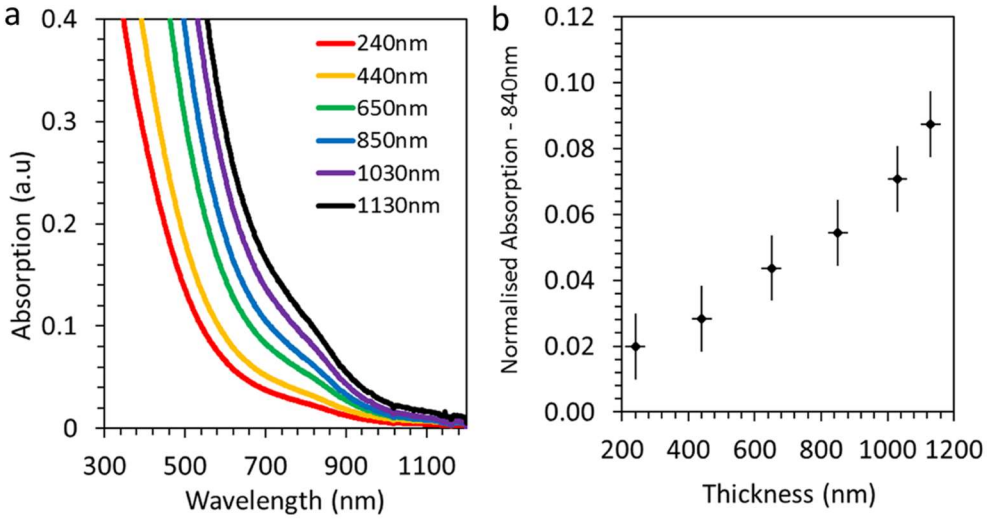

Figure 6.3-6 a) UV-VIS-NIR absorption spectra of CZTS thin films of increasing thickness (between 240nm and 1130nm) on glass substrates and b) absorption of incident light with a wavelength of 840nm, normalized with relative thin film thickness.

As can be seen in Figure 6.3-7, R_S was found to be around an order of magnitude higher than would be expected for a good device, this may be attributed to a high proportion of poorly conductive material within the absorber layer relating to the presence of excess ligands[57]. The observed increase in R_S results from the increase in the internal resistance of the absorber layer due to the increase in the material, which inhibits movement of charge carriers across the device.

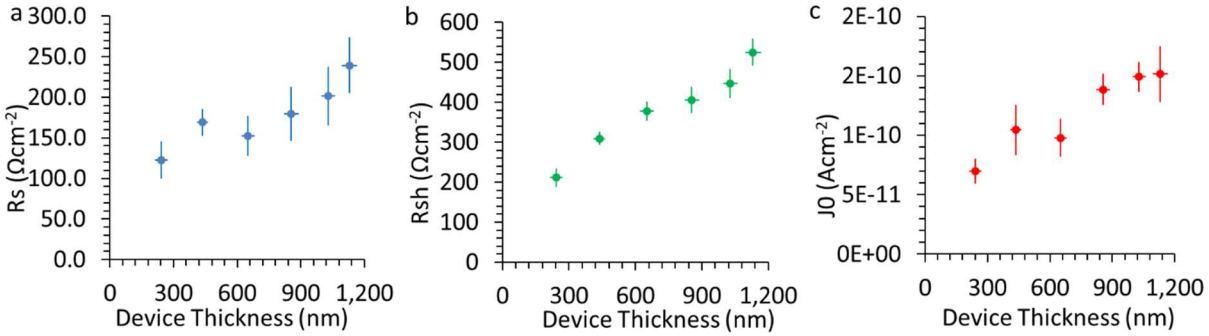

Figure 6.3-7 Performance characteristics of the devices described in Figure 6.3-5. Filled circles and error bars correspond to the average and standard deviation across seven to nine devices across three substrates. Resistance a) R_s and b) R_{sh} and dark saturation current c) J_0. Values are obtained from the two diode model of the light and dark J-V curves respectively.

6.4 Surface Passivation

The electronic properties of the thin films are influenced by the large interfacial area of thin films composed of CZTS NCs. In more traditional chalcogenide PV, high temperature reactive environment anneals are used to reduce grain boundaries. However, the objective of this thesis is to remove that requirement and develop low temperature semiconductor thin film processing methods, for the passivation of the interfaces formed between individual layers of the semiconductor thin films. Colloidal quantum dot (QD) solar cells, where the NCs are of similar dimensions, are achieving relatively high PCE but CZTS have not so far. This in part could be due to either the improved surface chemistry of PbS QDs, which researchers have extensively developed, or it may be due to the inherently different transport mechanisms exhibited by PbS relating to quantum mechanical processes, for example

tunnelling[58]. Quantum confinement in CZTS has been reported[59] but this is relatively weak compared to lead chalcogenide materials owing to the small Bohr radius (~5nm)[59], [60]. We do not observe it in the materials used here. There are however, similarities in the roles that traps play[4], [58], [61], [62], and similar defect mitigation strategies[23], [62], [63] are adopted here to enable low temperature grain growth.

6.4.1 Cadmium Chloride Solution Passivation

A characteristic of 2nd generation photovoltaic technologies is the importance of grain growth[2], [7]. $CdCl_2$ has also been shown to be effective at passivating NC surfaces which also aids grain growth and is well known to improve the performance of CdTe[2], [7] and PbS NC devices[26], [27]. Conventionally a cadmium chloride chemical treatment is used in combination with a low temperature (<300°C) thermal annealing[26], [27]. This principle is applied to our system to form a methodology for passivation of the CZTS NC surfaces.

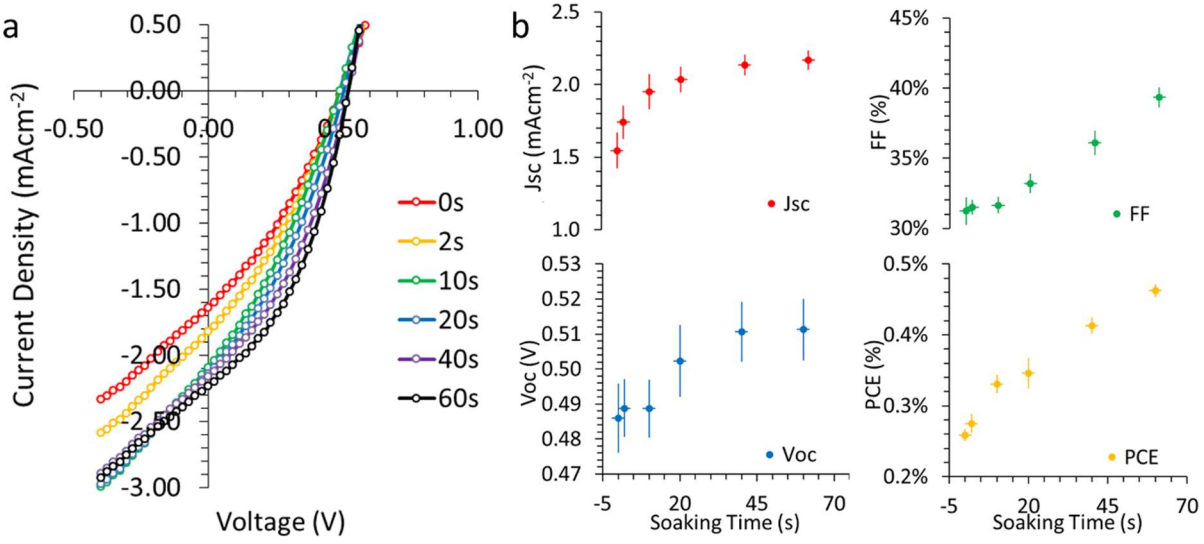

Figure 6.4-1 a) J_{sc}, V_{oc}, FF *and PCE characteristics of FTO/CdS/CZTS/Au devices treated with saturated* $CdCl_2$ *solution for between 0 and 60 seconds. b) Device performance characteristics; filled circles and error bars correspond to the average and standard deviation across seven to nine devices across three substrates.*

The role of $CdCl_2$ treatment can be partially understood through the use of FTIR spectroscopy. CZTS films that were treated with $CdCl_2$ over time show a reduction in the characteristic C-H and O-H- (2800-3000cm^{-1} and 3000-3800cm^{-1} respectively) peaks of the residual aliphatic ligands such as oleic acid and oleylamine, as shown in Figure 6.4-2. This indicates that the $CdCl_2$ treatment effectively strips organic ligands from the NC, and thereby leading to an overall reduction in the R_s within the CZTS thin films as is evident in Figure 6.4-3a.

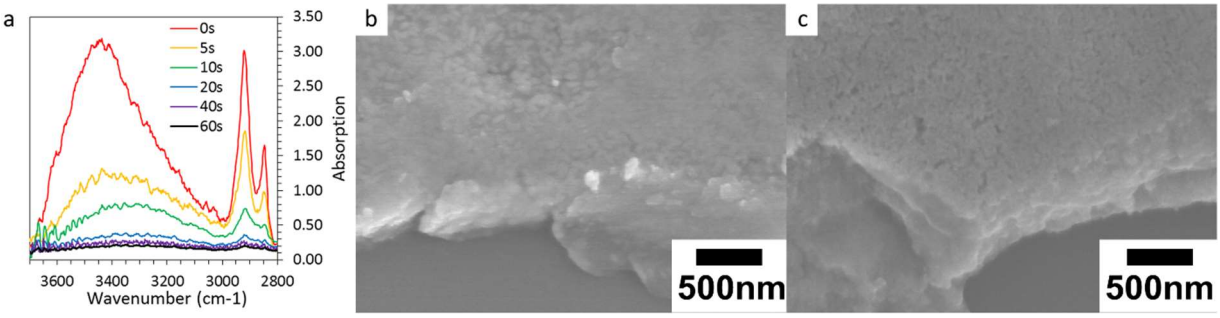

Figure 6.4-2 a) FTIR spectra of CZTS thin films exposed to $CdCl_2$ treatment for between 0 and 60 seconds. SEM images of CZTS films on glass, b) before and c) after 60s of $CdCl_2$ treatment.

This may contribute to the reduction in R_s as organic material is removed, increasing the overall density of the CZTS thin films. By soaking in a $CdCl_2$ methanol solution for up to 60 seconds a systematic increase in device metrics is observed as shown in Figure 6.4-1. The best efficiency devices were achieved for a 321 nm thick CZTS layer, with J_{sc} = 2.24±0.06 $mAcm^{-2}$, V_{oc} = 0.51±0.1V, FF = 39±0.6%, and PCE = 0.46 ± 0.25%. The overall increase in device performance (in particular PCE and J_{sc}) is consistent with the hypothesis of defect passivation, as is evidenced by the dramatic drop in J_0 values (see Figure 6.4-3c) with increasing soaking time.

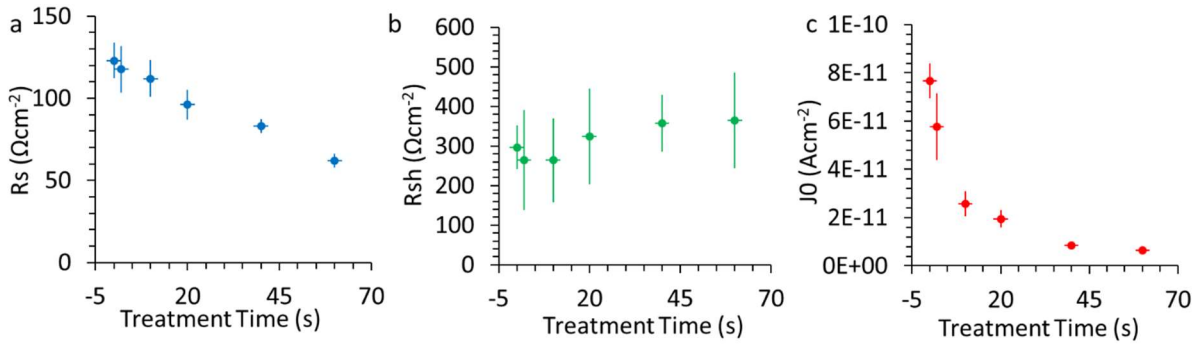

Figure 6.4-3 Performance characteristics of the devices shown in Figure 6.4-1.. Filled circles and error bars correspond to the average and standard deviation across seven to nine devices across three substrates. Resistance a) R_s and b) R_{sh} and dark saturation current c) J_0 values are obtained from the two diode model of the light and dark J-V curves respectively.

6.4.2 N_2/H_2 Plasma Passivation

Plasmas with different gas compositions can be used to produce reactive environments which can modify surface chemistries[64]. Here a 4% hydrogen in nitrogen mix is used at a RF frequency of 13.6MHz and 25 W power while the vacuum was held at 100mTorr bleeding the gas mixture through a needle valve. The presence of hydrogen gas in the mixture was introduced in an attempt to hydrogenate dangling bonds and also to getter any residual oxygen. This environment was used for different periods of time between each spin coating[64].

The microstructural effect of the plasma can be seen in Figure 6.4-5b. It is obvious that with prolonged exposure material is etched away. If the plasma is carried out for longer than 30 seconds, the porosity of the film significantly increases. It is assumed the etch rate is greater for the organic materials and this is removed first. The chemical effect of the plasma was understood using FTIR spectroscopy (Figure 6.4-5a). Increasing plasma treatment time results in a reduction in the characteristic C-H peaks of the residual aliphatic ligands such as oleic acid and oleylamine. This indicates that the N_2/H_2 plasma is effective at organic ligand removal. The use of plasma is well known to increase the hydrophobic nature of

surfaces[28], and it was observed that even after short treatments the wetting of subsequent NC thin films improved.

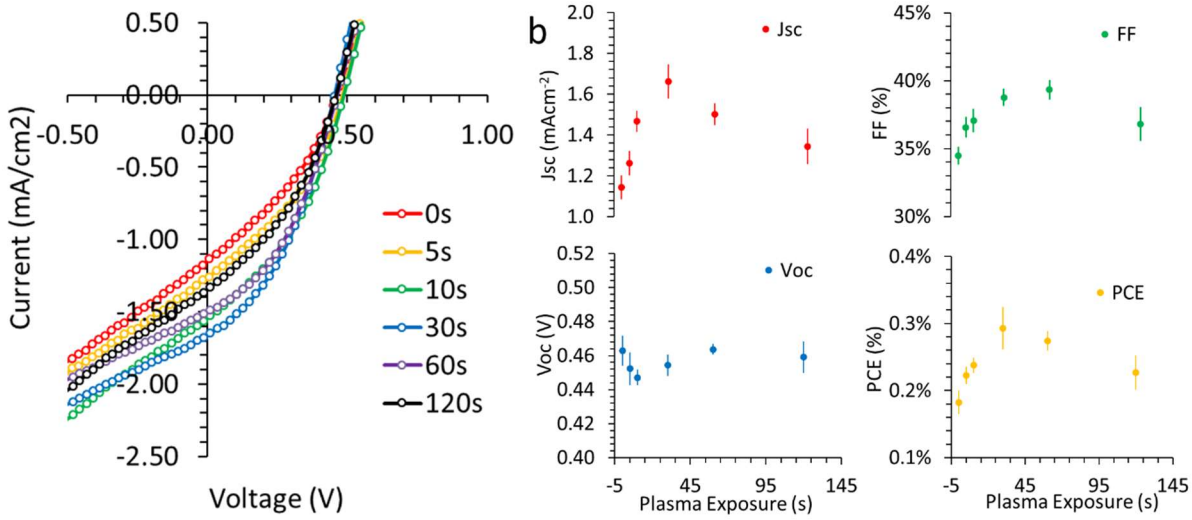

Figure 6.4-4 a) J_{sc}, V_{oc}, FF a*nd PCE characteristics of FTO/CdS/CZTS/Au devices treated with* N_2/H_2 *plasma for different lengths of time. b) Device performance characteristics; filled circles and error bars correspond to the average and standard deviation across seven to nine devices across three substrates.*

The effect on device performance with increasing plasma treatment is shown in Figure 6.4-4). In comparison to the $CdCl_2$ treatment, the effects of plasma treatment resulted in an almost 50% increase in J_{sc}, and which substantially accounts for the overall increase in the PCE. This improvement can be ascribed to an initial drop in R_s with increasing plasma exposure. However, as is evident from Figure 6.4-6, at first the associated R_s decreases as organic material is removed. With increasing plasma exposure, the reduction in R_s plateaus, suggesting that its efficacy is limited. The corresponding initial rise in R_{sh} may indicate the passivation of the NC surface enabling improved wetting, but with excessive plasma treatment, ablation of the inorganic component causes voids to form. This is clearly the determining factor in the subsequent deterioration of device performance with prolonged plasma treatment as shown in Figure 6.4-5 as J_{sc} also follows the same trend.

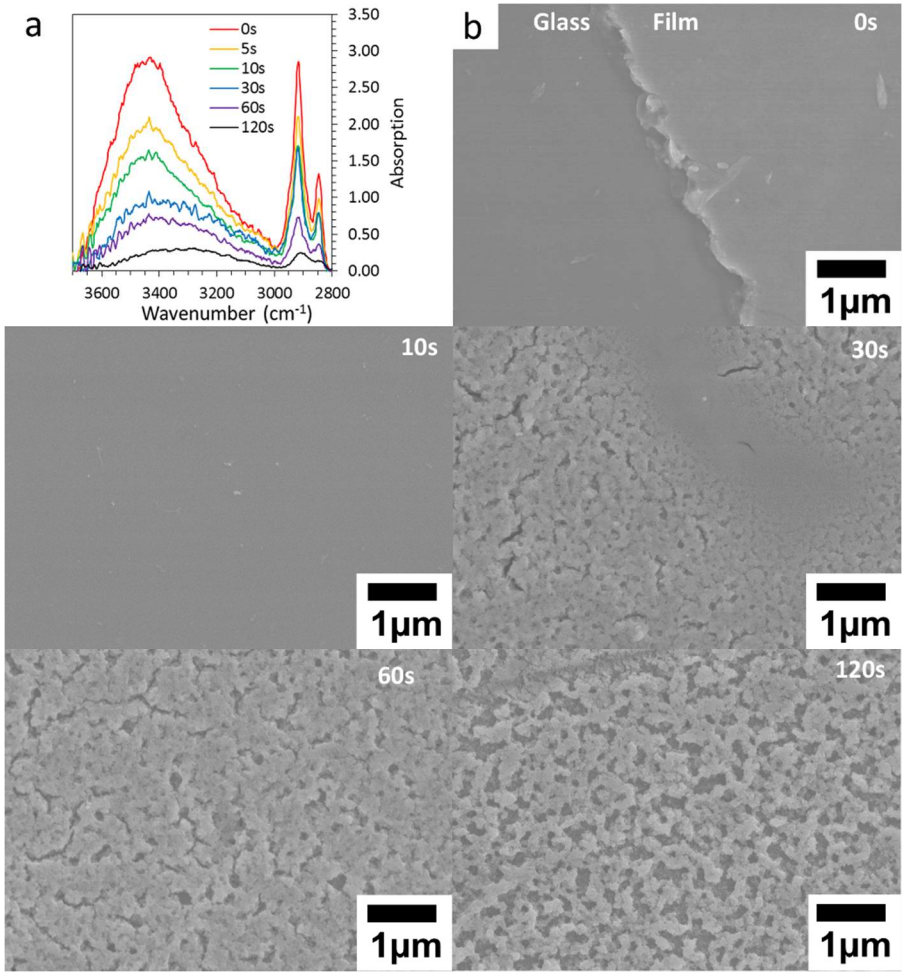

Figure 6.4-5 a) FTIR spectra of CZTS thin films exposed to N_2/H_2 plasma for different lengths of time. SEM images of CZTS films on glass, b) before and c) after 120s of plasma treatment.

Overall an efficiency maximum is achieved for a 305 nm thick CZTS layer treated with N_2/H_2 plasma for 30s, with J_{sc} = 1.7 ± 0.08 mAcm^{-2}, V_{oc} = 0.45 ± 0.6V, *FF* = 39 ± 0.6%, and PCE = 0.29 ± 0.32%. This correlates to approximately 60% of the C-H, O-H bond removal according to the FTIR (see Figure 6.4-5). As with the $CdCl_2$ treatment, the overall increase in device performance is consistent with the hypothesis of defect passivation, as is evidenced by the dramatic drop in J_0 values (see Figure 6.4-6c) with increasing N_2/H_2 plasma treatment time, up to 30s. Beyond 30s, the dramatic drop in R_{sh} *(see* Figure 6.4-6*b),* corresponding to an in short circuit pathways caused by the formation of voids within the CZTS films (see Figure 6.4-5b), begins to dominate device characteristics, with an ultimately detrimental effect on conversion efficiency.

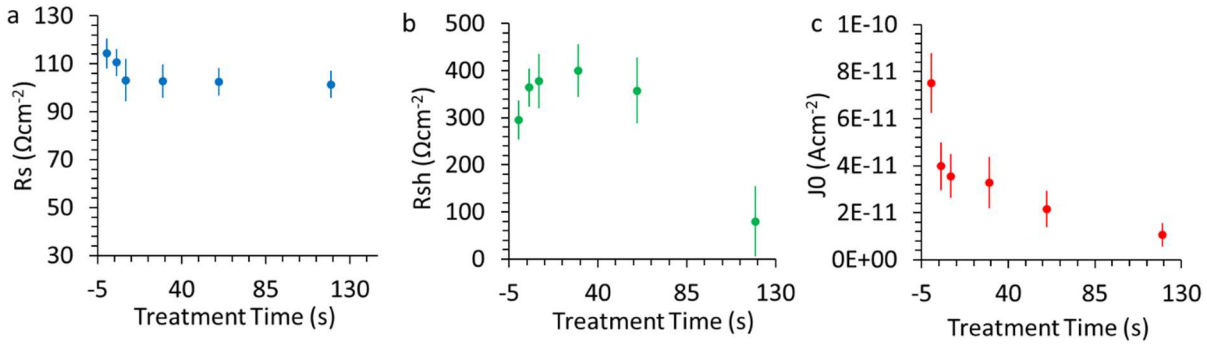

Figure 6.4-6 Performance characteristics of the devices shown in Figure 6.3-4.. Filled circles and error bars correspond to the average and standard deviation across seven to nine devices across three substrates. Resistance a) R_s and b) R_{sh} and dark saturation current c) J_0 values are obtained from the two diode model of the light and dark J-V curves respectively.

6.4.3 Annealing

Annealing is the most established way of promoting grain growth in crystalline semiconductors[2], [5]. As the purpose of this study was to work in a lower temperature regime and non-corrosive atmosphere a temperature range of 50-300°C was chosen. Previous studies have shown that annealing above 350°C in air leads to the breakdown of the CZTS and subsequent formation of binary oxides and sulphides, such as Cu_2S and SnO_2.[6] This also mitigates the potential for thermal inter-diffusion of CdS into the CZTS layer[19], [20].

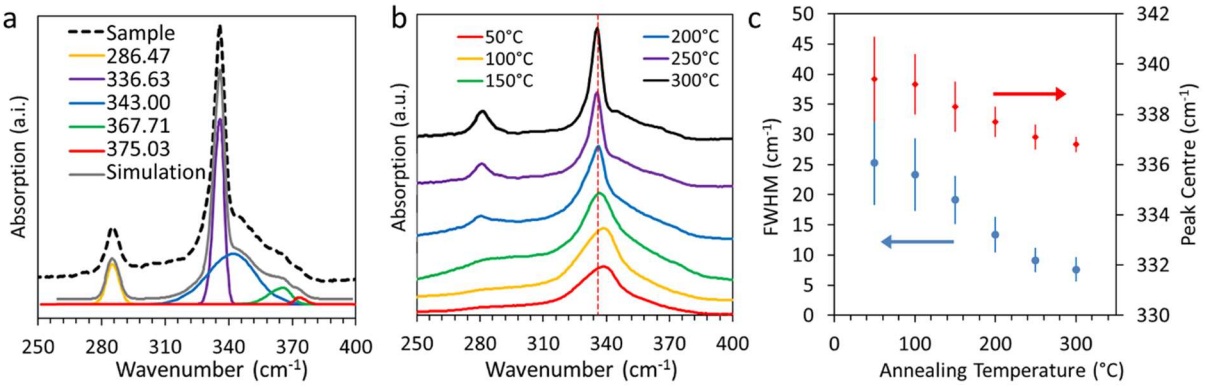

Figure 6.4-7 a) De-convolution showing the constituent Raman peaks of a 319nm CTZTS thin film annealed at 300°C for two minutes. b) Raman spectra taken of ~300nm (±23nm) CZTS thin films annealed for two minutes at temperatures between 50°C and 300°C. c) Change in FWHM and peak centres determined by fitting a model Gaussian curve to each spectra (Y-axis error bars correspond to relative fit of model curve).

The evolution of microstructural properties is traced using Raman spectroscopy as shown in Figure 6.4-7b. Each Raman peak was fitted to a Gaussian model which

was used to determine the FWHM and line-width of each de-convoluted peak (Figure 6.4-7a). A decrease in the FWHM of the major CZTS peak (at ~338 cm^{-1}) can be seen as the anneal temperature increases. This corresponds to an increase in the grain size as discussed by Gouadec et al[65]. With increasing temperature, the primary CZTS peak also shifts from 338 cm^{-1} to 336 cm^{-1} for films annealed at 50°C and 300°C respectively. This corresponds well with literature observations related to phonon confinement of the laser light in smaller grains[65], [66]. Films annealed above 150°C also show a second CZTS scattering peak around ~ 287 cm^{-1} evolving with increasing temperature. This, along with the ~336 cm^{-1} peak, corresponds to the two major vibrational modes of the kesterite CZTS structure[33], [67], [68].

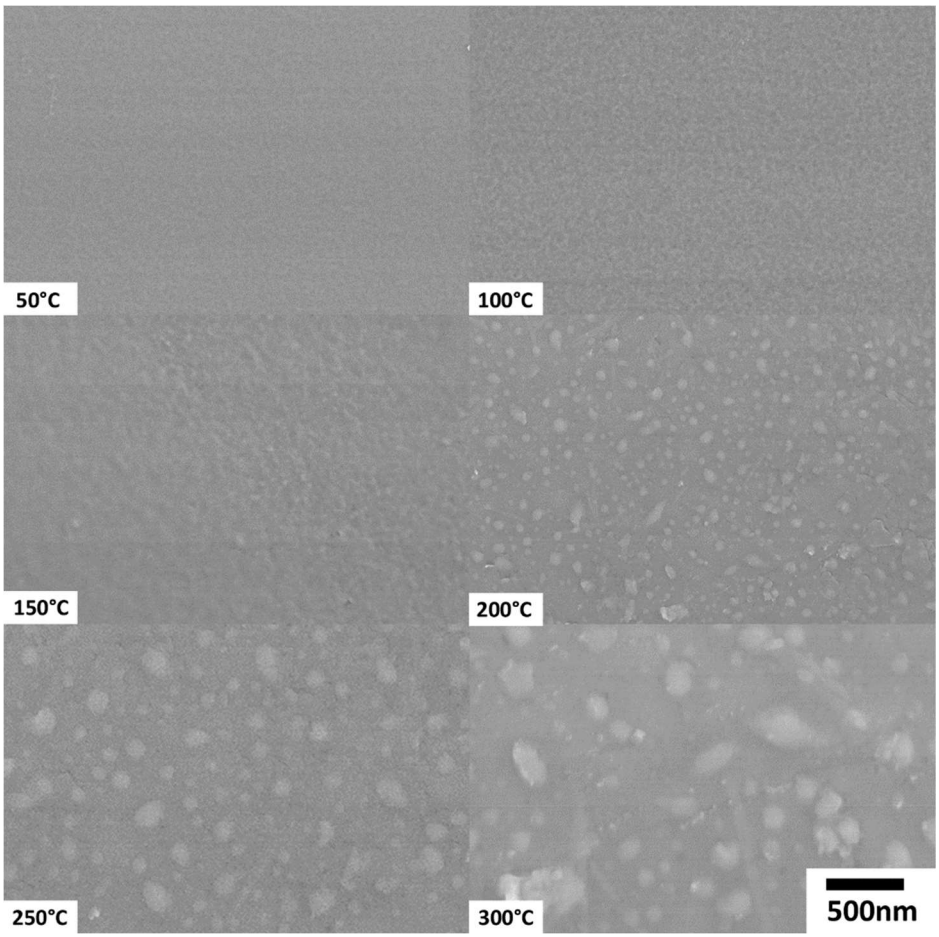

Figure 6.4-8 SEM images of ~300nm (±23nm) CZTS thin films annealed for two minutes at 50°C, 100°C, 150°C, 200°C, 250°C and 300°C respectively.

The appearance, growth and coalescence of surface artefacts with increasing annealing temperature, as shown in Figure 6.4-8, may correspond to the grain growth derived peak broadening observed previously in this study. It is interesting to note that the surface artefacts are observed at temperatures much below the bulk melting point for CZTS, indicating the mechanism of grain growth is chemically enhanced and/or due to the higher surface area of a NC[26], [69]. There is no evidence of film cracking in these samples. We hypothesise this is due to the conformal nature of layer-by-layer processing aided by the small pyridine ligand dimensions.

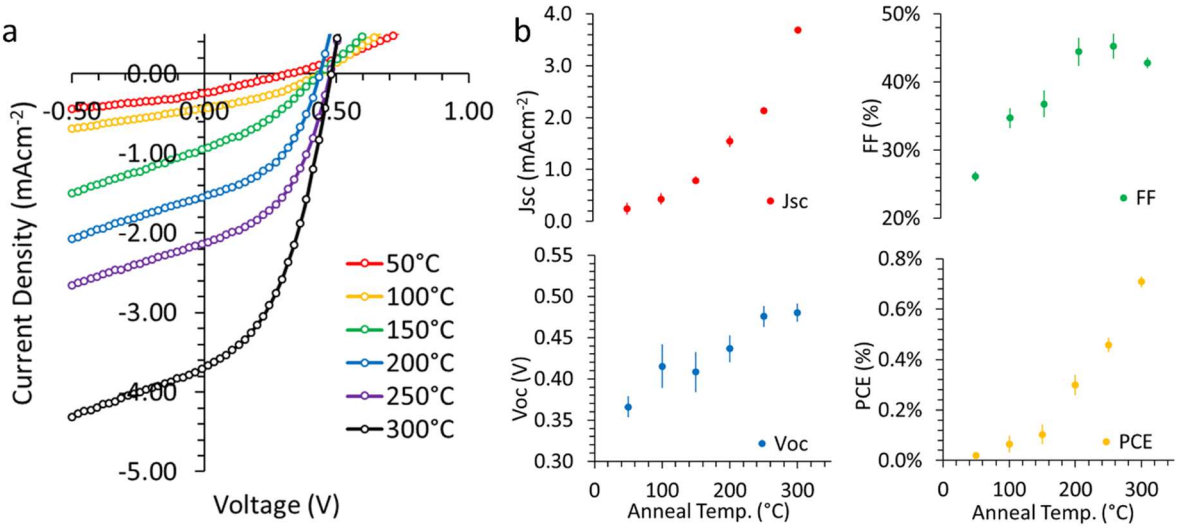

Figure 6.4-9 a) J-V curves and b) J_{sc}, V_{oc}, FF a*nd PCE characteristics of FTO/CdS/CZTS/Au devices annealed for two minutes at 50°C, 100°C, 150°C, 200°C, 250°C and 300°C; filled circles and error bars correspond to the average and standard deviation respectively (across seven-nine devices on three substrates).*

Following this through to device performance; when CZTS NC thin films are annealed at temperatures that are too low to induce significant grain growth (i.e. below 150°C) the resulting device performance is shown to be poor (as shown in Figure 6.4-9a). A dramatic increase in PCE, J_{sc} and *FF* values with a respective increase in temperature (as shown in Figure 6.4-9b) is most likely caused by the reduction in short circuit current densities due to the increase in CZTS grain size within the NC

thin films. Overall an efficiency maximum is achieved for a ~310nm thick CZTS layer, with J_{sc} = 3.7 ± 0.04 mAcm^{-2}, V_{oc} = 0.48 ± 0.1V, FF = 43 ± 0.8%, and PCE = 0.71 ± 0.2%.

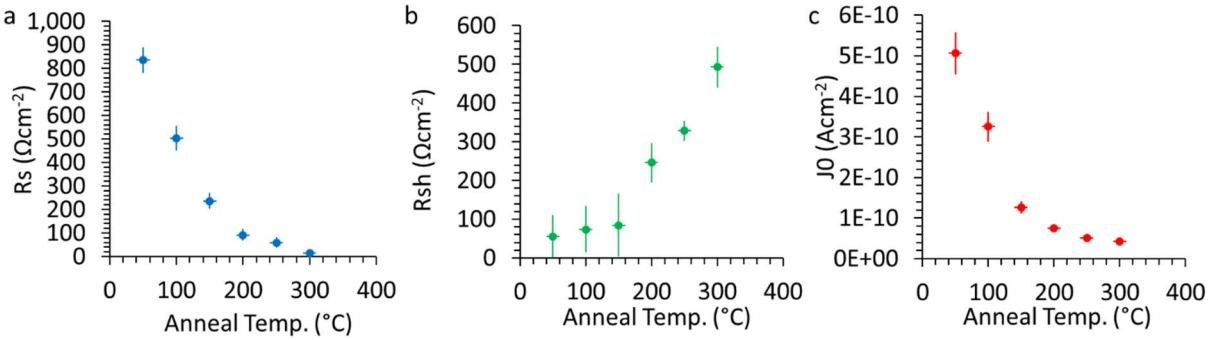

Figure 6.4-10 Performance characteristics of the devices shown in Figure 6.4-9. Filled circles and error bars correspond to the average and standard deviation across seven to nine devices across three substrates. Resistance a) R_s and b) R_{sh} and dark saturation current c) J_0 values are obtained from the two diode model of the light and dark J-V curves respectively.

Devices figures of merit, R_s and J_0, both see marked improvements with increasing anneal temperature (see Figure 6.4-10). This can be associated with enhanced grain growth which directly impacts the power conversion efficiency. R_{sh} also improves, which is rather contrary to our observation of surface crystal formation, wherein one would typically expect the increased annealing temperatures to encourage the formation of cracks in the device, thereby forming short circuit pathways through the electrodes. It is surmised that there must be some microscopic defects that facilitate the formation of shunt pathways through the films at low anneal temperatures. Densification of the films brought about by the observed crystal growth may explain the mitigation of such defects upon annealing at higher temperatures.

6.4.4 Carrier Lifetime

Efficient device operation depends on the balance between light absorption and efficient carrier extraction[31]. A thick active layer may absorb more light and generate additional carriers but those generated near either contact may have transit

times to the opposing contact that exceeds their respective lifetime. Analysis of the recombination limited lifetime of the carriers generated in a known thickness of materials sheds light on the prevalence of recombination sites within the active layer[56].

Photovoltage decay measurements are used to determine the electron decay lifetime and give an indication of charge carrier recombination and mobility[46], [56]. In order to ensure an intermediate injection level, the contribution of the CdS n-type layer to the photovoltage and the number of excess charges in the space charge region are assumed to be negligible. Under this injection condition, the excess minority electron concentration in the absorber layer should be greater than its thermal equilibrium concentration. However, it still remains smaller than the majority hole concentration at equilibrium. The lifetime of the minority carrier (τ) can be calculated from the linear fit of the onset of the photovoltage decay, using the following equation

$$\tau = \frac{kT}{q}\left[\frac{1}{\frac{dV_{oc}}{dt}}\right] \qquad 6.4\text{-}1$$

where k is the Boltzmann constant, T is temperature and q is the elementary charge.

As can be seen in Figure 6.4-11, plasma and $CdCl_2$ treatments have only a slight effect on carrier lifetime. However, in the annealed samples there is a systematic difference with temperature indicating that increasing anneal temperature reduces recombination and enhances carrier extraction.

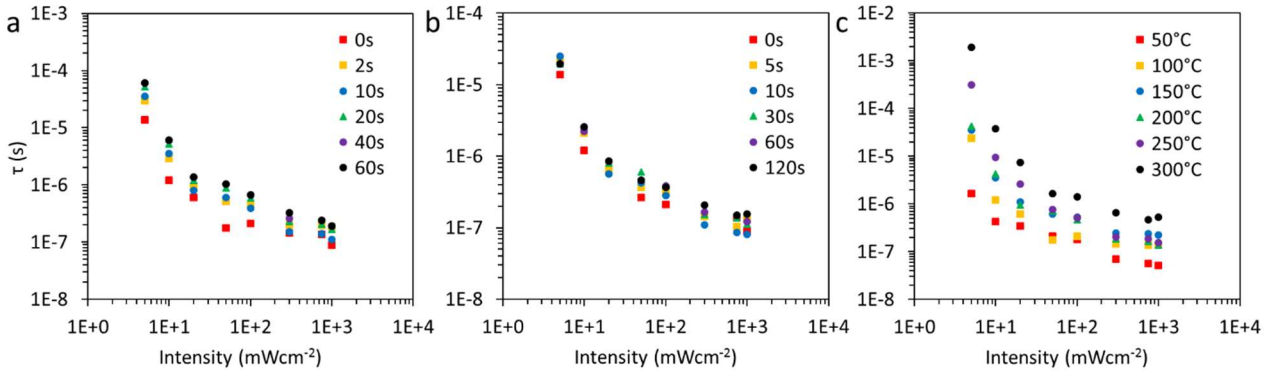

Figure 6.4-11 Recombination carrier lifetime (τ) plotted as a function of illumination intensity of FTO/CdS/CZTS/Au devices treated with a) N_2/H_2 plasma, b) $CdCl_2$ solution and c) low temperature annealing.

6.4.5 Device Optimisation

The final campaign of the device fabrication sought to amalgamate the beneficial approaches studied thus far. The highest efficiency achieved was for an 800 nm thick CZTS layer, with J_{sc} = 5.24 ± 0.42 mAcm^{-2}, V_{oc} = 0.49 ± 0.05V, FF = 38 ± 0.12%, and PCE = 1.0 ± 0.4%. In contrast to the first thickness experiment it was found that increasing absorber thickness increased the J_{sc} substantially. This is attributed to an increase in the depletion width due to increased carrier concentration allowing for more light to be effectively absorbed and extracted from the devices.

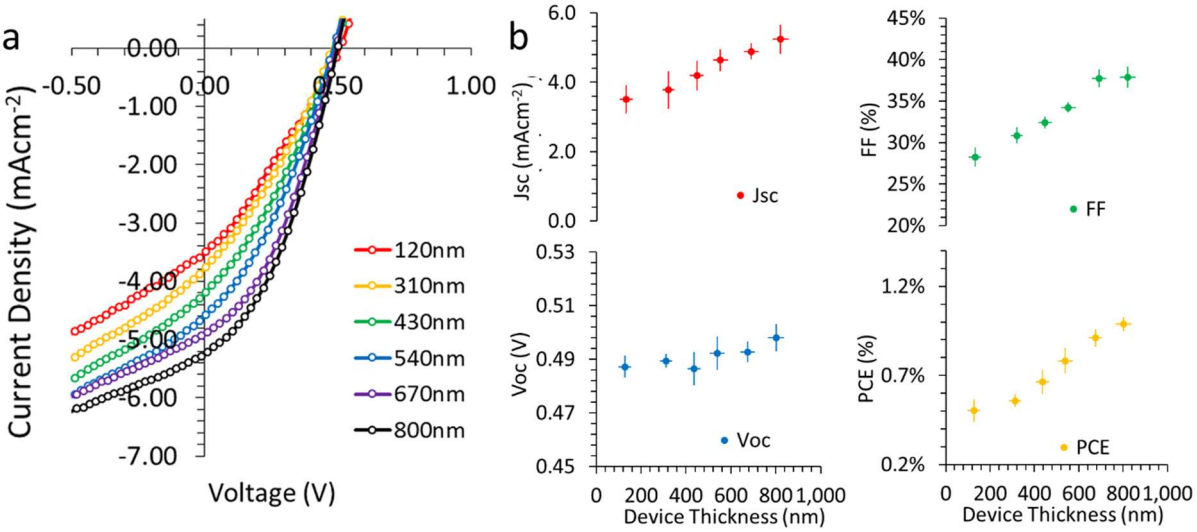

Figure 6.4-12 a) J-V curves and b) J_{sc}, V_{oc}, FF and PCE characteristics of "optimised" FTO/CdS/CZTS/Au devices comprising CZTS thin films with a corresponding thickness of 120nm, 310nm, 430nm, 540nm, 670nm and 800nm; filled circles and error bars correspond to the average and standard deviation respectively (across seven-nine devices on three substrates).

As before high R_s reduces J_{sc} and contributes to a generally poor *FF* in comparison to best performing CZTS-CdS devices from the literature. The low R_{sh} (as shown in Figure 6.4-13) is likely to be the cause of the subdued V_{oc} values compared to the theoretical value for the CZTS-CdS junction. For comparison, R_s and R_{sh} resistances of one of the best reported Mo/CZTS/CdS/ZnO/ITO solar cells (η = 7.2%) obtained by Ford et al. achieve 4.9 Ωcm^2 and 850 Ωcm^2 respectively[70]. However, in the case of Ford et al. their use of high temperature sulphurisation techniques to encourage passivation and grain growth of the CZTS photoactive layer (thereby removing short circuit pathways) is a major factor in their remarkably good device performance values.

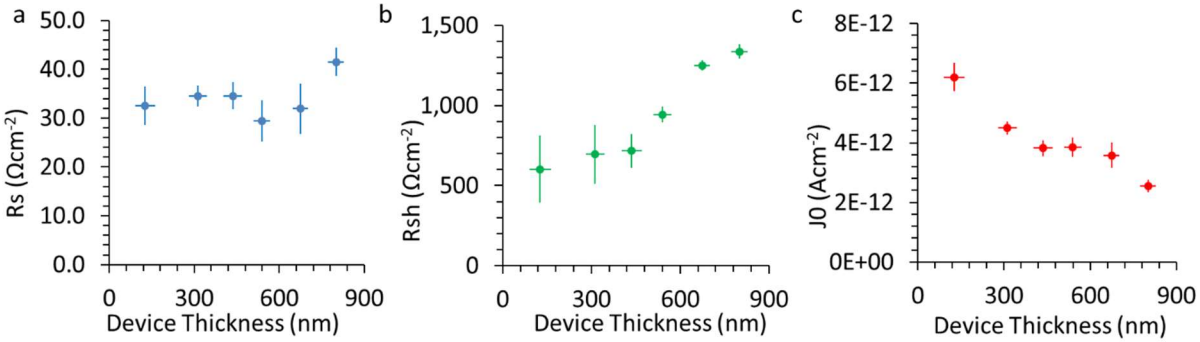

Figure 6.4-13 Performance characteristics of the devices shown in Figure 6.4-12. Filled circles and error bars correspond to the average and standard deviation across seven to nine devices across three substrates. Resistance a) R_s and b) R_{sh} and dark saturation current c) J_0 values are obtained from the two diode model of the light and dark J-V curves respectively.

A kink type anomaly in the light *J-V* curve is present in the third quadrant of the *J-V* curve of thinner devices as shown in Figure 6.4-14a. The corresponding device metric values for this device are as follows; J_{sc} = 3.00±0.35 mAcm^{-2}, V_{oc} = 0.45±0.1V, *FF* = 34±0.3%, and PCE = 0.52 ± 0.50%. Despite representing a significant improvement in both V_{oc} and J_{sc}, over earlier devices comprising an equivalently thick photoactive layer (~120nm). The kink has the effect of reducing the *FF* and therefore the *PCE* of the device. The observed kink can be ascribed to an extreme form of voltage-dependent photo current, which is possibly caused by an excessively thin p+

layer, relative to pseudo-intrinsic region of the photo-absorber[19], [20], which results in high energy doping at the absorber front surface[52], [53]. Increasing the absorber thickness removes the kink artefact in the *J-V* curve (as shown in Figure 6.4-14b) by making the pseudo-intrinsic region relatively much thicker than the doped p+ region.

Overall, annealing, $CdCl_2$ and N_2/H_2 treatments together with absorber layer thickness optimisation worked in combination to additively enhance the device performance, resulting in the champion device shown in Figure 6.4-14.

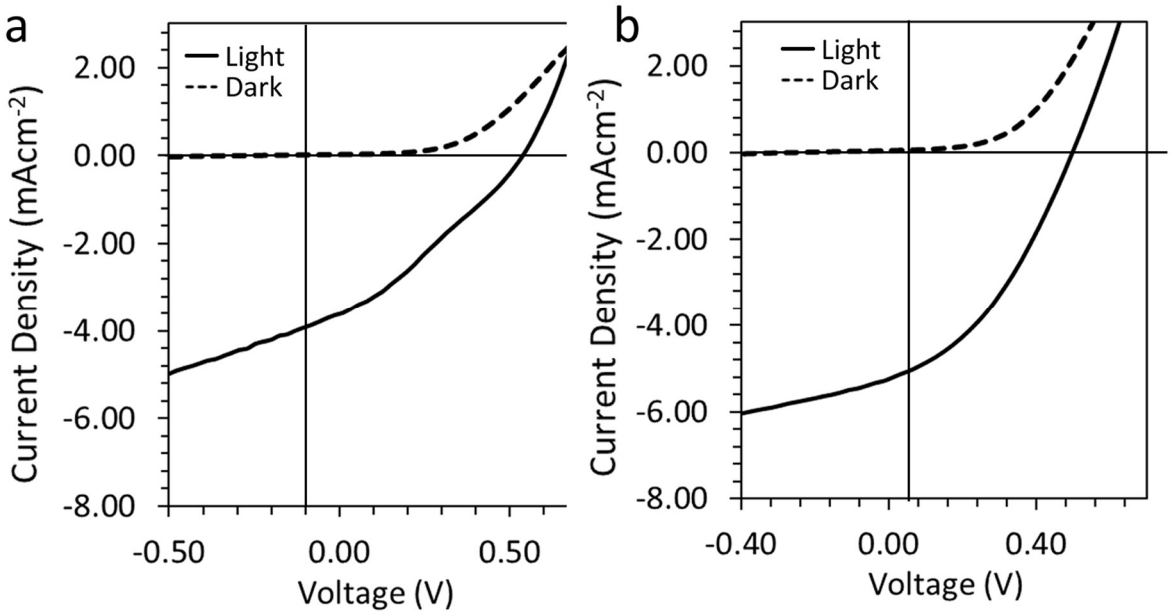

Figure 6.4-14 Dark and light J-V characteristics of FTO/CdS/CZTS/Au device of a) a device with a 120nm thick CZTS absorber layer displaying a characteristic "kink" and b) the "Champion" device.

The key technical characteristics of CZTS based devices, fabricated using a number of different routes, have been described in Table 6.1-1. From these published results it is clear that the use of high temperature annealing techniques in the fabrication of CZTS active layers, results in higher photovoltaic efficiencies for the devices in which they feature. In each case it is hypothesised that the high temperature causes enhanced grain growth and a subsequent reduction in the total

number of grain boundaries within the photo-active CZTS layer. It is also hypothesised that high temperatures are responsible for passivating the grain boundaries, thereby reducing the number of localised trapped states, which would otherwise inhibit the transportation of photo-generated charges within the device[25].

Table 6.4-1: Summary of best performing CZTS NC photovoltaic devices produced during each of the four investigations carried out as part of this work, including using in-air fabrication, annealing and passivation techniques.

Experiment	***J_{sc} (mAcm^{-2})***	***V_{oc} (V)***	***FF (%)***	***η (%)***	***Fabrication Methodology***
No Treatment Strategy - Thickness	1.47	0.42	32	0.21	Temperature Anneal: 200°C Thickness: 1130nm
$CdCl_2$	2.17	0.51	39	0.46	Temperature Anneal: 200°C $CdCl_2$ Treatment: 60s Thickness: 320nm
Plasma	1.66	0.45	39	0.29	Temperature Anneal: 200°C Plasma Treatment: 30s Thickness: 305nm
Annealing	3.69	0.48	43	0.71	Temperature Anneal: 200°C Thickness: 310nm
Optimised Treatment Strategy- Thickness	5.24	0.49	38	1.00	Temperature Anneal: 300°C CdCl2 Treatment: 60s Plasma Treatment: 30s Thickness: 800nm

As is shown in Table 6.4-1 the devices produced as part of the investigations undertaken in this work show a similar trend, wherein the use of higher fabrication temperatures and/or surface passivation techniques resulted in the best performing CZTS-CdS hetero-structure devices. However, in contrast to the earlier published results, the best performing devices produced in this work achieved similar

conversion efficiencies having been fabricated in ambient conditions, in part due to the passivation treatment strategies developed herein.

6.5 Conclusions

It has been shown that it is possible to form CZTS solar cells without the need for a high temperature anneal step, using a sulphur or selenium environment, or by processing devices in a dry-box. The first step was to perfect a ligand exchange routine to replace the long chain insulating surfactant with a shorter more volatile one. Optimising the ink formulation enabled fabrication of conformal stress-free semiconductor thin films. Using a combination of annealing, chemical passivation and reactive plasma treatment it has been shown that *PCE* can be improved. This was achieved by promoting grain growth and passivating dangling bonds at grain boundaries thus decreasing recombination and improving charge extraction. Device *PCE* performance lags behind the benchmarks of established high temperature methods but does give an insight into the mechanisms involved in improving devices performance. Within the framework of the literature I have also understood the mechanisms for instability and linked the physical and chemical properties of CZTS NC thin films with corresponding device performance.

6.6 References

[1] W. Wang, M. T. Winkler, O. Gunawan, T. Gokmen, T. K. Todorov, Y. Zhu, and D. B. Mitzi, "Device characteristics of CZTSSe thin-film solar cells with 12.6% efficiency," *Adv. Energy Mater.*, vol. 4, no. 7, p. 1301465, May 2014.

[2] T. Todorov, O. Gunawan, S. J. Chey, T. G. De Monsabert, A. Prabhakar, and D. B. Mitzi, "Progress towards marketable earth-abundant chalcogenide solar cells," *Thin Solid Films*, vol. 519, no. 21, pp. 7378–7381, Aug. 2011.

[3] O. Gunawan, T. K. Todorov, and D. B. Mitzi, "Loss mechanisms in hydrazine-processed $Cu_2ZnSn(Se,S)_4$ solar cells.," *Appl. Phys. Lett.*, vol. 97, no. 23, p. 233506, 2010.

[4] S. Chen, X. G. Gong, A. Walsh, and S.-H. Wei, “Defect physics of the kesterite thin-film solar cell absorber Cu[sub 2]ZnSnS[sub 4],” *Appl. Phys. Lett.*, vol. 96, no. 2, p. 021902, 2010.

[5] W. Liu, D. B. Mitzi, M. Yuan, A. J. Kellock, S. J. Chey, and O. Gunawan, “12% Efficiency CuIn(Se,S) 2 Photovoltaic Device Prepared Using a Hydrazine Solution Process †,” *Chem. Mater.*, vol. 22, no. 3, pp. 1010–1014, 2010.

[6] J. J. Scragg, T. Ericson, T. Kubart, M. Edoff, and C. Platzer-Björkman, “Chemical insights into the instability of Cu2ZnSnS4 films during annealing,” *Chem. Mater.*, vol. 23, no. 20, pp. 4625–4633, 2011.

[7] I. Repins, N. Vora, C. Beall, S.-H. Wei, Y. Yan, M. Romero, G. Teeter, H. Du, B. To, M. Young, and R. Noufi, “Kesterites and Chalcopyrites: A Comparison of Close Cousins,” in *MRS Proceedings*, 2011, vol. 1324.

[8] S. Delbos, “Këwhile thin films for photovoltaics : a review,” *EPJ Photovoltaics*, vol. 3, p. 35004, Aug. 2012.

[9] K. Ramasamy, M. a. Malik, and P. O’Brien, “Routes to copper zinc tin sulfide Cu2ZnSnS4 a potential material for solar cells,” *Chem. Commun.*, vol. 48, no. 46, p. 5703, Jun. 2012.

[10] P. J. Dale, K. Hoenes, J. Scragg, and S. Siebentritt, “A review of the challenges facing kesterite based thin film solar cells,” *Conf. Rec. IEEE Photovolt. Spec. Conf.*, pp. 002080–002085, Jun. 2009.

[11] M. Green, “The nature of quantum dot capping ligands,” *J. Mater. Chem.*, vol. 20, no. 28, p. 5797, 2010.

[12] Y. Wu, C. Wadia, W. Ma, B. Sadtler, and a P. Alivisatos, “Synthesis and photovoltaic application of copper(I) sulfide nanocrystals.,” *Nano Lett.*, vol. 8, no. 8, pp. 2551–2555, 2008.

[13] J. M. Luther, P. K. Jain, T. Ewers, and a P. Alivisatos, “Localized surface plasmon resonances arising from free carriers in doped quantum dots.,” *Nat. Mater.*, vol. 10, no. 5, pp. 361–366, May 2011.

[14] Y. Zhao, H. Pan, Y. Lou, X. Qiu, J. Zhu, and C. Burda, “Plasmonic Cu 2-xS nanocrystals: Optical and structural properties of copper-deficient copper(I) sulfides,” *J. Am. Chem. Soc.*, vol. 131, no. 12, pp. 4253–4261, Apr. 2009.

[15] C. Wu, Z. Zhang, Y. Wu, P. Lv, B. Nie, L. Luo, L. Wang, J. Hu, and J. Jie, “Flexible CuS nanotubes-ITO film Schottky junction solar cells with enhanced light harvesting by using an Ag mirror.,” *Nanotechnology*, vol. 24, no. 4, p. 045402, Feb. 2013.

[16] S. Gupta, Y. Batra, B. R. Mehta, and V. R. Satsangi, “Study of charge separation and interface formation in a single nanorod CdS-Cu(x)S heterojunction solar cell using Kelvin probe force microscopy.,” *Nanotechnology*, vol. 24, no. 25, p. 255703, 2013.

[17] C. Steinhagen, M. G. Panthani, V. Akhavan, B. Goodfellow, B. Koo, and B. a Korgel, “Synthesis of Cu(2)ZnSnS(4) nanocrystals for use in low-cost photovoltaics.,” *J. Am. Chem. Soc.*, vol. 131, no. 35, pp. 12554–5, Sep. 2009.

[18] U. Dasgupta, S. K. Saha, and A. J. Pal, “Fully-depleted pn-junction solar cells based on layers of Cu2ZnSnS4 (CZTS) and copper-diffused AgInS2 ternary nanocrystals,” *Sol. Energy Mater. Sol. Cells*, vol. 124, pp. 79–85, May 2014.

[19] S. Suehiro, K. Horita, K. Kumamoto, M. Yuasa, T. Tanaka, K. Fujita, K. Shimanoe, and T. Kida, “Solution-processed Cu2ZnSnS4 nanocrystal solar cells: Efficient stripping of surface insulating layers using alkylating agents,” *J. Phys. Chem. C*, vol. 118, no. 2, pp. 804–810, 2014.

[20] D. Lee and K. Yong, “Solution-processed Cu2ZnSnS4 superstrate solar cell using vertically aligned ZnO nanorods.,” *Nanotechnology*, vol. 25, no. 6, p. 065401, Mar. 2014.

[21] W. Shockley and H. J. Queisser, “Detailed Balance Limit of Efficiency of p-n Junction Solar Cells,” *J. App. Phys.*, vol. 32, no. 3, p. 510, 1961.

[22] A. Chirilă, P. Reinhard, F. Pianezzi, P. Bloesch, A. R. Uhl, C. Fella, L. Kranz, D. Keller, C. Gretener, H. Hagendorfer, D. Jaeger, R. Erni, S. Nishiwaki, S. Buecheler, and A. N. Tiwari, “Potassium-induced surface modification of Cu(In,Ga)Se2 thin films for high-efficiency solar cells.,” *Nat. Mater.*, vol. 12, no. 12, pp. 1107–11, Nov. 2013.

[23] P. Nagpal and V. I. Klimov, “Role of mid-gap states in charge transport and photoconductivity in semiconductor nanocrystal films,” *Nat. Commun.*, vol. 2, p. 486, Sep. 2011.

[24] J. Gao and J. C. Johnson, “Charge trapping in bright and dark states of coupled PbS quantum dot films,” *ACS Nano*, vol. 6, no. 4, pp. 3292–3303, Apr. 2012.

[25] D. A. R. Barkhouse, O. Gunawan, T. Gokmen, T. K. Todorov, and D. B. Mitzi, “Device characteristics of a 10.1% hydrazine-processed Cu2ZnSn(Se,S)4 solar cell,” *Prog. Photovoltaics Res. Appl.*, vol. 20, no. 1, pp. 6–11, Nov. 2012.

[26] J. Jasieniak, B. I. MacDonald, S. E. Watkins, and P. Mulvaney, “Solution-processed sintered nanocrystal solar cells via layer-by-layer assembly,” *Nano Lett.*, vol. 11, no. 7, pp. 2856–2864, Jul. 2011.

[27] B. Lei, W. W. Hou, S. H. Li, W. Yang, C. H. Chung, and Y. Yang, “Cadmium ion soaking treatment for solution processed CuInS xSe2-x solar cells and its effect on defect properties,” *Sol. Energy Mater. Sol. Cells*, vol. 95, no. 8, pp. 2384–2389, Aug. 2011.

[28] C. C. Wu, C. I. Wu, J. C. Sturm, and A. Kahn, “Surface modification of indium tin oxide by plasma treatment: An effective method to improve the efficiency, brightness, and reliability of organic light emitting devices,” *Appl. Phys. Lett.*, vol. 70, no. 11, p. 1348, 1997.

[29] F.-H. Wang, H.-P. Chang, C.-C. Tseng, C.-C. Huang, and H.-W. Liu, “Influence of hydrogen plasma treatment on Al-doped ZnO thin films for amorphous silicon thin film solar cells,” *Curr. Appl. Phys.*, vol. 11, no. 1, pp. S12–S16, Jan. 2011.

[30] Y. Roussillon, D. M. Giolando, D. Shvydka, a. D. Compaan, and V. G. Karpov, “Blocking thin-film nonuniformities: Photovoltaic self-healing,” *Appl. Phys. Lett.*, vol. 84, no. 4, pp. 616–618, 2004.

[31] J. Nelson, *The Physics of Solar Cells*, vol. 53, no. 5. London: Imperial College Press, pp.126-141, 2012.

[32] S. E. Habas, H. a S. Platt, M. F. a M. Van Hest, and D. S. Ginley, "Low-cost inorganic solar cells: From ink to printed device," *Chem. Rev.*, vol. 110, no. 11, pp. 6571–6594, 2010.

[33] a.-J. Cheng, M. Manno, a. Khare, C. Leighton, S. a. Campbell, and E. S. Aydil, "Imaging and phase identification of Cu2ZnSnS4 thin films using confocal Raman spectroscopy," *J. Vac. Sci. Technol. A Vacuum, Surfaces, Film.*, vol. 29, no. 5, p. 051203-051220, 2011.

[34] J. M. Luther, M. Law, M. C. Beard, Q. Song, M. O. Reese, R. J. Ellingson, and A. J. Nozik, "Schottky solar cells based on colloidal nanocrystal films," *Nano Lett.*, vol. 8, no. 10, pp. 3488–3492, 2008.

[35] D. Zhitomirsky, I. J. Kramer, A. J. Labelle, A. Fischer, R. Debnath, J. Pan, O. M. Bakr, and E. H. Sargent, "Colloidal quantum dot photovoltaics: The effect of polydispersity," *Nano Lett.*, vol. 12, no. 2, pp. 1007–1012, Feb. 2012.

[36] H. Sheng, L. Wenjun, and Z. Zhigang, "Band positions and photoelectrochemical properties of Cu2ZnSnS4 thin films by the ultrasonic spray pyrolysis method," *J. Phys. D. Appl. Phys.*, vol. 46, no. 23, p. 235108, Jun. 2013.

[37] J. Xu, X. Yang, Q.-D. Yang, T.-L. Wong, and C.-S. Lee, "Cu2ZnSnS4 Hierarchical Microspheres as an Effective Counter Electrode Material for Quantum Dot Sensitized Solar Cells," *J. Phys. Chem. C*, vol. 116, no. 37, pp. 19718–19723, 2012.

[38] T. Nakada, M. Hongo, and E. Hayashi, "Band offset of high efficiency CBD-ZnS/CIGS thin film solar cells," *Thin Solid Films*, vol. 431–432, pp. 242–248, May 2003.

[39] M. Gloeckler and J. R. Sites, "Efficiency limitations for wide-band-gap chalcopyrite solar cells," *Thin Solid Films*, vol. 480–481, pp. 241–245, 2005.

[40] K. Orgassa, U. Rau, Q. Nguyen, H. W. Schock, and J. H. Werner, "Role of the CdS buffer layer as an active optical element in Cu(In,Ga)Se2 thin-film solar cells," *Prog. Photovoltaics Res. Appl.*, vol. 10, no. 7, pp. 457–463, Nov. 2002.

[41] a Santoni, F. Biccari, C. Malerba, M. Valentini, R. Chierchia, and a Mittiga, "Valence band offset at the CdS/Cu 2 ZnSnS 4 interface probed by x-ray photoelectron spectroscopy," *J. Phys. D. Appl. Phys.*, vol. 46, no. 17, p. 175101-175118, May 2013.

[42] W. Bao and M. Ichimura, "Prediction of the Band Offsets at the CdS/Cu2ZnSnS4 Interface Based on the First-Principles Calculation," *Jpn. J. Appl. Phys.*, vol. 51, no. 10, pp. 267-276, 2012.

[43] J. C. Ramos, D. L. Kabir, I. Mejia, M. Mireles, C. a. Martinez, and M. a. Quevedo-Lopez, "Inkjet Printed Thin Film Transistors Using Cadmium Sulfide as Active Layer Prepared by In-Situ Micro-Reaction," *ECS Solid State Lett.*, vol. 2, no. 9, pp. P67–P69, 2013.

[44] a. Balandin, K. L. Wang, N. Kouklin, and S. Bandyopadhyay, "Raman spectroscopy of electrochemically self-assembled CdS quantum dots," *Appl. Phys. Lett.*, vol. 76, no. 2, p. 137-145, 2000.

[45] J. W. Thomson, K. Nagashima, P. M. MacDonald, and G. a. Ozin, "From sulfur-amine solutions to metal sulfide nanocrystals: Peering into the oleylamine-sulfur black box," *J. Am. Chem. Soc.*, vol. 133, no. 13, pp. 5036–5041, Apr. 2011.

[46] P. Wurfel and U. Wurfel, *Physics of solar cells : from basic principles to advanced concepts*. pp. 243-261, 2009.

[47] A. Kumar and C. Zhou, "The race to replace tin-doped indium oxide: Which material will win?," *ACS Nano*, vol. 4, no. 1, pp. 11–14, Jan. 2010.

[48] T. Minami, "Present status of transparent conducting oxide thin-film development for Indium-Tin-Oxide (ITO) substitutes," *Thin Solid Films*, vol. 516, no. 17, pp. 5822–5828, Jul. 2008.

[49] Y.-N. Kim, H.-G. Shin, J.-K. Song, D.-H. Cho, H.-S. Lee, and Y.-G. Jung, "Thermal Degradation Behavior of Indium Tin Oxide Thin Films Deposited by Radio Frequency Magnetron Sputtering," *J. Mater. Res.*, vol. 20, no. 6, pp. 1574–1579, Mar. 2005.

[50] S. Guha and V. Narayanan, "Oxygen vacancies in high dielectric constant oxide-semiconductor films," *Phys. Rev. Lett.*, vol. 98, no. 19, p. 196101, May 2007.

[51] V. Bilgin, I. Akyuz, E. Ketenci, S. Kose, and F. Atay, "Electrical, structural and surface properties of fluorine doped tin oxide films," *Appl. Surf. Sci.*, vol. 256, no. 22, pp. 6586–6591, Sep. 2010.

[52] F. Pfisterer, "The wet-topotaxial process of junction formation and surface treatments of Cu2S-CdS thin-film solar cells," *Thin Solid Films*, vol. 431–432, no. 3, pp. 470–476, May 2003.

[53] W. D. Gill and R. H. Bube, "Photovoltaic properties of Cu2S-CdS heterojunctions," *J. Appl. Phys.*, vol. 41, no. 9, pp. 3731–3738, 1970.

[54] J. Pan, M. Gloeckler, and J. R. Sites, "Hole current impedance and electron current enhancement by back-contact barriers in CdTe thin film solar cells," *J. Appl. Phys.*, vol. 100, no. 12, p. 124505, 2006.

[55] C. Persson, "Electronic and optical properties of Cu2ZnSnS4 and Cu2ZnSnSe4," *J. Appl. Phys.*, vol. 107, no. 5, p. 053710-053719, 2010.

[56] K. W. Johnston, "Efficient Schottky quantum dot photovoltaics: The roles of depletion, drift, and diffusion," *Appl. Phys. Lett.*, vol. 92122111, no. 12, 2008.

[57] C. a Cattley, A. Stavrinadis, R. Beal, J. Moghal, A. G. Cook, P. S. Grant, J. M. Smith, H. Assender, and A. a R. Watt, "Colloidal synthesis of lead oxide nanocrystals for photovoltaics.," *Chem. Commun. (Camb).*, vol. 46, no. 16, pp. 2802–2804, Apr. 2010.

[58] J. P. Clifford, J. P. Clifford, K. W. Johnston, K. W. Johnston, L. Levina, L. Levina, E. H. Sargent, and E. H. Sargent, "Schottky barriers to colloidal quantum dot lms," *Appl. Phys. Lett.*, vol. 91, no. 25, pp. 5–7, 2007.

[59] A. Khare, A. W. Wills, L. M. Ammerman, D. J. Norris, and E. S. Aydil, "Size control and quantum confinement in Cu2ZnSnS4 nanocrystals," *Chem. Commun.*, vol. 47, no. 42, p. 11721, 2011.

[60] F. J. Fan, L. Wu, M. Gong, G. Liu, Y. X. Wang, S. H. Yu, S. Chen, L. W. Wang, and X. G. Gong, "Composition-and band-gap-tunable synthesis of wurtzite-derived Cu 2ZnSn(S1-xSex)4 nanocrystals: Theoretical and experimental insights," *ACS Nano*, vol. 7, no. 2, pp. 1454–1463, Jan. 2013.

[61] K. W. Johnston, A. G. Pattantyus-Abraham, J. P. Clifford, S. H. Myrskog, D. D. MacNeil, L. Levina, and E. H. Sargent, "Schottky-quantum dot photovoltaics for efficient infrared power conversion," *Appl. Phys. Lett.*, vol. 92, no. 15, 2008.

[62] W. K. Metzger and M. Gloeckler, "The impact of charged grain boundaries on thin-film solar cells and characterization," *J. Appl. Phys.*, vol. 98, no. 6, p. 063701-063721, 2005.

[63] A. Nag, M. V. Kovalenko, J. S. Lee, W. Liu, B. Spokoyny, and D. V. Talapin, "Metal-free inorganic ligands for colloidal nanocrystals: S2-, HS-, Se2-, HSe-, Te2-, HTe -, TeS3 2-, OH-, and NH 2 - as surface ligands," *J. Am. Chem. Soc.*, vol. 133, no. 27, pp. 10612–10620, Jul. 2011.

[64] B. Gorka, B. Rau, P. Dogan, C. Becker, F. Ruske, S. Gall, and B. Rech, "Influence of Hydrogen Plasma on the Defect Passivation of Polycrystalline Si Thin Film Solar Cells," *Plasma Process. Polym.*, vol. 6, no. S1, pp. S36–S40, Jun. 2009.

[65] G. Gouadec and P. Colomban, "Raman Spectroscopy of nanomaterials: How spectra relate to disorder, particle size and mechanical properties," *Prog. Cryst. Growth Charact. Mater.*, vol. 53, no. 1, pp. 1–56, Mar. 2007.

[66] W. F. Zhang, Y. L. He, M. S. Zhang, Z. Yin, and Q. Chen, "Raman scattering study on anatase TiO 2 nanocrystals," *J.Phys. D. Appl. Phys.*, no. 33, pp. 912–916, 2000.

[67] A. Khare, B. Himmetoglu, M. Johnson, D. J. Norris, M. Cococcioni, and E. S. Aydil, "Calculation of the lattice dynamics and Raman spectra of copper zinc tin chalcogenides and comparison to experiments," *J. Appl. Phys.*, vol. 111, no. 8, p. 083707, 2012.

[68] D. Dumcenco and Y.-S. Huang, "The vibrational properties study of kesterite Cu2ZnSnS4 single crystals by using polarization dependent Raman spectroscopy," *Opt. Mater. (Amst).*, vol. 35, no. 3, pp. 419–425, Jan. 2013.

[69] H. Zhang, R. L. Penn, R. J. Hamers, and J. F. Banfield, "Enhanced Adsorption of Molecules on Surfaces of Nanocrystalline Particles," *J. Phys. Chem. B*, vol. 103, no. 22, pp. 4656–4662, 1999.

[70] Q. Guo, G. M. Ford, W. Yang, B. C. Walker, E. A. Stach, and H. W. Hillhouse, "Fabrication of 7.2% Efficient CZTSSe Solar Cells Using CZTS Nanocrystals.pdf," *J. Am. Chem. Soc*, vol. 132, no. 49, pp. 17384–17386, 2010.

Chapter 7 - Conclusion

7.1 Scope of this thesis

The aim of the thesis was to develop a synthesis for CZTS nanocrystals suitable for in air photovoltaic device production. Preliminary experiments demonstrated the reaction dynamics of TMSS with each of the Cu, Zn and Sn metal cation complexes in isolation. This yielded useful information about the precursor formation of each metal cation and their relative reactivity with oleylamine and shed light on which binary compounds were most likely to be useful in a quaternary one pot synthesis. This was used to inform the design of a synthesis for nearly mono-disperse CZTS nanocrystals at a range of temperatures over which two distinct CZTS phases could be selected. Nanocrystals prepared at 140°C were shown to be tetragonal CZTS whereas those prepared at temperatures greater than 170°C produced the hexagonal phase. Both nanocrystal forms exhibited homogeneous elemental composition as shown by STEM-EDX analysis.

The formation of hexagonal CZTS nanocrystals is often attributed to the induced growth from the preferentially formed Cu_xS nanocrystals due to the high reactivity of the Cu salt toward the sulfur precursor. In short, precursors and surfactants used in the syntheses strongly influence the composition and crystallographic phase of the final CZTS nanocrystals. The results presented here show that CZTS nanocrystals can be changed from a kesterite to a wurtzite phase by increasing the temperature of the reaction.

Outside the controlled (moisture free) glovebox environment, excessive agglomeration of the CZTS NCs lead to heavily aggregated semiconductor thin films with poor optoelectronic properties. To combat this, a method to improve surface

passivation using a co-ligand strategy was developed. The nanocrystal formation mechanism for Cu_2S-CZTS seed nucleation and growth through cation inter-diffusion was understood by analysing the LSPR response of the copper deficient Cu_2S type seed structure. Once understood, the co-ligand reaction was optimised to produce small, near-monodisperse and pure CZTS nanocrystals that remain stable in ambient conditions for many weeks and can withstand the solution processing required for fabrication of nanocrystal thin film solar cells.

This allowed the fabrication of CZTS solar cells without the need for a high temperature anneal step, using a sulphur or selenium environment, or by processing devices in a dry-box. By implementing a ligand exchange routine to replace the long chain insulating ligands with shorter and more volatile pyridine molecules, optimisation of the ink formulation was achieved, which then enabled the fabrication of conformal stress free semiconductor thin films.

Using a combination of annealing, chemical passivation and reactive plasma treatment the PCE of Au-CZTS-CdS-FTO nanocrystal thin film devices can be improved. This was achieved by promoting grain growth and passivating dangling bonds at grain boundaries, thus decreasing recombination and improving charge extraction. An investigation into the effects of these three techniques resulted in CZTS devices with efficiencies that lag behind the benchmark of established high temperature methods. Despite this, the findings of these investigations provide an insight into the mechanisms involved in improving devices performance. Within the framework of the literature I have also understood the mechanisms of CZTS nanocrystal instability and linked the physical and chemical properties of CZTS nanocrystal thin films with corresponding device performance.

Compared to commercially available solar cells the efficiencies reported here are very poor, being at least an order of magnitude less than what is required for commercial applications. However, within the area of in-air, low temperature processed CZTS based devices, to the best of my knowledge, this work has resulted in the fabrication of devices with the highest efficiency reported. More importantly several fundamental questions regarding the nature of CZTS NC surface passivation have been addressed, namely;

1. CZTS phase transition is highly temperature and precursor dependent.
2. Using LSPR information about the quality of particles produced can be related to the chemical composition at the NC surface.
3. Solvent and ligand choice is crucial when working under ambient conditions. In particular, amines although preferable for nanocrystal synthesis do not make coating conformal films easy and therefore co-ligand strategies are required to strike a balance between coating ease and NC chemistry, both of which influence the NC optoelectronic properties.
4. Instead of using high temperature sulfurisation techniques, a combination of alternate passivation treatments have been developed based around thermal annealing, reactive plasma treatment and small molecule thin film treatment.

Overall the thesis has developed a set of design rules to be adopted by researchers in the field, which incorporate choice of precursor, surface ligand, coating method and thin film post processing strategies. Lastly the thesis has discovered problems that researchers need to both understand and address in order to progress the use of CZTS in the future. As is outlined the following section.

7.2 Further work

1. Modifying the nanocrystal surface using novel organic or inorganic ligands can improve the robustness of chalcogenide nanocrystals to oxygen and moisture, as well as enhancing the surface passivation and charge transport properties of nanocrystal solid films. However, it is generally very difficult to simultaneously passivate both anionic and cationic surface sites by organic ligands alone, as there are always some dangling bonds on the surface. Epitaxial growth can not only eliminate both the anionic and cationic surface dangling bonds but also generate a new nanocrystal system with novel properties. Exchanging the Cu, Zn and Sn cations with Cd to form a CdS shell around the CZTS core would have a better chance of achieving complete passivation of the nanocrystal surface and thus improve charge transport within nanocrystal solar cells.

1. The application of bi-continuous interpenetrating network morphologies with optimal domain sizes has been shown to enhance the device performance of numerous organic[1] and PbS[2], [3] based nanostructured devices. These bulk heterojunction structures exploit an interpenetrating morphology with a large interfacial area to increase light absorption while maintaining efficient charge separation and extraction. Dasgupta et al.[4] have demonstrated the improvements in device performance afforded by maximising the absorber thickness to achieve fully-depleted CZTS-thin film solar cells. Further work into the application of nanostructured n-type donor materials such as TiO_2 and ZnO would likely improve device performance for ultra-thin CZTS devices.

2. Considerable non-uniformities have been observed in all major thin-film PV technologies[5], [6]. Variations in grain size, chemical composition and surface

morphology, often aggravated by barrier controlled transport mechanisms are known to inhibit device performance. Researchers have shown that by depositing an interfacial layer of active electrolyte onto a semiconductor thin film, inherent non-uniformities can be actively passivated upon the incidence of sun light[6], [7]. Even though the specific mechanisms of the work published thus far remain elusive, the potential for improvements in solar cell operational endurance could dramatically reduce lifetime costs of solar power.

7.3 References

[1] D. Zhitomirsky, I. J. Kramer, A. J. Labelle, A. Fischer, R. Debnath, J. Pan, O. M. Bakr, and E. H. Sargent, "Colloidal quantum dot photovoltaics: The effect of polydispersity," *Nano Lett.*, vol. 12, no. 2, pp. 1007–1012, Feb. 2012.

[2] E. J. D. Klem, D. D. MacNeil, P. W. Cyr, L. Levina, and E. H. Sargent, "Efficient solution-processed infrared photovoltaic cells: Planarized all-inorganic bulk heterojunction devices via inter-quantum-dot bridging during growth from solution," *Appl. Phys. Lett.*, vol. 90, no. 18, p. 183113-183120, 2007.

[3] M. C. Scharber, D. Mühlbacher, M. Koppe, P. Denk, C. Waldauf, A. J. Heeger, and C. J. Brabec, "Design rules for donors in bulk-heterojunction solar cells - Towards 10 % energy-conversion efficiency," *Adv. Mater.*, vol. 18, no. 6, pp. 789–794, Mar. 2006.

[4] U. Dasgupta, S. K. Saha, and A. J. Pal, "Fully-depleted pn-junction solar cells based on layers of Cu2ZnSnS4 (CZTS) and copper-diffused AgInS2 ternary nanocrystals," *Sol. Energy Mater. Sol. Cells*, vol. 124, pp. 79–85, May 2014.

[5] M. Graetzel, R. a. J. Janssen, D. B. Mitzi, and E. H. Sargent, "Materials interface engineering for solution-processed photovoltaics," *Nature*, vol. 488, no. 7411, pp. 304–312, Aug. 2012.

[6] Y. Roussillon, D. M. Giolando, D. Shvydka, a. D. Compaan, and V. G. Karpov, "Blocking thin-film nonuniformities: Photovoltaic self-healing," *Appl. Phys. Lett.*, vol. 84, no. 4, pp. 616–618, 2004.

[7] D. K. Koll, A. H. Taha, and D. M. Giolando, "Photochemical 'self-healing' pyrrole based treatment of CdS/CdTe photovoltaics," *Sol. Energy Mater. Sol. Cells*, vol. 95, no. 7, pp. 1716–1719, 2011.